Progress in Nuclear Magnetic Resonance Spectroscopy 102–103 (2017) 120–195

Contents lists available at ScienceDirect

Progress in Nuclear Magnetic Resonance Spectroscopy

journal homepage: www.elsevier.com/locate/pnmrs

Dynamic nuclear polarization for sensitivity enhancement in modern solid-state NMR

Aany Sofia Lilly Thankamony [1], Johannes J. Wittmann [1], Monu Kaushik, Björn Corzilius *

Institute of Physical and Theoretical Chemistry, Institute of Biophysical Chemistry, and Center for Biomolecular Magnetic Resonance (BMRZ), Goethe University Frankfurt, Max-von-Laue-Str. 7-9, 60438 Frankfurt, Germany

Edited by Geoffrey Bodenhausen and Beat Meier

ARTICLE INFO

Article history:
Received 27 February 2017
Accepted 8 June 2017
Available online 23 July 2017

ABSTRACT

The field of dynamic nuclear polarization has undergone tremendous developments and diversification since its inception more than 6 decades ago. In this review we provide an in-depth overview of the relevant topics involved in DNP-enhanced MAS NMR spectroscopy. This includes the theoretical description of DNP mechanisms as well as of the polarization transfer pathways that can lead to a uniform or selective spreading of polarization between nuclear spins. Furthermore, we cover historical and state-of-the art aspects of dedicated instrumentation, polarizing agents, and optimization techniques for efficient MAS DNP. Finally, we present an extensive overview on applications in the fields of structural biology and materials science, which underlines that MAS DNP has moved far beyond the proof-of-concept stage and has become an important tool for research in these fields.

Contents

* Corresponding author.
E-mail address: corzilius@em.uni-frankfurt.de (B. Corzilius).
[1] These authors contributed equally.

http://dx.doi.org/10.1016/j.pnmrs.2017.06.002
0079-6565/

1. Introduction

1.1. Structure determination by solid-state NMR

Solid-state nuclear magnetic resonance (NMR) spectroscopy is a powerful technique for the identification of chemical compounds as well as for the determination of molecular structures and dynamics of various kinds of materials. This versatility is based on several interactions that provide information about the local electronic environment of the nuclei or inter-spin distances. Thus, invaluable information about connectivity and conformation can be obtained with atomic resolution.

Several (multidimensional) NMR experiments under magic-angle spinning (MAS) conditions [1,2] have been designed over the past decades that allow a tailored extraction of the desired structural information while providing high spectral resolution [3–9]. Since MAS NMR is not relying on rotational averaging of anisotropic interactions by fast molecular tumbling of the analyte molecule, the method is not limited by the molecular size as is the case with high-resolution NMR in solution. This makes MAS NMR especially amenable for atomistic structural investigations of large or insoluble biomolecules and biomolecular complexes. It can also provide structural insights into functional materials. In particular, low-dimensional structures (*e.g.*, fibrillar and 2-dimensional arrangements, surface layers), as well as arrangements lacking general long-range order (*e.g.*, microcrystals, amorphous phases) are not accessible by means of X-ray crystallography and are therefore particularly interesting targets for MAS NMR.

Thus, it has been possible to address many problems in structural biology such as the arrangement of amyloidogenic peptides and proteins within (proto-)fibrils [10–14], large oligomeric complexes [15], membrane proteins [16,17], prokaryotic gas vesicles [18], etc. Currently, large strides are taken towards the investigation of such species within the environment of whole biological cells [19–21]. In materials science, MAS NMR has been applied to catalysis [22,23], glasses, functional materials [24,25], energy materials [26,27], biomass [28–31], soil [32–34], sediments [35], polymers [36–38], geomaterials [39–41], hybrid biomaterials [42–44], sol-gel materials [45,46], micro or macroporous materials (*e.g.*, MOFs) [47–49], etc.

1.2. Sensitivity issue

However, the low intrinsic sensitivity of NMR caused by the small thermal population differences of the spin states restricts many possible applications due to unreasonably long measurement times. To a certain degree, lower experimental temperatures and/or higher external magnetic fields can improve the signal-to-noise ratio. If nuclei with low gyromagnetic ratio are to be detected, polarization transfer schemes from nuclei with large gyromagnetic ratios (high-γ nuclei), such as ^{1}H or ^{19}F, are frequently exploited for increasing the sensitivity per unit time [50]. Recently, MAS with spinning frequencies beyond 100 kHz in combination with direct ^{1}H detection has shown promising developments in terms of resolution and sensitivity [51,52].

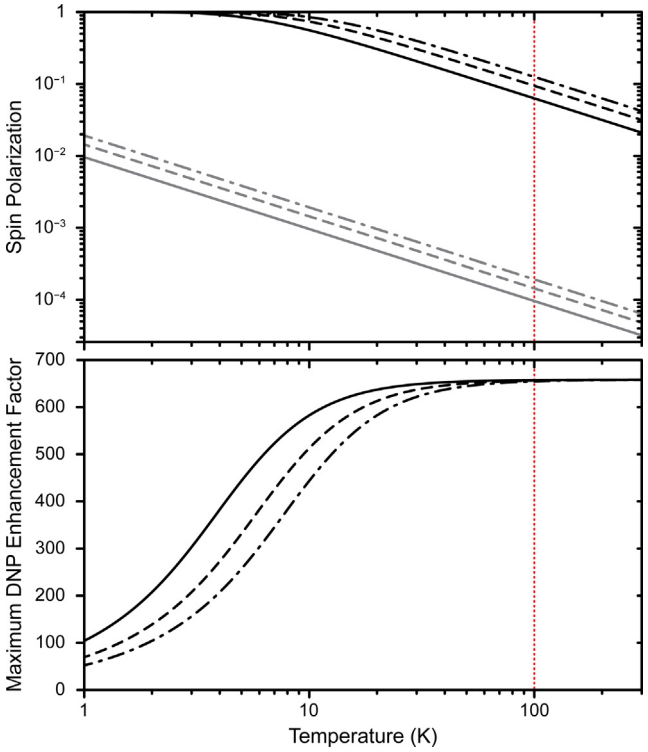

Fig. 1. Calculated absolute electron (black) and nuclear (gray) spin polarization following Eq. (1) (top) and maximum theoretical DNP enhancement factor after Eq. (2) (bottom) for a ^{1}H nuclear spin coupled to an $S = 1/2$ electron spin with $g = 2$. Magnetic fields are 9.4 T (solid line), 14.1 T (dashed line) and 18.8 T (dash-dotted line). The typical operational temperature of 100 K for MAS-DNP is marked by a vertical red dotted line.

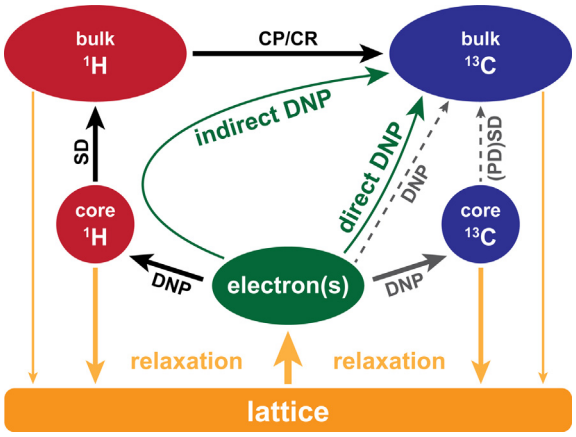

Fig. 2. Schematic representation of possible DNP transfer pathways in a system containing ^{1}H and ^{13}C. The latter nucleus was chosen for demonstration purposes; the scheme is valid for arbitrary low-γ nuclei. Green arrows distinguish between indirect (*e.g.*, *via* heteronuclear transfer from ^{1}H to ^{13}C) and direct DNP transfer. (PD)SD and CP/CR stand for (proton-driven) spin diffusion and cross polarization/cross relaxation.

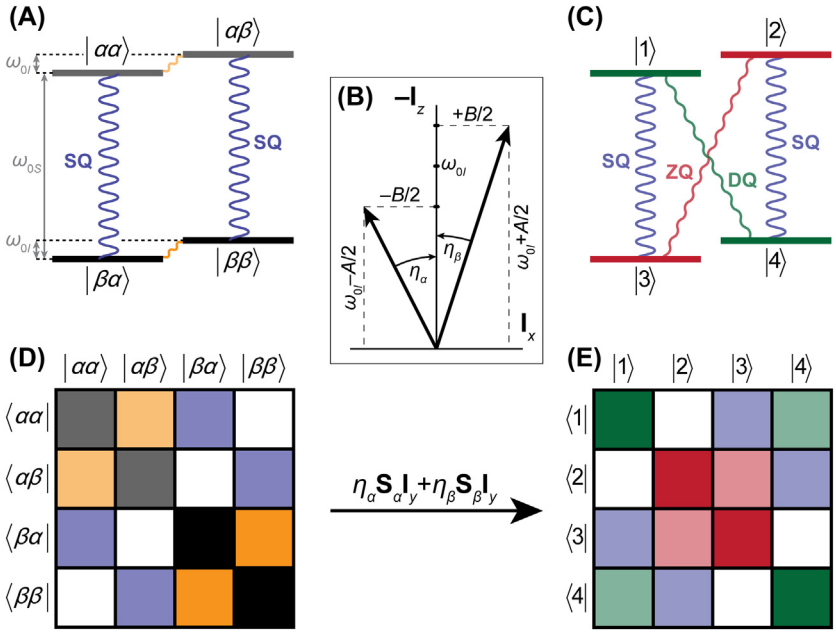

Fig. 3. (A) Energy scheme of a two-spin system with $S = 1/2$, $I = 1/2$ in the Zeeman basis. SQ coherences excited by the μw field are depicted in blue, coherences introduced by the pseudo-secular HFI in orange. (B) Depiction of the eigenframe branching of the nuclear states in the different (α, β) electron spin polarization subspaces. (C) Energy scheme in the eigenbasis of the static spin Hamiltonian (including HFI, but neglecting the μw field). SQ, DQ, and ZQ coherences are shown in blue, green, and red, respectively, as are eigenstates connected by the DQ or ZQ coherences. (D) Matrix representation of the Hamiltonian in the Zeeman basis [same color code as in (A)]. Neglecting μw-induced coherences the Hamiltonian is block-diagonal; the β electron spin subspace is shown in lighter colors. (E) Hamiltonian after diagonalization [same color code as in (C)].

Nevertheless, the overall gains are small as the signal intensity is governed by a thermal population difference, determined by the Boltzmann factor:

$$P = \tanh\left(\frac{\gamma\hbar B_0}{2k_B T}\right). \quad (1)$$

Here, P is the spin polarization, γ is its gyromagnetic ratio, and $\hbar$ and k_B are the reduced Planck constant and the Boltzmann constant, respectively. Besides the variation of the external magnetic field B_0, and the temperature T, a much higher polarization gain is obtained if hyperpolarization techniques are employed, since they can generate much larger, non-thermal population differences. Among these are para-hydrogen induced polarization (PHIP) [53], chemically-induced dynamic nuclear polarization (CIDNP) [54], spin-exchange optical pumping (SEOP) [55], and dynamic nuclear polarization (DNP) [56,57]. The latter stands out due to its broad applicability in material science and biomolecular NMR spectroscopy. This is based on its capability to provide substantial nuclear hyperpolarization at high magnetic fields under MAS conditions (see Fig. 1).

1.3. Concept of DNP

As proposed by Overhauser in 1953 [56] and subsequently verified by Carver and Slichter [57], the much larger polarization of electron spins can be transferred to nuclear spins upon saturation of electron paramagnetic resonance (EPR) transitions by means of microwave (μw) irradiation. In theory, a DNP enhancement factor, ε, equal to the ratio between the gyromagnetic ratios of the electron spin, S, and the nuclear spin, I, can be obtained:

$$\varepsilon_{\max} = \frac{P_S}{P_I}\left(\approx \frac{\gamma_S}{\gamma_I} \quad \text{for} \quad \gamma_S\hbar B_0 \ll k_B T\right). \quad (2)$$

This factor is ~660 for ^{1}H and is accordingly larger for nuclei with smaller gyromagnetic ratios. In the decades following the initial discovery, several experimental and theoretical studies have been performed pushing the achieved enhancement factors (*i.e.*, the intensity or integrated intensity ratio between spectra enhanced by μw irradiation and those in the absence of μw) towards the theoretical maximum [58–64]. As the experimental time necessary for the accumulation of a required signal-to-noise ratio scales inversely with the square of the signal intensity and thus with the enhancement factor, tremendous time savings and novel possibilities for NMR spectroscopy can be achieved.

For most of the analytes under study, the application of DNP requires doping the (diamagnetic) sample with paramagnetic centers as sources of polarization. Usually, stable radicals fulfilling certain criteria serve as polarizing agents (PAs). These criteria are mainly governed by several possible mechanisms for DNP, besides other considerations regarding sample constitution. Furthermore, in order to provide the required μw irradiation and to match DNP conditions, specialized instrumentation (*i.e.*, μw source, DNP MAS NMR probe as well as cryogenic gas supply for MAS) has to be utilized. The theoretical and practical consequences of this broad scientific field, comprising specialized engineering, radical chemistry, EPR and state-of-the-art MAS NMR, create a scenario where all involved researchers are expected to intuitively understand the complex interplay between these fields.

1.4. Scope of this review

This review will provide an in-depth overview about the theoretical and practical aspects of DNP under MAS conditions at high magnetic fields. Here we will focus on topics of current state-of-the-art that have already proven applicability towards problems in structural biology and materials science.

In the following two sections, a detailed description of the theory of DNP mechanisms prominent under MAS conditions is given. Here, we will cover not only the quantum-mechanical description of the initial polarization transfer mechanisms but also the processes responsible for spreading and potential drainage of enhanced polarization within a large network of nuclear spins.

Furthermore, important methods of read-out and utilization of enhanced nuclear spin polarization by MAS NMR are described. In the same vein, we draw the connection between EPR properties of the PAs and the resulting DNP field- or frequency profiles. The specialized instrumentation required for MAS DNP, including modifications to existing MAS NMR instrumentation, is illustrated in Section 4. The focus lies on recent developments, for example, the development of high-power high-frequency μw sources and cryogenic MAS instrumentation, that played a crucial role for bringing DNP up to speed with contemporary NMR at high magnetic fields. In the subsequent Section 5, the development of the large variety of available PAs together with their DNP-relevant properties are covered. Concepts for optimizing various experimental parameters as well as sample preparation techniques proven for efficient DNP are reviewed in Section 6. Finally, the large potential of DNP for accelerating conventional NMR experiments and enabling novel experimental techniques is illustrated using several examples and applications in biology and materials research.

Especially in the last sections, it will become clear that DNP-enhanced MAS NMR has moved well beyond the proof-of-principle phase. However, the transition from a mostly explorative technique to a powerful method capable of providing invaluable structural data has only occurred very recently, in particular in the field of structural biology. This is underlined by the fact that of all published studies in which DNP enhancement substantially contributed to the extraction of structural information, more than 50% have been published just during the last two years. A similar boom has been observed in the field of materials research slightly earlier.

This review is limited in scope to principles relevant for MAS NMR and accompanying techniques such as (high-field) quadrupolar and wideline NMR. For a detailed description of other DNP-based hyperpolarization techniques, including dissolution DNP for hyperpolarized NMR in solution or magnetic resonance imaging or spectroscopy (MRI/MRS) and related topics, we refer the reader to several other excellent reviews [65–73].

2. Mechanisms and transfer pathways

For a full understanding of DNP, we have to review the complete chain of polarization transfer from the electron spin of the PA to the nucleus where it is finally detected using typical MAS NMR schemes as illustrated in Fig. 2. We can generally separate the involved chain of events into three steps:

(1) The initial DNP transfer
(2) The propagation of the polarization to the nuclei of interest
(3) The direct detection or heteronuclear transfer of polarization for indirect detection.

We will briefly describe these three steps and provide a thorough review in the following subsections.

For the first point, the usual approach is to restrict the number of considered spins to the bare minimum required in order to describe a specific mechanism. In this context, we have to consider the solid effect (SE), the cross effect (CE), and the Overhauser effect (OE). These mechanisms can be explained with a minimum of just two or three spins, allowing us to derive analytical solutions that describe the underlying quantum mechanics. For the description of SE (Section 2.1.1), we will review the situation of a static sample that can approximately describe PAs featuring (nearly) isotropic EPR spectra under MAS, and discuss the ramifications if the EPR spectrum of the PA features a significant anisotropy. The CE mechanism varies rather strongly when comparing samples under MAS with the static case; we will focus on the MAS situation here (Section 2.1.2), but briefly review the steps required for description of static CE (Section 2.1.2.6). OE theory has not yet been described in detail for insulating solids, therefore, we review the general principles for electron–nuclear (e–n) cross-relaxation in Section 2.1.3. These general concepts are almost exclusively based on liquid-state DNP experiments, however, significant progress to describe OE-enabling dynamics in solids has been made recently. Thermal mixing (TM) is another mechanism that is closely related to CE when many electrons and nuclei interact strongly at low temperatures (typically $T < 10$ K). As these conditions are generally not fulfilled during MAS DNP, we will not discuss TM in detail.

After the polarization has been transferred to the directly hyperfine-coupled nuclei, it has to propagate to the nuclei of interest, which are typically on molecules that are located at some distance from the PA. Therefore, this usually involves homonuclear spin diffusion (Section 2.2) through the cryoprotecting matrix and competes with the dynamic loss of polarization by spin-lattice relaxation.

Finally, the enhanced polarization is utilized on the nucleus of interest. This can happen in an indirect manner where advantage is taken of efficient spin diffusion through the ^{1}H network. The polarization that has built up on ^{1}H is then transferred to low-γ nuclei for detection or further evolution. Alternatively, polarization that has built up directly on the low-γ nuclear spins can be read out or used in typical MAS NMR schemes. This direct DNP approach is often favored for alternative transfer pathways and can result in complementary information as compared to indirect DNP experiments (see Section 2.3.2).

2.1. Initial DNP transfer: DNP mechanisms

2.1.1. Solid effect

2.1.1.1. Spin dynamics in static samples. The solid effect in its simplest form is a two-spin process. It relies on the excitation of nominally forbidden electron–nuclear (e–n) double- and zero-quantum coherences by μw irradiation; these transitions are partly allowed due to a mixing of nuclear spin states. Like in common EPR techniques such as electron spin-echo envelope modulation (ESEEM) or electron–electron double resonance (ELDOR), the pseudo-secular hyperfine coupling is the driving interaction of such processes.

In the simplest case, a two-spin system of one $S = 1/2$ electron spin and one $I = 1/2$ nucleus can be described in a four-dimensional Hilbert space comprised of the Zeeman basis $\{|\alpha\alpha\rangle, |\alpha\beta\rangle, |\beta\alpha\rangle, |\beta\beta\rangle\}$ (Fig. 3). Here α and β symbolize the magnetic quantum number of each spin (*i.e.*, $\alpha \rightarrow m_i = +1/2$ and $\beta \rightarrow m_i = -1/2$). A dipolar coupling between the two spins introduces off-diagonal elements, perturbing this eigenbasis and introducing mixing between the Zeeman basis states. This can be deduced by the general spin Hamiltonian described by

$$\hat{H}_{\mathrm{SE}} = \frac{\mu_{\mathrm{B}}}{\hbar} \vec{B}\,\mathbf{g}\,\vec{\mathbf{S}} - \frac{\mu_{\mathrm{n}} g_{\mathrm{n}}}{\hbar} \vec{B}\,\vec{\mathbf{I}} + \vec{S}\,\mathbf{A}\,\vec{\mathbf{I}}\,. \tag{3}$$

Here, the first two terms are the electron and nuclear Zeeman interactions while the last term is the hyperfine interaction (HFI). Using the typical convention for the definition of the laboratory frame defined by the external (static) magnetic field component with magnitude B_0 oriented along z as well as the (linearly polarized) μw field component oriented along x and oscillating with frequency $\omega_{\mu\mathrm{w}}$, the magnetic field vector is defined as

$$\vec{B} = \begin{pmatrix} 2B_1 \cos(\omega_{\mu\mathrm{w}} t) \\ 0 \\ B_0 \end{pmatrix}, \tag{4}$$

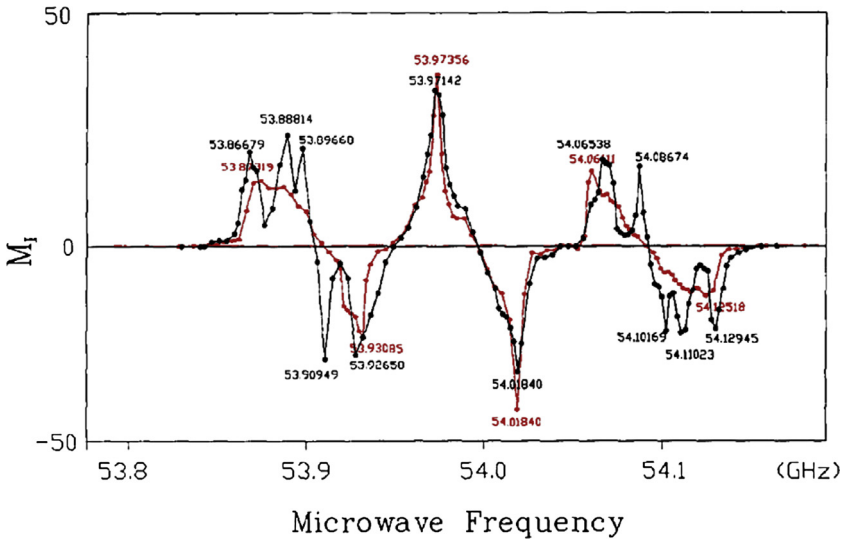

Fig. 4. Comparison between DNP-enhanced ^{13}C signal intensity of diamond under static (black) and MAS (red) conditions. Data acquired at 1.9 T. The graph is an overlay of two figures from the original publication; reprinted with permission from [78].

the Hamiltonian can then be written as

$$\hat{H}_{SE} = \frac{\mu_B g_{zz}}{\hbar} B_0 \mathbf{S}_z + \frac{\mu_B g_{xx}}{\hbar} B_1 \cos(\omega_{\mu w} t)(\mathbf{S}_+ + \mathbf{S}_-) - \frac{\mu_n g_n}{\hbar} B_0 \mathbf{I}_z - \frac{\mu_n g_n}{\hbar} B_1 \cos(\omega_{\mu w} t)(\mathbf{I}_+ + \mathbf{I}_-) + \vec{\mathbf{S}}\,\mathbf{A}\,\vec{\mathbf{I}}\,. \tag{5}$$

Upon transformation of this Hamiltonian into the frame rotating with $\omega_{\mu w}$ around z and truncation according to average Hamiltonian theory (AHT) after first order, the frequently used e–n Hamiltonian is obtained:

$$\hat{H}'_{SE} = \Omega_{0S}\mathbf{S}_z - \omega_{0I}\mathbf{I}_z + A_{zx}\mathbf{S}_z\mathbf{I}_x + A_{zy}\mathbf{S}_z\mathbf{I}_y + A_{zz}\mathbf{S}_z\mathbf{I}_z + \frac{\omega_{1S}}{2}(\mathbf{S}'_+ + \mathbf{S}'_-). \tag{6}$$

Prime symbols represent operators in the μw rotating frame; Ω_{0S} is the frequency offset between μw and electron Zeeman frequency, $\Omega_{0S} = \omega_{\mu w} - \omega_{0S}$. Note that here and in the following, the nuclear Zeeman frequency, ω_{0I}, is always considered to be positive; cases for nuclei with negative g_n value can be treated in a completely analogous manner. For simplification, the nuclear spin operators are transformed into a hybrid frame defined by the z-axis parallel to the static field and the dipolar HFI tensor frame, so that the e–n connection vector is pointing in the $\mathbf{I}'_x$ direction (Fig. 3):

$$\hat{H}'_{SE} = \Omega_{0S}\mathbf{S}_z - \omega_{0I}\mathbf{I}_z + A\mathbf{S}_z\mathbf{I}_z + \frac{B}{2}\mathbf{S}_z(\mathbf{I}'_+ + \mathbf{I}'_-) + \frac{\omega_{1S}}{2}(\mathbf{S}'_+ + \mathbf{S}'_-). \tag{7}$$

Here, per definition, $A = A_{zz}$ and $B = \sqrt{A_{zx}^2 + A_{zy}^2}$. Ignoring the μw-driven coherence [*i.e.*, the last term in Eq. (7)] the Hamiltonian is block diagonal in each (*i.e.*, α and β) electron spin subspace. Therefore, each subspace can be independently diagonalized, resulting in an effective m_S-dependent state mixing.

2.1.1.2. Definition of the eigenframe without μw. Under the assumptions introduced above, the eigenframe of the static part of the Hamiltonian is tilted around its y-axis by the presence of the pseudo-secular HFI. Each electronic subspace is tilted as described by the respective branching angle

$$\eta_{\alpha/\beta} = \arctan\left(\frac{B}{A \mp 2\omega_{0I}}\right). \tag{8}$$

The mixed eigenstates deviate from the Zeeman basis. The new eigenbasis $\{|1\rangle, |2\rangle, |3\rangle, |4\rangle\}$ is given by

$$\begin{aligned} |1\rangle &= p_\alpha|\alpha\alpha\rangle - q_\alpha|\alpha\beta\rangle \\ |2\rangle &= p_\alpha|\alpha\beta\rangle + q_\alpha|\alpha\alpha\rangle \\ |3\rangle &= p_\beta|\beta\alpha\rangle - q_\beta|\beta\beta\rangle \\ |4\rangle &= p_\beta|\beta\beta\rangle + q_\beta|\beta\alpha\rangle. \end{aligned} \tag{9}$$

With the mixing coefficients $p_i = \cos\left(\frac{\eta_i}{2}\right)$ and $q_i = \sin\left(\frac{\eta_i}{2}\right)$. This state mixing of nuclear Zeeman states is a requirement for SE to occur.

At high field typically encountered in DNP-enhanced MAS NMR, the hyperfine coupling is about two or more orders of magnitude smaller than the nuclear Zeeman interaction. Therefore, the branching angles can be approximately simplified to

$$\eta_{\alpha/\beta} \approx \mp\frac{B}{2\omega_{0I}} \text{ for } |A|, |B| \ll \omega_{0I}. \tag{10}$$

In this case the mixing coefficients become:

$$\begin{aligned} p_{\alpha/\beta} &\approx 1 \\ q_{\alpha/\beta} &\approx \mp\frac{B}{4\omega_{0I}}. \end{aligned} \tag{11}$$

Subsequently, the Zeeman basis $\{|\alpha\alpha\rangle, |\alpha\beta\rangle, |\beta\alpha\rangle, |\beta\beta\rangle\}$ as well as the quantum numbers m_S and m_I adequately describe the system due to the relatively weak mixing, while perturbing e–n coherences can still be excited by the μw field.

2.1.1.3. SE matching and coherences excited by μw. In order to induce SE mixing within the spin pair, an e–n zero-quantum (ZQ) or double-quantum (DQ) transition has to be excited. The respective coherences build up when the connected eigenstates are degenerate in the μw rotating frame. ZQ transitions occur between $|2\rangle$ and $|3\rangle$ (or $|\alpha\beta\rangle$ and $|\beta\alpha\rangle$ in the unperturbed basis), DQ transitions between $|1\rangle$ and $|4\rangle$ (or $|\alpha\alpha\rangle$ and $|\beta\beta\rangle$). Therefore, the respective matching conditions are fulfilled when

$$\omega_{\mu w} = \omega_{0S} \mp \omega_{0I}. \tag{12}$$

Here, the difference in Larmor frequencies corresponds to the DQ transitions, whereas the sum is relevant to the ZQ transitions.

The effective SE transition moments can be obtained by transforming the μw Hamiltonian

$$H'_{\mu w} = \frac{\omega_{1S}}{2}(\mathbf{S}'_{+} + \mathbf{S}'_{-}) \tag{13}$$

into the eigenframe of the static Hamiltonian according to the difference in branching angles[2]:

$$\eta^{-} = \frac{\eta_{\alpha} - \eta_{\beta}}{2}. \tag{14}$$

Then the effective μw Hamiltonian is

$$H''_{\mu w} = \frac{\omega_{1S}}{2}\left\{(\mathbf{S}'_{+} + \mathbf{S}'_{-})\cos\eta^{-} + \frac{1}{2}[(\mathbf{S}'_{+}\mathbf{I}'_{+} + \mathbf{S}'_{-}\mathbf{I}'_{-}) - (\mathbf{S}'_{+}\mathbf{I}'_{-} + \mathbf{S}'_{-}\mathbf{I}'_{+})]\sin\eta^{-}\right\}. \tag{15}$$

In the pseudo-high-field approximation ($|A|, |B| \ll \omega_{0I}$), η^{-} can be simplified to

$$\eta^{-} \approx -\frac{B}{2\omega_{0I}}, \tag{16}$$

and subsequently the final, effective μw Hamiltonian is obtained:

$$H''_{\mu w} = \frac{\omega_{1S}}{2}\{(\mathbf{S}'_{+} + \mathbf{S}'_{-}) - \frac{B}{4\omega_{0I}}[(\mathbf{S}'_{+}\mathbf{I}'_{+} + \mathbf{S}'_{-}\mathbf{I}'_{-}) - (\mathbf{S}'_{+}\mathbf{I}'_{-} + \mathbf{S}'_{-}\mathbf{I}'_{+})]\}. \tag{17}$$

The EPR single-quantum (SQ) transition moment (first term) is practically unchanged while the e–n DQ and ZQ transition moments (second and third terms of Eq. (17), respectively) are introduced with an effective scaling factor, $B/2\omega_{0I}$, compared to the SQ transition. Due to the small magnitude of this factor, the transition probability is relatively low ($\sim 10^{-4}$–10^{-8} relative to that of the SQ). Thus, large absolute μw field strengths are required in order to sufficiently drive these transitions and build up significant coherence.

As long as a SE transition is selectively excited (*i.e.*, the homogeneous linewidth of all possible transitions is small compared to the effective μw field strength), the system can be separated into the ZQ and DQ subspaces and evolution of the spin system can be described by a pseudo (doublet) spin following the simple Bloch equations [74]. Such a simplification will be useful for analysis of effective polarization transfer rates as is explained in more detail in Section 2.2.

2.1.1.4. SE under MAS. If the two-spin system exhibits a relatively large anisotropy, for example if a mono-nitroxide PA is considered, the spin eigenstates show significant periodic modulations due to MAS. In this case, electron SQ as well as e–n DQ and ZQ transitions can be induced transiently during level anti-crossings (LACs) [75]. These μw-driven LACs occur when the energy levels of connected spin states cross each other in the frame rotating with the μw frequency (see also below for a more detailed description in context of CE in Section 2.1.2 and Fig. 6). If the variations in eigenstate energy due to anisotropy is larger than ω_{0I}, SQ as well as ZQ and/or DQ LACs will occur alternatingly. This situation is similar to the typically described differential SE (for further details see Sections 2.2.1.5 and 3.2.1), where enhancement by ZQ and DQ transitions partially cancel in a static sample with an inhomogeneously broadened EPR signal [76]. However, SQ LACs inflict a large saturation of the electron spin [75], which will reduce the polarization available for transfer to the nuclear spin [77].

In cases where the anisotropy is small compared to ω_{0I} (*e.g.*, for trityl- and BDPA-type radicals), SE-enabling ZQ or DQ transitions can be selectively excited. Nevertheless, modulations in spin energies might still reduce the net excitation efficiency of the e–n ZQ or DQ transition of an individual spin-packet, however, virtually all spin-packets will experience a SE-inducing LAC during a rotor period. This might in fact increase the overall DNP enhancement under MAS as compared to the static case [75]. In a singular demonstration, Zhou and co-workers have compared DNP of natural and synthetic diamonds under static and MAS conditions within the same experimental setup at a rather low field of 1.9 T [78,79]. Interestingly, a splitting pattern—caused by anisotropic HFI to ^{14}N in nitrogen centered radicals—was observed in the DNP frequency profile for the static sample; that pattern was smeared out under MAS as is shown in Fig. 4. Unfortunately, the absolute ^{13}C enhancement factors could not be evaluated. Further experimental quantitative comparisons of these two cases (*i.e.*, static *vs.* MAS) with systems operating exclusively under SE have not been reported to our knowledge.

2.1.2. Cross effect

2.1.2.1. Spin dynamics under MAS. The theoretical description of the CE is considerably more complex than that of the SE. Not only does the required additional electron spin increase the dimensionality of the Hilbert space to at least 8, but the description of CE under MAS also differs significantly from that of a static sample. Recent quantum-mechanical descriptions of the spin dynamics have been given independently by Hu et al. [80] and Hovav et al. [81]. In both cases, the CE was treated as a static effect, where a μw field is applied to Zeeman states that are coupled by electronic and hyperfine interactions. As we will see, this situation relies on a peculiar set of matching conditions, where the difference in effective Larmor frequencies of the two electron spins matches the nuclear Zeeman frequency while at the same time one of the two electron spins is on resonance with the incident μw frequency:

$$(\Delta\omega_{0S} = |\omega_{0S,1} - \omega_{0S,2}| = \omega_{0I}) \quad \wedge \quad (\omega_{\mu w} = \omega_{0S,1} \vee \omega_{0S,2}) \tag{18}$$

In an ideal, hypothetical case, one could imagine a system of two electron spins with isotropic Zeeman interactions where the overall breadth of each EPR resonance is sufficiently small compared to ω_{0I}. Such a gedankenexperiment has been elaborated in detail by Wollan [61]. In reality, finding two paramagnetic species which fulfil this condition is rather unpractical. A few serendipitous cases could be thought of, for example, a system of trityl- and BDPA-type radicals would roughly match the above condition for ^{13}C and allow CE within a radical mixture as Michaelis et al. have demonstrated at a field of 5 T [82]. However, even in this case the breadth of the trityl spectrum is of the same order as ω_{0I}, which leads to anisotropy in CE matching.

A revolutionary description of CE under MAS has been proposed by Thurber and Tycko and almost simultaneously by Mentink-Vigier et al. in 2012 [75,83]. In their theory, the spin system periodically undergoes level anti-crossing (LAC) events, during which polarization can be exchanged between electron and nuclear spins. This model not only allows for a temporal separation of μw irradiation and CE matching events but also predicts the nuclear depolarization by MAS, which has recently been demonstrated experimentally [84–86]. A more detailed description of such LACs is given in Section 2.1.2.5 and practical aspects of nuclear depolarization are covered in Section 6.1.2.

As the simplest spin system capable of describing the CE, two electron spins ($S_1 = 1/2$ and $S_2 = 1/2$) and one nuclear spin have to be considered including electron–electron (e–e) coupling; the nucleus has to be hyperfine coupled to at least one of the electron spins:

$$\hat{H}_{CE} = \frac{\mu_B}{\hbar}\vec{B}(\mathbf{g}_1\vec{\mathbf{S}}_1 + \mathbf{g}_2\vec{\mathbf{S}}_2) - \frac{\mu_n g_n}{\hbar}\vec{B}\,\vec{\mathbf{I}} + \vec{\mathbf{S}}_1\mathbf{D}\vec{\mathbf{S}}_2 + (\vec{\mathbf{S}}_1\mathbf{A}_1 + \vec{\mathbf{S}}_2\mathbf{A}_2)\,\vec{\mathbf{I}}\,. \tag{19}$$

[2] Due to the opposite signs of the two branching angles this difference corresponds to the full angle between the two nuclear spin quantization axes.

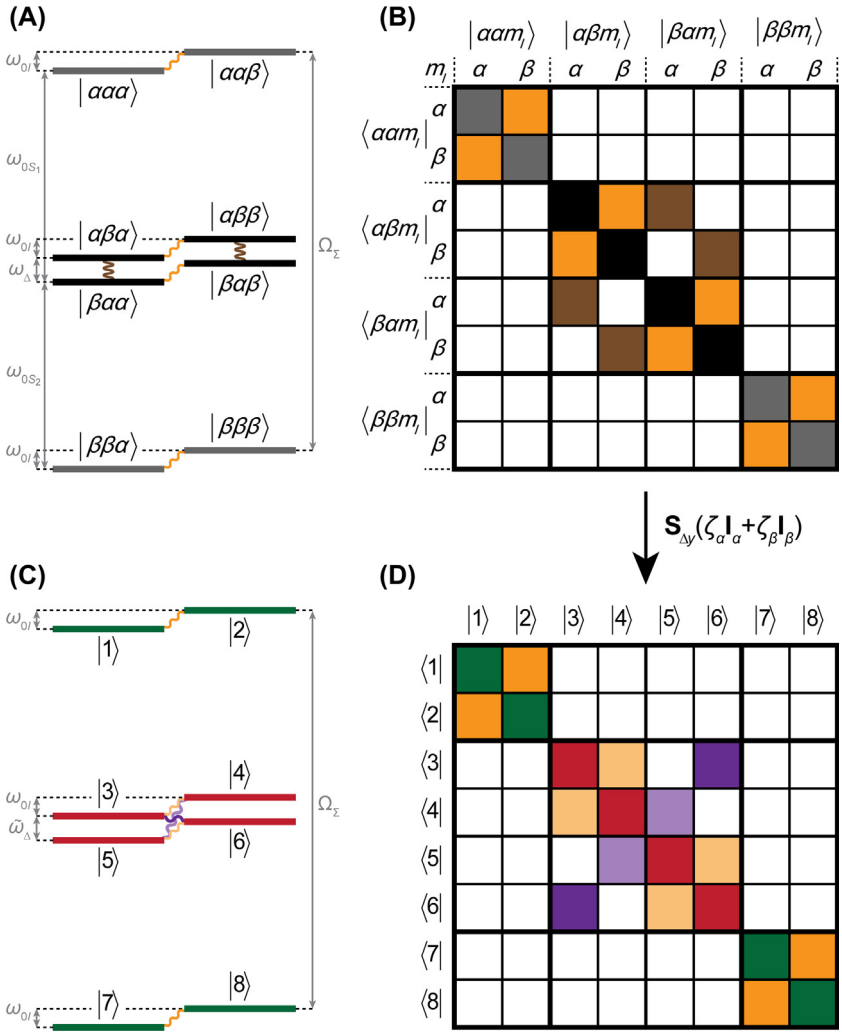

Fig. 5. (A) Energy scheme of the three-spin system containing two electron spins and one nuclear spin with $S_1 = 1/2$, $S_2 = 1/2$, and $I = 1/2$, respectively. (B) Matrix representation of the Hamiltonian in the Zeeman basis. Electronic ZQ states are marked in black, electronic DQ states that do not participate in CE are shown in gray. Electronic ZQ coherences induced by e–e dipolar coupling are depicted in brown, coherences introduced by the pseudo-secular HFI in orange. (C) Energy scheme and (D) matrix representation in the eigenbasis of the combined Zeeman and e–e interaction (including HFI but neglecting the μw terms). Electronic DQ and ZQ states are shown in green and red, respectively; (part of) the pseudo-secular HFI (orange) is transformed into e–e–n flip-flop-flip coherences marked in purple within the ZQ subspace.

Upon rotating-frame truncation, according to the oscillating μw field in Eq. (4), the Hamiltonian is reduced to components commuting with $\mathbf{S}_{iz}$, and μw-driven SQ elements appear:

$$\begin{aligned}\hat{H}'_{\mathrm{CE}} &= \Omega_{0S_1}\mathbf{S}_{1z} + \Omega_{0S_2}\mathbf{S}_{2z} - \omega_{0I}\mathbf{I}_z \\ &+ d(3\mathbf{S}_{1z}\mathbf{S}_{2z} - \vec{\mathbf{S}}'_1\vec{\mathbf{S}}'_2) - 2J\vec{\mathbf{S}}'_1\vec{\mathbf{S}}'_2 \\ &+ (A_{1zz}\mathbf{S}_{1z} + A_{2zz}\mathbf{S}_{2z})\mathbf{I}_z + (A_{1zx}\mathbf{S}_{1z} + A_{2zx}\mathbf{S}_{2z})\mathbf{I}_x + (A_{1zy}\mathbf{S}_{1z} + A_{2zy}\mathbf{S}_{2z})\mathbf{I}_y \\ &+ \frac{\omega_{1S_1}}{2}\mathbf{S}'_{1x} + \frac{\omega_{1S_2}}{2}\mathbf{S}'_{2x}.\end{aligned} \tag{20}$$

The effective e–e dipole coupling, $d = \frac{1}{2}D_{zz} - J$, and the exchange-coupling constant, $J = \frac{1}{3}(D_{xx} + D_{yy} + D_{zz})$, can be extracted from the full e–e coupling tensor. We can conveniently separate diagonal and off-diagonal elements:

$$\begin{aligned}\hat{H}'_{\mathrm{CE}} &= \underbrace{\Omega_{0S_1}\mathbf{S}_{1z} + \Omega_{0S_2}\mathbf{S}_{2z} - \omega_{0I}\mathbf{I}_z + D_d\mathbf{S}_{1z}\mathbf{S}_{2z} + (A_1\mathbf{S}_{1z} + A_2\mathbf{S}_{2z})\mathbf{I}_z}_{\hat{H}'_{\mathrm{CE,on}}} \\ &+ \underbrace{D_0(\mathbf{S}'_{1x}\mathbf{S}'_{2x} + \mathbf{S}'_{1y}\mathbf{S}'_{2y}) + (A_{1x}\mathbf{S}_{1z} + A_{2x}\mathbf{S}_{2z})\mathbf{I}_x + (A_{1y}\mathbf{S}_{1z} + A_{2y}\mathbf{S}_{2z})\mathbf{I}_y + \omega_{1S_1}\mathbf{S}'_{1x} + \omega_{1S_2}\mathbf{S}'_{2x}}_{\hat{H}'_{\mathrm{CE,off}}},\end{aligned} \tag{21}$$

with $D_d = 2(d - J)$, $D_0 = -(d + 2J)$, and $A_i = A_{i,zz}$; we have also dropped one index 'z' from the pseudo-secular HFI coupling constants.

As mentioned above, Thurber and Tycko as well as Mentink-Vigier et al. have introduced a way to understand the CE under MAS by considering the time evolution of the anisotropic Hamiltonian during one rotor period. We can identify three separate events that occur periodically and generally do not coincide with each other: μw events, CE matching events, and e–e events. Accordingly, we will consider three cases:

(1) the μw frequency is on resonance with one of the two electron spins and the frequency separation between the two electron spins is arbitrary;
(2) the frequency separation of the two electron spins equals the nuclear Larmor frequency;
(3) the Larmor frequency of the two electron spins is equal.

In the latter two cases, the μw frequency will be off-resonance with respect to both electron spins by an arbitrary value.

2.1.2.2. Microwave (spin-flip) events. In case (1), we assume that the μw-resonance condition is fulfilled for one electron spin, *j*. Furthermore, the other electron spin, *i*, shall be far off-resonance, so that $|\Omega_{0S_{k\neq j}}| \gg |D_0|$, and we neglect mixing of nuclear spin states by hyperfine couplings. Furthermore, we assume negligible differences in Rabi frequencies between the electrons, so that we can define a common Rabi frequency ω_{1S}. In that case, we can drop all state mixing terms of the static Hamiltonian, so that solely the μw excitation acts on Zeeman states:

$$\hat{H}'_{\mathrm{CE,SQ}} = \Omega_{0S_1}\mathbf{S}_{1z} + \Omega_{0S_2}\mathbf{S}_{2z} - \omega_{0I}\mathbf{I}_z + D_d\mathbf{S}_{1z}\mathbf{S}_{2z} + (A_1\mathbf{S}_{1z} + A_2\mathbf{S}_{2z})\mathbf{I}_z + \frac{\omega_{1S}}{2}(\mathbf{S}'_{1_+} + \mathbf{S}'_{1_-} + \mathbf{S}'_{2_+} + \mathbf{S}'_{2_-}). \tag{22}$$

During evolution of anisotropic Zeeman and dipolar interactions, the μw-resonance condition is met if $|\Omega_{0S_j}| = \frac{1}{2}|D_d \pm A_j|$. The signs depend on the magnetic spin states of the off-resonance electron and the nucleus. This leads to equilibration of the connected Zeeman states and saturation of the respective EPR transition.

After such a resonance condition has been passed through during an LAC, the resulting change in polarization will decay slowly with T_{1S} and therefore is memorized by the system for a certain period. The non-equilibrium populations can subsequently be transferred to the other electron and the nucleus in a concerted fashion during a CE event, or only to the other electron during a dipolar flip-flop event. We will first describe a CE event, and then discuss the importance of e–e events.

2.1.2.3. Cross-effect (flip-flop-flip) events. In order to understand the actual CE transfer event under MAS, we have to transform the Hamiltonian into a frame in which the full e–e dipolar interaction is diagonal. The static Hamiltonian (excluding μw terms) is block diagonal with two outer 2×2 blocks representing the e–e DQ subspace and one central 4×4 block representing the corresponding ZQ subspace (Fig. 5). Thus, it can be rearranged as follows:

$$\hat{H}'_0 = \Omega_\Sigma\mathbf{S}_{\Sigma z} + \omega_\Delta\mathbf{S}_{\Delta z} - \omega_{0I}(\mathbf{S}_\Sigma + \mathbf{S}_\Delta)\mathbf{I}_z + \frac{D_d}{4}(\mathbf{S}_\Sigma - \mathbf{S}_\Delta) + D_0\mathbf{S}_{\Delta x} + (A_\Sigma\mathbf{S}_{\Sigma z} + A_\Delta\mathbf{S}_{\Delta z})\mathbf{I}_z + \mathbf{S}_{\Sigma z}(A_{\Sigma x}\mathbf{I}_x + A_{\Sigma y}\mathbf{I}_y) + \mathbf{S}_{\Delta z}(A_{\Delta x}\mathbf{I}_x + A_{\Delta y}\mathbf{I}_y), \tag{23}$$

with $\mathbf{S}_{\Sigma z} = \frac{1}{2}(\mathbf{S}_{1z} + \mathbf{S}_{2z})$, $\mathbf{S}_{\Delta z} = \frac{1}{2}(\mathbf{S}_{1z} - \mathbf{S}_{2z})$, $\mathbf{S}_\Sigma = \mathbf{S}_1^\alpha\mathbf{S}_2^\alpha + \mathbf{S}_1^\beta\mathbf{S}_2^\beta$, $\mathbf{S}_\Delta = \mathbf{S}_1^\alpha\mathbf{S}_2^\beta + \mathbf{S}_1^\beta\mathbf{S}_2^\alpha$, $\mathbf{S}_{\Delta x} = \frac{1}{2}(\mathbf{S}'_{1_+}\mathbf{S}'_{2_-} + \mathbf{S}'_{1_-}\mathbf{S}'_{2_+})$, $\Omega_\Sigma = \Omega_{0S_1} + \Omega_{0S_2}$, $\omega_\Delta = \omega_{0S_1} - \omega_{0S_2}$, $A_\Sigma = A_1 + A_2$, $A_\Delta = A_1 - A_2$, $A_{\Sigma a} = A_{1a} + A_{2a}$, and $A_{\Delta a} = A_{1a} - A_{2a}$ for $a \in \{x, y\}$. The Σ index denotes operators within the DQ space while Δ marks operators confined to the ZQ space.

The tilting transformation below [Eq. (26)] acts exclusively on the ZQ subspace; thus we first separate that from the DQ subspace:

$$\hat{H}'_\Sigma = \Omega_\Sigma\mathbf{S}_{\Sigma z} - \omega_{0I}\mathbf{S}_\Sigma\mathbf{I}_z + \frac{D_d}{4}\mathbf{S}_\Sigma + \mathbf{S}_{\Sigma z}(A_\Sigma\mathbf{I}_z + A_{\Sigma x}\mathbf{I}_x + A_{\Sigma y}\mathbf{I}_y)$$
$$\hat{H}'_\Delta = \omega_\Delta\mathbf{S}_{\Delta z} - \omega_{0I}\mathbf{S}_\Delta\mathbf{I}_z + \frac{D_d}{4}\mathbf{S}_\Delta + D_0\mathbf{S}_{\Delta x} + \mathbf{S}_{\Delta z}(A_\Delta\mathbf{I}_z + A_{\Delta x}\mathbf{I}_x + A_{\Delta y}\mathbf{I}_y). \tag{24}$$

Each of these can now be transformed into the eigenframe of the HFI acting in the respective subspace:

$$\hat{H}'_\Sigma = \Omega_\Sigma\mathbf{S}_{\Sigma z} - \omega_{0I}\mathbf{S}_\Sigma\mathbf{I}_z + \frac{D_d}{4}\mathbf{S}_\Sigma + A_\Sigma\mathbf{S}_{\Sigma z}\mathbf{I}_z + B_\Sigma\mathbf{S}_{\Sigma z}\mathbf{I}''_x$$
$$\hat{H}'_\Delta = \omega_\Delta\mathbf{S}_{\Delta z} - \omega_{0I}\mathbf{S}_\Delta\mathbf{I}_z + \frac{D_d}{4}\mathbf{S}_\Delta + D_0\mathbf{S}_{\Delta x} + A_\Delta\mathbf{S}_{\Delta z}\mathbf{I}_z + B_\Delta\mathbf{S}_{\Delta z}\mathbf{I}'_x, \tag{25}$$

with $B_\Sigma = \sqrt{A_{\Sigma x}^2 + A_{\Sigma y}^2}$ and $B_\Delta = \sqrt{A_{\Delta x}^2 + A_{\Delta y}^2}$. The sole off-diagonal term which mixes the two electronic spin manifolds, $D_0\mathbf{S}_{\Delta x}$, is located in the ZQ space. Thus, it can be eliminated by a transformation acting selectively on that space, using the unitary operator:

$$U_\Delta = \exp[i\mathbf{S}_{\Delta y}(\zeta_\alpha\mathbf{I}_\alpha + \zeta_\beta\mathbf{I}_\beta)], \tag{26}$$

with $\mathbf{S}_{\Delta y} = \frac{1}{2i}(\mathbf{S}'_{1_+}\mathbf{S}'_{2_-} - \mathbf{S}'_{1_-}\mathbf{S}'_{2_+})$. The angles ζ_i are derived from the e–e ZQ mixing coefficients as

$$\zeta_{\alpha,\beta} = \arctan\left(\frac{2D_0}{2\omega_\Delta \pm A_\Delta}\right). \tag{27}$$

The resulting Hamiltonian has the form:

$$\hat{H}''_\Delta = \tilde{\omega}_\Delta\mathbf{S}'_{\Delta z} - \omega_{0I}\mathbf{S}_\Delta\mathbf{I}_z + \frac{D_d}{4}\mathbf{S}_\Delta + \tilde{A}_\Delta\mathbf{S}'_{\Delta z}\mathbf{I}_z + (\tilde{B}_\Delta\mathbf{S}'_{\Delta z} + \tilde{K}\mathbf{S}'_{\Delta x})\mathbf{I}'_x. \tag{28}$$

Alternatively, this can be expressed in terms of the raising and lowering operators as:

$$\hat{H}''_\Delta = \tilde{\omega}_\Delta\mathbf{S}'_{\Delta z} - \omega_{0I}\mathbf{S}_\Delta\mathbf{I}_z + \frac{D_d}{4}\mathbf{S}_\Delta + \tilde{A}_\Delta\mathbf{S}'_{\Delta z}\mathbf{I}_z + \left[\frac{\tilde{B}_\Delta}{2}\mathbf{S}'_{\Delta z} + \frac{\tilde{K}}{4}(\mathbf{S}'_{1_+}\mathbf{S}'_{2_-} + \mathbf{S}'_{1_-}\mathbf{S}'_{2_+})\right](\mathbf{I}'_+ + \mathbf{I}'_-). \tag{29}$$

For simplicity, we assume that $|\frac{A_\Delta}{2}| \ll |\omega_\Delta|$ at all times. This is a reasonable assumption except for the situation when $\omega_\Delta \approx 0$. Nevertheless, even in this case it is safe to assume that $|\frac{A_\Delta}{2}| \ll |D_0|$. Therefore, we can approximate that

$$\zeta_\alpha \approx \zeta_\beta \approx \zeta = \arctan\left(\frac{D_0}{\omega_\Delta}\right). \tag{30}$$

Under this assumption, we obtain the following simplified, effective frequencies:

$$\begin{aligned}\tilde{\omega}_\Delta &\approx \omega_\Delta\cos\zeta + D_0\sin\zeta\\ \tilde{A}_\Delta &\approx A_\Delta\cos\zeta\\ \tilde{B}_\Delta &\approx B_\Delta\cos\zeta\\ \tilde{K} &\approx -B_\Delta\sin\zeta.\end{aligned} \tag{31}$$

We can interpret this situation as follows within a basis where the $|\alpha\beta m_I\rangle$ and $|\beta\alpha m_I\rangle$ Zeeman states in the ZQ subspace are mixed with the coefficients $q_\zeta \approx \sin\frac{\zeta}{2}$ and $p_\zeta \approx \cos\frac{\zeta}{2}$ due to e–e coupling:

$$\begin{aligned}|1\rangle &= |\alpha\alpha\alpha\rangle, & |2\rangle &= |\alpha\alpha\beta\rangle\\ |3\rangle &= p_\zeta|\alpha\beta\alpha\rangle - q_\zeta|\beta\alpha\alpha\rangle, & |4\rangle &= p_\zeta|\alpha\beta\beta\rangle - q_\zeta|\beta\alpha\beta\rangle\\ |5\rangle &= p_\zeta|\beta\alpha\alpha\rangle + q_\zeta|\alpha\beta\alpha\rangle, & |6\rangle &= p_\zeta|\beta\alpha\beta\rangle + q_\zeta|\alpha\beta\beta\rangle\\ |7\rangle &= |\beta\beta\alpha\rangle, & |8\rangle &= |\beta\beta\beta\rangle,\end{aligned} \tag{32}$$

Note that the states in the DQ subspace (*i.e.*, $|1\rangle, |2\rangle, |7\rangle, |8\rangle$) remain unaffected. $\tilde{\omega}_\Delta$, ω_{0I}, D_d, and $\tilde{A}_\Delta$ determine the spin energies in the e–e ZQ subspace (*i.e.*, $|3\rangle, |4\rangle, |5\rangle, |6\rangle$). Terms scaling with $\tilde{B}_\Delta$ describe simultaneous e–n transitions connecting $|3\rangle$ and $|4\rangle$ as well as $|5\rangle$ and $|6\rangle$, effectively representing the SE in this system. Finally, terms scaling with $\tilde{K}$ describe e–e–n triple-spin transitions between $|3\rangle$ and $|6\rangle$ as well as $|4\rangle$ and $|5\rangle$. Upon transformation of the off-diagonal terms into the interaction frame of the diagonal elements of the Hamiltonian in Eq. (29), we immediately find that all components that scale with $\tilde{B}_\Delta$ (*i.e.*, e–n transitions) oscillate with ω_{0I}, but components proportional to $\tilde{K}$ (*i.e.*, e–e–n transitions) can become time independent when the CE matching condition is fulfilled:

$$\tilde{\omega}_\Delta = \pm\omega_{0I}. \tag{33}$$

For further simplification, in the typical case where $|\tilde{\omega}_\Delta| = \omega_{0I} \gg |D_0|$, we can conclude that ζ_i is small:

$$\zeta = \arctan\left(\frac{D_0}{\omega_\Delta}\right) \approx \frac{D_0}{\omega_\Delta}. \tag{34}$$

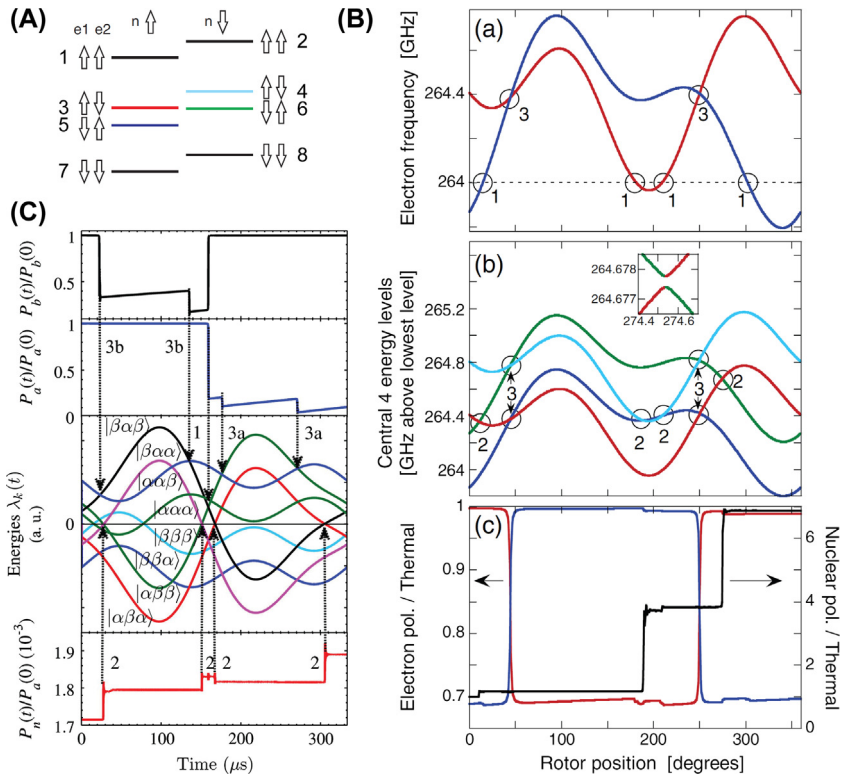

Fig. 6. Simulations of the evolution of spin eigenstates of an e–e–n system under MAS. (A) Definition of the spin states used by Thurber and Tycko [83]. Note, that numbers have been added in order to match the nomenclature in Eq. (32). (B) Evolution of SQ (EPR) excitation frequencies (a), eigenenergies of the four central (ZQ subspace) states (b), and spin polarizations (c) during one rotor period. Circles mark μw events (1), CE events (2), and e–e events (3) as described by Thurber and Tycko. (C) Similar depiction by Mentink-Vigier et al. [75] showing electron spin polarization, eigenenergies, and nuclear polarization (top to bottom). Further details are given in the original publications. (A) and (B) are reprinted with permission from [83], and (C) reprinted from [75].

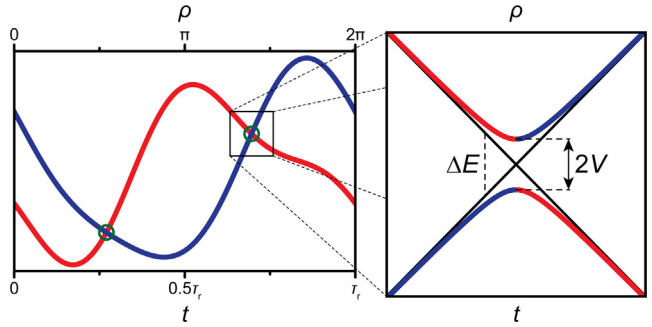

Fig. 7. Schematic representation of time and rotor-angle dependence of the eigenenergies of two arbitrary spin states (red and blue lines) over one rotor period. Green circles mark two occurring LACs. The black square delimits the area enlarged on the right. Close to the LAC, the rate of change in the energy difference ΔE as well as in the mixing element V can often be neglected so that the Landau-Zener equation, Eq. (45), is applicable.

Therefore, we can approximate the effective frequencies by:

$$\begin{aligned}\tilde{\omega}_\Delta &\approx \omega_\Delta\left[1+\left(\frac{D_0}{\omega_\Delta}\right)^2\right] = \pm\omega_{0I} \approx \omega_\Delta \\ \tilde{A}_\Delta &\approx A_\Delta, \tilde{B}_\Delta \approx B_\Delta \\ \tilde{K} &\approx -\frac{B_\Delta D_0}{\omega_\Delta},\end{aligned} \tag{35}$$

and we obtain the simplified Hamiltonian:

$$\begin{aligned}\hat{H}_\Delta^{\mathrm{CE}} \approx{}& \omega_{0I}(\mathbf{S}_{\Delta z} - \mathbf{S}_\Delta \mathbf{I}_z) + \frac{D_d}{4}\mathbf{S}_\Delta + A_\Delta \mathbf{S}_{\Delta z}\mathbf{I}_z \\ &+ \frac{B_\Delta}{2}\left(\mathbf{S}_{\Delta z} \mp \frac{D_0}{2\omega_{0I}}\left(\mathbf{S}'_{1+}\mathbf{S}'_{2-} + \mathbf{S}'_{1-}\mathbf{S}'_{2+}\right)\right)\left(\mathbf{I}'_+ + \mathbf{I}'_-\right).\end{aligned} \tag{36}$$

In summary, the CE matching does not require any μw irradiation but is driven by a combination of the off-diagonal e–e coupling and pseudo-secular HFI. After a non-equilibrium polarization has been established on one electron spin during a μw event, the resulting polarization difference can now be transferred to the nucleus by a concerted e–e–n triple-spin flip. The transition moment of this event is approximately equal to $D_0 B_\Delta/\omega_{0I}$. By comparison of this CE transition moment with that of the SE, $\omega_{1S}B_\Delta/2\omega_{0I}$, we find that for CE the dipole coupling effectively takes the role of the μw field in SE. Therefore, considering typical dipole coupling constants and available μw field strengths, polarization transfer of the CE has a ~50× larger transition moment and consequently a ~2500× higher transition probability.

Due to the influence of the sign in the matching condition of Eq. (33)—which leads to opposite signs of the generated e–e–n coherences in Eq. (36)—it is important to distinguish which of the two electrons is saturated in the μw event. Finally, this results in the two lobes of opposite nuclear polarization enhancement in a field profile (see Section 3.2.2).

However, it is quite intuitive that the irradiated electron will at certain times switch places with the other electron in frequency space and that the second electron spin will at some time also undergo a μw event. Without adiabatic e–e events this would have two consequences: both electrons would become equally saturated and opposite CE transfers would occur with equal likelihood, effectively cancelling the net CE enhancement. Fortunately, e–e flip-flop events occur between these events, leading to polarization exchange of the two electron spins and ensuring that μw and CE events may result in the accumulation of a net nuclear polarization enhancement.

2.1.2.4. Electron–electron (flip-flop) events. An e–e flip-flop event occurs when the mixing between the connected states in the ZQ space is maximum so that e–e coherences can evolve. This is achieved when $p_\zeta = \sqrt{\frac{1}{2}}$ and occurs for

$$|D_0| \gg |\omega_\Delta|. \tag{37}$$

Therefore, we can intuitively expect that an e–e event occurs when two electron Zeeman states are nearly degenerate:

$$\omega_\Delta \approx 0 \tag{38}$$

In this strong coupling regime, the spin states are more appropriately expressed in their singlet/triplet eigenbasis:

$$\begin{array}{ll} |T_+\alpha\rangle = |\alpha\alpha\alpha\rangle, & |T_+\beta\rangle = |\alpha\alpha\beta\rangle \\ |S_0\alpha\rangle = \frac{1}{\sqrt{2}}(|\alpha\beta\alpha\rangle - |\beta\alpha\alpha\rangle), & |T_0\beta\rangle = \frac{1}{\sqrt{2}}(|\alpha\beta\beta\rangle - |\beta\alpha\beta\rangle) \\ |T_0\alpha\rangle = \frac{1}{\sqrt{2}}(|\alpha\beta\alpha\rangle + |\beta\alpha\alpha\rangle), & |S_0\beta\rangle = \frac{1}{\sqrt{2}}(|\alpha\beta\beta\rangle + |\beta\alpha\beta\rangle) \\ |T_-\alpha\rangle = |\beta\beta\alpha\rangle, & |T_-\beta\rangle = |\beta\beta\beta\rangle. \end{array} \tag{39}$$

In order to assess changes in Zeeman state populations, we have to consider the Hamiltonian in the Zeeman basis and treat the non-diagonal e–e coupling as a perturbation:

$$\hat{H}_\Delta^{\mathrm{e-e}} = \omega_\Delta \mathbf{S}_{\Delta z} - \omega_{0I}\mathbf{S}_\Delta \mathbf{I}_z + \frac{D_d}{4}\mathbf{S}_\Delta + A_\Delta \mathbf{S}_{\Delta z}\mathbf{I}_z + \frac{D_0}{2}(\mathbf{S}'_{1_+}\mathbf{S}'_{2_-} + \mathbf{S}'_{1_-}\mathbf{S}'_{2_+}). \tag{40}$$

The e–e flip-flop terms become time-independent in the interaction frame when

$$\omega_\Delta = \pm\frac{A_\Delta}{2} \tag{41}$$

In practical terms, the HFI can be neglected and we arrive again at Eq. (38).

If this condition is fulfilled, polarization is exchanged efficiently between the two electron spins with a transition moment D_0. This exchange ensures that polarization is effectively swapped between all "opposing" CE events and between μw events that involve different electron spins. Therefore, given that e–e polarization exchange is quantitative, all opposing (μw or CE) events separated by e–e events act in a cumulative manner instead of mutually cancelling.

2.1.2.5. Adiabaticity of events. Up to now we have treated all events only in a static frame, where the state mixing is time independent and a certain equilibrium state would be reached after a sufficiently long time. Under MAS, however, eigenstates are evolving under the rotation of the interaction tensors (Zeeman, e–e, HFI) within the external magnetic field. This leads to periodic modulation of their energy separation and occurrence of typically several of the above-mentioned matching events during one rotor cycle, as shown in Fig. 6.

The transient crossing of these matching conditions constitutes a LAC event. If any state-mixing interaction would be absent during degeneracy of the states, then there were no possibility for the system to exchange populations between crossing states and an ideal level crossing event would be achieved. In contrast, if a sufficiently strong mixing interaction is present, populations can exchange adiabatically during the ideal LAC; the system remains in an eigenstate at all times.

For a quantitative description of the degree of adiabaticity of LACs, the rate with which the degeneracy is crossed as well as the mixing potential have to be considered. For a precise treatment, a quantum-mechanical propagation of the density operator yields the populations of all states during the rotor cycle. Typical DNP build-up time constants are more than four orders of magnitude longer than the MAS rotor period. Concurrently, the propagation under the Liouville-von Neumann equation has to be performed over very short time steps to account for the non-commuting properties of the Hamiltonian at different times. This leads to prohibitively time-consuming calculations. Certain scenarios can be investigated though, for example, a quasi-equilibrium where a periodic evolution is achieved by iterative propagation, or initial rates can be obtained based on given starting conditions.

For a semi-quantitative assessment, however, the Landau-Zener equation can be evoked:

$$P_{\mathrm{LAC}} = 1 - \exp(-2\pi\Gamma), \tag{42}$$

with the adiabaticity parameter

$$\Gamma = \frac{V^2}{\partial\Delta E/\partial t}. \tag{43}$$

The Landau-Zener equation describes the adiabaticity of an LAC, P_{LAC}, under the condition that the crossing rate, $\partial\Delta E/\partial t$, as well as the mixing interaction, V, are time-independent during the crossing. The adiabaticity or probability to observe an ideal LAC reaches 1 for $\Gamma \to \infty$ or $|V| \gg |\partial\Delta E/\partial t|$, or reaches 0 for $\Gamma \to 0$ or $|V| \ll |\partial\Delta E/\partial t|$; the latter case describes a level crossing.

For LACs that are relevant for CE, the crossing rate as well as the mixing interaction are time dependent. For typical modulation amplitudes during MAS (*e.g.*, due to Zeeman anisotropy of >1 GHz in nitroxides) and relatively small dipole couplings (*e.g.*, ~20 MHz), the above "Landau-Zener scenario" is sufficiently fulfilled in many cases (see Fig. 7); however, there are several situations where this approximation is clearly invalid. For example, for LACs that occur close to turning points of the eigenstate evolution or close to inversion points of the mixing interaction, this approximation is clearly violated. Nevertheless, we can gain insight and compare several situations with this analytical perturbation treatment.

The crossing rate can be expressed in terms of the rotor angle (ρ) instead of time (t):

$$\partial\rho = \omega_{\mathrm{r}}\partial t, \tag{44}$$

which yields the MAS-dependent Landau-Zener equation

$$P_{\mathrm{LAC}} = 1 - \exp\left(-\frac{2\pi V^2}{\omega_{\mathrm{r}}\partial\Delta E/\partial\rho}\right). \tag{45}$$

The crossing rate for bis-nitroxides has been estimated to be in the range of $\omega_{\mathrm{r}}\partial(\Delta E/h)/\partial\rho \approx 20$ THz s^{-1} for typical μw events, and of ≈ 30 THz s^{-1} for CE and e–e events at an MAS frequency of 7 kHz [83]. In comparison, the mixing interaction is given for each case of CE-relevant LAC:

$$2V = \begin{cases} \omega_{1S} & \text{for} \quad \text{μw event} \\ D_0 B/\omega_{0I} & \text{for} \quad \text{CE event} \\ D_0 & \text{for} \quad \text{e—e event} \end{cases} \tag{46}$$

Assuming typical values of $\omega_{1S}/2\pi \approx 1$ MHz [87], $D_0/2\pi \approx 20$ MHz, $B_\Delta/2\pi \approx 1$ MHz, and $\omega_{0I}/2\pi = 400$ MHz, P_{LAC} of μw events is ~50%. This indicates significant saturation by μw irradiation over a few rotor cycles, considering typical electron spin–lattice relaxation time constants of $T_{1S} \approx 100$—1000 μs. At the same time, e–e flip-flops are highly efficient, resulting in $P_{\mathrm{LAC}} \approx 1$, ensuring that a net polarization difference is maintained between the two electrons. Nevertheless, a non-vanishing probability (~10^{-6}) for level crossings remains, so that over a few rotor periods a partial equilibration of polarization can accumulate. This results in a reduction of DNP efficiency, and also in dynamic nuclear *de*polarization in the absence of μw irradiation. The impact on practical aspects of this situation will be discussed in Section 6.1.2.

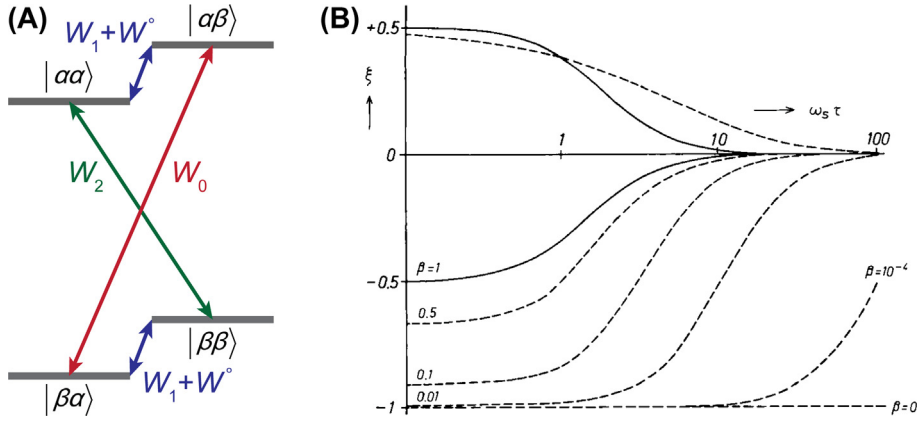

Fig. 8. (A) Definition of auto- and cross-relaxation rate constants responsible for OE in an e–n system with $S = 1/2$, $I = 1/2$. (B) Coupling factor ξ for dipolar interactions (positive ordinate area) based on Solomon's equations for rotational (solid lines) and translational (dashed lines) diffusion [93]. The negative ordinate area contains coupling factors due to scalar interactions for different values of the parameters β which depends on the ratio of Heisenberg exchange and electronic relaxation rates. Reproduced with permission from [94].

CE events, on the other hand, show only a rather small adiabaticity factor on the order of 0.1%. This seems almost vanishingly small. However, nuclear spin–lattice relaxation occurs only on the order of $\sim 10^3$–10^4 rotor cycles, so that even small transfer steps (smaller than the thermal nuclear polarization) can accumulate in order to build up the large observed enhancement factors of $\varepsilon > 10^2$.

2.1.2.6. Cross effect in static samples. Under static conditions, CE matching [Eq. (33)] can only result in DNP when the μw resonance condition is fulfilled at the same time. In this case, the same diagonalization of the e–e interaction as after Eq. (26) can be performed so that the effective Hamiltonian, Eq. (29), is obtained. By subsequent transformation of the μw Hamiltonian into the frame of the diagonal part of Eq. (29), several cases of frequency matching can be deduced and effective transition moments can be obtained.

Of course, the requirement for simultaneous matching of CE and μw conditions reduces the number of actively contributing PA molecules randomly distributed within an amorphous frozen solution. However, DNP by CE can not only be driven "actively" by generation of μw-driven coherences, but can also "spontaneously" occur due to imbalances in spin polarization with respect to thermal equilibrium. This situation is similar to the individual CE events under MAS which are temporally decoupled from μw events. Such imbalances can be effectively caused by spectral diffusion of electron polarization upon μw irradiation, causing electron spin saturation to spread to spin packets that are off-resonance with respect to the μw frequency. These effects have been studied in detail and dubbed "indirect CE" by Vega and coworkers (see Section 2.2.2.3) [88].

2.1.3. Overhauser effect in insulating solids

The OE has been neglected in solid-state DNP (be it with or without MAS) until recently, because of its reliance on internal dynamics causing fluctuations of the HFI which in turn result in e–n cross-relaxation (see Fig. 8A). In conducting solids or liquid solutions, these dynamics can be provided by itinerant conduction electrons or molecular diffusion, respectively. In dielectrics, where mobile charge or spin carriers are absent, it was thought that no mechanism exists which can provide the required amplitude of the spectral density function at the relevant Larmor frequency combinations of e–n ZQ and DQ transitions. Nevertheless, the OE has been unquestionably identified in MAS DNP experiments. While the first report was an accidental observation in a ^{1}H SE study of (water-soluble) sulfonated-BDPA (SA-BDPA) [89], the OE was unambiguously proven shortly afterwards in a dedicated study of similar types of PAs [90]. Retroactively, hints of OE can be found in earlier published studies on BDPA [91], as well as in an investigation of the flavin mononucleotide (FMN) semiquinone radical that occurs as endogenous PA in flavodoxin [92].

OE DNP can simply be described by considering one electron spin and one nuclear spin. However, in contrast to the previously described SE, the nuclear spin has to experience a fluctuating scalar or dipolar HFI. Such fluctuations due to the presence of dynamics with characteristic correlation times on the order of $\omega_{0S} \pm \omega_{0I}$ can bring about several (incoherent) transitions, namely electron and nuclear SQ as well as e–n DQ and ZQ transitions. These latter DQ and ZQ transitions result in additional electron relaxation pathways (*i.e.*, e–n cross-relaxation) upon saturation of the EPR transition by μw irradiation, besides the most probable SQ relaxation. If there exists an imbalance between DQ and ZQ relaxation rates (described by rate constants W_0 and W_2, respectively), nuclear hyperpolarization can be accumulated. In the case of ^{1}H (or any nucleus with positive γ_I), dominant ZQ relaxation leads to positive OE DNP enhancement; accordingly, larger rates of DQ relaxation to negative enhancement factors. Nuclear SQ relaxation, either being induced by the fluctuating HFI (rate constant W_1) or caused by dynamics not related to the presence of the electron spin (W°) causes a reduction of the magnitude of enhancement. This situation is depicted in Fig. 8A.

For a quantitative description the simple Solomon equations [93],

$$\frac{\partial}{\partial t}\begin{pmatrix} P_S(t) \\ P_I(t) \end{pmatrix} = -\begin{pmatrix} \rho_S & \sigma_{SI} \\ \sigma_{SI} & \rho_I \end{pmatrix}\begin{pmatrix} P_S(t) - P_S^0 \\ P_I(t) - P_I^0 \end{pmatrix}, \tag{47}$$

can be solved for a steady-state solution of the nuclear spin polarization [94]:

$$\varepsilon_{OE} = 1 - \frac{\gamma_S}{\gamma_I} s\xi f. \tag{48}$$

Here, $\varepsilon_{OE} = \frac{P_I^\infty}{P_I^0}$ and $s = 1 - \frac{P_S^\infty}{P_S^0}$ are the OE enhancement and saturation factor, respectively. Superscript indices '∞' mark parameters in the steady-state, while '0' denotes parameters in thermal equilibrium. ρ_S and ρ_I are the electron and nuclear auto-relaxation rate constants, while σ_{SI} is the e–n cross-relaxation rate constant. $\xi = \frac{\sigma_{SI}}{\rho_I} = \frac{W_2 - W_0}{W_0 + 2W_1 + W_2}$ and $f = \frac{\rho_I}{\rho_I + W^\circ} = \frac{W_0 + 2W_1 + W_2}{W_0 + 2W_1 + W_2 + W^\circ}$ are the coupling and the leakage factors, respectively.

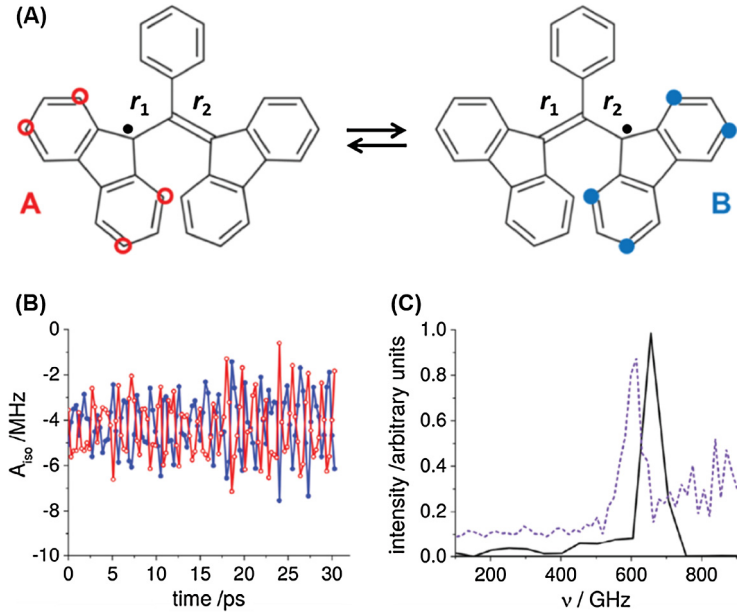

Fig. 9. (A) Two structures of BDPA showing two distinct sets of hydrogens (red and blue). Due to asymmetry in the distances between the fluorene groups and the central carbon ($r_1 \neq r_2$), these structures are inequivalent and the two sets of ^{1}H show different scalar HFI. (B) MD time trace of scalar HFI of the two sets of ^{1}H (red and blue) in BDPA in vacuum, showing large amplitude of correlated fluctuations which occur out-of-phase with each other. (C) Fourier-transform of the time trace shown in (B), revealing a distinct frequency component near 650 GHz (black line); when embedded in amorphous OTP, this peak shifts slightly to lower frequency and broadens, leading to a wide background distribution. Figure reproduced with permission from [99].

W_0, W_2, as well as W_1, have to be derived from relaxation models based on dipolar or scalar HFI. In the seminal review of Hausser and Stehlik, several models have been described in detail, including intra- as well as intermolecular dynamics. For example, purely translational or rotational diffusion models lead to a dependence of the coupling factor on the electron Larmor frequency and the molecular correlations times as shown in Fig. 8B [94].

The saturation factor can be deduced in the simplest description from a steady-state solution of the Bloch equations under continuous wave (cw) irradiation [95]:

$$s = 1 - \frac{1 + \Omega_{0S}^2 T_{2S}^2}{1 + \Omega_{0S}^2 T_{2S}^2 + \omega_{1S}^2 T_{1S} T_{2S}}, \tag{49}$$

Here, it should be noted that, given sufficient μw power for significant saturation (*i.e.*, $\omega_{1S}^2 T_{1S} T_{2S} > 1$), off-resonance excitation of the PA can also cause OE. This results in an expected broadening of the OE field profile with respect to the EPR line (see Section 3.2.3). Similar observations have been made in solution OE DNP given sufficient homogeneous broadening of the EPR line by Heisenberg exchange for off-resonance excitation [96].

Of course, rotational and translational diffusion models are generally not applicable in the solid-state. Nevertheless, by OE DNP using BDPA as PA, significant ^{1}H signal enhancement factors on the order of 80 have been observed in an amorphous matrix of ortho-terphenyl (OTP) at a high field of 18.8 T [97]. Similarly, surprising experimental observations were made by Prisner and co-workers with high-field (9.2 T) OE DNP in solution. Here—even for small molecules such as water—rotational and translational correlation times are typically long compared to the inverse electron Larmor frequency ($\omega_{0S}/2\pi = 259$ GHz). Therefore, based on the detailed description by Hausser and Stehlik, vanishing OE enhancement would be predicted at this high field as is seen in Fig. 8B [94]. However, a rather large $\varepsilon_{OE} \approx 100$ has been observed on ^{1}H in water. As an explanation, the model by Hausser and Stehlik has been extended to include transient contacts between the solvent and the PA with short correlation times which can be described by molecular dynamics (MD) simulations [72]. Very recently, similar findings have also been reported by Bennati and co-workers [98].

In the solid-state, the reason for OE-supporting fluctuations in the systems investigated so far is still vividly debated. A direct comparison between protonated and deuterated BDPA has identified the scalar-coupled protons on the BDPA molecule as responsible for the large, positive OE DNP enhancement. Furthermore, the unique field dependence—with increasing enhancement at higher external magnetic field (see Section 6.2.1)—might not only prove extremely valuable for DNP applications at fields of 18.8 T and above, but it was also expected to play an important role in solving this puzzle [90]. Very recently, Pylaeva et al. have presented a study of OE DNP based on classical and *ab initio* molecular dynamics (MD) simulations combined with spin dynamics simulations. According to their findings, two sets of protons (A and B, marked red and blue in Fig. 9A) show not only the largest scalar HFI, but also a very strong sensitivity of the scalar HFI to internal dynamics. Note that such fluctuations of the scalar HFI can contribute to the ZQ but not to the DQ and SQ rates mentioned above. The unique situation proposed is caused by the delocalization of the electron spin over the two fluorene rings *via* the bridging allyl. Asymmetry of the distance between the fluorene moieties and the central carbon atom then leads to an inequivalence of spin density on the two fluorenes and thus of the scalar HFI of the two sets of ^{1}H. MD simulations have furthermore revealed that internal vibrational (ground state) dynamics cause a time-dependence of the distances r_1 and r_2, which in turn leads to correlated fluctuations of the scalar HFI (Fig. 9B). Fourier-transformation of this time-dependence revealed a clear peak near 650 GHz for BDPA (Fig. 9C). While this study may explain the observed DNP enhancement from BDPA by OE in an intuitively comprehendable manner, no experimental evidence for such a vibrational mode has been provided thus far. Therefore it remains to be seen whether this hypothesis will be accepted as the valid theory for OE in dielectric solids.

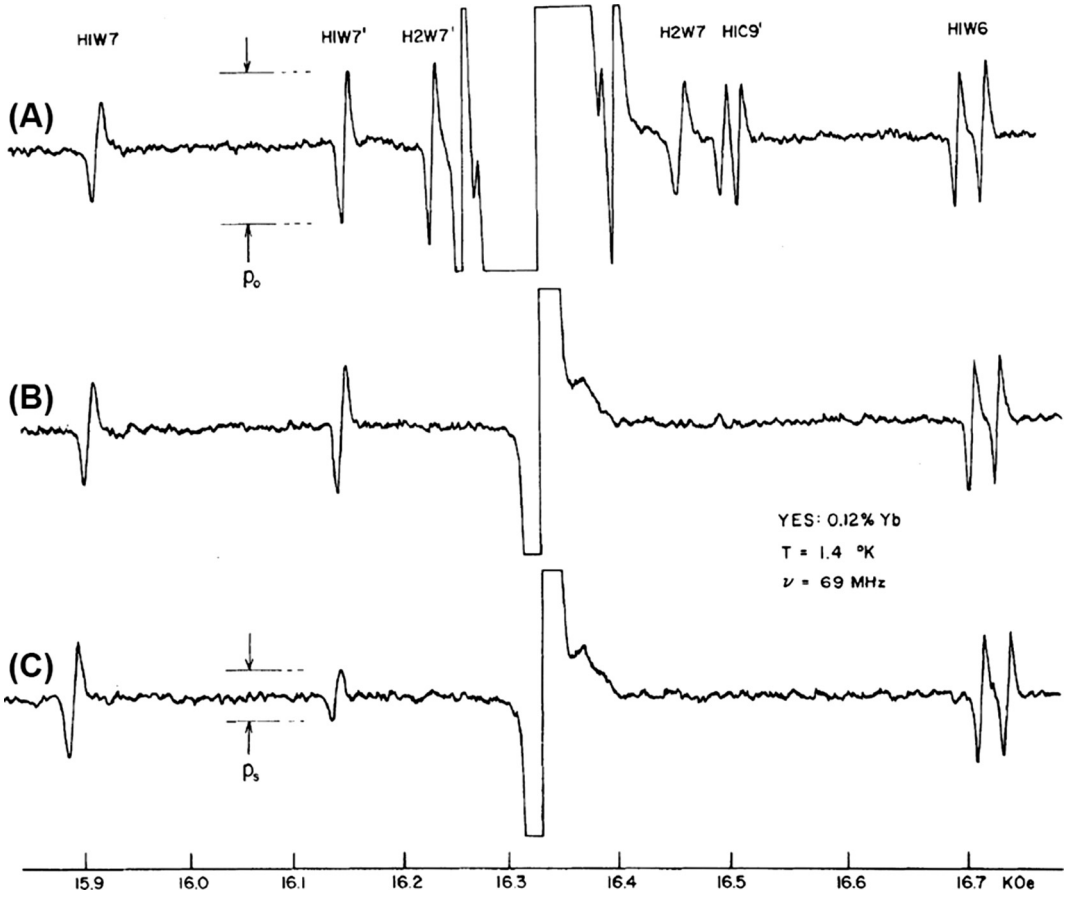

Fig. 10. Direct experimental observation of the spin-diffusion barrier in YES:Yb at 69 MHz ^{1}H frequency and 1.4 K. Labeled signals correspond to protons within 6.2 Å of Yb^{3+} impurity; the bulk NMR signal at 16.33 kOe is 1000 × off-scale. (A) ^{1}H spectrum in thermal equilibrium. (B) After irradiation of the bulk for 2–6 min, many ^{1}H signals from outside the diffusion barrier are saturated by strong homonuclear coupling. (C) Only very few ^{1}H signals inside the diffusion barrier remain at lattice temperature even after 100 min of bulk saturation. Figure reprinted with permission from [115].

2.2. Integral DNP process: from electron spin to nuclear bulk

2.2.1. General concepts and early descriptions

2.2.1.1. Generation, accumulation and loss of enhanced nuclear polarization. In the above sections we have reviewed several quantum-mechanical DNP transfer mechanisms. In all discussed cases of cw DNP, the effective rate of transfer (or the net polarization transferred per LAC event) is small [75,83,100]. For simple considerations, we are reminded that the magnitude of steady-state DQ or ZQ coherence would be small due to the almost vanishing transition moments of the SE. In this case—without any longitudinal relaxation—continuous excitation and concurrent decay of the built-up ZQ or DQ coherence would lead to slow but steady saturation of the connected polarization states. Within the isolated e–n spin pair, a maximum DNP enhancement factor of only $0.5 \times \gamma_S/\gamma_I$ (~330 for ^{1}H) would be achieved even for complete saturation, contradicting Eq. (2). This is even exacerbated as one electron typically serves ~100–10,000 nuclear spins; the maximum enhancement factor would then scale with the e–n number ratio, N_S/N_I, resulting in negligible enhancement. The situation would be similar for CE due to the equilibration of the electron spin polarization difference by CE events [75,83,100].

However, large net enhancements can be achieved on all nuclei as electron spin polarization recovers by spin-lattice relaxation during or between the coherent transfer steps [101,102]. At the same time, nuclear polarization is also undergoing much slower spin-lattice relaxation leading to a reduction in steady-state polarization. The magnitude of the observed steady-state enhancement depends on a rather complicated interplay between DNP transfer mechanism, homonuclear spin diffusion and effective electron and nuclear spin-lattice relaxation which in turn strongly depend on sample constitution and experimental conditions (see Section 6). Thus, only a semi-quantitative description for net observables has been derived for the SE which strongly relies on homonuclear spin diffusion (see below). A microscopic (quantum-mechanical) treatment is rather tedious and in most cases analytical derivations are impeded by the large number of spins to be taken into account. In Section 2.2.2.2, we review the general description of the problem, as well as several approaches including stark simplifications of the underlying problem and numerical simulations. However, we will first describe extensive studies from the early days of DNP, where attempts to understand the general processes involved in spreading of enhanced nuclear polarizations were made.

2.2.1.2. The coupling between electron spins and the nuclear spin bath. In simple and intuitive models, enhanced polarization is transferred only to nuclei in the direct vicinity of the electron spin(s), a model described early as the strict shell-of-influence or influence-sphere model [103,104]. Once directly transferred to a hyperfine-coupled nucleus, nuclear polarization is then expected to spread spatially by homonuclear spin diffusion [101,105,106]. This situation is in principle very similar to the relaxation of nuclear spins by paramagnetic dopants or impurities which has been exhaustively studied in the early days of magnetic resonance [101,107–111]. In fact, a paramagnetic species can act both as

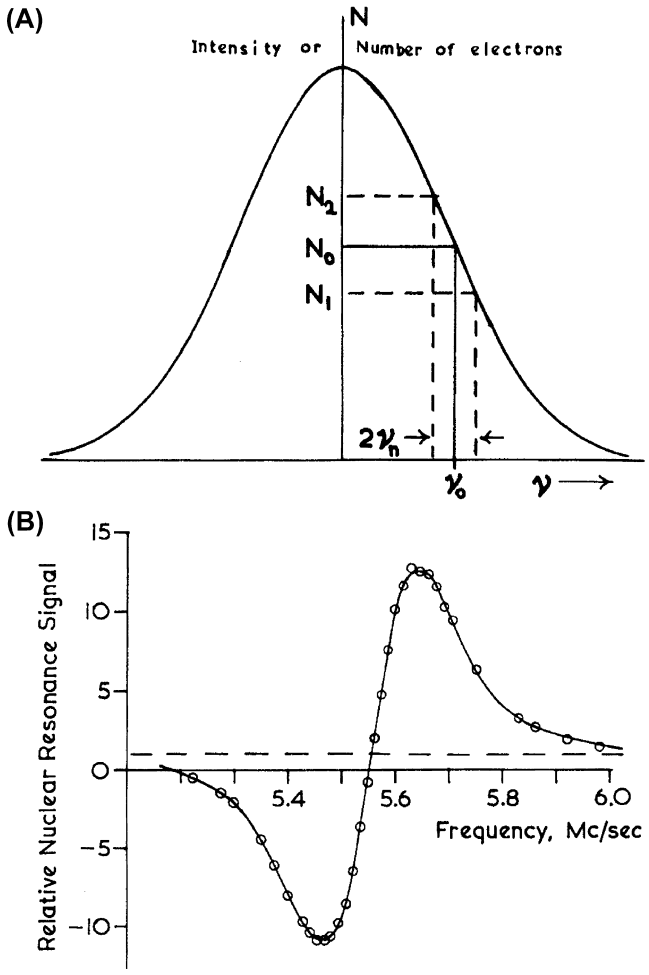

Fig. 11. Differential solid effect with an inhomogeneously broadened EPR line. Net signal enhancement results from imbalances in effective e–n ZQ and DQ transition intensity (A) and resembles the derivative of the EPR (SQ) absorption line (B). Figure reproduced from [76] with permission.

polarization source or as relaxation sink in DNP-active or DNP-inactive centers, respectively. This has been described previously in order to quantitatively predict steady-state nuclear enhancements [112,113].

2.2.1.3. Nuclear spin relaxation by paramagnetic sites and the diffusion barrier. In the above-mentioned models [101,107–111], paramagnetic centers are directly hyperfine-coupled to nuclear spins in close proximity. These core nuclei are subsequently communicating with the bulk lattice by homonuclear spin diffusion. Upon rf saturation of the bulk spins, their longitudinal magnetization is mainly repleted by fast spin-lattice relaxation of the core nuclei. Therefore, two bottlenecks can be identified: (i) core nuclear spin relaxation is fast and bulk relaxation is limited by spin diffusion or (ii) spin diffusion is fast but core spin relaxation is the limiting factor [104]. Since spin diffusion relies on net energy conserving nuclear flip-flop transitions, large hyperfine couplings will offset the Larmor frequency of the core nuclei and quench diffusion to less hyperfine-shifted nuclear spins. The cut-off distance below which the effective communication between nuclei in dipolar contact to the electron spin (core nuclei) and nuclei that are virtually unaffected by the electron (bulk nuclei) ceases, is known as spin-diffusion barrier [114], and has been demonstrated (Fig. 10) by Wolfe on a sample of yttrium-ethyl-sulfate doped with ytterbium (YES:Yb) [115]. The very definition of the barrier can be based on the above-mentioned bottlenecks: nuclear spins that have a stronger coupling to the lattice phonons than to the bulk spins are within the spin-diffusion barrier, while spins that are strongly dipolar-coupled with the bulk homonuclear bath are outside of that barrier.

2.2.1.4. Spreading of enhanced nuclear polarization by spin diffusion. As already mentioned, the situation in DNP is rather similar to nuclear relaxation induced by paramagnetic centers where a repletion of bulk magnetization by core spins is following the rf saturation of the bulk; in DNP, core spins are hyperpolarized and the enhanced polarization is spread to the bulk by spin diffusion [101,106]. Therefore, all considerations derived for paramagnetic relaxation in the solid state should also be applicable to DNP. However, nuclear spins undergo spin-lattice relaxation at the same time as being hyperpolarized, either due to long-wavelength phonons, (local) temperature-activated dynamics in the bulk, or paramagnetic relaxation towards inactive PAs (*e.g.*, those not fulfilling the DNP matching condition) acting as drain for hyperpolarization [108,116]. Consequently, a significant—and in many cases largest—amount of enhanced nuclear polarization is lost to the lattice [101].

2.2.1.5. Role of electron–electron interactions and spectral diffusion. Very early after the discovery of the SE [117–120] the effects of inhomogeneously broadened EPR lines, where the overall line width exceeds $2\omega_{0I}$, were studied by several groups [76,121,122]. In this general case, the differential solid effect (DSE) was formulated. It was theoretically predicted and experimentally confirmed that the DNP field profile is proportional to the first derivative of the EPR absorption line (see Fig. 11) [76]. Due to the cancellation of positive, (+), and negative, (−), enhancements simultaneously caused by ZQ and DQ transitions from different spin packets, the overall net enhancement can be reduced by one or more orders of magnitude with respect to the maximum enhancement that could be reached by selective saturation of the ZQ or DQ transition.

Given sufficient μw power to achieve a strong induction of the "forbidden" SE (DQ/ZQ) transitions, it has been shown that a significantly larger enhancement can be obtained than what would be

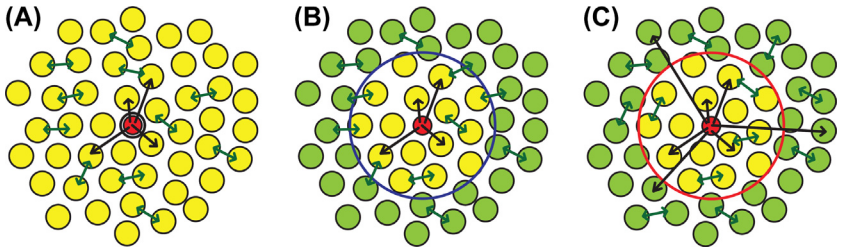

Fig. 12. Models utilized by Smith et al. for the description of transfer pathways between an electrons spin (red) and core nuclei (yellow) as well as bulk nuclei (green) as described in the text. A "soft" spin-diffusion barrier (slowly penetrable) is marked by a blue circle, a "hard" spin-diffusion barrier (impenetrable) by a red circle. The size of the spin-diffusion barrier and number of nuclei within it do not represent actual values. Reprinted from [77] with permission.

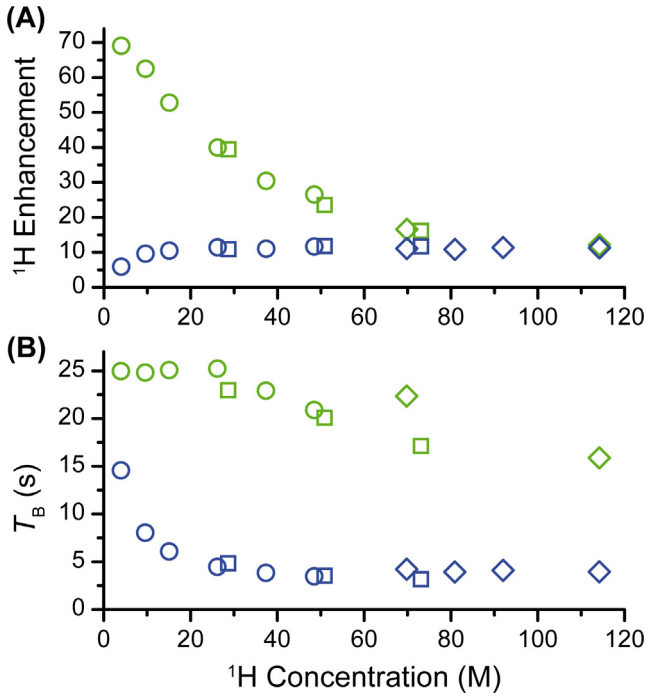

Fig. 13. Comparison of DNP enhancement factor (A) and build-up time constant (B) between 40 mM trityl OX063 (green) and 10 mM Gd-DOTA (blue) for various ^{1}H concentrations in the matrix. Open circles represent samples prepared with d_8-glycerol, whereas open squares and diamonds correspond to samples prepared with d_5- and h_8-glycerol, respectively. The glycerol/water ratio was 60/40 (v/v) in all cases. All data points were recorded under 8 W microwave power at a temperature of ~86 K. Reprinted from [74] with permission.

predicted from the slope of the inhomogeneously broadened EPR line [112]. This was explained by the expectation that electron spins switch their "state" between DNP-active (*i.e.*, irradiated by a μw field matching the SE frequency) and inactive (*i.e.*, irradiated with a μw field off-resonance with respect to the SE matching condition). This switch is induced by changes in the local field due to interactions with close-by nuclei or other electrons (*i.e.*, spectral diffusion). Thus, a larger fraction of electron spin packets can act as active PAs and contribute to an increase of net enhancement.

2.2.2. Recent theoretical and experimental advances

2.2.2.1. The role of spin diffusion in SE DNP. The above-mentioned descriptions and problems have also been addressed in several modern approaches. Due to the large size of the spin system under consideration, a phenomenological treatment *via* effective rate equations provides a computationally less expensive way of describing the polarization transfer. As has been already elaborated in several works mentioned above [61,77,101,106], this situation can be classically described by a system of coupled differential equations as long as the magnitude of the coherences that may build up at any point in time is negligible:

$$\begin{aligned}\frac{dP_I^j}{dt} &= k_{DNP}^j(P_S - P_I^j) + \sum_{n=1}^{N_I} k_{SD}^{nj}(P_I^n - P_I^j) + \frac{1}{T_{1I}^j}(P_I^{eq} - P_I^j)\\ \frac{dP_S}{dt} &= -k_0 P_S + \sum_{n=1}^{N_I} k_{DNP}^n(P_I^n - P_S) + \frac{1}{T_{1S}}(P_S^{eq} - P_S).\end{aligned} \tag{50}$$

Here, P_S and P_I^j are the spin polarizations of the electron and the j^{th} nucleus; T_{1S} and T_{1I}^j are the electron and nuclear longitudinal relaxation time constants, respectively, k_{DNP}^j is the effective rate constant of DNP transfer to the j^{th} nucleus, and k_{SD}^{nj} describes the spin-diffusion rate constant between the n^{th} and j^{th} nuclei. Finally, k_0 is the rate constant of electron spin saturation due to off-resonance excitation of the SQ transition by the μw field.

Using this rather simple model, Smith et al. have compared three different scenarios (Fig. 12) [77]: (A) the polarization is transferred from the electron to the bulk and spin-diffusion rates between all nuclei are equal; in other words no spin-diffusion barrier exists; (B) the polarization can only be directly transferred to core nuclei and then has to cross a "soft" diffusion barrier before it can spread uniformly through the bulk; (C) the polarization is directly transferred in parallel to nuclei within and to those outside a "hard" spin-diffusion barrier with respective rate constants while no polarization is exchanged between the two baths. By experimental determination of three observables—the nuclear relaxation time constant without DNP, the buildup time constant under microwave irradiation and the net nuclear enhancement factor at infinite polarization time (for further details how these parameters are influenced by DNP see Section 6.1.1)—it was concluded that only model C is in qualitative agreement with experiment. However, a quantitative assessment of the size of the spin-diffusion barrier was not possible due to an insufficient set of experimental observables.

A semi-analytical definition of the barrier has been described by Hovav et al. based on the effective truncation of dipolar flip-flop terms by HFI: the transition between core and bulk nuclei can be found where the magnitude of the homonuclear flip-flop terms d_{ij} with all other nuclei become larger than the respective difference in hyperfine coupling to the electron $\Delta A_{ij} = A_i - A_j$ [123]:

$$\zeta\left|\frac{d_{ij}}{2}\right| > |\Delta A_{ij}|. \tag{51}$$

The parameter ζ describes paramagnetic quenching and results in the broadening of the nuclear flip-flop degeneracy condition due to faster nuclear decoherence. The vague character of this parameter also prohibited reliable analysis of the barrier's dimensions in this case.

Further experimental indication of different bottlenecks governing the net transfer of polarization from the PA to the bulk has been provided by comparing ^{1}H SE caused by trityl (OX063) and Gd-DOTA within otherwise identical samples (Fig. 13). By adjusting the protonation level of the solvent matrix a starkly different behavior has been observed: for trityl, enhancement factors are largest for maximum deuteration and decrease nearly hyperbolically with increasing ^{1}H concentration while build-up rates show little variation; for Gd-DOTA the enhancement factor and build-up rates increase and level off at a protonation level of ~40%. This difference is explained by rate-limiting DNP transfer but (relatively) fast spin diffusion through the bulk in the case of trityl, whereas for Gd-DOTA initial DNP is fast with subsequent rate-limiting spin diffusion.

The purely classical, diffusive treatment neglects any coherent interactions which might play a role in the spreading of polarization. This has been investigated by Brüschweiler and Ernst, where a linear chain of spins was simulated quantum numerically and deviations from uniform spreading of polarization (which would be expected under steady-state diffusion without relaxation) were identified [124]. Nevertheless, such a quantum-mechanical treatment is extremely difficult to extend to a general network of N nuclear or electron spins. This stems from the fact, that—in order to include relaxation which is necessary for DNP—a transformation from Hilbert space (with a dimensionality scaling with $2N$) to Liouville space is required. The resulting space with $4N \times 4N$ elements makes solution of the Liouville-von Neumann equation very demanding.

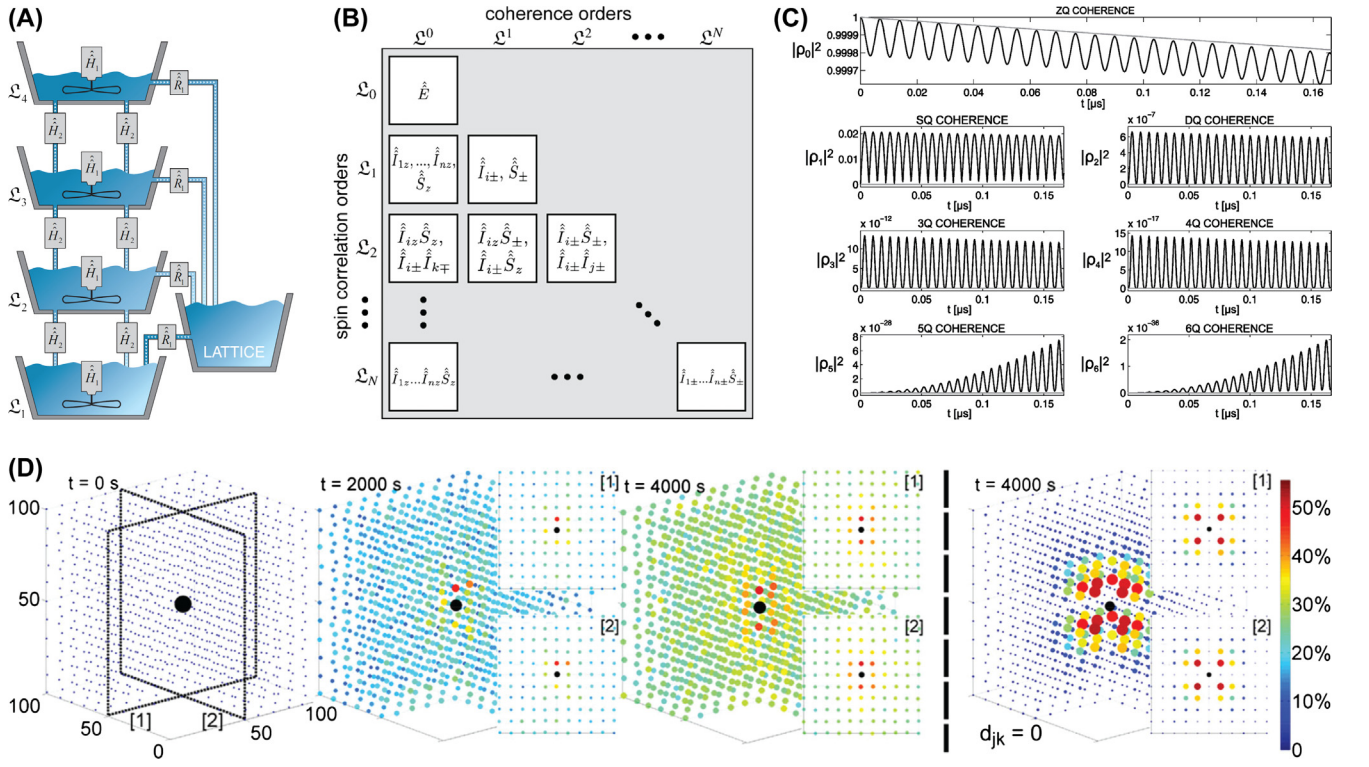

Fig. 14. Simulation of DNP on large spin systems. (A) Schematic illustration of the flow of the density matrix norm in the spin correlation order subspaces. Fast relaxation leaves high product order subspaces unpopulated. (B) Separation of the Liouville state space into subspaces of operators of equal spin correlation order (vertical axis) or coherence order (horizontal axis). (C) Time dependence of the norm of the ZQ coherence subspace and higher coherence subspaces. Only the norm for the ZQ coherence subspace is non-vanishing if the Krylov-Bogolyubov averaged Hamiltonian is used (gray line) while oscillations occur for all subspaces with the non-averaged Hamiltonian (black lines). (D) Simulation of the polarization dynamics of 1330 nuclear spins (^{13}C) arranged on a regular grid in a cube around one central electron (black). The diameter and the color of the spheres indicate the nuclear spin polarization expectation value. The rightmost simulation shows the result with inhibited spin diffusion. Subfigure (A) reprinted from [128], (B) and (C) from [129], (D) from [130], with permission.

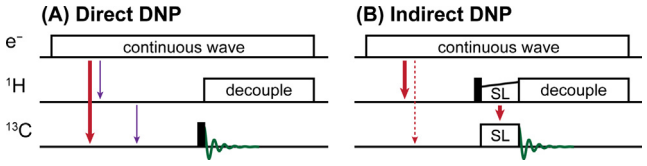

Fig. 15. (A) Polarization generated by direct DNP (thick red arrow) can be directly read out on the desired nuclei (*e.g.*, ^{13}C). Recently, it has been shown that incoherent polarization transfer pathways (cross relaxation from hyperpolarized proton spins; thin purple arrows) may contribute to the obtained spectra. (B) Pathway of polarization transfer for indirect DNP. ^{1}H hyperpolarization generated by DNP is transferred to ^{13}C by CP (thick red arrows). Depending on the width of the DNP resonance condition, a simultaneous direct polarization of the low-γ nuclei can occur (dashed thin red arrow), which is filtered out by appropriate phase cycling.

Therefore, a hybrid treatment has been adapted towards DNP by Hovav et al. where they describe a linear chain of one electron spin and a few nuclear spins, while accounting for relaxation as well [123]. In this hybrid treatment, changes in spin population (not polarization) are modeled with effective rate equations which are based on a complete diagonalization of the spin Hamiltonian. By defining a direct hyperfine coupling only between the electron spin and the closest nuclear spin but allowing for dipolar evolution between all nuclei within the chain, it was found that direct transfer pathways exist between the electron spin and nuclei further removed along the chain. This result shows—from a theoretical viewpoint—that a classical treatment is insufficient for a complete description of the spreading of hyperpolarization. From a more practical viewpoint, it becomes clear that by a combination of HFI and a strong dipolar-coupled network of core and bulk nuclear spins, additional transfer pathways exist which could alleviate the problem imposed by the spin-diffusion barrier. A more realistic description of a three-dimensional system, with much larger ratio of nuclei to electron spins would be highly desirable because this could allow for a quantitative comparison between theoretical prediction and experimental observation.

2.2.2.2. Simulations of DNP with large nuclear/electron spin ratio. Unfortunately, the model described in the section above is very difficult to generalize towards larger spin systems due to restrictions in computational power [123]. Recently, Kuprov has proposed the utilization of Fokker-Planck formulism in order to achieve higher efficiency of density operator propagation [125]. Even though the dimensionality of spin operators in Liouville space has to be extended by the spatial dimensions in Fokker-Planck space, the time slicing—necessary when the Hamiltonian is not self-commuting at all times—can be performed more efficiently particularly for situations involving complex spatial evolution of the spin Hamiltonian [126]. This can be beneficial for experiments under MAS. This formalism has been incorporated into the Spinach simulation library [127], which could lead to promising advances in theoretical modeling of complex situations for DNP under MAS.

Strides towards a general description of a system containing a rather large number of nuclear spins per electron spin have been taken by Köckenberger and co-workers (Fig. 14). For example, Karabanov et al. have shown that the large (Liouville) state-space can be effectively reduced because the norm of subspaces of higher spin-order does not significantly build up on the time scale of typical experiments (Fig. 14A). Therefore, only subspaces up to a

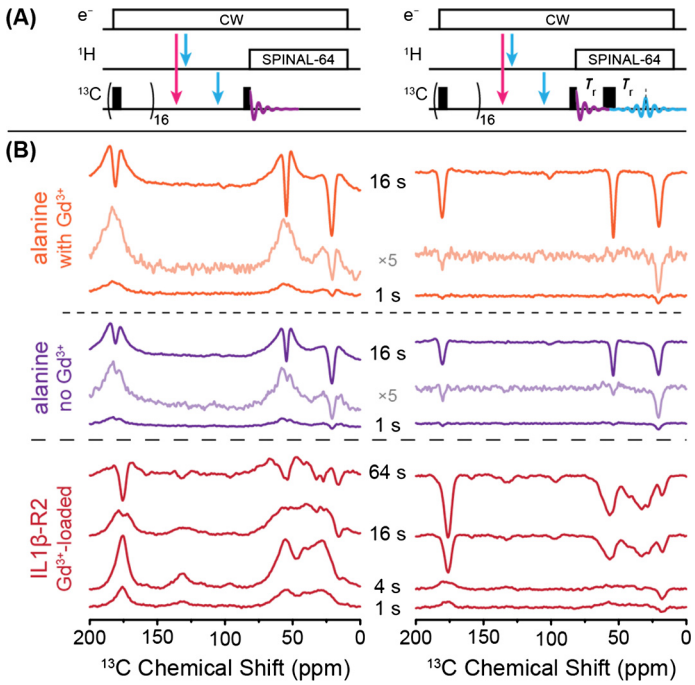

Fig. 16. (A) Pulse sequence for read-out of enhanced ^{13}C polarization generated by direct DNP (magenta arrow) or generated indirectly by cross relaxation from DNP-enhanced ^{1}H (cyan arrows). Read-out is performed by single-pulse excitation (left) or by Hahn echo (right). (B) MAS NMR spectra of three different samples (U-^{15}N,^{13}C-IL1β-R2 protein loaded with Gd^{3+} as well as U-^{13}C-alanine in the presence or absence of Gd^{3+}) doped with AMUPol, recorded using the pulse sequences in (A). Positive signals arise from direct ^{13}C (+)-DNP whereas ^{1}H–^{13}C cross-relaxation leads to negative signals. Reprinted with permission from [141].

certain spin-order have to be considered, leading to polynomial scaling instead of exponential scaling of the state-space with the number of spins. This facilitates simulations of large spin systems, even though the scaling power is still significant [128]. The same authors have also extended this state-space restriction approach by applying Krylov-Bogolyubov averaging of the fast oscillations during spin-evolution. Due to the presence of the electron spin and acceleration of higher spin-order decoherence, the state-space can be very effectively truncated for DNP-relevant systems (Fig. 14B and C). This allowed for simulations of SE [129] as well as CE [131] with a large number of nuclear spins up to 10^3; in such a large system, the SE DNP process is governed by kinetically constrained diffusion (Fig. 14D) [130]. Further extension of the theoretical model by incorporation of a kinetic Monte Carlo algorithm for the description of spin diffusion allowed the authors to predict that more efficient bulk hyperpolarization could be achieved by increasing the minimum distance between the electron spin and the closest nuclei [132]. This result is similar to the findings of Griffin and co-workers where it was concluded that a significant amount of nuclear spin polarization is lost to fast-relaxing core nuclei [74,77]. Although Köckenberger and co-workers have developed these models for conditions suitable for dissolution DNP (large ^{13}C concentration, very low temperature), results could be qualitatively applicable to MAS DNP as well. However, in order to obtain quantitative predictions in the latter case, sample rotation under MAS would have to be explicitly included.

2.2.2.3. Spectral diffusion in the context of DNP: direct vs. indirect CE. Developments in high-field EPR spectroscopy have allowed to investigate the role of spectral diffusion which occurs under DNP-relevant conditions. A detailed study has been led at the Weizmann Institute (Rehovot, Israel) in a collaboration between the Goldfarb and Vega laboratories using an integral EPR/NMR/DNP spectrometer operating at W-band (94 GHz e^-, 140 MHz ^{1}H, 3.4 T) [88,133]; this study has very recently been extended to a field of 7 T (198 GHz e^-, 300 MHz ^{1}H) [134]. An additional (pump) μw-frequency source was used for ELDOR spectroscopy, allowing the measurement of electron (de-)polarization after off-resonance saturation [135]. A similar approach had been utilized by Granwehr and Köckenberger, however, their resonator-free setup in combination with longitudinal detection (LOD) of electron spin polarization is only suitable for experiments under TM conditions (*i.e.*, at very low temperatures) [136].

The above-mentioned ELDOR experiments enabled the identification of spectral diffusion pathways active under typical DNP saturation. Using such a technique the authors have experimentally confirmed the correlation between differential polarization within the electron spin pair and the polarization of the coupled nucleus under CE (see Sections 2.1.2 and 6.1.2) [133]. Furthermore, it has been shown that the required selective electron depolarization can be inflicted either directly by μw irradiation of the spin packet of one of the electrons within the CE-matching pair, or indirectly by excitation of an off-resonance spin packet and subsequent spectral diffusion of electron polarization. These processes have been dubbed *direct CE* (dCE) and *indirect CE* (iCE) [88]. It should be noted that this distinction is highly relevant under static conditions where the narrow matching condition for dCE can be achieved only by a rather small number of active spin pairs whereas iCE can benefit from significantly increased fraction of actively polarizing pairs due to effective spectral diffusion. Under MAS, the spin packets modulate their Larmor frequency [75,83], which leads to a situation comparable to iCE (see above, Section 2.1.2).

2.3. Utilization of enhanced polarization

2.3.1. DNP build-up under microwave irradiation

Since DNP causes a build-up of longitudinal magnetization, this process is indistinguishable from the return to thermal polarization due to spin-lattice relaxation. Even though early experiments using DNP enhancement in combination with MAS utilized a gated

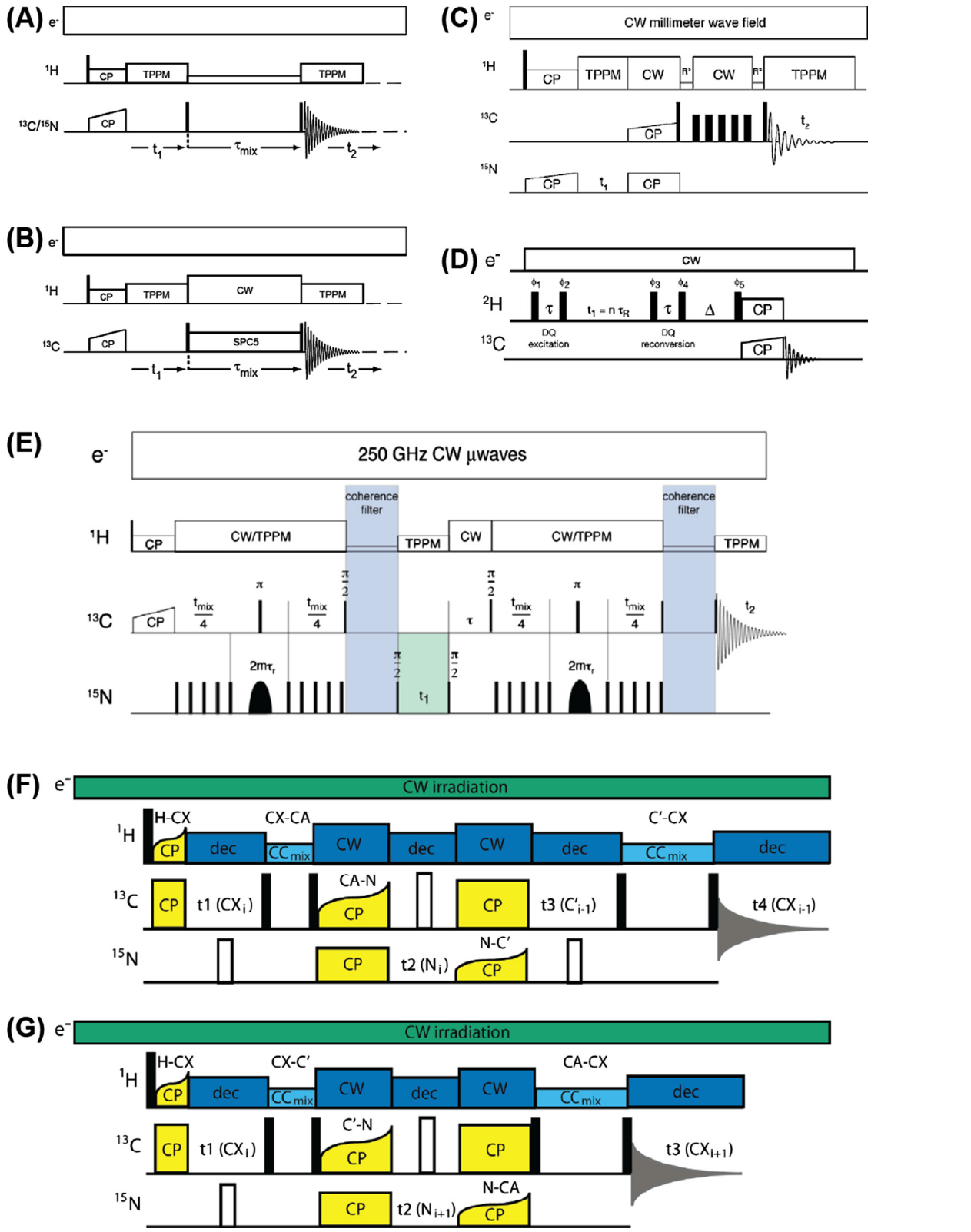

Fig. 17. Various MAS NMR pulse sequences employing DNP enhancement. (A) Homonuclear correlation spectroscopy by proton-driven spin diffusion and (B) by SPC5 double-quantum mixing; reprinted from [137] with permission. (C) Heteronuclear correlation spectroscopy by double CP in combination with homonuclear mixing; reprinted from [146] with permission. (D) Double-quantum (DQ) ^{2}H–^{13}C correlation spectroscopy; reproduced from [147] with permission. (E) Frequency-selective transferred-echo double resonance (FS-TEDOR); reprinted from [148] with permission. (F) "Backward" (4D CX(Cα)NC′CX i → i − 1) and (G) "forward" (3D CX(C′)N(Cα)CX i → i + 1) S^3 correlation experiments; reproduced from [149] with permission.

μw irradiation where the acceleration voltage of the gyrotron μw source was cut right before NMR acquisition [91], it was shown that this instrumentation-taxing technique is unnecessary [137]. Consequently, experiments can be performed virtually unchanged from their "conventional" variants by allowing the polarization transfer chain explained earlier to occur during the regular recycle delay while the sample is continuously irradiated by μw. Thus, modification of typical MAS NMR pulse sequences is generally not required.

2.3.2. Indirect vs. direct DNP

As shown in Fig. 15, DNP can be performed either directly on the nuclear species to be detected (*i.e.*, low-γ nucleus) or indirectly by first hyperpolarizing ^{1}H and then transferring the enhanced polarization to the low-γ nuclei for detection or further evolution/-transfer [91]. These scenarios are usually known as direct and indirect DNP.[3] Here, it should be noted that these definitions should generally be based on the pathway of enhanced polarization from the PA to the nuclear spin that is detected. In the following, we will see that there are several ways how this pathway can be controlled. In particular, experimental parameters such as field/frequency matching can be adjusted in favor of a specific DNP mechanism, or a suitable pulse sequence/phase cycle can be employed which allows a selective read-out of the sought-after polarization.

2.3.3. Active DNP pathways

In the case of bis-nitroxide PAs, the field profiles of ^{1}H and low-γ nuclei such as ^{13}C are almost congruent (see Section 3.2.2). Consequently, both DNP transfer pathways are equally active, although they may occur with different rates. Polarization that has built up by unwanted transfer pathways has to be discarded by the pulse sequence used for read-out, however, in most cases, appropriate phase cycles are already implemented in the conventional pulse programs (*e.g.*, Hartmann-Hahn cross-polarization) in order to suppress spurious contributions.

In the case of PAs with narrow EPR lines, the SE mechanism allows for selection of the DNP transfer pathway. By choosing the respective SE matching condition, Eq. (12), either ^{1}H or the low-γ nuclear species can be selectively hyperpolarized while the other species remains close to thermal polarization (see Section 3.2.1). Therefore, in these cases, the DNP matching has to be adjusted when changing between indirect and direct DNP detection schemes by adjusting the magnetic field or the μw frequency.

2.3.4. Pulse sequences for indirect or direct DNP read-out

Most commonly performed is indirect DNP, where the polarization is generated on a suitable nuclear species, normally ^{1}H, and is then transferred to the nuclear species of interest such as ^{2}H, ^{13}C, ^{15}N, ^{17}O, ^{27}Al, ^{29}Si, etc. (Fig. 15). This transfer is typically performed by cross-polarization (CP), after which either the free induction decay (FID) is recorded or further magnetization transfer steps can be employed. Any potential polarization that has built up by direct DNP is filtered by an appropriate CP phase cycle, in the same way as the thermal polarization of the nuclear spins to be detected is discarded in a conventional CPMAS experiment. Indirect DNP has the advantage that by hyperpolarizing a strongly-coupled nuclear spin network, the DNP transfer process is very efficient and short build-up time periods as well as a uniform spreading of enhanced polarization can be achieved.

For direct DNP, on the other hand, no heteronuclear transfer step is involved and a simple single-pulse excitation is used for read-out of the FID or for further transfer. In the cases where low-γ nuclei are detected, the initial direct DNP transfer and the subsequent spreading through the bulk can be considerably slower and less efficient, especially when the local spin concentration is small. Therefore, spatial polarization gradients must be expected and have indeed been observed experimentally [138,139]. Also, increased line widths of the DNP-enhanced MAS NMR spectrum in comparison with the non-enhanced spectrum have been reported due to selective hyperpolarization of nuclei that are close to the paramagnetic PA [139–141]. Nevertheless, direct DNP can be performed in the absence of ^{1}H (*i.e.*, where CP cannot be employed) [142], or where the direct transfer pathway is preferred, for example, in order to distinguish between surface and bulk sites [143,144] or to constrain enhanced polarization within a certain distance/volume around the PA [139,140].

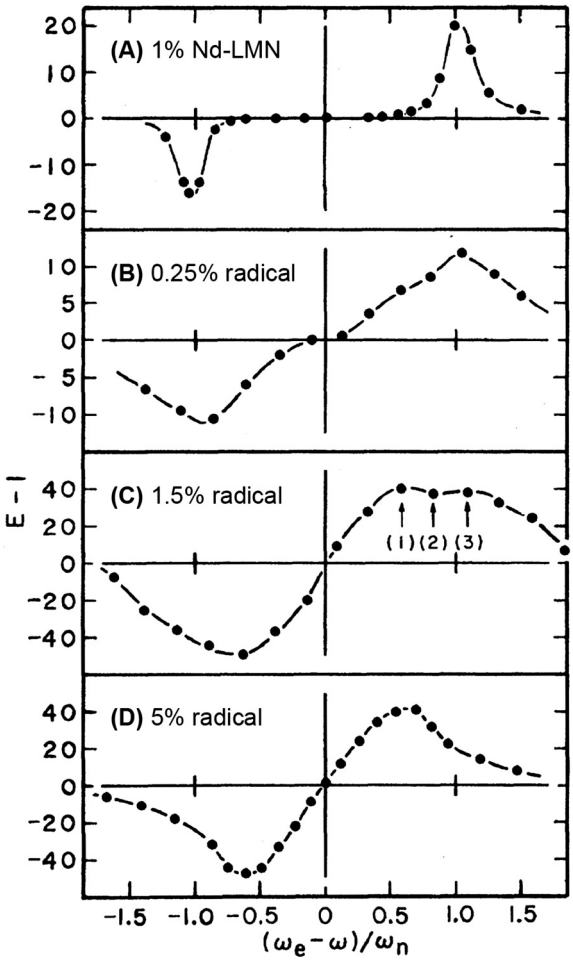

Fig. 18. ^{1}H enhancements as function of static applied magnetic field at 4.2 K and 70 GHz: (A) 1% Nd^{3+} in LMN; (B), (C), and (D) 0.25, 1.5, and 5% Ley's radical by weight in polystyrene, respectively. The magnetic field axis is shifted for comparison as $g \approx 2.7$ for Nd-LMN, and $g \approx 2.0$ for Ley's radical. Reprinted with permission from [59].

2.3.5. Simultaneous indirect and direct DNP

Differentiation between direct and indirect DNP processes is only clear when no heteronuclear contact exists except the controlled (coherent) transfer pathway during the CP contact period. Recently, it has been shown that non-coherent transfer of polarization can also occur during DNP build-up between hyperpolarized ^{1}H and ^{13}C due to cross-relaxation (see Fig. 16) [139,141,145]. In this case, a negative signal enhancement is generated on ^{13}C suggesting dipolar ^{1}H–^{13}C cross-relaxation dynamics to be responsi-

[3] Direct and indirect DNP as transfer pathways are not to be confused with direct and indirect CE as DNP mechanisms (dCE/iCE) which are described in Section 2.2.2.3.

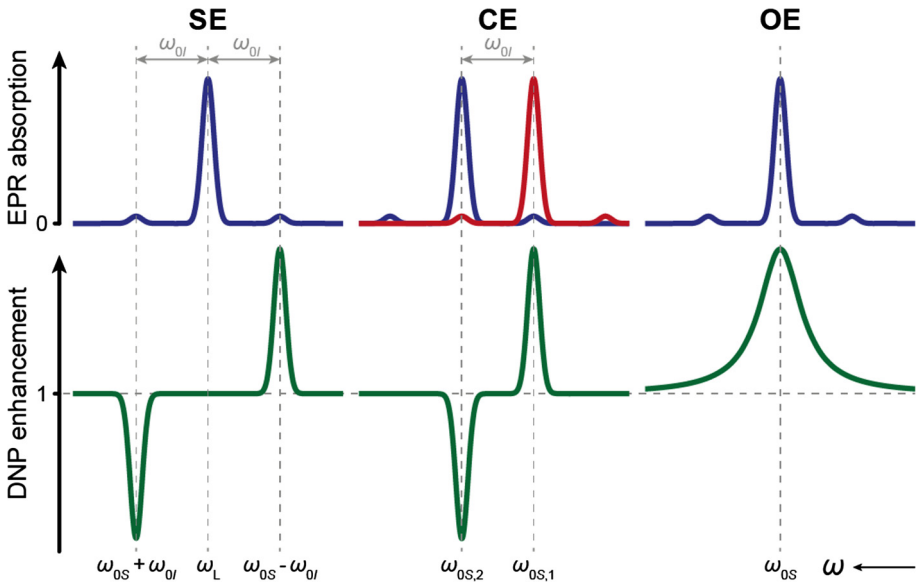

Fig. 19. Theoretically predicted DNP field profiles (green) of SE, CE, and OE, based on simple EPR line shapes (blue and red). Small satellite peaks at an offset corresponding to ω_{0I} are the forbidden e–n DQ and ZQ transitions and are largely exaggerated in intensity. For CE, the EPR lines of two electron spins with ideal CE matching condition $\Delta\omega_{0S} = \omega_{0I}$ are shown in different colors.

ble. For biomolecules, methyl groups have been identified as effective cross-relaxation promotors under DNP, even at temperatures of 100 K [141].

In the case of a bis-nitroxide PA, both nuclear species (*i.e.*, ^{1}H and ^{13}C) are hyperpolarized at the same time. Subsequently, a combination of (+)-DNP enhancement by direct ^{13}C DNP and of (−)-DNP by indirect DNP due to cross-relaxation is observed, partially cancelling each other. Nevertheless, due to the spatial selectivity of the two processes—direct DNP requires close vicinity of a PA while indirect DNP is emanating from methyl groups substantially removed from the PA—filtering schemes can be applied in the form of decoherence filters or ^{1}H saturation schemes [141,145]. The former technique removes contributions from fast-decaying coherences of ^{13}C nuclear spins in close vicinity of the PA while the latter suppresses the build-up of (−)-DNP by cross-relaxation from ^{1}H. When the ^{1}H SE condition can be induced selectively, enhancement due to indirect DNP by cross-relaxation can also be selectively observed without filtering techniques [139].

The additional selectivity provided by these methods is highly promising towards the generation of non-uniform and spatially constrained polarization which can potentially be utilized for spectral isolation of a sought-after molecular species within a complex mixture. First steps in this direction have been taken with the direct labeling of biomolecules with PA-tags (see also Section 6.3.4); the possibility of straightforward background removal by subtraction of non-enhanced (^{1}H-saturated) spectra underscores the importance of such methods.

2.3.6. Examples of NMR pulse sequences used for MAS DNP

Generally, most MAS NMR pulse sequences can be applied in combination with DNP without further modifications. Therefore, we will only present a small selection of NMR pulse sequences reported in combination with DNP which is based mostly on historical developments. However, the performance of pulse sequences—in particular those including long mixing periods—might be affected by the presence of the PAs which act as centers for enhanced longitudinal and transverse relaxation (see Section 6.4.2).

Many examples of DNP-enhanced multidimensional pulse sequences have been reported during the last years. Earliest reports included homonuclear chemical-shift correlation spectroscopy [137], heteronuclear correlation spectroscopy by double CP (DCP) in combination with homonuclear mixing [146], double-quantum (DQ) ^{2}H–^{13}C correlation spectroscopy [147], and frequency selective TEDOR (FS-TEDOR) in combination with DNP [148] (see Fig. 17), as well as indirect detection of ^{14}N by HMQC [150].

The large sensitivity gain by DNP has also stimulated the development and application of techniques that are otherwise not possible. For example, Märker et al. have applied a ^{15}N–^{13}C DCP-based heteronuclear correlation experiment (DCP-HETCOR) on a deoxyribonucleoside derivative in natural isotopic abundance which—in combination with ^{13}C–^{13}C *J*-refocused INADEQUATE—allowed for the complete assignment of ^{13}C and ^{15}N resonances despite the very low probability of direct one-bond contacts (*i.e.*, 10^{-2}% for ^{13}C–^{13}C and 4×10^{-4}% for ^{13}C–^{15}N) [151]. Very recently, McDermott and co-workers have developed a novel 3D/4D sequential sidechain-sidechain (S^3) correlation spectroscopy experiment (see Fig. 17F and G). This technique is only possible due to the large sensitivity gains by DNP and allows full assignment of protein resonances in a fraction of the experimental time required for conventional MAS NMR despite the frequently encountered inhomogeneous broadening and subsequent overlap of resonances at cryogenic temperatures [149]. A much more exhaustive description of experiments enabled by DNP is given in the context of relevant applications with DNP in Section 7.

3. Enhancement profiles

Polarization transfer from electron spins to nuclear spins can only take place at appropriate resonance conditions defined by the DNP mechanisms [*i.e.*, the DNP matching conditions as given by Eqs. (12) as well as (33)] and as explained in detail in Section 2.1. This can be achieved in two ways: either the magnetic field is shifted such that the electron and nuclear Zeeman interactions fulfil the matching condition with a fixed μw frequency, or—given a frequency-tunable μw source is available—the μw frequency can directly be adjusted. Thus obtained profiles of field- or frequency-dependent enhancement factors are commonly referred to as DNP field or frequency profiles, respectively; these two methods yield—except for the typical inversion of the abscissae—practi-

cally equivalent profiles. The oftentimes rich information contained in such profiles can be used to optimize DNP experiments or to investigate DNP mechanisms in more detail. Due to the widespread use of fixed-frequency gyrotron sources for MAS DNP (see Section 4.2.1), field profiles are most commonly recorded with sweepable NMR magnets which are now commercially available [152]. Alternatively, when a frequency-tunable μw source is utilized, the acquisition of frequency profiles is the most convenient method in a static DNP setup; however, the limited bandwidth of the μw resonating structure has be taken into account [153].

3.1. Development of fundamental DNP theory

Discussions of DNP field profiles have played a major role in the development of DNP theory. In fact, the very first hypothesis of CE was based on the observation of unexpected changes in the DNP field profiles at 2.5 T (70 GHz e^-; 106 MHz ^1H) [58,59]. In these important experiments, Hwang and Hill observed a drastic change in the DNP enhancement profiles with varying concentration of Ley's radical [154] in polystyrene (see Fig. 18). SE was the only DNP mechanism known for solids at that time, and Jeffries and Schmugge had already established that (+)- and (−)-DNP enhancement peaks were then separated by $2\omega_{0I}$, based on the experiments on a lanthanum magnesium double nitrate crystal doped with 1% Nd^{3+} (Nd-LMN) [155]. With higher concentrations of Ley's radical in polystyrene, Hwang et al. observed a decrease in the separation of the (+)- and (−)-DNP extrema. This was attributed to the variation in e–e spin interactions and was dubbed *spin–spin effect*. Further experimental and theoretical research in this direction led to the establishment of CE as a viable DNP mechanism [61,62]. To date, CE is the most commonly employed mechanism when DNP is applied as structural investigation technique (see Section 7).

Analysis of DNP profiles of sample systems where SE is dominating—especially when differential SE was observed with inhomogeneously broadened EPR spectra—stipulated a deeper understanding of the role of spatial and spectral spin diffusion (Section 2.3.2) to explain the efficient transfer of enhanced polarization to the nuclear spin bulk [76,101,106,121,122]. Consequently, the information obtained from DNP profiles led to the development of advanced theories of (integral) DNP mechanisms [156]. While DNP profiles due to SE can oftentimes be predicted quite accurately on basis of the EPR spectrum of the PA [157], CE is associated with much more complicated and less intuitive DNP profiles [158]. Furthermore, OE DNP was observed in insulating solids by analysis of DNP profiles [89,90,97]. In the following, we summarize the key points that characterize active DNP mechanisms (*i.e.*, SE, CE, and OE) under typical experimental conditions based on the theoretical discussion in Section 2.1.

3.2. Differences due to DNP mechanisms and polarizing agents

3.2.1. Solid effect

SE is mainly observed with monomeric radicals featuring a relatively small EPR spectral breadth so that CE matching is inefficient; alternatively, also radicals with broad EPR linewidth can induce SE when their concentration is small and thus, intermolecular e–e interactions required for CE are negligible. In the simplest case, the shape of the DNP field profile can be directly deduced from the EPR spectrum of a PA [74,139,158]. According to Eq. (12), excitation of the e–n DQ or ZQ transitions leads to positive, (+), or to negative, (−), nuclear polarization enhancement, respectively. These conditions are separated by $2\omega_{0I}$. In the case of a narrow EPR spectrum—where ZQ and DQ transitions are sufficiently separated—the net (+)- and (−)-DNP enhancement peaks are well resolved and occur at frequencies $\omega_{0S} - \omega_{0I}$ and $\omega_{0S} + \omega_{0I}$, respectively (see SE case in Fig. 19 and green spectrum in Fig. 20).

Inhomogeneous broadening of EPR spectra by typical mechanisms such as Zeeman anisotropy or unresolved HFI directly affects DNP field profiles as well. Even when the ZQ and DQ SE transitions are sufficiently separated (yellow spectrum in Fig. 20), the

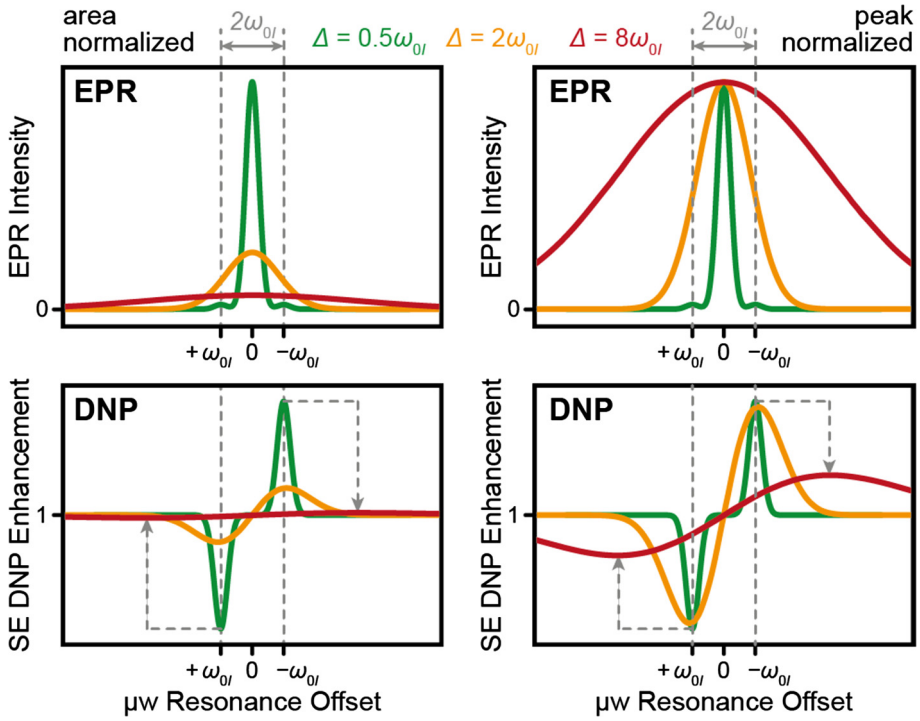

Fig. 20. Theoretical analysis of field profiles predicted by inhomogeneously broadened EPR spectra, demonstrating the transition from well-resolved SE (green) *via* partial overlap of ZQ and DQ transitions (orange) to differential SE (red). The left column shows spectra and profiles normalized to the full area under the EPR absorption spectrum while the right column data is normalized to the maximum peak absorption.

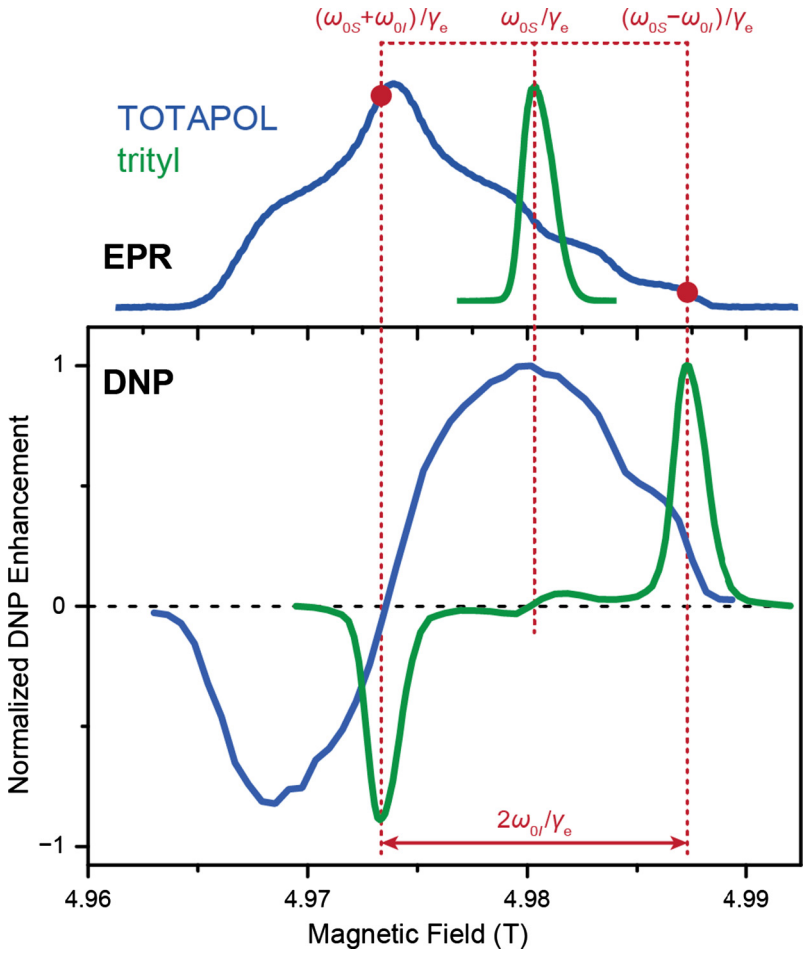

Fig. 21. Experimental DNP field profiles of TOTAPOL (blue) and trityl OX063 (green) in comparison with their respective EPR spectra at 140 GHz μw frequency. For trityl, DNP by SE is excited at the DQ and ZQ transitions of the EPR resonance (outer red dotted lines). For TOTAPOL, excitation of the SQ EPR transition of one spin packet (middle red line) leads to possible CE matching with spin packets resulting in opposite DNP sign, albeit with different probabilities (red dots).

resulting reduction of the excitation efficiency achievable with a fixed-frequency μw source leads to a proportional reduction of the maximum bulk signal enhancement due to a smaller number of spin-packets actively participating in SE induction [159]. This reduction can (in part) be compensated for by electron spectral diffusion [134,160], or—in the case of MAS DNP—rotor-angle dependent evolution of anisotropic interactions [75,83,156]. Also, frequency modulation has been shown to result in higher enhancement factors in static DNP [161–164]. In all of these cases, a larger number of electron spins were excited by μw irradiation as would be expected from the homogeneous linewidth of the spin packets as long as sufficient μw power was available for operation in the (partial) saturation limit of the SE. Unfortunately, this power requirement is usually not met for MAS DNP—even when a high-power gyrotron is used—due to the small transitions moments of the SE [74,89,139].

If the overall breadth due to inhomogeneous broadening of the EPR line exceeds $2\omega_{0I}$ (red spectrum in Fig. 20), overlap of the ZQ and DQ transitions causes mutual cancellation of (+) and (−) enhancements and hence reduction of the net nuclear bulk polarization in addition to the less effective spin packet excitation described in preceding paragraph. As we have already explained in Section 2.2.1.5, for very large EPR line widths ($\Delta \gg 2\omega_{0I}$), the DNP profile resembles the first derivative of the EPR spectrum [76]. Consequently, the separation between the maxima of (+)- and (−)-DNP peaks becomes greater than $2\omega_{0I}$.

A simple yet effective method for simulation of SE DNP profiles has been presented by Shimon et al. and is based on the differential (net) amplitude of DQ and ZQ transitions obtained by the EPR spectral shape function [158]. This method can easily be applied if the EPR spectrum is available (most preferably recorded with the same μw frequency used for DNP) and has proven highly useful in the identification of transitions between active DNP mechanisms [139,165], as is outlined in Section 3.3.1.

3.2.2. Cross effect

PAs with broad and anisotropic EPR spectra often favor the CE mechanism, given sufficient inter- or intramolecular e–e dipole coupling is provided. The shape of the CE field profile caused by such an inhomogeneous EPR line is difficult to understand or predict. As a *gedankenexperiment*, a spin system featuring two narrow lines which are separated by the nuclear Larmor frequency would achieve an ideally efficient CE [61]. In this case, the field profile would consist of two DNP peaks of different relative sign, separated by the nuclear Larmor frequency. These peaks coincide with the two EPR absorption lines: by direct excitation of either the low- or high-frequency EPR transition a CE three-spin-flip is induced, leading to either (+) or (−) nuclear enhancement, respectively (see CE case in Fig. 19). Such idealized systems are difficult to design due to the limitations on *g*-factor variation of available radicals; nevertheless, a mixture of BDPA and trityl type radicals

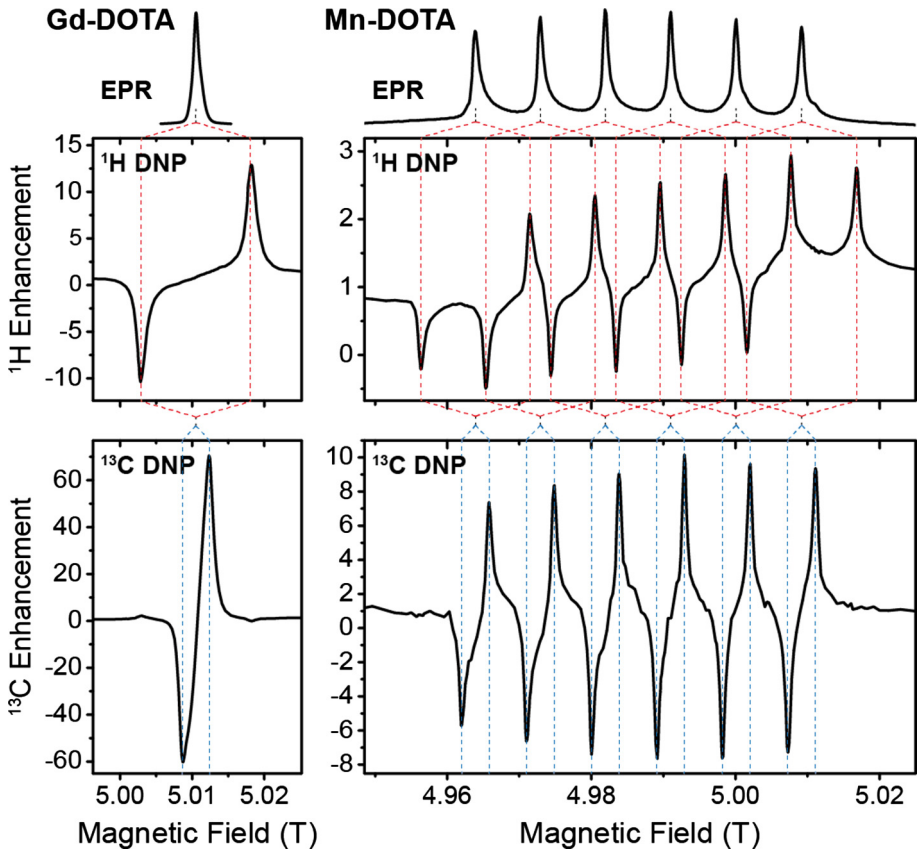

Fig. 22. ^{1}H and ^{13}C DNP field profiles of Gd-DOTA and Mn-DOTA PAs. EPR spectra shown on top of DNP profiles. All data recorded at 140 GHz μw frequency with 10 mM PA concentration in a 60/40 (vol%) glycerol/water solution at ~86 K. Figure adapted with permission from [139],.

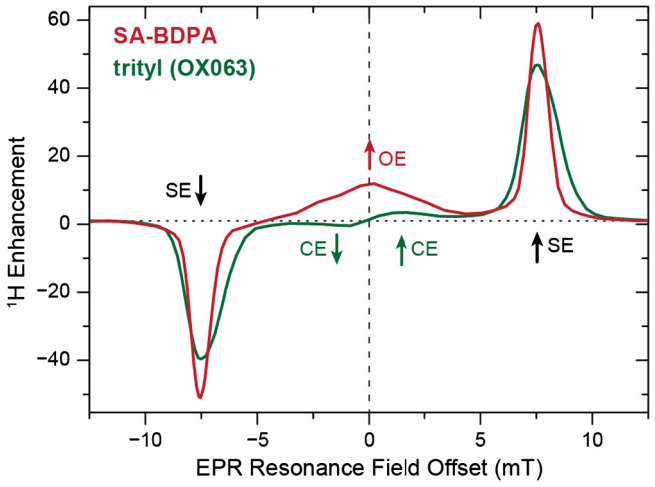

Fig. 23. ^{1}H DNP enhancement field profiles of SA-BDPA (red) and trityl OX063 (green) measured at 140 GHz μw frequency (5 T) at 40 mM PA concentration in each case. Field profiles are centered around the EPR resonance maximum for each radical. Besides the prominent SE at the marked position, SA-BDPA shows significant OE with a saturation-broadened peak at the EPR transition; in contrast, trityl shows small contribution from CE with inflection of enhancement at the EPR transition. Data taken from [89].

can mimic such a scenario for DNP of low-γ nuclei [82]. This situation is discussed in more detail in Section 5.2.3.

For strongly anisotropic, inhomogeneously broadened EPR lines (*i.e.*, $\Delta > \omega_{0I} > \delta$), contributions from all spin packets within the spectral envelope have to be considered in a disordered sample. Excitation of the absorption line at an arbitrary field/frequency combination will in most cases lead to both (+)- and (−)-DNP with concomitant partial cancellation. Subsequently, the DNP profile spreads across the whole EPR absorption spectrum and most importantly, no plateau occurs (Fig. 21). Under static conditions with randomly oriented monomeric radicals, a rather straightforward matching probability between spin packets can be evoked. Thus, for each point in field or frequency, the probabilities of finding matching partners separated by $\Delta\omega_{0S} \approx \pm\omega_{0I}$ [see Eq. (33)] that result in (+) or (−) enhancement are weighted against each other, yielding a relative enhancement factor [158].

For a typical bis-nitroxide system, this analysis would have to account for the correlation between the molecular frames of the two interconnected radical moieties. The complexity is further exacerbated under MAS as explained in Section 2.1.2. As we have additionally laid out in Section 2.2.2, quantum-mechanical propagation of the full density operator in Liouville space is currently not feasible. Very recently, Mentink-Vigier et al. have introduced a semi-classical theory for simulation of such CE profiles under MAS, based on the solution of Bloch-like differential equations and numerical analysis of the adiabaticities of level anti-crossing (LAC) events within the Landau-Zener approximation [156].

3.2.3. Overhauser effect

As already discussed in Section 2.1.3, initially unexpected ^{1}H signal enhancements by OE DNP have been reported in dielectric solids under MAS [89,90,97]. Since the OE operates by incoherent e–n cross relaxation, it can theoretically be driven by direct or indirect saturation of the EPR resonance line. Up to now, only direct saturation has been reported experimentally [89,90,97]; however, the slight asymmetry of maximum (+)- and (−)-DNP enhancement

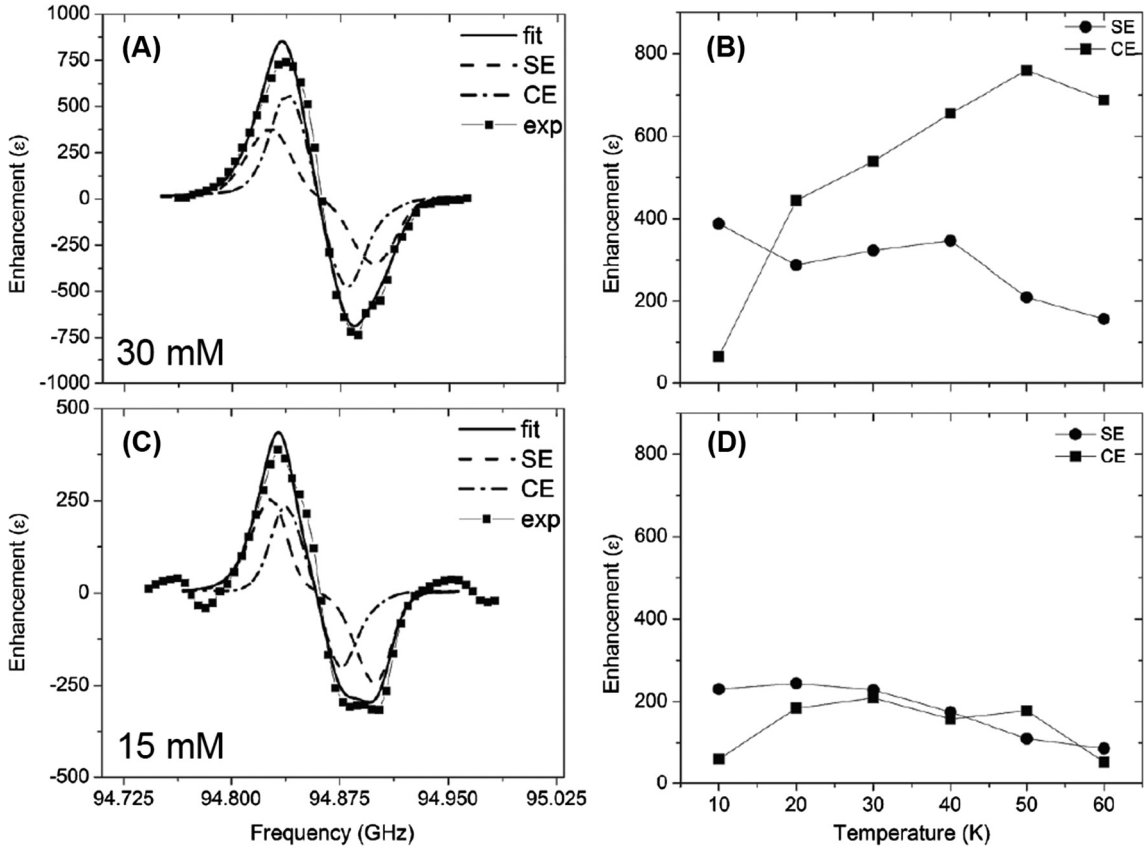

Fig. 24. (A) Experimental DNP frequency profile (squares) overlaid with the best-fit simulated ^{13}C DNP profile (solid line) for 30 mM trityl at 30 K. The simulated DNP profile consists of the sum of simulated SE (dashed line) and CE (dash-dotted line) profiles. (B) relative contribution of SE (circles) and CE (squares) as a function of temperature for the same sample. (C) and (D) show corresponding data for 15 mM PA concentration. Reprinted from [169] with permission.

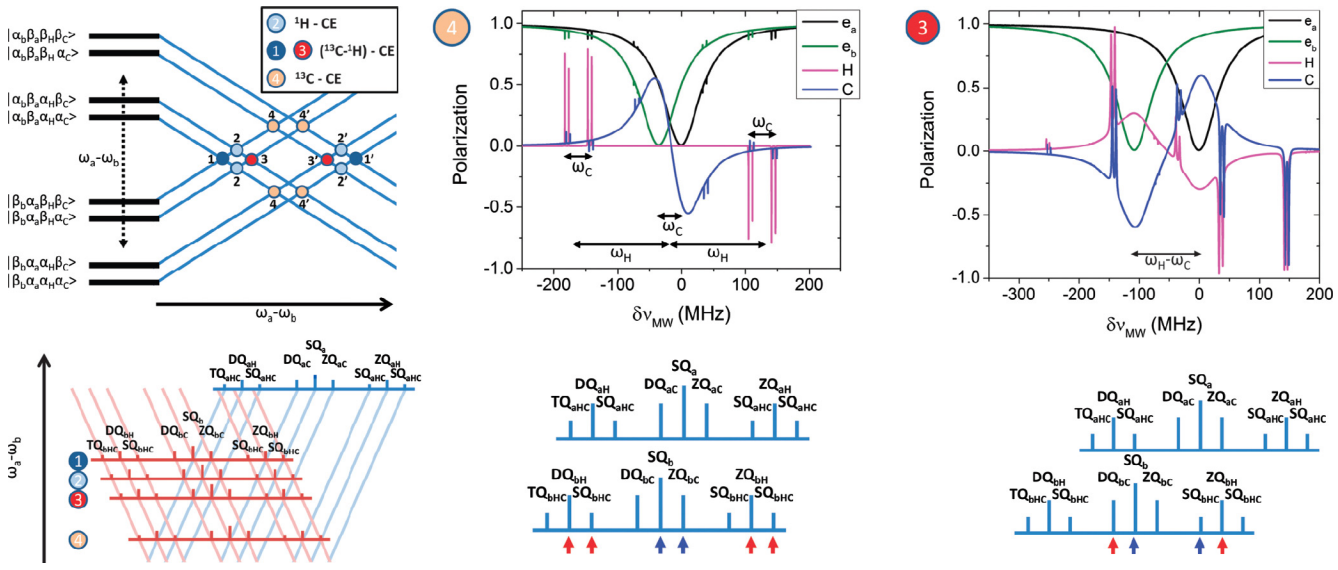

Fig. 25. Illustration of heteronuclear CE. Left: Eight central spin states of an e_1–e_2–^1H–^{13}C four-spin system as function of the electron Larmor frequency difference. Middle: Simulated electron and nuclear spin polarization profiles for the ^{13}C CE matching condition; right: same polarization profiles at the ^{13}C–^1H CE matching condition. Matching between the different possible spin transitions are shown in the lower depictions; for further details, the reader is referred to the original publication. Reproduced from [175] with permission.

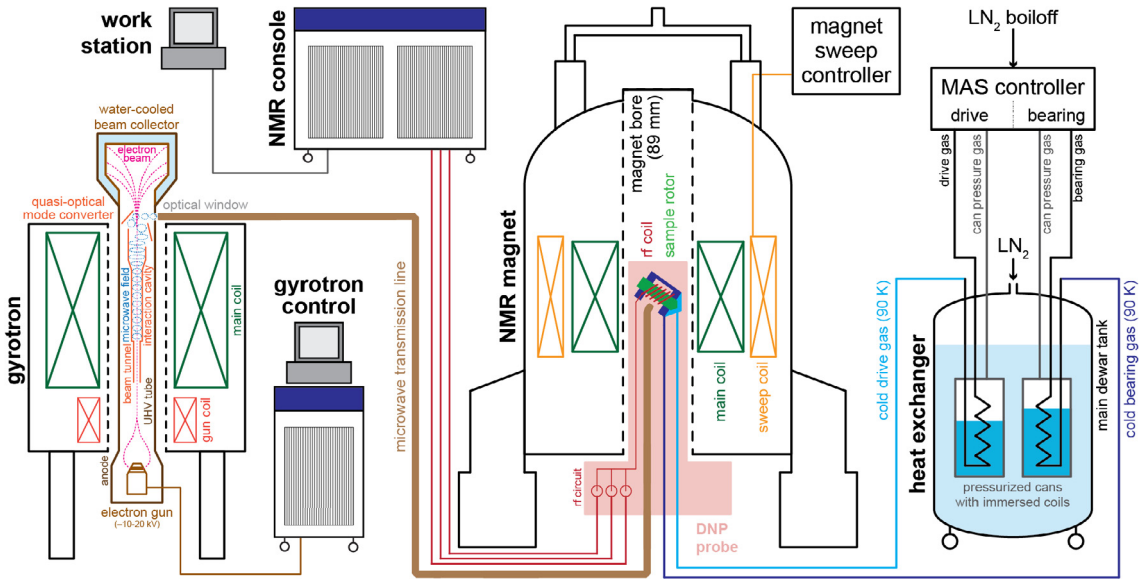

Fig. 26. Schematic representation of a typical experimental setup for DNP-enhanced MAS NMR spectroscopy. Besides the requirements for conventional solid-state NMR spectroscopy, microwaves generated by a gyrotron are transmitted into the probe. A cryo-MAS unit provides stable sample spinning at cryogenic temperatures.

factors observed at the SE conditions for trityl and SA-BDPA [74,89] might be attributable to an indirect saturation of the EPR line and subsequent OE by e–n cross relaxation.

DNP enhancement of one specific sign is theoretically expected and has been observed experimentally [89,166]. As shown in Fig. 19 (OE case), the DNP condition is centered around the EPR spectrum and generally resembles the EPR line shape. However, in all cases reported so far, a broadening of the OE DNP profiles with respect to the EPR spectrum has been observed. This is caused by a highly efficient saturation even at low μw power, so that off-resonance saturation has to be considered as is described in Section 2.1.3.

3.2.4. High-spin metal ions

The DNP mechanisms responsible for enhancement by high-spin metal ion PAs (Gd^{3+} and Mn^{2+}) have been analyzed based on their field profiles [139,159,167]. Representative examples of field profiles are shown in Fig. 22. The theoretical description follows the same principles as laid out for PAs with $S = 1/2$ in Section 2.1. However, the situation is not trivial due to the occurrence of multiple spin transitions with different properties. The EPR spectra of half-integer high spin systems often feature a narrow and isotropic (to first order) central transition (CT) and highly anisotropic satellite transitions (STs) spreading over a large field/frequency range due to zero-field splittings (ZFS.) As a result, the narrow CT evidently allows for SE [139], whereas the role of STs is still unclear. The large angular dependence of ZFS might support CE under MAS [167]. However, clear indications for such CE matching between STs or between a ST and the CT has not been presented yet. Therefore, for all examples of DNP with high-spin PAs presented thus far, a treatment of the CT alone is believed to be sufficient to explain occurrences of both SE and CE [139,168].

3.3. Information content

3.3.1. Identification of DNP mechanism

Even though knowledge of the sample composition and environment (*e.g.*, PA type and concentration, temperature, external magnetic field) might already indicate the dominant DNP mechanism, the exact prediction is not straightforward; indeed, even a transition from one dominant mechanism to another can occur when changing experimental parameters. As described in the preceding sections, the shape of the field profile can yield valuable information about the DNP mechanism active within a sample under certain experimental conditions.

Certain selection criteria have to be fulfilled for effective contribution of a specific DNP mechanism. CE requires a PA which allows for frequency matching according to Eq. (33) (*i.e.*, $|\Delta\omega_{0S}| = \omega_{0I}$) while at the same time sufficient e–e dipole couplings have to be present. If one of those criteria is not met, CE is absent or inefficient. For example, SA-BDPA shows no sign of CE due to the small EPR linewidth even though sufficient e–e dipole couplings are expected at the high concentration. In many cases two mechanisms can be observed to exist next to each other. For example, SA-BDPA shows OE being active besides SE; for trityl OX063, minor contributions from CE ^{1}H DNP are evident along with major enhancements due to SE [74,89]. This situation is illustrated in Fig. 23.

Such a combination of different DNP mechanisms is much less obvious when PAs with EPR line widths exceeding the nuclear Larmor frequency are considered (*i.e.*, $\Delta > \omega_{0I} > \delta$). Intuitively, efficient CE is expected if a dipolar coupling between electron spins is provided. However, SE can still contribute significantly to the observed DNP enhancement. This situation has been investigated in detail by the Vega group in the context of static DNP. Shimon et al. corroborated the relative contribution of CE and SE from TEMPOL in static samples and found a transition between the different mechanisms depending on experimental parameters such as sample temperature and incident μw power [158]. Interestingly, the absolute contribution of the ^{1}H CE decreased at low temperatures (<30 K); this observation has also been reproduced by similar experiments with the biradical TOTAPOL [165] as well as with the monoradical trityl for ^{13}C DNP [169]. The latter example is shown in Fig. 24. Significant extension of electron spin lattice relaxation at lower temperatures has been proposed as the possible explanation of this phenomenon. The decrease of CE efficiency when lowering the temperature is rather unexpected and not observed under MAS conditions. In contrast, under MAS overall DNP enhancements increase with decreasing temperatures; this has been experimentally shown down to 24 K [170]; furthermore, enhancement factors are higher than those obtained under static conditions [171]. How-

ever, to the best of our knowledge, no similar attempt to disentangle relative contributions of SE and CE has been undertaken so far for MAS DNP.

3.3.2. Multinuclear DNP

Another interesting effect has been reported already more than 40 years ago by Borghini, De Boer and Morimoto in relation to their analysis of ^{1}H and ^{2}H DNP enhancement profiles. They observed (weak) DNP features occurring at $\omega_{\mu w} = \omega_{0S} \pm 2\omega_{0I}(^{1}\mathrm{H})$ as well as $\omega_{\mu w} = \omega_{0S} \pm \omega_{0I}(^{1}\mathrm{H}) \pm \omega_{0I}(^{2}\mathrm{H})$ at temperatures of 700 mK [172,173]. These features were identified as forbidden multi-spin SE transitions, where an electron spin flips together with two protons or one proton/deuteron pair in a concerted manner. Such multi-nuclear SE transitions with up to four protons flipping at the same time have also been observed indirectly by depletion of the electron spin polarization at 80 K by Smith et al.; however, no DNP enhancement by multi-nuclear flips could be observed at this temperature. Nominally, such multi-spin transitions are strongly forbidden, nevertheless, the large number of nuclear combinations paired with indirect homonuclear couplings introduced by strong HFI is expected to increase the effective transition probabilities [174].

The aforementioned heteronuclear multi-spin SE has also been observed for ^{1}H and ^{13}C in samples doped with 15 mM trityl at

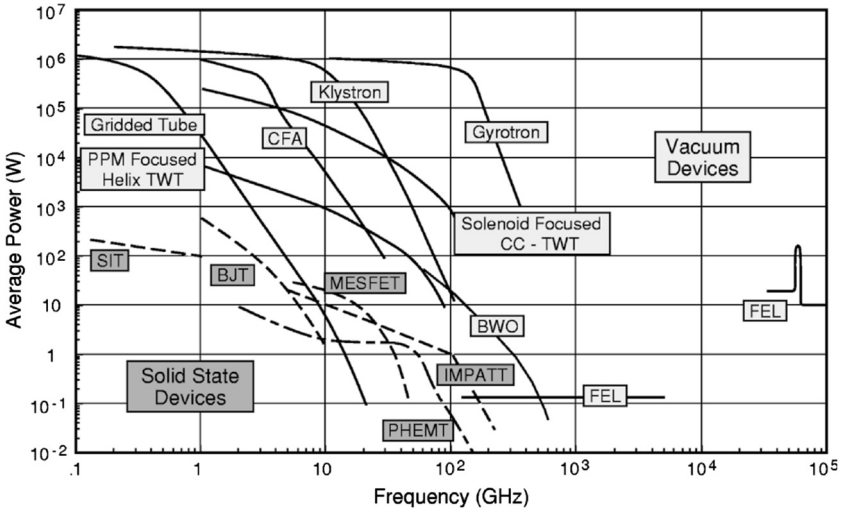

Fig. 27. Frequency dependence of the output power of different electronic devices capable of producing high-frequency electromagnetic irradiation. For abbreviations and further explanations, the reader is referred to the original publication. Reprinted with permission, from [185].

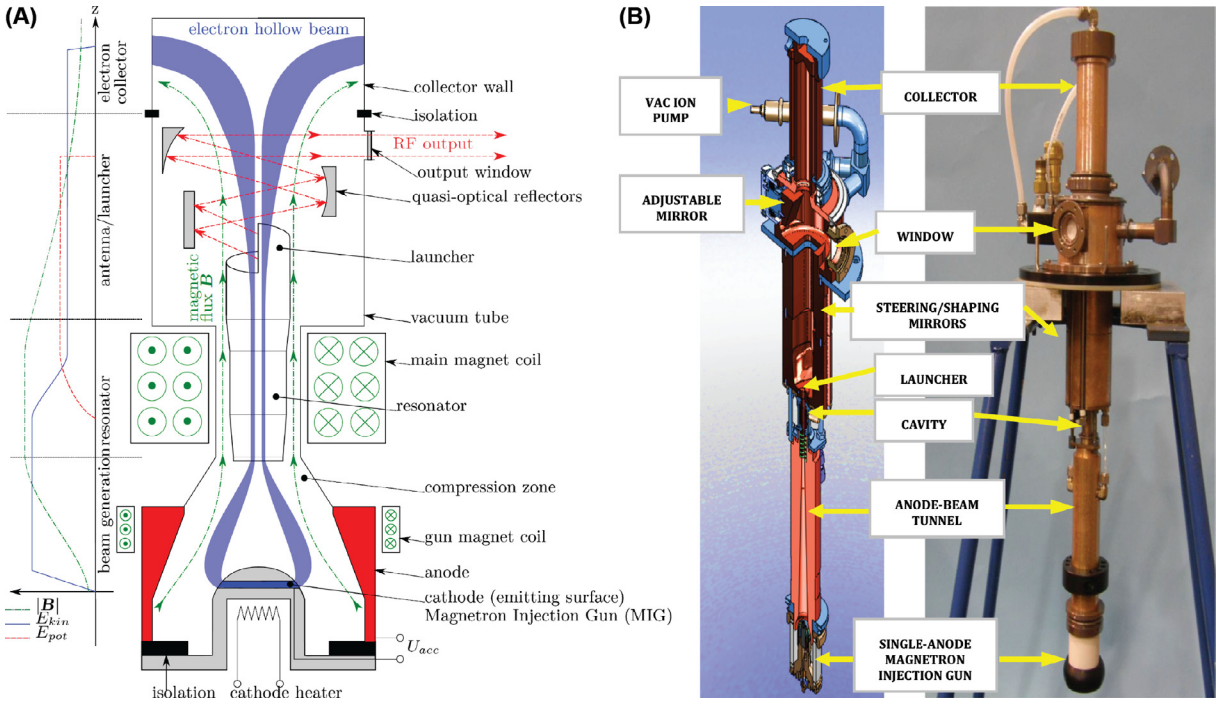

Fig. 28. (A) Schematic drawing of a gyrotron showing the essential components for μw generation; the left plot shows the qualitative profiles of magnetic field (green), electron beam kinetic energy (blue) and μw field potential energy (red). See text for further description. Figure is reproduced from [203] with permission. (B) Computer-generated model (left) and photograph (right) of a 395 GHz gyrotron commercially available from Bruker Biospin. Reprinted from [152] with permission.

temperatures of up to 30 K (see Fig. 24C) [169]. Shimon et al. have performed a detailed experimental analysis of this effect and have proposed several multi-spin transfer pathways to occur in parallel as direct (*i.e.*, coherently μw-driven) or indirect (*i.e.*, due to electron spin polarization depletion) DNP mechanisms (see also Fig. 25) [175]. Later, this model was extended to account for experimental observation of simultaneous heteronuclear CE between ^{1}H and ^{2}H [176]. For detailed explanation of these effects we refer the reader to the original publications.

4. Instrumentation

Due to the unique experimental conditions (*i.e.*, high-power, high-frequency μw irradiation, cryogenic MAS), application of DNP requires significant modifications of existing MAS NMR instrumentation. Since 2009, specialized hardware has been offered commercially by Bruker Biospin for a magnetic field of 9.4 T [177]; recently the scope has been extended by instruments operating at fields of 14.1 and 18.8 T [152].

A schematic drawing of a typical DNP MAS setup is shown in Fig. 26. A short description of the most important components and their implication on effective DNP enhancements is given in the following. For an extensive treatment of the technical details of the individual components, the reader is referred to several excellent reviews [146,152,178–180].

4.1. High-frequency microwave sources

4.1.1. Gyrotrons

Until the mid of the 1990s, the available μw sources had been the limiting factor for the external magnetic field at which the DNP NMR experiments were conducted. Pioneered by Griffin and co-workers, [91,181,182] the introduction of gyrotrons as sources of high-power/high-frequency μw radiation dramatically extended this limit (see Fig. 27). Moderate- to high-field DNP setups are accessible today as a result of intensive research [152,177,183,184].

Gyrotrons were originally developed for plasma heating in Tokamak fusion experiments by producing pulsed outputs in the $>$ 1 MW power range; an excellent historical review on the general development of these devices has been written by Nusinovich et al. [186]. For DNP experiments, gyrotrons have been introduced as a truly continuous μw source by a combined effort of Richard Temkin at the Plasma Science and Fusion Center (PSFC) and Robert Griffin at the Francis Bitter Magnet Laboratory (FBML) at MIT [182]. While the original setup operated at 140 GHz, the scope has been extended by development of gyrotrons by academic research groups with purpose for DNP applications at 250, 330, and 460 GHz (MIT) [146,187–190], 400 and 460 GHz (Osaka) [191–193], 187 GHz (Warwick) [194], 200 GHz (WUSTL) [195], and 260–530 GHz (EPFL) [196–198]. Furthermore, gyrotrons for DNP applications have been developed or designed by *Bruker Biospin*/*Communication & Power Industries* (CPI) (263, 395, and 527 GHz) [152,177,199], *Gycom* (259 GHz) [200] and *Bridge12* (395 GHz) [201].

Gyrotrons for continuous wave (cw) operation provide reliable monochromatic μw irradiation frequencies up to 1 THz and deliver continuous output power at the sample in the order of 10 W and higher. Such high power levels are necessary for MAS DNP as the size of the sample exceeds the μw wavelength several-fold; thus, the sample is not situated inside a μw-resonating structure. In contrast, for EPR and static DNP experiments a resonator is typically used, alleviating the requirement for large incident power by efficient conversion between incident μw power and field amplitude.

As electron cyclotron maser devices, gyrotrons rely on the acceleration of an annular-shaped electron beam—which is emitted from an electron gun cathode—into a longitudinal magnetic field (see Fig. 28). Within this field, the electrons gyrate with their cyclotron resonance frequency and pass an interaction cavity. Here, the cyclotron maser instability causes transverse bunching of the electrons and an electromagnetic field is generated [202]. This field in turn interacts with the movement of the electrons in the beam, amplifying the bunching and allowing the extraction of transverse kinetic energy in the form of μw irradiation which is then guided into an overmoded, corrugated waveguide (see Section 4.4.2) by a quasi-optical mode converter.

Under stable operation conditions, up to 200 W of power can be extracted while the power from the overall kinetic energy of the beam is ~1.5 kW. This results in an energy efficiency of ~10–15% [189]; this figure is considerably smaller (~1%) when a high-frequency gyrotron operates at the second harmonic of the cyclotron condition (thus requiring a smaller magnetic field) [204]. This high power output is possible because a gyrotron operates as a fast-wave device with minimal power deposition in the highly-overmoded interaction cavity. Virtually all excess (waste) power is deposited within a water-cooled collector situated behind the quasi-optical mode converter. This situation is different for slow-wave devices which can also provide high frequencies, but are limited with respect to the output power because of significant power deposition within the small interaction structure (see section below).

For practical purposes, the cyclotron frequency must coincide with the Larmor frequency of the electron spins of the PA. Therefore, a second superconducting magnet of similar field strength as the NMR magnet (or an integer fraction thereof if overtones are used) is required. However, due to relativistic effects of electrons within the high-energy beam, the magnetic field of the gyrotron magnet has to be increased by ~2% so that DNP matching conditions can be achieved with typical nitroxides or other radicals. There are plans to overcome this requirement for a second superconducting magnet—bearing significant cost and lab space

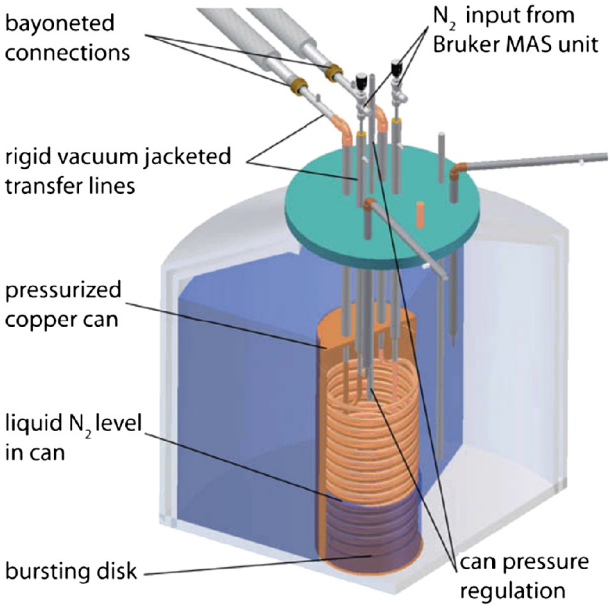

Fig. 29. Typical heat exchanger used for producing cold gas for sample spinning. A conventional MAS unit produces a regulated flow of gas, which is cooled to a target temperature inside a pressurized copper can. The output temperature of the cryogenic gas is controlled by the pressure of the inner can. Reprinted from [215] with permission.

burden—by a miniaturized gyrotron to be used inside a two-center magnet [205–208].

4.1.2. Other sources

In addition to the above, μw irradiation generated by an extended interaction oscillator/klystron (EIO/EIK) [170,209], a backward wave oscillator (BWO) [206], or a solid-state source [162,163] has been employed for MAS DNP. EIKs and EIOs are linear-beam devices with high-power capability and a relatively large bandwidth that can either spontaneously generate the high-frequency μw field (EIOs) or amplify a low-power driving input (EIKs). In both cases, this is accomplished through interaction of the accelerated electron beam with a cavity, which can consist of a single gap (EIO) or can be constituted by multiple coupled gaps (EIK) [210]. However, the dimension of the interaction cavity of these "slow-wave" devices decreases with increasing frequency. If long life-time should be guaranteed, this restricts the achievable maximum powers.

Similar limitations are also faced in the case of BWOs. These are vacuum tube devices, where μw frequency oscillations are created by propagating a traveling wave backwards against the electron beam. Thus, the group velocity of the generated electromagnetic wave is opposite to the direction of the electron beam. BWOs have a broad tuning range and can in principle be operated in both cw and pulsed mode, however, output powers decrease rather quickly at frequencies higher than approximately 100 GHz [211].

Solid-state sources—which usually operate by up-conversion of a low μw frequency to the desired output—are robust, cheap and allow for control of the output power, frequency and phase in a simple way. Furthermore, employment of fast μw gating by PIN diode switches or mixers and frequency modulation by an arbitrary waveform generator (AWG) before up conversion allow the generation of simple rectangular or amplitude/frequency shaped pulses, similar to applications in modern pulsed EPR [153,162,212,213]. The major drawback is the extremely low maximum power tolerated by these solid-state devices in the range of a few tens of mW that typically requires a combination with a high-frequency amplifier based on the above-mentioned principles.

In these situations where MAS DNP enhancement factors are limited by insufficient μw power, lowering the experimental temperature to 20 K and below can alleviate the problem [163]. However, increasing demand by high-frequency DNP applications has already stimulated significant advances in maximum output power and frequency of these rather cheap and compact devices and further developments might make these sources viable alternatives to gyrotrons for common MAS DNP applications.

4.2. Control of DNP matching conditions

4.2.1. Magnetic field variation

A drawback of commercially available gyrotrons for DNP applications [152] is that they generate a fixed μw frequency. Therefore, the static external magnetic field of the NMR magnet is initially set to a certain value such that electron and nuclear Larmor frequencies are adjusted for optimum enhancement obtainable with typical nitroxide-based PAs.

A greater flexibility is obtained if the NMR magnet is equipped with an additional superconducting sweep coil. This allows for fine-tuning of the magnetic field and consequently, the matching conditions for maximum SE or CE enhancement [Eqs. (12) and (33), respectively] can be reached for other PAs as well. It is important to note that—in particular for PAs with narrow matching conditions—sweeping the field may be required to achieve (direct) DNP for different nuclei. Examples for such field-swept DNP enhancement profiles are illustrated in Section 3 as well as in Fig. 35.

Superconducting magnets with such tuning capabilities are now commercially available with fields up to 18.8 Tesla. However, the accessible field range is limited by the sustainable current limit of the sweep coil and the field can only be swept over a restricted range. Thus, the DNP conditions for certain radical–nuclei combinations may or may not be accessible depending on the type of PA (for details see Section 5) and magnet setup used. Furthermore, the sweep rate often is rather limited and temporary field instability/drift as well as changes in homogeneity following charging or discharging the sweep coil have to be considered.

4.2.2. Microwave frequency tunability

Accounting for these above-mentioned limitations, recently developed frequency-tunable gyrotrons have potential advantages and would simplify the experimental setup because they could alleviate the necessity for field sweepability of the NMR magnet. Rather small frequency tuning within a range of ~100 MHz can be achieved by temperature-controlled changes in (single-mode) interaction cavity dimensions [177]. For a larger frequency range the interaction cavity has to be re-designed such that several longitudinal modes are accessible by magnetic field and/or beam voltage variation. Such devices have first been introduced for DNP operation at 460 and 330 GHz with a tuning range of up to 1.2 GHz [187,188]. However, the output power can vary significantly over the tuning range due to differences in efficiency and overlap of different interaction modes. More recently, tuning ranges of up to 3 GHz have been reported for several devices operating at frequencies between 200 and 530 GHz [189–192,195,196]. Nevertheless, such frequency tunability has barely been utilized yet in order to address varying matching conditions due to different DNP mechanisms or PAs, or for the acquisition of DNP frequency profiles under MAS [209].

4.2.3. Fast microwave frequency modulation

An interesting application of frequency tunability has first been demonstrated using solid-state sources under either static or MAS conditions: by modulation of the μw frequency in the kHz range, a significant increase in DNP enhancement was observed [161–164]. A modulation capability has henceforth been adopted for frequency-tunable gyrotrons, where variation of the beam voltage allows for fast modulation of output frequency [193].

In the context of static DNP, the effect can be easily explained by the increase of the number of directly excited spin packets within an inhomogeneously broadened EPR spectrum [161]. For MAS, the situation is more complex due to rotational evolution of the spin Hamiltonian (see Section 2.1.2) and an extended theoretical treatment of the problem still has to be developed in order to properly explain the effect.

4.3. Cryogenic MAS

A rigid dipolar-coupled spin network and sufficiently long electron and nuclear spin relaxation times are prerequisites for high DNP enhancements. Thus, typical MAS DNP of biomolecular samples or surface-wetted materials generally require cryogenic temperatures between 20 K [163] and 180 K [214]. The region between ~100 and 180 K can rather easily be achieved with commercial instrumentation and liquid nitrogen (LN_2) as cryogen. Custom instrumentation with optimized thermal insulation can reach temperatures as low as 80 K [215,216]. For even lower temperatures, cooling with liquid Helium (LHe) is necessary [170,178,217]. In both cases the liquid cryogens are also often used for *in-situ* generation of very pure MAS gas by evaporation.

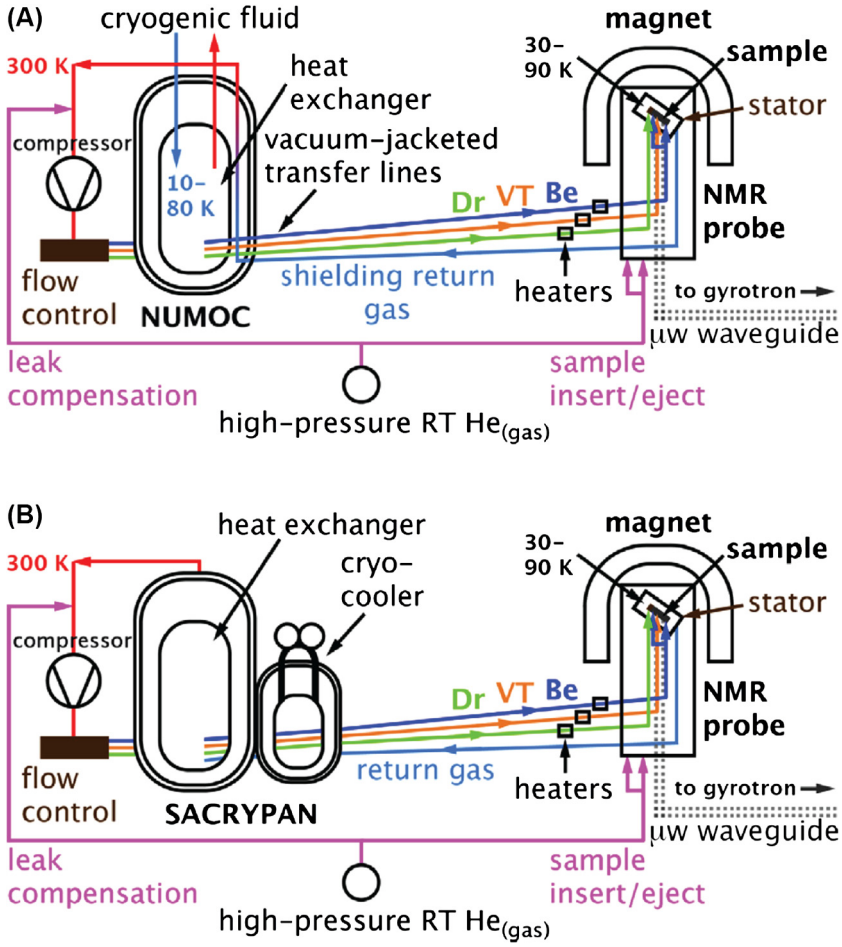

Fig. 30. Schematic drawing of a closed-loop system for helium- or N_2-cooled MAS with cooling by (A) cryogenic fluid (LHe or LN_2) or (B) a cryo-cooler. Reprinted from [217] with permission.

4.3.1. Nitrogen cooling

Several engineering challenges have been mastered to provide stable MAS with cryogenic gas, specifically nitrogen at favorable temperatures close to the liquefaction point [152,215]. A steady flow for each of the cold spinner gases (*i.e.*, bearing and drive with a gas flow in the order of 50–100 l/h [152]) has to be produced by external heat exchangers, which can be regulated according to the required spinning frequencies and sample temperature. A "coil-in-can design" has proven very effective for providing long-term stability and preventing liquefaction of the spinner gas to avoid major spinning instabilities [184,215]. This design relies on the spinner gas flowing through a coiled copper tube that is situated within a pressurized copper-can submerged in LN_2 (see Fig. 29). By externally adjusting the pressure of N_2 gas inside the can, the liquid level and thus the contact surface and heat transfer rate between coil and LN_2 can be controlled. In early designs, both spinner gas lines were cooled within one can; more recent designs feature separate cans for bearing, drive and variable temperature (VT) gas lines, allowing for greater adjustability. Vacuum jacketed transfer lines then transport the cold gases to the DNP probe, entering the sample chamber either through the probe body, or from the top of the vertical magnet bore.

Use of LN_2 for MAS feed gases (boil-off) and for cooling thereof results in significant costs of operation. In total, the consumption of LN_2 adds up to several hundreds of liters per day for a typical setup described above. Recently, it has been shown that consumption of LN_2 can be dramatically reduced by utilization of nitrogen generators and refrigerators [183,184].

4.3.2. Helium cooling

Further reduction of the sample temperature can be desirable for increase in DNP enhancement, especially when available μw power is limited (see also Section 6.2.4). This can be achieved by using Helium as spinner gas for MAS [91,178,217,218]. In particular, due to the large running-costs associated with LHe, a low-consumption design is essential. For example, the return gas can be recycled in a closed-circle setup as shown in Fig. 30 [178,219].

Alternatively, LHe boil-off can be directly used to selectively cool the sample with the VT line, while MAS operation is provided with RT or precooled gas [170,220]. In this design, a rotor material with low thermal conductivity such as ZrO_2 allows for anchoring the (axially) outer regions of the rotor at room temperature by the bearing and drive gas while the central region—separated from the bearing spaces by baffles—is cooled down to 20 K. However, this low temperature can only be reached if extra-long rotors are used so that the temperature gradient between bearing and sample region is reduced. Furthermore, recycling of the cost-expensive helium is not possible in this case.

4.3.3. Fast MAS and cryogenic temperatures

Due to the increasing viscosity of N_2 as temperatures approach the liquefaction point, maximum MAS rates are significantly reduced as compared to conventional MAS NMR experiments with room temperature gas. Originally, the instrumentation for cryogenic MAS has been developed for rotor diameters between 2.5 and 7 mm [91,184,215,218,221]. In these cases, spinning rates were limited to ~15 kHz.

With the advent of fast MAS applications and ^{1}H detection, fast-spinning MAS DNP probes have recently become available. This extended the available spinning frequencies up to 40 kHz at 100 K by using smaller diameter rotors (1.3 mm), allowing not only for mechanistic investigations of DNP under these conditions (see also Section 6.2.2) but also for higher sensitivity and resolution [86].

4.4. DNP NMR probe and microwave transmission

4.4.1. Cryogenic probe design

In addition to conventional solid-state NMR functionality, DNP probes have to be designed to account for μw transmission and cryogenic MAS. The latter requires an air dielectric transmission line rf circuit design [222]. This allows for removing the tuning and matching elements from the cold rf coil and positioning of those within the probe box that is ideally stabilized at room temperature [215].

The large temperature gradient within the probe is typically sustained by incorporation of thermally insulated transfer lines for cold MAS gas as well as a VT line for additional sample cooling capacity. In order to prevent significant temperature reduction and subsequent condensation of humidity within the probe body, the exhaust line has to be thermally insulated as well; the cold exhaust can be used to pre-cool MAS/VT feed gases in order to reduce cryogen consumption [217]. Insulation can be provided by vacuum

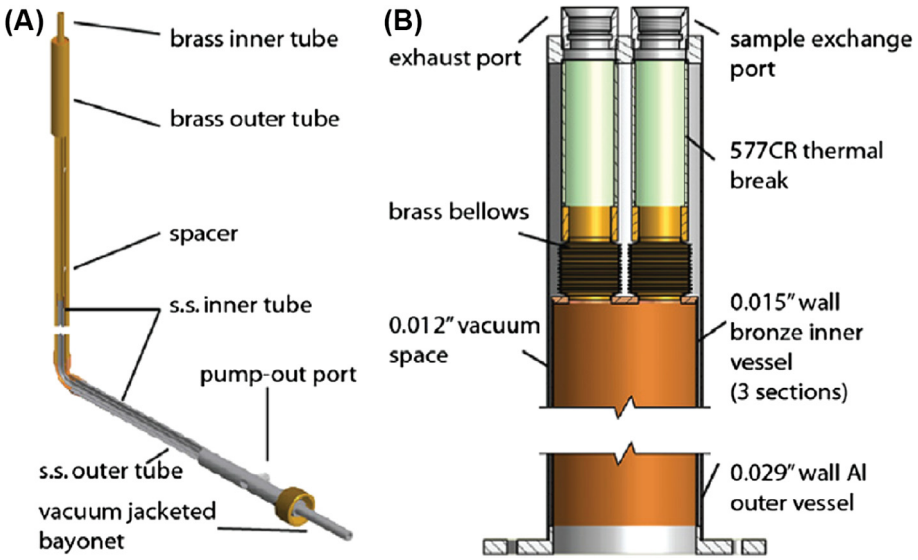

Fig. 31. (A) Model for the vacuum-jacketed, thermally insulated transfer lines inside the probe. Brass tubing is used for durable vacuum retention. (B) A vacuum-jacketed Dewar is incorporated with a sample exchange port and an exhaust port. Fiberglass and brass bellows act as thermal breaks. Reprinted from [184] with permission.

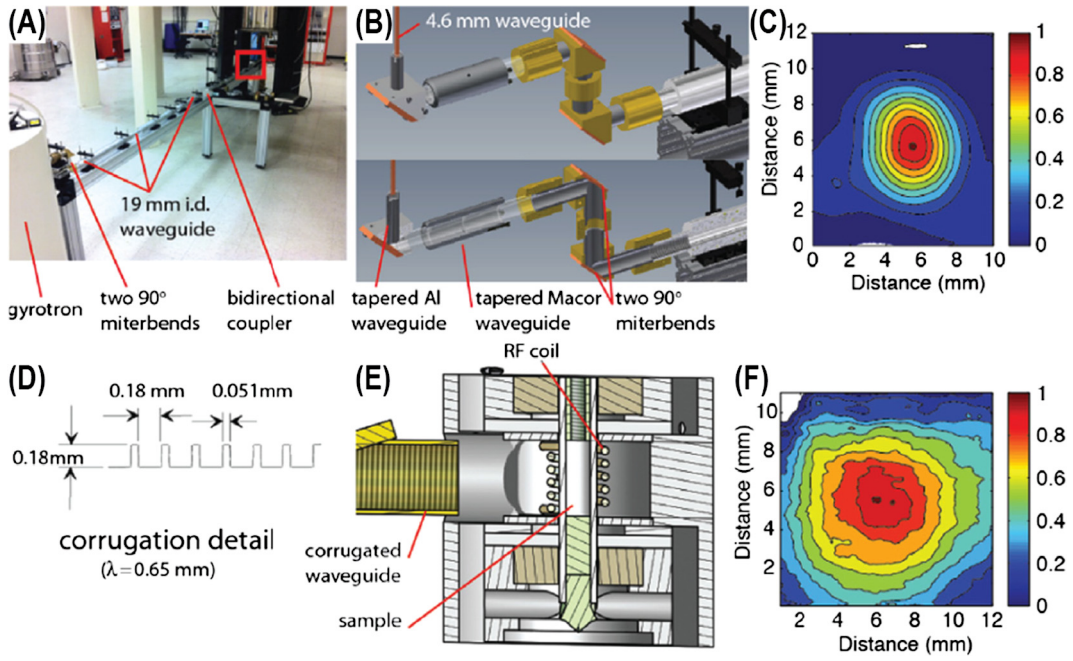

Fig. 32. (A) Photograph of the μw transmission line of a typical DNP setup. (B) Model of tapers and miter bends that are used to focus the microwave beam into the vertical waveguide leading to the stator. (C) Thermal image of the microwave beam in the middle of the wave guide. (D) Schematic drawing of the corrugations. Depth and spacing fulfil the $\lambda/4$ condition. (E) Cross-section of the stator with the end of the waveguide directing the μw irradiation on the rotor. (F) Image of the beam leaving the wave guide towards the sample. Reprinted from [184] with permission.

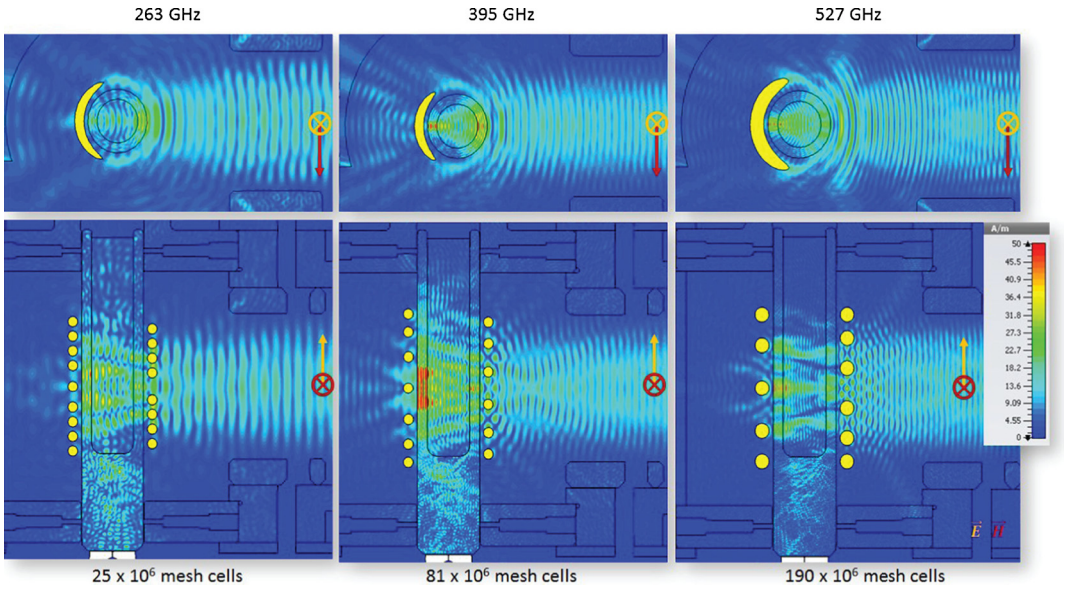

Fig. 33. Simulated μw magnetic field magnitude distribution inside the coil of a 3.2 mM MAS probe at 263, 395 and 527 GHz. The microwave beam enters from the right side. Rows show views along the rotor axis (top) and in a plane perpendicular to this axis (bottom). Reprinted from [152] with permission.

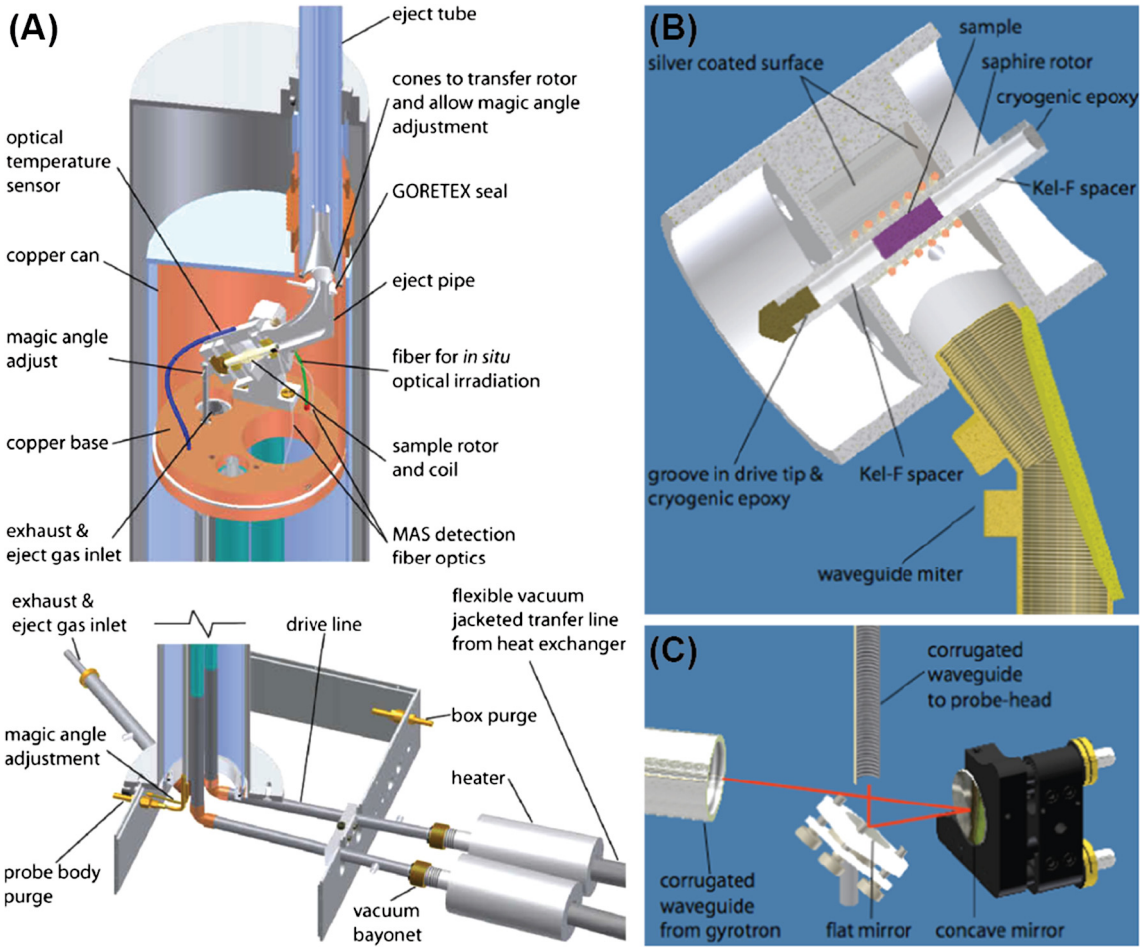

Fig. 34. (A) Schematic drawing of a MAS DNP probe with possibility for *in-situ* optical irradiation. Further modifications to standard MAS NMR functionality are the angled eject tube for convenient cryogenic sample (un-)loading. (B) Enlarged view of the corrugated waveguide that transmits μw irradiation to the sample. (C) Quasi-optical system of mirrors delivers the microwaves from the gyrotron towards the stator. Reprinted from [215] with permission.

jacketing of coaxial tubes and employing materials with small thermal conductivity. Stainless steel fulfils these criteria, however, even "non-magnetic" austenitic steel alloys (*e.g.*, 316, 321 series) tend to magnetize due to mechanical stress and repeated temperature cycling [215]. Therefore, stainless steel should not be used near to the homogeneous region of the magnetic field (*i.e.*, the sweet spot). Fiberglass can be an alternative, but brass has proven superior vacuum retention properties as well as durability and can be easily soldered to the stainless-steel section of the transfer lines; in the same vein bronze has successfully been used for construction of the cryostat that shields the magnet bore from the cryogenic temperatures [184]. Such a design is shown in Fig. 31.

Additionally, a thermal break is incorporated within the electrically and thermally well-conducting copper transmission line. A section of stainless steel near the probe body can serve as such, but reduction of electrical conductivity of this part of the resonant circuit and subsequent loss of rf efficiency has to be compensated by a non-magnetic silver/gold plating with thickness on the order of the rf penetration depth [215].

4.4.2. Microwave transmission from source to sample

Usually, the μw beam is converted from its initial higher mode generated inside the gyrotron interaction cavity to a Gaussian mode of propagation by the use of a quasi-optical mode converter typically consisting of a Vlasov antenna [189,194]. The Gaussian beam then exits the gyrotron tube *via* a sapphire window optimized in thickness for minimal reflection losses and is guided into an overmoded circular waveguide for transmission in an HE_{11} mode (Fig. 32A). Due to the excellent coupling between a Gaussian beam propagating in free space and this hybrid mode propagating inside an overmoded waveguide, negligible insertion losses occur even in the absence of special coupling elements such as horns, given that the beam width is significantly smaller than the inner diameter of the waveguide. Corrugation of the inner waveguide surface further minimizes transmission losses so that <0.1 dB m^{-1} attenuation [223] can be achieved (Fig. 32D); however, care has to be taken for good alignment of the waveguide. Miter bends are used for changes in propagation direction, for example for adjustment between differences in the gyrotron output window and the probe input port orientation, or if vertical level changes have to be accounted for.

Alternatively, also quasi-optical systems of transmission have been developed for DNP. These feature the advantage of extremely low transmission losses and simple manipulation of the μw polarization properties by a Martin-Puplett interferometer that can be utilized to increase power efficiency of spin excitation and larger DNP enhancements for a given output power [224]. However, due to the rather long wavelengths in the 0.6–2 mm range, the angular spread of the μw beam is significant. This requires a significant number of parabolic mirrors with large diameter and relatively short focal lengths so that the μw beam can be transmitted efficiently over the necessary distance [194]. Therefore, such a system can only be employed if space is not a limiting factor.

The μw beam enters the probe *via* one of the above-mentioned paths. Due to the space restriction within the longitudinal bore of the superconducting magnet, an efficient design can be achieved by utilizing the hollow inner conductor of the coaxial rf waveguide of the transmission line probe as the circular overmoded μw waveguide. Since this conductor is part of the rf resonant circuit, care has to be taken to provide electrical isolation between the externally connected end of the waveguide and the rf transmission line, for example by quasi-optical coupling between the elements [215]. Alternatively, the μw beam can also be coupled to the DNP probe from the top of the bore [194].

4.4.3. Inside the sample chamber

4.4.3.1. Microwave irradiation of the sample. In a typical design, a miter bend in close vicinity of the MAS stator changes the direction of propagation such that the μw beam is launched orthogonally to the rotor axis. The waveguide is terminated shortly before reaching the rf coil (Fig. 32E). As shown in Fig. 33, the wave fronts are significantly diffracted (and reflected) due to the rf coil featuring a pitch of similar magnitude as the wavelength. This can create a non-uniform distribution of the μw field amplitude and induce phase shifts across the sample.

The dielectric properties of typically used sapphire rotors improve the μw-field filling factor; at the same time MAS leads to a partial averaging of angular field inhomogeneity. Nevertheless, a field inhomogeneity with an amplitude variation of a factor ~3

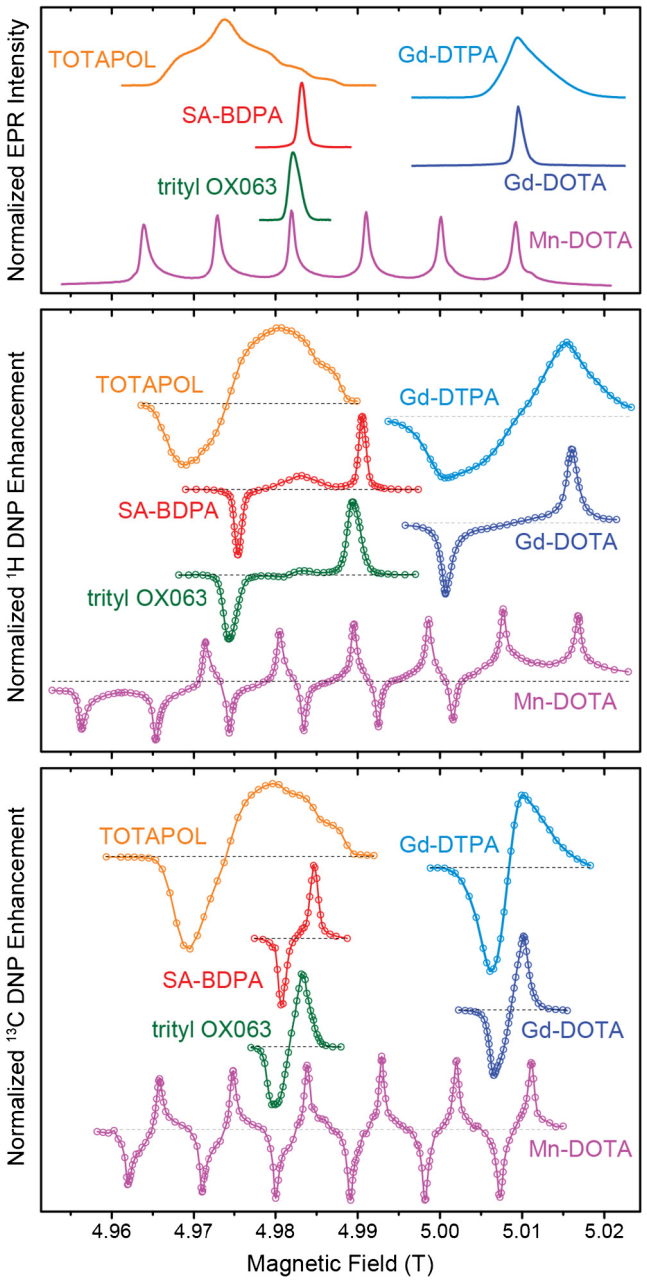

Fig. 35. Comparison of the EPR lineshapes and the corresponding ^{1}H and ^{13}C DNP field profiles of different PAs. Figure taken with permission from [139].

has to be accounted for [87]. Furthermore, thermal conductivity of sapphire is similar to that of copper at temperatures of around 100 K, which ensures efficient dissipation of heat deposited by dielectric losses within the sample during μw irradiation. Rotors made of ZrO_2—which are generally more robust and less expensive—have less favorable transmission/reflection properties at μw frequencies as well as lower thermal conductivity, so that reduced enhancement factors and increased sample heating is observed [177].

Efforts have been taken to improve the conversion factor (*i.e.*, the ratio between incident μw power and generated field amplitude) within the framework of an MAS stator, for example by addition of an astigmatic lens optimized for the cylindrical rotor shape [87], or by reflective coating of the inner stator surface so that a significant *Q* factor increase could be achieved [215]. Also, varying the rf coil pitch with larger separations in the central section has been tried in order to minimize diffraction interference [152]. Alternative approaches employ μw irradiation of the sample along the spinning axis [91,183,194]. Such a design does not require modification of a commercially available stator, prevents diffraction by the coil and potentially improves power conversion and irradiation efficiency, for example, by providing a reflective surface at the far end of the sample chamber [91]. However, in such a design, the presence of the waveguide or quasi-optical mirrors along the rotor axis introduces additional problems regarding sample ejection.

4.4.3.2. Sample changing: injection and ejection of rotors. Due to operation under cryogenic conditions, removal of the cold probe from the cryostat for access to the stator requires exposure to ambient environment. This in turn necessitates a full temperature cycling of the probe to room temperature and back to ~100 K in order to remove any condensation. This procedure is not only time-consuming but also introduces the possibility of failure due to handling or thermomechanical wear. Therefore, modern DNP probes are usually equipped with a semi-automatic sample inject/eject system.

A model developed by the Griffin group at MIT is shown in Fig. 34 [215]. This design has been adapted by Bruker in their commercial instruments [177]. The rotor is injected either from the top of the bore or through the bottom of the probe and is pneumatically driven in and out of the stator by controlled pressure bursts of nitrogen gas. This greatly eases experiments, especially when a large number of samples is involved, such as for systematic investigations of optimal DNP conditions, or when screening sample-composition dependent parameters [225]. Under certain conditions it is also possible to inject pre-cooled rotors containing temperature-sensitive samples [177].

4.4.3.3. Light-activation. For the investigation of photo-activated processes, the DNP probe can be modified with a light irradiation channel (Fig. 34). This is typically achieved by introduction of an optical fiber that connects to a laser system outside the probe

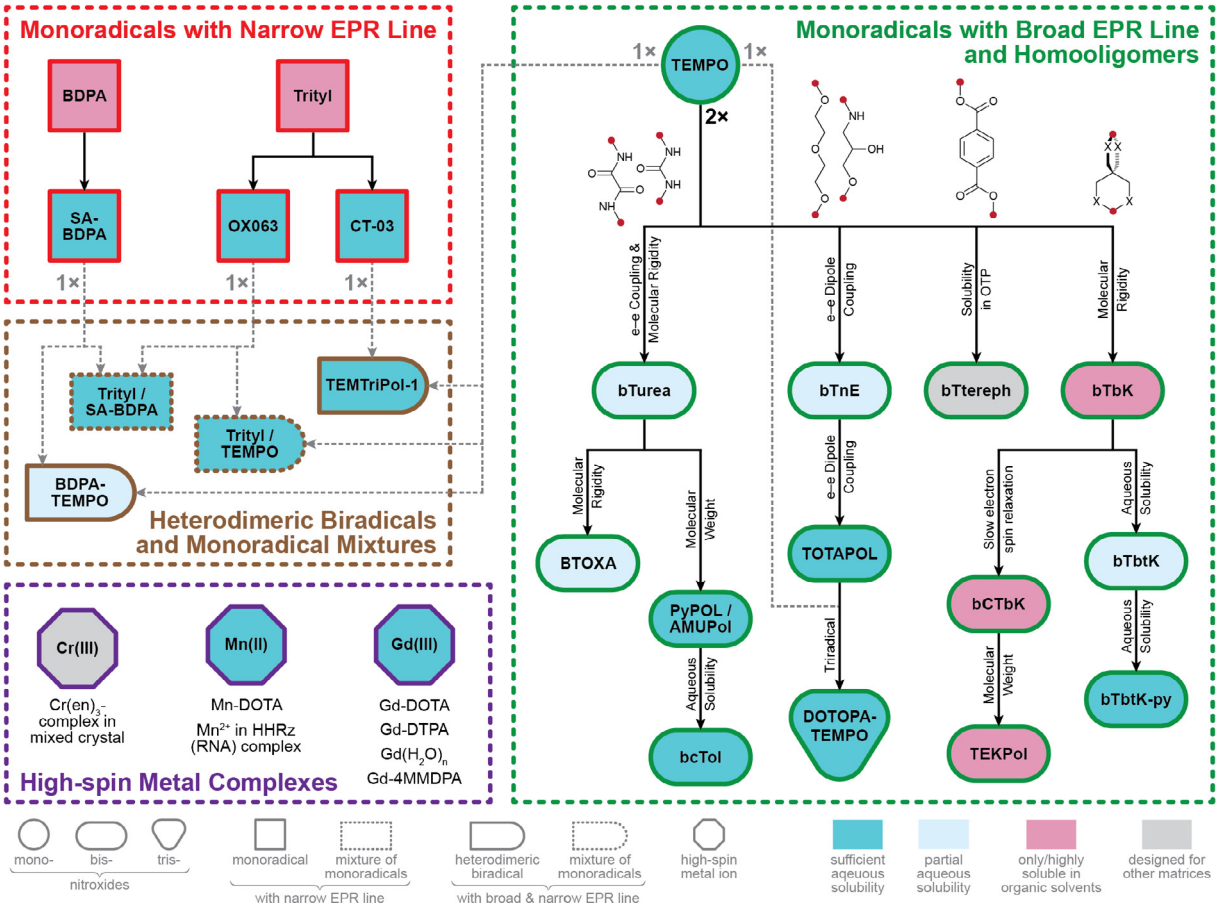

Fig. 36. Overview of the development of PAs for MAS DNP. The shape of the boxes encodes radical type, the number of unpaired electrons per PA molecule and distinguishes between narrow and wide EPR lineshapes; solubility of the individual families is color coded; for details see figure legend. Factors accompanying dashed arrows indicate the number and type of monoradicals that are chemically bonded to form bi- and triradicals. Chemical structures show molecular tethers connecting the TEMPO moieties at the positions indicated in red.

and is terminated inside the MAS stator. Such modifications have been employed, for example, to study temperature-trapped states within the photo-cycle of membrane proteins of the rhodopsin-family, such as bacteriorhodopsin [226,227] or channelrhodopsin [228]. For more details of these applications see Section 7.2.2.

5. Polarizing agents

DNP requires the presence of unpaired electrons in the form of free radicals or metal ions with an open d- or f-shell in order to enhance NMR signals by transferring polarization from electron spins to the nearby nuclear spins [229]. Therefore, such PAs play a very important role for DNP. Most commonly, PAs are exogenous (*e.g.*, small paramagnetic molecules such as mono- or biradicals) which are added to the system (usually by dissolving the sample in—or impregnating it with—a radical-containing, glass-forming cryoprotecting mixture, see Section 6.3). Recently, endogenous PAs have come into focus, where stable radicals or paramagnetic metal ions are present in the analyte molecule [92,140]. This is further described in Section 6.3.4.

Generally, PAs are evaluated based on several parameters, as their efficiency is influenced by the solubility, concentration and electron spin properties at experimental temperatures. As illustrated in Fig. 35, the DNP mechanism evoked by PAs depends on several factors such as the homogeneous linewidth (δ) as well as the inhomogeneous breadth (Δ) of the EPR spectrum, its *g*-anisotropy, and the nuclear Larmor frequency (ω_{0I}). The development and design of new PAs for proficient DNP mechanisms under MAS and high magnetic field are growing areas of research.

In the following section, we describe different PAs used mainly for MAS DNP by exploiting SE and CE. In the case of the latter mechanism, we classify the PAs into two main classes: monomeric radicals (including mixtures thereof) as well as homo- and hetero-dimeric biradicals. Then, we will review the utilization of metal ions that can give rise to both SE and CE. Fig. 36 shows an overview of the developments in the design of PAs discussed in detail in this section.

5.1. Radicals with narrow EPR line for solid effect DNP

In order to satisfy the requirements for SE, PAs with a small homogeneous EPR linewidth (δ) and inhomogeneous breadth (Δ) in relation to the nuclear Larmor frequency (*i.e.*, $\delta, \Delta < 2\omega_{0I}$) are considered. As already laid out in Section 2.2.1.5, excessive inhomogeneous or homogeneous broadening leads to differential SE with starkly reduced net enhancement.

At high magnetic fields, this limits the choice of suitable PAs due to the dominant Zeeman interaction, thus excluding the use of any radicals featuring significant *g*-anisotropy. To date, applications of MAS DNP using SE at high magnetic field ($B_0 \geqslant 5$ T) have mostly been performed with two exogenous PA types, namely BDPA and trityl. Therefore, we will limit the description to these systems. Furthermore, a reduced flavin mononucleotide (FMN) semiquinone has been used in a single study as endogenous PA; this system will be discussed in Section 6.3.4.

5.1.1. BDPA-type radicals

1,3-bisdiphenylene-2-phenyl allyl (BDPA, for chemical structure see Fig. 37) [230] was the first stable radical PA utilized for

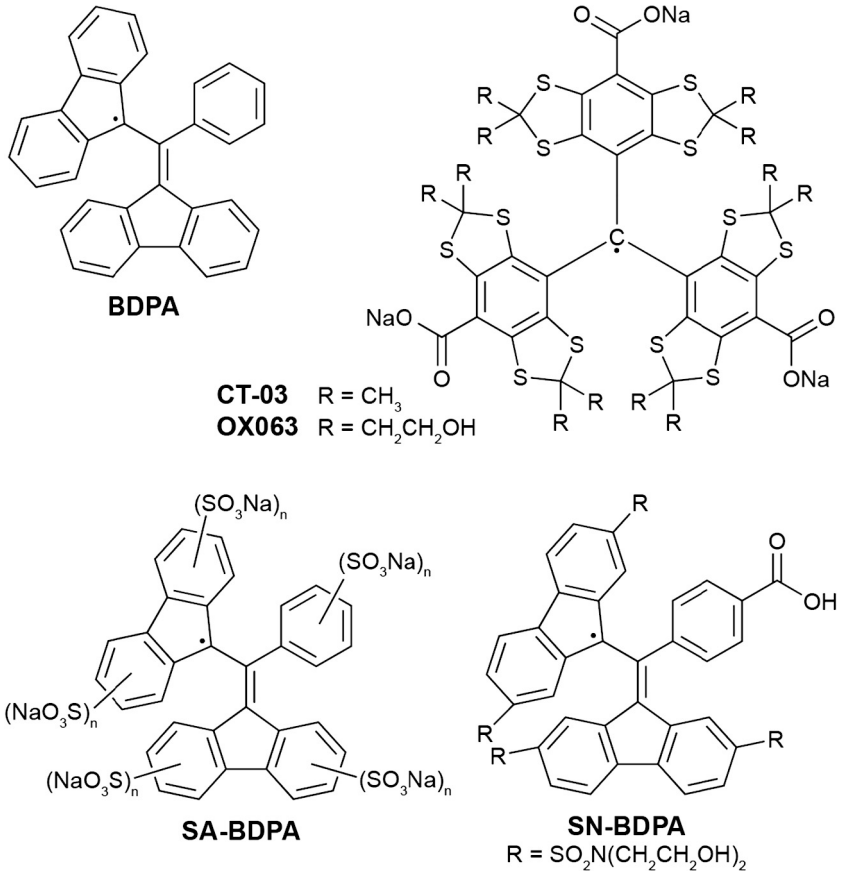

Fig. 37. Chemical structures of BDPA [230], its sulfonated (SA-BDPA) and sulfonamide (SN-BDPA) derivatives [89] and trityl-type radicals OX063 and CT-03 (the latter is also known as Finland trityl) [233,234].

DNP under MAS [63,91,231]. Its narrow EPR line width of 20 MHz [173,232] is caused by inhomogeneously broadening due to the HFI with the 21 protons on the aromatic rings. This width is maintained over a large external magnetic field range; only at a field of 9.4 T and higher, the *g*-anisotropy broadening becomes of similar magnitude [90]. The high chemical stability and ease of dilution in polystyrene makes BDPA an ideal sample for calibration purposes [63,91]. Even though BDPA is an excellent PA, its biological applications are limited due to its lack of solubility in aqueous mixtures.

Haze et al. expanded the potential biological applications of BDPA by synthesizing a highly water-soluble and air-stable derivate, sulfonated-BDPA (SA-BDPA) [89]. It has a narrow EPR linewidth similar to BDPA, which makes SA-BDPA a very efficient PA for SE DNP. In the same study, a sulfonamide derivative (SN-BDPA) was introduced as well, which allows for highly modular chemical variability. In a 40 mM frozen solution of SA-BDPA in d_8-glycerol/D_2O/H_2O, a ^{1}H enhancement factor of 110 was obtained for MAS experiments. The SE performance is slightly better as compared to trityl OX063 (see below), however, the slow electron spin-lattice relaxation ($T_{1S} = 56$ ms at 80 K and 5 T) may cause saturation at moderate μw power [89]. This tendency of saturation in combination with the large number of HFI-coupled ^{1}H spins in BDPA (and its derivatives) give rise to OE DNP in insulating solids as we have laid out in Sections 2.1.3 and 3.2.3.

5.1.2. Trityl-type radicals

A highly prominent group of water-soluble PAs with narrow EPR line width is based on triphenylmethyl (trityl) radical also known as triarylmethyl (TAM) radical (see Fig. 37). Towards the end of the 1990s, Ardenkjær-Larsen et al. investigated such radicals as probes for EPR oximetry. The requirements for good sensitivity towards oxygen-induced line broadening included high chemical stability, water solubility, narrow EPR spectra as well as an inherently small inhomogeneous linewidth [233].

One resulting trityl derivative, OX063, fulfils these requirements to a very large degree and shows efficient SE [233]. In OX063, all aromatic hydrogens are replaced by hydrophilic functional groups, providing not only chemical stability by steric hindrance and water-solubility but also removing the relatively large isotropic HFI. In contrast to another prominent trityl derivative, Finland trityl CT-03 [234], OX063 does not contain relaxation-promoting methyl groups, which alleviates the need for deuteration in order to reduce the homogeneous EPR linewidth [235]. The inhomogeneous linewidth of OX063 in frozen solution is ~50 MHz (FWHH) at 5 T, and it scales linearly with the external field strength since the *g*-anisotropy is the major cause of broadening at high magnetic fields [139].

OX063 is a versatile PA for MAS, yielding a ^{1}H enhancement factor of up to 91 (with a linear dependence on the μw power) [74]. The spin-lattice relaxation time is sufficiently fast ($T_{1S} = 1.3$ ms at 80 K and 5 T), thus significant EPR saturation is avoided during SE DNP [74,77,89]; it has also been demonstrated as a powerful PA for DNP of nuclei with small gyromagnetic ratios such as ^{2}H ($\varepsilon \geqslant 700$) [147], ^{13}C ($\varepsilon = 480$) [82] and ^{17}O ($\varepsilon \approx 115$) [236]. In all these latter cases, OX063 is the most efficient PA studied so far. This is explained by the fact that the EPR linewidth is of a similar magnitude as the nuclear Larmor frequencies, in fact allowing for CE to be efficient (see below).

Besides these applications as PA for MAS DNP, trityl OX063 is popular for its pivotal role in dissolution DNP [237]. Here, trityl greatly outperforms nitroxides when ^{13}C is directly hyperpolarized within neat, amorphous pyruvic acid (doped with OX063) [238]. OX063 has been patented and is the sole approved PA for the commercial HyperSense dissolution DNP system [239]. In that context, two carbon centered perchloro-triphenylmethyl (chlorinated trityl) radicals aimed for dissolution DNP have been investigated [240]. The authors observed unexpected behavior including an inversion of enhanced NMR signals that was tentatively ascribed to hetero-nuclear effects due to the presence of magnetically active ^{35}Cl and ^{37}Cl nuclei (both $I = 3/2$ with significant nuclear quadrupole interactions) within the PA. Further reports on such hetero-nuclear assisted DNP effects—where a $^{35/37}$Cl–^{13}C transfer pathway has been postulated—are not conclusive [241].

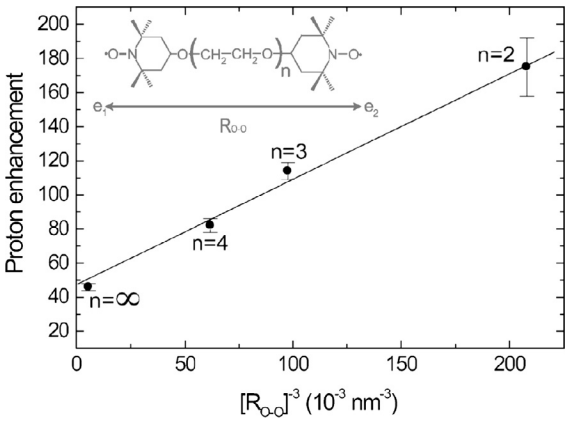

Fig. 38. ^{1}H DNP enhancement factors in the bTnE series as a function of e–e dipole coupling. The inset shows the chemical structure of bTnE. Figure reprinted with permission from [254].

5.2. Nitroxides and biradicals for cross effect DNP

So far, CE has been proven the most efficient polarization-transfer mechanism in DNP and is widely applied to materials and biological systems at high magnetic fields (>5 T). It dominates over other potential mechanisms when the inhomogeneously broadened EPR linewidth (*e.g.*, due to *g*-tensor anisotropy) is larger than the nuclear Larmor frequency (*i.e.*, $\Delta > \omega_{0I} > \delta$). As described in Section 2.1.2, the CE is a three-spin process that requires significant dipolar coupling between the two electrons, which therefore have to be in close spatial relationship (generally at a distance <25 Å) [242,243]. This requirement can be fulfilled in two ways. On the one hand, a sufficiently high concentration of monomeric radicals eventually leads to intermolecular spatial proximity. On the other hand, two (or more) radical moieties interconnected by a molecular linker of particular length enable CE.

Besides the necessity of sufficient e–e coupling, the separation of the EPR resonance frequencies of the two electron spins has to match the nuclear Larmor frequency (*i.e.*, $|\omega_{S,1} - \omega_{S,2}| = \omega_{0I}$). Therefore, the CE performance of individual (bis-)nitroxide radicals is strongly orientation-dependent because the Larmor frequency of the electron spin is dominated by the anisotropic *g*-tensor at high magnetic fields [244,245]. This anisotropy is the reason that the EPR frequency separation scales linearly with the external magnetic field and thus also with the nuclear Larmor frequency. This, on the other hand, ensures that the CE matching condition can be fulfilled at practically any NMR frequency or field.

Further advantages of these radicals are their solubility in aqueous or organic media (depending on the type of nitroxide used) and their chemical stability under a wide range of conditions [244]. Furthermore, nitroxides are extensively used for spin-labeling purposes and are therefore offered in a large variety of derivatives tailored for different applications and conditions [246–249].

Another important parameter for efficient CE DNP is electron-spin relaxation. Both, the spin-lattice relaxation time (T_{1S}) and electron spin-spin relaxation time (T_{2S}), play an important role in

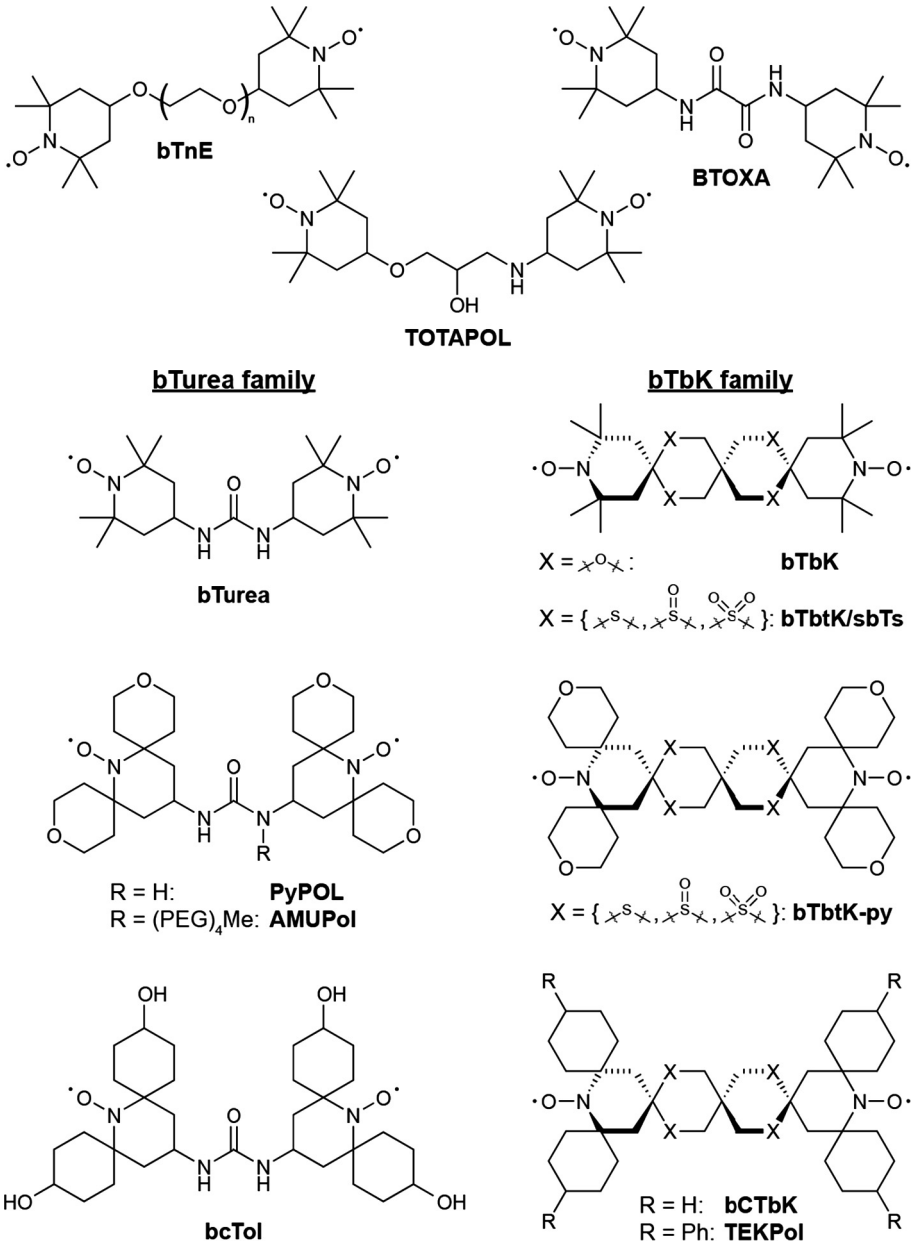

Fig. 39. Chemical structures of several bis-nitroxide PAs. See text for details and original publications where these PAs were introduced.

saturation of the EPR transition and excitation of CE under μw irradiation [81,250]. The electronic relaxation-time constants strongly depend on the molecular mass and polarity of the solvent, which has to be considered during PA design [251]. Systematic attempts to improve these parameters are further elaborated in the following sections.

5.2.1. Monomeric radicals

As we have laid out in Section 3.2.2, the first DNP experiments evoking the CE were reported in the early stages of DNP by Hwang et al. They described the CE in polystyrene doped with diphenyl-picryl-hydrazyl (DPPH), galvinoxyl and Ley's radical [59,60]. In 1976, Wollan explained the theory of CE with ^{1}H DNP experiments on erbium-doped yttrium ethyl sulfate (YES:Er) [61,62]. However, biological samples cannot be doped with these radicals for DNP, as they are typically prepared in aqueous media. Griffin and co-workers first utilized the nitroxide radical TEMPO (2,2,6,6-tetramethyl-1-piperidiny-1-oxyl) dissolved in glycerol/water (60/40 vol%) solution and enhanced the ^{1}H signals of glycine 185-fold at 5 T and 14 K [181]. It was also shown that large enhancements were obtained with 40 mM TEMPO concentration, demonstrated on the amino acid arginine and the 18.7 kD protein T4-lysozyme in MAS experiments [218]. Even though reasonable enhancement factors were obtained with these monomeric radicals, the high radical concentrations required can lead to paramagnetic quenching and line broadening in NMR spectra [225,252,253].

5.2.2. Nitroxide biradicals (and higher oligoradicals)

5.2.2.1. The advent of bis-nitroxide PAs: BTnE and TOTAPOL. Biradicals were introduced by Griffin, Swager and co-workers at MIT in order to reduce the required radical concentration and to improve the efficiency of CE by providing sufficient intramolecular e–e dipolar coupling. By the interconnection of two TEMPO molecules using di-, tri-, or tetra-ethylene glycol chains—yielding a series of bis-TEMPO-n-ethyleneglycol (BTnE) biradicals—Hu et al. demonstrated that the size of the e–e dipolar coupling

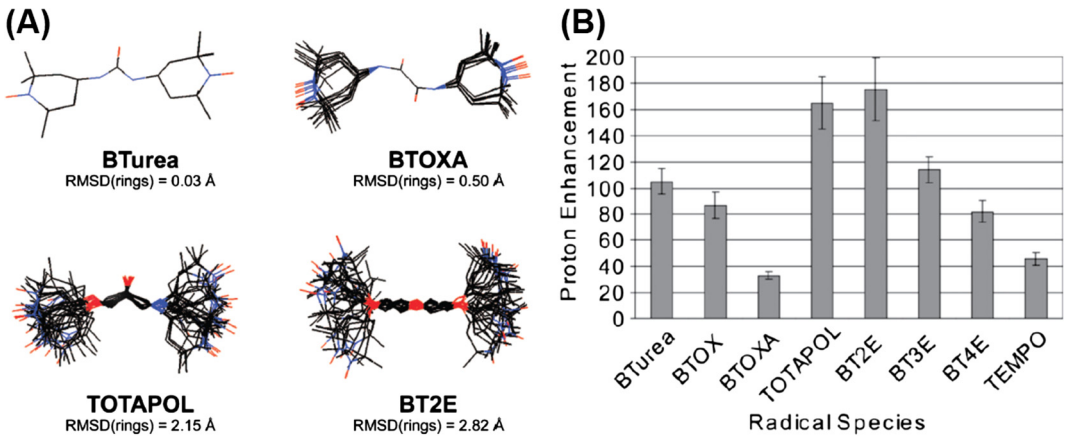

Fig. 40. (A) Structures of bTurea, BTOXA, TOTAPOL, and BT2E, refined using geometrical constraints obtained from EPR lineshapes, with given root-mean-square deviations (RMSD) for the atoms of the TEMPO rings. Reprinted from [244] with permission. (B) ^{1}H DNP enhancement factors of several PAs (10 mM in electron spin concentration each) in standard solutions (2 M ^{13}C-urea, 60/30/10 (w/w/w) d_6-DMSO/D_2O/H_2O) at 90 K and 5 T. Figure reprinted from [229] with permission.

directly affects the CE mechanism [see Fig. 38, also see Eq. (36) and Section 2.1.2.3]. However, those radicals were insoluble in a glycerol/water solution required for biomolecular studies [254].

This issue was overcome by the introduction of the water-soluble biradical 1-(TEMPO-4-oxy)-3-(TEMPO-4-amino)propan-2-ol (TOTAPOL), which was a milestone for the development of exogenous PAs in solid-state DNP NMR [221]. It has the ability to dissolve in aqueous media containing salt and glycerol and is highly stable at room temperature. Outstanding signal enhancements were obtained with TOTAPOL which is one of the most commonly used exogenous PAs for solid-state materials and biological systems to date [143,209,255–263].

5.2.2.2. Tri-radicals and higher: the DOTOPA series. In 2010, Thurber et al. introduced a new triradical DOTOPA-TEMPO. By increasing the number of nitroxide functionalities per molecule, the larger number of close e–e contacts suggest a higher probability of CE matching. The DNP performance of DOTOPA-TEMPO was compared with 4-amino TEMPO and TOTAPOL; even though large enhancements for ^{1}H NMR signals of proteins in frozen glycerol/water solutions were observed in static samples with low μw-power, DOTOPA-TEMPO is less soluble in water [163]. Later on, the same group synthesized DOTOPA-TEMPO-based oligo triradicals, as well as nitroxide-based biradical and tetraradical compounds; these radicals varied in e–e distances, T_{1S}, relative orientations of nitroxide groups and solubility. Among them, DOTOPA-TEMPO-based triradicals showed better water solubility and indirect DNP enhancement factors ($\varepsilon = 92–128$) for ^{15}N, ^{13}C-labeled melittin tetramer in partially protonated glycerol/water at 30 mM total nitroxide concentration. The experiments were performed under MAS in a temperature range of 25–30 K at 9.4 T and with an output μw power of approximately 0.8 W. The triradicals satisfied the requirements for CE, while tetraradicals showed lower enhancements because of the poor solubility and longer e–e distances than the triradical, as well as rapid electronic spectral diffusion [264].

5.2.2.3. Rigidity of the linker: bTurea, BTOXA, and the bTbK series. In TOTAPOL, two TEMPO moieties are linked with a propan-2-ol group that is flexible and can adopt many molecular orientations (see Fig. 40A). In early attempts to shorten the tether, and also to study a more rigid alignment of the two nitroxides, Hu et al. introduced two novel linker groups, resulting in bis-TEMPO-urea (bTurea) and bis-TEMPO-oxalyl amide (BTOXA) [244]. Both biradicals failed to generate enhancement factors that can approach those obtained with TOTAPOL or BT2E; in particular, BTOXA yielded virtually equal performance as TEMPO monoradicals. This was tentatively attributed to the possibility that the dipole coupling was too large in combination with an unfavorable mutual orientation, especially in the case of BTOXA where the two nitroxide *g*-tensor frames are almost collinear. A comparison of the enhancement factors obtained with the above PAs is shown in Fig. 40B.

At that point, in the first decade of the 2000s, PA design efforts were guided by the prediction that the ideal mutual orientation of two nitroxides for optimal CE matching efficiency were such that the *x*-axes of the *g*-tensor eigenframes of the two electron spins would have to be collinear, but that their *z*- and *y*-axes would have to be rotated by 90°. In this case, the EPR spectrum could be irradiated at the high-field side (corresponding to g_{zz} orientation)—where experimentally the largest DNP enhancement is observed—and each saturated electron spin would be accompanied by a nitroxide with a resonance frequency given by g_{yy}. This scenario would yield the most-efficient CE matching, see Eq. (33). From a molecular-geometry perspective, this condition would be found if the N—O bonds are collinear, while the C—N(O)—C planes of the two nitroxides are orthogonal to each other.

Such an arrangement was accomplished within a new biradical, bis-TEMPO-bisketal (bTbK) in which the two TEMPO moieties are linked by a spiro-center locking the radicals in the suitable relative orientation. With bTbK, NMR signal intensities were enhanced with ε being 1.4-fold larger as compared to TOTAPOL [265]. However, the main limitation of bTbK was its poor solubility in aqueous media.

This triggered a search for water-soluble rigid biradicals incorporating the electron spin properties and DNP efficiency found in bTbK. One approach was the substitution of the oxygen atoms in the spiro-linker by more polarizable sulfur groups in mixed oxidation states. This resulted in a better water solubility of the resulting bis-TEMPO-bis-thioketal (bTbtK) biradicals in DMSO/water [266]. Solubility was further enhanced by Kiesewetter et al. by substitution of the protecting dimethyl groups by tetrahydropyran (THP) rings. The resulting bTbtK-py/SPIROPOL yielded an enhancement of 230 in glycerol/water solvent and finally outperformed TOTAPOL, which at that point seemed to have serendipitously fulfilled the most desirable properties of an ideal CE-efficient PA [267].

5.2.2.4. The larger the better: bCTbK, PyPol/AMUPol, and the TEKPol series. At the same time, the groups of Tordo and Ouari (Aix-Marseille University) were leading an extraordinary undertaking to probe the chemical space for possible improvements of PAs

[268,269]. This led to the development of a new rigid biradical for non-aqueous solvents. The bulky derivative of bTbK, bis-cyclohexyl-TEMPO-bisketal (bCTbK), was introduced by Zagdoun et al. by replacing the geminal dimethyl groups of bTbK by spirocyclohexyl moieties [270]. This increased the size and rigidity of the radical and resulted in slower electron spin relaxation. They have shown that T_{1S} of bCTbK in TCE impregnating a hybrid mesostructured silica material was twice as long and that larger enhancement factors were obtained compared to bTbK under similar conditions.

This approach was then extended towards two novel water-soluble radicals PyPol and AMUPol in 2013 by Sauvee et al. [271]. Structurally these are based on bTurea, and water solubility has been maximized by nitroxide-protecting THP rings and linker-decorating polyethyleneglycol (PEG) chains. The enhancement factors obtained for AMUPol in glycerol/water system were 3.5–4 times larger than for TOTAPOL at 9.4 and 14.1 T at a typical temperature of 97 K. The structural flexibility of the urea linker might seem to contradict this high efficiency. However, Michaelis et al. have also reported that larger conformational flexibility can improve DNP performance in a systematical study of several thiourea-type bis-nitroxides [272]. Very recently, it has also been shown that AMUPol exhibits a rather strong e–e exchange interaction of $J/2\pi = 43$ MHz that is expected to support CE-enhancement and explain the significant advantage over TOTAPOL, particularly at high magnetic fields [273].

Furthermore, the non-aqueous soluble radical TEKPol—a heavier analog of bTbK—was also introduced [274]. Similar to AMUPol, large enhancement factors of more than 200 were obtained for TEKPol in TCE that was also ascribed to the slow electron spin relaxation. Interestingly, it also yielded relatively large DNP enhancement at higher temperatures (180–200 K). Current development of bTurea-based PAs is ongoing in systematic studies in order to improve DNP efficiency and solubility within several research groups and promising results have been recently published [275–277]. An example of such a systematic effort is shown in Fig. 41.

5.2.2.5. Other approaches. Alternative routes to achieve water-solubility of bTbK were demonstrated in the form of host-guest complexes. Mao et al. have encapsulated bTbK in a cyclodextrin (Captisol) that resulted in improved water solubility of the PA and larger DNP efficiency as compared to TOTAPOL [278]. Later on, a related approach was used again to solubilize hydrophobic biradicals by surfactant encapsulation within micelles. Large signal enhancements were obtained by bTbK that was solubilized in a water/glycerol mixture with the help of deuterated surfactant sodium octyl sulfate [279] or by TEKPol that was incorporated into micelles formed by the protonated neutral surfactant polysorbate 80 (Tween-80) [280]. The solubilization in micelles preserves the glassy nature of the mixture and enables the DNP activity of the biradical.

Furthermore, systems such as OTP and the anti-inflammatory drug indomethacin have metastable amorphous phases but are not miscible with biradicals like TOTAPOL. Hence, Ong et al. introduced the novel organic biradical bis-TEMPO terephthalate (bTtereph), which has similar EPR and DNP properties as TOTAPOL. They succeeded in uniformly distributing bTtereph in OTP and indomethacin by a procedure that is common in pharmaceutical sample preparation (*i.e.*, in the absence of solvent) and obtained a ^{1}H signal enhancement factor of 58 for the amorphous phase of OTP [281].

5.2.3. Heterodimeric biradicals and mixtures

The advantages of two specific radical types can be combined within heterodimeric biradicals where the respective radical moieties can differ in their EPR spectral and/or relaxation properties. For example, one radical with slow spin-lattice relaxation paired with another fast-relaxing radical can boost CE efficiency if the slow-relaxing radical species is irradiated by μw [82,229,282]. This leads to efficient saturation of this radical type, while the accompanying (fast-relaxing) radical ensures a large polarization differential to be transferred to the nuclei. Equally, irradiation of a radical moiety with a narrow EPR line causes similarly efficient EPR saturation; a paired radical with large spectral anisotropy can then provide efficient CE matching over a large range of molecular orientations.

A proof of concept has been demonstrated experimentally by Hu et al.; in a mixture of TEMPO and trityl (20 mM each), the DNP enhancement factor could be increased 4-fold as compared

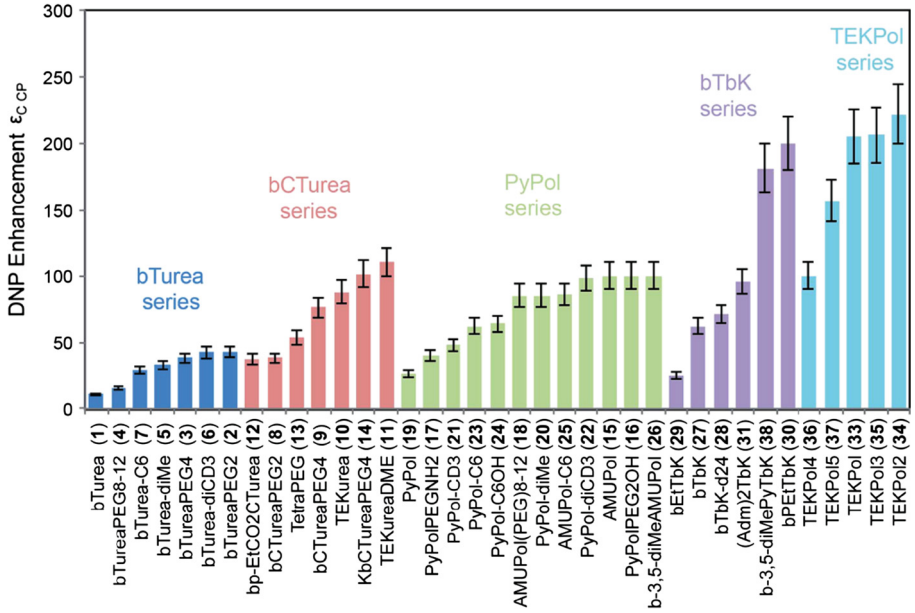

Fig. 41. ^{1}H DNP enhancement factors from several bis-nitroxide PAs at a concentration of 16 mM in frozen solutions of TCE (9.4 T, 110–115 K). For chemical structure of selected PAs see Fig. 39; for structures of all given PAs see original publication. Figure taken with permission from [276].

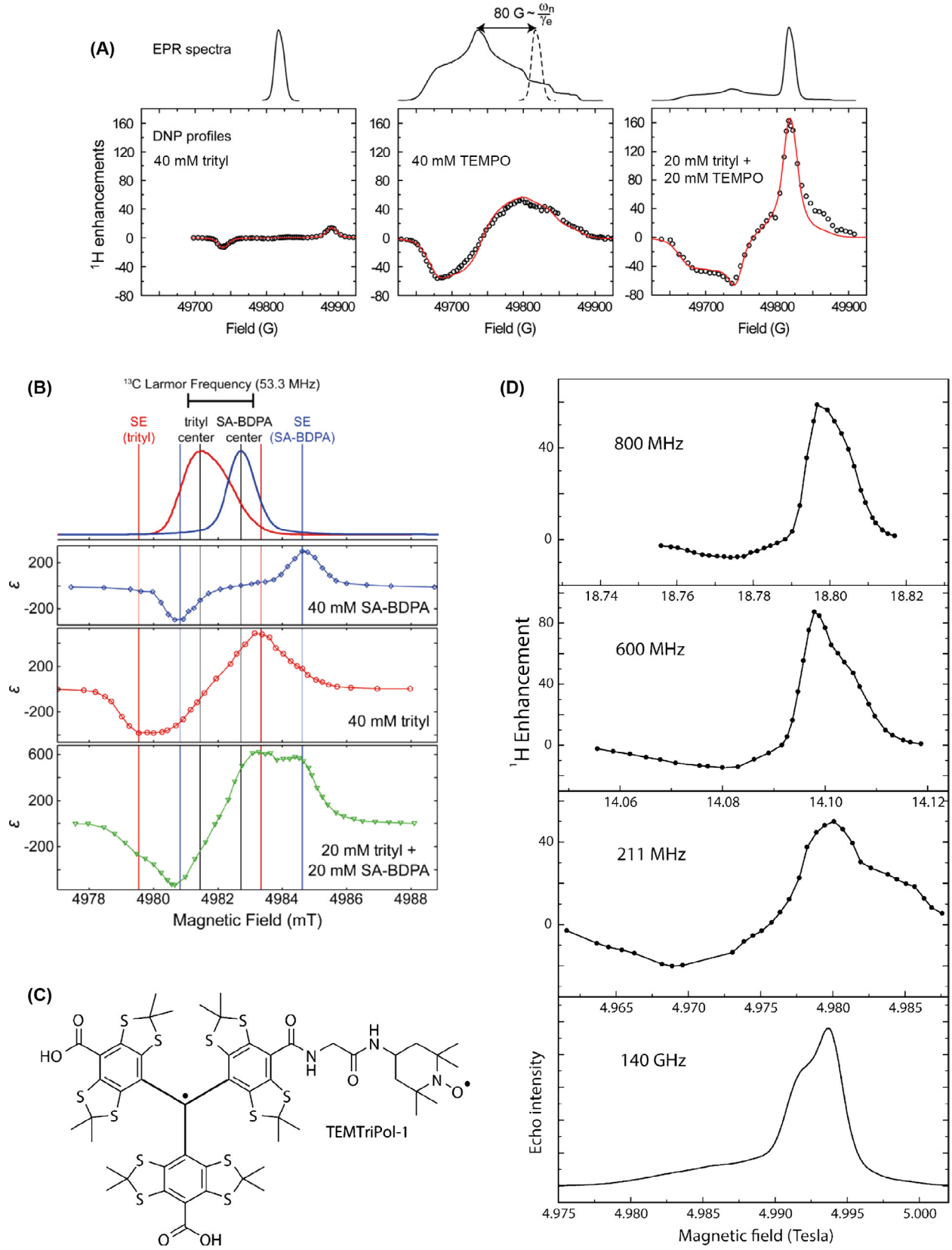

Fig. 42. DNP with radical mixtures or heterodimeric PAs. (A) ^{1}H DNP with trityl/TEMPO mixture at 5 T (140 GHz e^{-}; 211 MHz ^{1}H) [282]. (B) ^{13}C DNP with trityl/SA-BDPA mixture at 5 T (140 GHz e^{-}; 53 MHz ^{13}C) [82]. (C) Chemical structure of TEMTriPol-1 and (D) ^{1}H DNP enhancements with that biradical at 18.8 T (527 GHz e^{-}; 800 MHz ^{1}H), 14.1 T (395 GHz e^{-}; 600 MHz ^{1}H), and 5 T (140 GHz e^{-}; 211 MHz ^{1}H) in comparison with echo detected EPR spectrum at 140 GHz [283]. See original publications for further experimental details. Subfigures reprinted or adapted from the original publications with permissions.

to a TEMPO solution with equal PA concentration (40 mM) [282]. One of the most striking observations was that this advantage can only be achieved if the (narrow and slowly relaxing) trityl is directly excited by μw, while irradiation of the (broad and fast relaxing) TEMPO function gave no significant advantage (see Fig. 42A).

Another example of such a radical mixture has been provided by Michaelis et al. [82]. A 34 MHz difference (at 5 T) between the EPR absorption maxima of trityl OX063 and SA-BDPA potentially allows for CE matching of a large variety of nuclei with small gyromagnetic ratios. In fact, ^{13}C (with a nuclear Larmor frequency of 53 MHz at 5 T) could be hyperpolarized with an enhancement factor of $\varepsilon = 620$ at a concentration of 20 mM of each radical, significantly surpassing enhancement factors obtained with solutions containing only one of the two radicals at equal electron spin concentration of 40 mM ($\varepsilon = 300$ for SA-BDPA; $\varepsilon = 480$ for OX063), see Fig. 42B. Interestingly, spectral decomposition of the DNP field profile into all possible contributions allowed for unambiguous identification of the CE contribution which resulted from SA-BDPA/OX063 pairs [82].

However, efforts to create stable and water-soluble heterodimeric biradicals that encompass these advantages and alleviate the detrimental effects of the large paramagnetic concentration of a molecular mixture have been hampered by chemical difficulties. Problems intrinsic to radical chemistry are potentiated in the presence of two radicals with different redox potentials. Activity of both radicals has to be maintained throughout the synthetic pathway, or one radical must be activated in the presence of the other. One combined effort of the Swager and Griffin labs resulted in the successful synthesis of a BDPA-TEMPO biradical that combined the advantages of a narrow and broad EPR line radical situated within one molecule, however, water-solubility was limited. Additionally, the chemical modification of the BDPA moiety resulted in a significant *g*-anisotropy that might partially invalidate the advantages of the otherwise very slowly relaxing spin with a narrow resonance line [284].

Nevertheless, a newly developed heterodimeric biradical that satisfies the CE matching condition with an electron pair featuring different electron relaxation rates has been successfully synthesized and tested for DNP efficiency at various field strengths by Mathies et al. [283]. TEMTriPol-1—in which a TEMPO nitroxide and a trityl radical are chemically interconnected (structure shown in Fig. 42C)—yielded a rather large ^{1}H signal enhancement of 65 in a 10 mM glycerol/water solution at 18.8 T (527 GHz e^{-}, 800 MHz ^{1}H). Interestingly, TEMTriPol-1 showed an anomalous dependence on the external magnetic field, yielding its best performance (in relation to other PAs) at high field ($\varepsilon = 65$ at 18.8 T; $\varepsilon = 87$ at 14.1 T), whereas its efficiency dropped at lower field ($\varepsilon = 50$ at 5 T), see Fig. 42D. This behavior has been explained by the strong exchange interaction ($J/2\pi = 73$ MHz) between the nitroxide and trityl moieties that disturbs the CE mechanism when J is of a similar order of magnitude as the nuclear Larmor frequency (*i.e.*, 211 MHz at 5 T; 600 MHz at 14.1 T; 800 MHz at 18.8 T) [283].

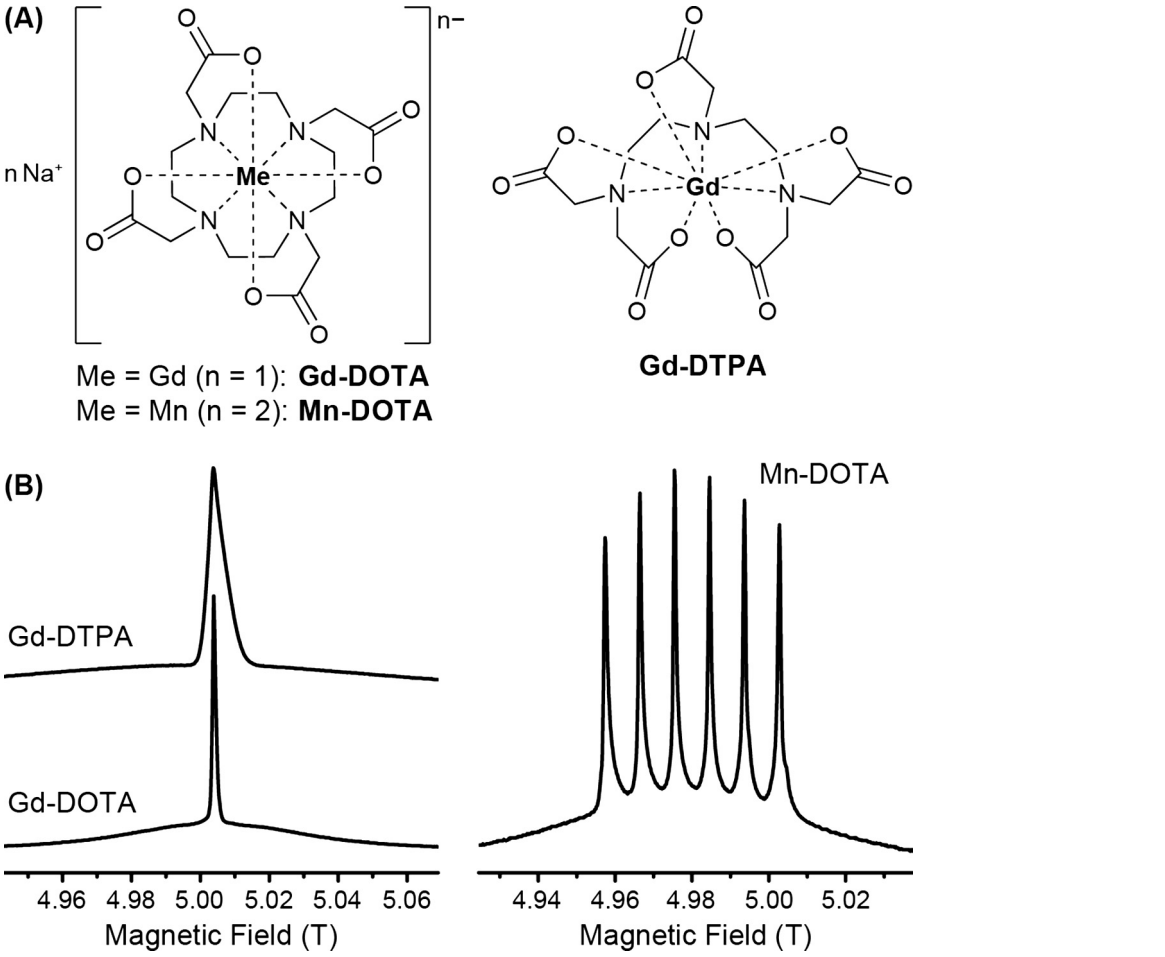

Fig. 43. (A) Chemical structures of the high-spin metal complexes Mn/Gd-DOTA and Gd-DTPA. (B) Field-swept EPR spectra of the metal complexes recorded at 1 mM in frozen solutions of d_8-glycerol/D_2O at 139.5 GHz and 80 K using a Hahn echo sequence. Subfigure (B) adapted with permission from [159].

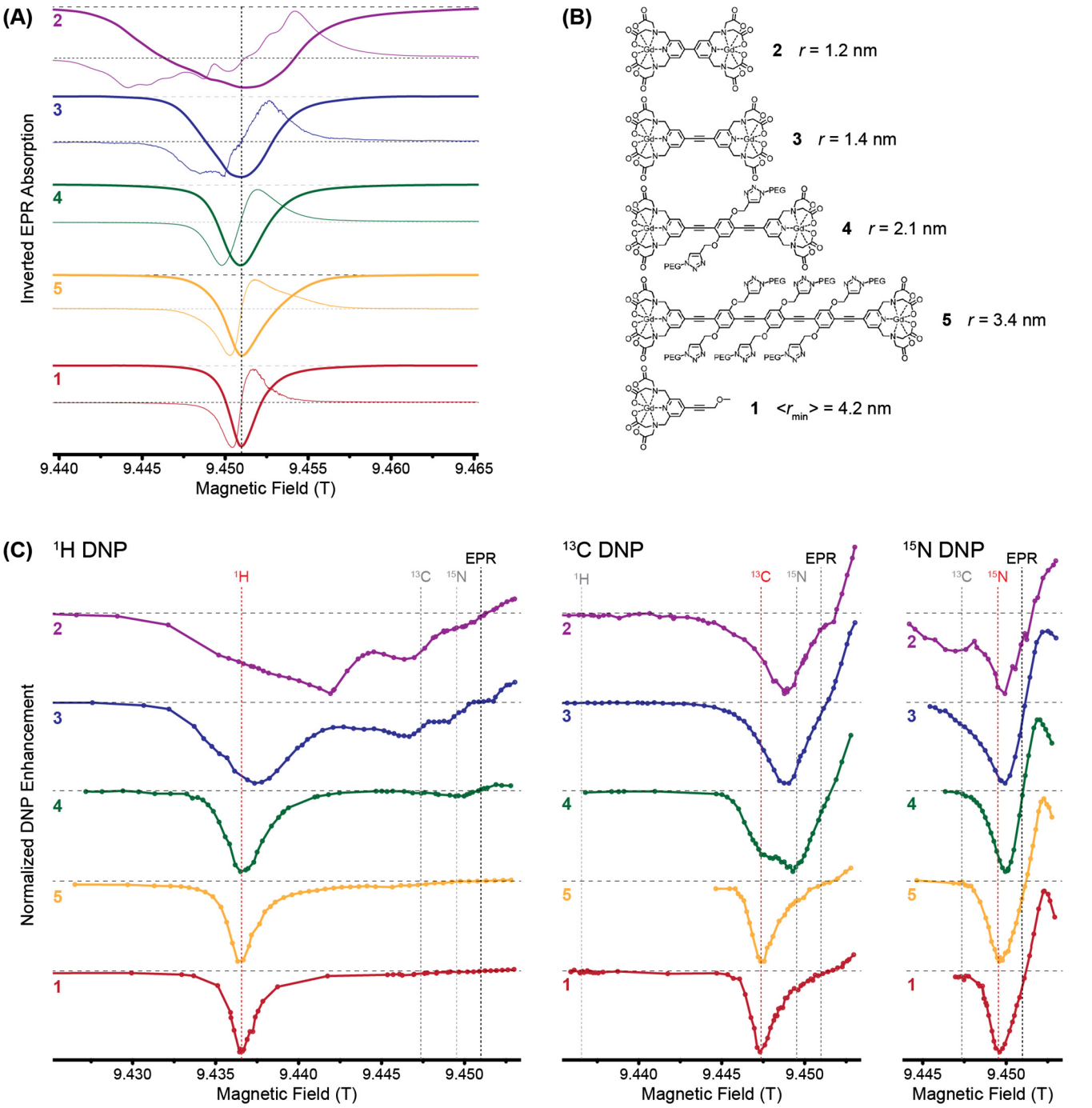

Fig. 44. (A) 263 GHz cw EPR spectra (recorded as field derivatives in thin lines, integral/absorption spectra in thick lines) of frozen solutions of mono(Gd-chelate) **1** and bis (Gd-chelate)s **2**–**5**. Spectra are inverted for better comparison with DNP field profiles. (B) Chemical structures of the investigated complexes. (C) 263 GHz ^{1}H, ^{13}C, and ^{15}N DNP field profiles of the same samples as in (A). Data taken from [168]. For further information, see original publication.

5.3. Paramagnetic metal ions

5.3.1. Ce(III) and Cr(V): early experiments

DNP using paramagnetic metal ions has first been reported immediately after the discovery of SE DNP. Abraham et al. studied Ce(III) as main constituent in $Ce_2Mg_3(NO_3)_{12}{\cdot}24\ H_2O$ or as impurity in diamagnetic $La_2Mg_3(NO_3)_{12}{\cdot}24\ H_2O$ (also known as LMN) and in CaF_2. Furthermore, they reported rather small enhancement factors by employing Cr(III) as impurity within synthetic sapphire (α-Al_2O_3) or utilizing ferric impurities in $K_3Co(CN)_6$ [76,113]. Later, Cr(V)—reduced *in situ* from Cr(VI) [285]—in complexes with diols and glycerol has been extensively used as PA for spin-polarized targets in scattering experiments [286–290]. All these experiments have been performed at low field and very low temperatures. In the transition metal complex of Cr(V), a single unpaired electron is located in the 3d-shell, yielding a $S = 1/2$ system with an isotropic g-factor ($g_{iso} = 1.981$) in liquid ethylene glycol; upon freezing of the solution, only a very small anisotropy is observed [286]. The rare earth Ce(III) has a $4f^1$ configuration with a free ion ^2F ground state ($S = 1/2$, $L = 3$, ground state $J = 5/2$) [291]. In trigonal LMN, this situation results in a large spin-orbit coupling (SOC) and effective Zeeman anisotropy with a parallel principal

axis component (PAC) $g_{\parallel} \approx 1.83$ and an almost vanishing perpendicular PAC $|g_{\perp}| \leqslant 0.1$ [292,293]. In contrast to these $S = 1/2$ systems, Cr(III) and Fe(III) feature high spin quantum numbers, leading to much more complex DNP enhancement profiles featuring more than one DNP condition as compared to what has been observed for doublet PAs [76].

5.3.2. Gd(III) and Mn(II) in chelate complexes

The increasing complexity of DNP parameters imposed by high-spin properties makes the prediction of DNP performance and the design of an efficient high-spin PA rather difficult [167]. Nevertheless, the search for efficient PAs for high-field MAS DNP constrains the space of possible PAs to a large degree. One of the most stringent requirements of a PA is the compatibility with current instrumentation, consisting of an NMR magnet without or with a limited sweep capability as well as a gyrotron, typically with a fixed-frequency output (see Section 4.2). This prohibits the use of metal ions or PAs that feature pronounced SOC, resulting in g-factors strongly deviating from the 'spin-only' $g_e = 2.0023$ of the free electron. Unfortunately, many transition metal ions in low-spin complexes such as Cu^{2+}, Co^{2+}, Fe^{3+} experience significant SOC due to an admixture of (energetically low-lying) excited states and consequently show significant g-anisotropy [291]. This impedes DNP applications using such $S = 1/2$ metal ions as PAs at high field despite exciting perspectives, given their relevance in biology and materials science.

A rather small group of high-spin transition-metal or rare-earth ions—including Gd^{3+} and Mn^{2+}—feature peculiar electron-spin properties. These are caused by the combination of a non-degenerate electronic ground state with no orbital momentum and (unpopulated) excited states lying high above the ground-state energy [291]. Half-filled electronic subshells quench the orbital momentum: Mn^{2+} has a $3d^5$ configuration with a ^6S ground state, whereas Gd^{3+} has 7 unpaired electrons in the highly screened f-shell ($4d^7$ configuration with ^8S state).[4] Despite their high-spin properties, the quenched SOC leads to a practically isotropic Zeeman interaction with g-values very close to $g = 2.00$, manifested in a rather narrow EPR central transition (CT) between the $m_S = \pm 1/2$ states in the half-integer (Kramer's type) systems. Satellite transitions (*i.e.*, transitions where m_S changes its absolute value) are influenced by ZFS in first order, which results in a very broad spectral feature, especially when amorphous solutions of such high-spin complexes are considered [294].

Given a highly symmetric complex geometry, the ZFS constant is typically in the range of a few hundred MHz up to a few GHz. For example, in high-affinity chelate complexes, the CT is only affected to a small degree by second-order effects that are less pronounced and can even be negligible at high magnetic fields [295]. The compatibility with cellular environments [296,297]—also considering the inherent chemical stability of Gd(III) or Mn(II) as well as the biological relevance of Mn(II)—makes such complexes highly interesting PAs for MAS DNP [139,140].

Gd^{3+} and Mn^{2+} bound in complexes of the chelators DOTA and DTPA (see Fig. 43) were first introduced as high-spin metal ion PAs for MAS DNP by Corzilius et al. in 2011. A very narrow EPR CT linewidth of 29 MHz at 5 T was observed for Gd-DOTA complex, which allowed induction of SE with an initially reported ^1H enhancement factor of ~12 in a urea model sample [159]. Due to the narrowing of the CT at higher magnetic fields, the detrimental field dependence of the SE transition probability proportional to B_0^{-2} [see Eq. (17)] is partially compensated for, leading to still significant performance with $\varepsilon = 8$ at 14.1 T. Direct DNP of low-γ nuclei (^{13}C and ^{15}N) was reported with enhancement factors in excess of 100, potentially allowing for site-directed DNP on biomolecules using site-directed spin-labeling (SDSL) with metal chelate tags; furthermore, the contribution of CE mechanism was demonstrated [139].

The latter observation stimulated the groups of Corzilius (Frankfurt) and Godt (Bielefeld) to design several bis(Gd-complex)es in which two Gd-binding chelate moieties are interconnected by linkers of varying lengths [168]. This has not only led to an increase in DNP efficiency in analogy to what has been achieved with bis-nitroxide PAs [254], but also has resulted in further understanding of the inter-electronic distance dependence for CE DNP of different nuclear spins (see Fig. 44).

Due to the strong isotropic HFI to the ^{55}Mn nucleus ($I = 5/2$, 100% natural abundance), Mn(II) suffers from a splitting of the EPR CT into a sextet with ~250 MHz separation; this reduces the achievable enhancement factors equally ~6-fold with respect to Gd(III) [139,159]. Nevertheless, the high biological relevance of Mn^{2+} and structural similarity with the diamagnetic Mg^{2+} ion justifies further investigation as potential endogenous PA. Such a premise was demonstrated on an inactivated hammerhead ribozyme where one Mn^{2+} ion was specifically bound to RNA. In this case, intra-molecular DNP was used to directly hyperpolarize ^{13}C within the same molecule [140].

5.3.3. Cr(III) in crystalline solids

Cr^{3+} can have similar properties as the above-mentioned metal ions, despite its $3d^3$ electronic configuration with atomic ^4F ground-state term. In an octahedral ligand field, this state transforms into a (non-degenerate) $^4A_{2g}$ ground state with $L = 0$, resulting in an isotropic Zeeman interaction and $g \approx 2.0$. However, significant deviation from ideal octahedral symmetry can reintroduce an excited-state admixture (mainly $^4T_{2g}$) and lead to larger deviations from the free-electron g_e [298]. Small distortions of the ligand-field symmetry may still conserve the pure ground-state properties but manifest themselves in a moderate ZFS of up to several GHz, as can be found in ruby [299–301].

An ideal system featuring a high trigonal symmetry of the metal site is found in a crystalline sample of $[Co(en)_3Cl_3]_2{\cdot}NaCl{\cdot}6\ H_2O$ (en = ethylenediamine, $C_2H_8N_2$, Fig. 45) paramagnetically doped with Cr^3 [303]; in this case, Cr^{3+} ($S = 3/2$) and Co^{3+} (low-spin $3d^6$, $S = 0$) are structurally interchangeable due to the similarity

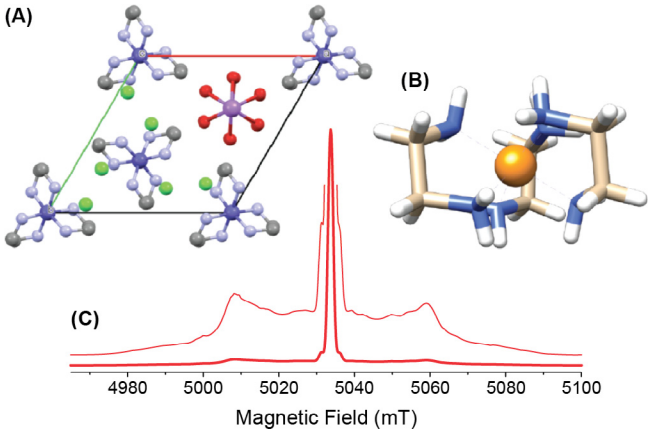

Fig. 45. (A) Crystallographic unit cell of $[Co(en)_3Cl_3]_2{\cdot}NaCl{\cdot}6H_2O$ (en = ethylenediamine, $C_2H_8N_2$). Projection of the crystal structure with the c axis perpendicular to the plane of the drawing. (B) Molecular unit with hydrogen atoms. (C) Field-swept 140 GHz EPR spectrum of 0.1% Cr(III)-doped $[Co(en)_3Cl_3]_2{\cdot}NaCl{\cdot}6H_2O$ using a Hahn echo sequence at a temperature of 80 K. Figure adapted from [302] with permission.

[4] Eu^{2+} and Tb^{4+} also exist in the same electronic configuration and show similar EPR spectroscopic properties, however, they are chemically less stable than Gd^{3+} and—as most lanthanides—tend to obtain a+3 oxidation state.

of ionic radii [304]. Therefore, paramagnetic doping with molar ratios between 0.1 and 3% can be achieved without effecting any change in the crystal structure [302]. The EPR spectrum (Fig. 45C) shows a narrow CT with practically isotropic $g = 1.987$ and an axial ZFS with a constant of $D = 740$ MHz at 80 K. By irradiation of the SE condition, a rather small ^{1}H enhancement was observed in the fully-protonated sample. More interestingly, significant direct-DNP enhancement factors on the order of 20–30 have been observed for ^{13}C and ^{59}Co at high doping ratios of 3%, with a strong dependence on the latter parameter. This was surprising in several ways. First, the rather narrow CT linewidth of ~40 MHz was relatively small compared to the ^{13}C and ^{59}Co Larmor frequencies (53 and 51 MHz, respectively); more importantly, any anisotropies resulting from ZFS or HFI would act equally on neighboring Cr^{3+} in the long-range ordered crystalline lattice, prohibiting the majority of matching conditions found in stochastically oriented (amorphous) samples [167]. This indicated that CE matching between the CT of one Cr^{3+} and a satellite transition of a neighboring ion might support DNP: while the former transition appears static, the latter are modulated by ZFS under MAS. As the second surprise, the nearest distance between a Cr^{3+} PA and ^{59}Co nucleus is 7.7 Å, proving that direct DNP can act over rather large distances [302].

6. Practical aspects

The observed outcome of a DNP experiment, such as the generation of enhanced nuclear polarization or quenching of NMR signal due to the presence of the paramagnetic PA, is a result of the interplay between various microscopic processes. In turn, these processes themselves are dependent on experimental conditions (*e.g.*, sample temperature, μw power, MAS frequency, etc.), the type of PA used, and the constitution of the sample. Clearly, sample preparation is a very important factor for DNP and can play a decisive role in the success of an experiment. For example, due to the complexity of samples in biomolecular as well as materials science applications, and the manifold molecular dynamics that determine the relaxation behavior, the overall enhancements are often found to be several-fold reduced as compared to model substances. An exception is the enhancement factor of 250 obtained for a ribozyme where relaxation-inducing methyl groups are absent in the purified sample [140]. Similarly, unfavorable freezing properties of the solvent can render a DNP experiment fruitless [281]. In the following, an overview is given about the influence of various parameters and guidelines for their optimization.

6.1. Build-up and depletion of the (enhanced) NMR signal

6.1.1. Accelerated build-up of polarization during SE

In the case of SE the observed DNP-build-up rate (under μw irradiation) is expected to be larger than the spin-lattice relaxation rate (without μw) [61,106,121]. Based on a simplified description, the effective bulk DNP rate, k_{DNP}^{eff}, and the observed relaxation rate, T_{1I}^{-1}, are additive towards the measured build-up rate, T_B^{-1} [77]:

$$\frac{1}{T_B} = k_{DNP}^{eff} + \frac{1}{T_{1I}}. \tag{52}$$

This is valid as long as spin diffusion within the bulk nuclear spin bath is faster than the effective transfer of polarization between electron spins and (observable) bulk nuclei. Then, the effective DNP rate depends on the μw field strength and accordingly on the incident μw power. Such an acceleration of longitudinal-polarization build-up is observed in experiments and potentially complicates the reliable measurement of DNP enhancement factors [62,74,77]. For a reproducible measurement, the enhancement at infinite polarization time, ε_∞, has to be measured. Practically this requires recording the DNP-enhanced signal intensity, I_{DNP}, while using a polarization build-up period, τ, which is significantly longer than T_B. This is then compared to the thermal-polarization signal intensity, I_{off}, that must also be recorded at recycle delays much longer than T_{1I}:

$$\varepsilon_\infty = \frac{I_{DNP}(\tau \gg T_B)}{I_{off}(\tau \gg T_{1I})}. \tag{53}$$

In a reasonable approximation, this can be achieved by choosing a polarization period or recycle delay approximately 5-fold longer than T_B or T_{1I}, respectively. More reliable is the acquisition of a full build-up curve after complete destruction of the polarization due to a pre-saturation train [225]. Exponential fitting allows for the extraction of a pre-exponential factor representing the polarization at infinite time. In many practical cases, an "instantaneous" DNP enhancement factor is provided by measuring DNP-enhanced signal intensity *vs.* thermal equilibrium at a finite build-up time well below the optimum $\sim 5 \times T_B$. For example, this can be due to prohibitively long build-up time constants typically encountered for (dilute) low-γ nuclei, weak thermal signals that do not allow for the acquisition of a full time profile, or ineffective off-signal sensitivity at $\sim 5 \times T_{1I}$. In these cases, care has to be taken because the instantaneous $\varepsilon(\tau)$ is a function of polarization time if $T_B \neq T_{1I}$:

$$\varepsilon(\tau) = \varepsilon_\infty \frac{1 - \exp(-\tau/T_B)}{1 - \exp(-\tau/T_{1I})}. \tag{54}$$

Thus, the destruction of the residual magnetization using a pre-saturation train or the use of an adequate number of dummy scans is of great importance for a reproducible quantification of the enhancement.

On the other hand, the acceleration of the polarization build-up accounts for an additional sensitivity advantage not included in ε_∞ [305]:

$$\kappa = \sqrt{\frac{T_{1I}}{T_B}}. \tag{55}$$

This factor κ only represents the advantage in S/N gained by faster build-up of DNP-enhanced signal *vs.* longitudinal relaxation in the same sample without μw irradiation and thus does not account for paramagnetic relaxation enhancement (PRE), which can be caused by the presence of the paramagnetic PA:

$$\frac{1}{T_{1I}} = \frac{1}{T_{1I}^\circ} + \Gamma_{1I}^{PRE}. \tag{56}$$

T_{1I}° is the relaxation time constant of the diamagnetic (undoped) reference and is stringently larger than or equal to T_{1I} of the sample doped with PA, since the latter is accelerated by the PRE rate, Γ_{1I}^{PRE}. Therefore, a reference sample of equal composition but lacking PA has to be measured for the accurate determination of off-signal intensity and spin-lattice relaxation time constant. An effective κ° is then obtained:

$$\kappa^\circ = \sqrt{\frac{T_{1I}^\circ}{T_B}}. \tag{57}$$

This additional acceleration due to PRE might indicate an additional increase in sensitivity at first glance, however, the SE enhancement strongly depends on the spin-lattice relaxation time constant of the bulk nuclear spins [74,77]:

$$\varepsilon_\infty \approx k_{DNP}^{eff} T_{1I}. \tag{58}$$

As soon as $T_{1I} \ll T_{1I}^\circ$, or from another viewpoint $\Gamma_{1I}^{PRE} \gg (T_{1I}^\circ)^{-1}$, Eq. (58) shows that the bulk DNP enhancement factor scales inversely with the PRE rate:

$$\varepsilon_\infty \approx \frac{k_{\mathrm{DNP}}^{\mathrm{eff}}}{\Gamma_{1I}^{\mathrm{PRE}}}. \tag{59}$$

Under the further assumption that $k_{\mathrm{DNP}}^{\mathrm{eff}} \ll T_{1I}$ (*i.e.*, operation of the SE far from saturation), K° then is simplified as

$$K^\circ = \sqrt{T_{1I}^\circ \Gamma_{1I}^{\mathrm{PRE}}}. \tag{60}$$

Here it becomes clear that the sensitivity loss due to reduction of DNP enhancement outweighs the benefit of faster acquisition due to PRE, so that a compromise has to be found. In most cases, typical SE PAs are quite poor PRE agents, so that sufficient DNP enhancement can be achieved with minimal reduction in T_{1I} [225].

6.1.2. Depolarization by MAS

In comparison to SE, the situation is completely different when a CE-active PA is concerned. As we have described in Section 2.1.2, CE transitions do not require μw irradiation in order to transfer polarization between electron spins and nuclear spins. This leads—especially under MAS—to a strong link between the nuclear polarization, P_I, and the difference in electron polarization, ΔP_S, between the two electron spins that in turn fulfil the CE matching condition Eq. (33). In thermal equilibrium P_I and ΔP_S are equal; this can be simply derived from the respective Boltzmann factors. However, if there is an induced imbalance, the relatively large CE transition moments [see Eq. (36)] will lead to a very efficient polarization transfer. For example, under saturation or inversion of the nuclear spin polarization, the recovery towards equilibrium is greatly accelerated by the presence of PAs potentially fulfilling the CE condition [306]. This coherent repolarization process is experimentally indistinguishable from nuclear spin-lattice relaxation processes, however, it is not to be confused with incoherent processes typically responsible for relaxation.

Equivalently, the nuclear spin polarization will also follow ΔP_S when the latter is perturbed. This effect is naturally sought-after during CE DNP by saturating the EPR spectrum at certain points within the spectral shape, so that the polarization differential ΔP_S is maximized. On the other hand, reduction of this differential in electron spin polarization (up to complete equilibration) over all possible CE pairs will reduce the observable non-DNP-enhanced NMR signal amplitude (down to vanishing). Such a (complete or partial) equilibration can be induced by large homogeneous EPR linewidths or electron spectral diffusion, so that μw-saturation at one frequency also causes saturation of electron spins off-resonance by the nuclear Larmor frequency, or by MAS without μw irradiation. In both cases sufficiently long electron spin longitudinal relaxation time constants, T_{1S}, are a prerequisite. In the latter case this condition can in many cases be quite easily fulfilled at intermediate-to-fast MAS frequencies, where T_{1S} is of similar size than the rotational period, $2\pi/\omega_r$, or larger. In that case, any non-adiabaticity of the e–e flip-flop events (see Section 2.1.2.5) leads to non-ideal exchange of polarization accumulating over several rotor periods and therefore partial equilibration of electron spin polarization. This process causes effective dynamic nuclear depolarization driven by CE under MAS in the absence of μw irradiation [85].

This depolarization is unique to CE-enabling PAs and is difficult to distinguish from paramagnetic bleaching or quenching that can occur at the same time (see below). Nevertheless, both effects have starkly different consequences. In fact, nuclear depolarization rather strongly depends on the MAS frequency and can be reverted to a large extent by μw-driven selective saturation of the EPR spectrum so that a large polarization differential is induced. In contrast, assuming uniform enhancement of all observed nuclear spins, bleaching is affecting both the DNP-enhanced as well as the non-enhanced NMR spectrum (*i.e.*, the on- and the off-spectrum, respectively). In the latter case (*i.e.*, bleaching) the NMR signal intensity might be greatly reduced even though large DNP enhancement factors would be measured, due to the reduced number of observable spins. In the former case (*i.e.*, depolarization) the enhancement factor might be overestimated because the DNP-enhanced spectrum is compared to an off-spectrum that is not in thermal equilibrium but effectively at a much higher spin-temperature. This might even result in quite unexpected observations such as apparent enhancement factors that exceed the theoretically possible ratio of γ_S/γ_I [see Eq. (2)] as has already been demonstrated in experiment [217].

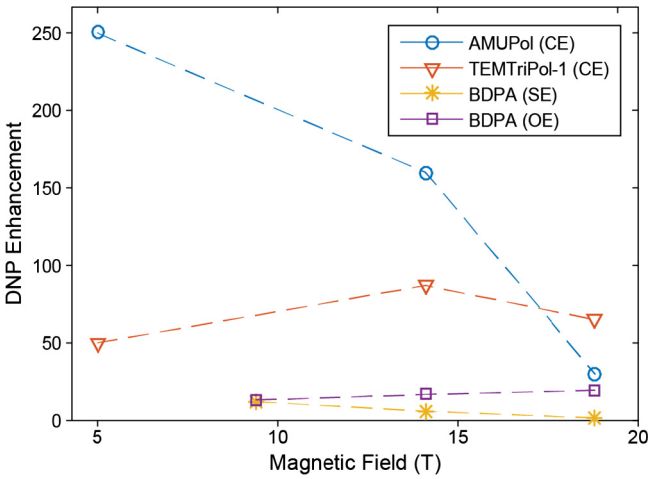

Fig. 46. Magnetic field dependence of ^{1}H DNP enhancement factors for different PAs. Data taken from [283] (AMUPol, TEMTriPol-1) and [90] (BDPA). Enhancement factors obtained by SE and CE drop significantly with increasing values of B_0. Note, that the increase between 5 and 14.4 T observed for TEMPTriPol-1 is due to a change in mechanism [283]. Only the OE in BDPA shows a favorable field dependence over the whole accessible range.

6.1.3. The absolute sensitivity ratio

The presence of the paramagnetic species causes a reduction of the number of detectable nuclear spins by bleaching effects in the vicinity of the electron spins. One possible reason for this is a broadening of NMR resonances due to increased transverse relaxation of nuclear spins (coherence quenching), possibly in combination with strong paramagnetic shifts. Furthermore, even when detected low-γ nuclei are virtually unaffected by the PA, global ^{1}H relaxation in the rotating frame can reduce efficiency of typically employed techniques such as heteronuclear CP.

These effects have been systematically studied in homogeneous frozen solutions using TOTAPOL as PA [252]. Furthermore, a direct comparison between different PAs and effective DNP mechanisms was presented [225]. Besides these experiments in environments relevant for biological studies, a quantitative study of ^{29}Si CP and CP/CPMG experiments on hybrid mesoporous silica impregnated with aqueous biradical solutions was reported by Rossini et al. [253]. In all cases, a reduction of the non-enhanced (μw-off) signal intensity in the presence of radicals was observed. The ratio between the thermal polarization signal intensity of a DNP sample doped with PA, I_{off}, and that of diamagnetic reference sample, I°, is therefore often given as a so-called bleaching or quenching factor ξ:

$$\xi = 1 - \frac{I_{\mathrm{off}}}{I^\circ}. \tag{61}$$

Together with the acceleration factor κ° from Eq. (57), this can be combined into an effective DNP signal-to-noise enhancement E:

$$E = \varepsilon_\infty (1-\xi)\kappa^\circ = \varepsilon_\infty \frac{I_{\mathrm{off}}}{I^\circ}\sqrt{\frac{T_{1I}^\circ}{T_{\mathrm{B}}}}. \tag{62}$$

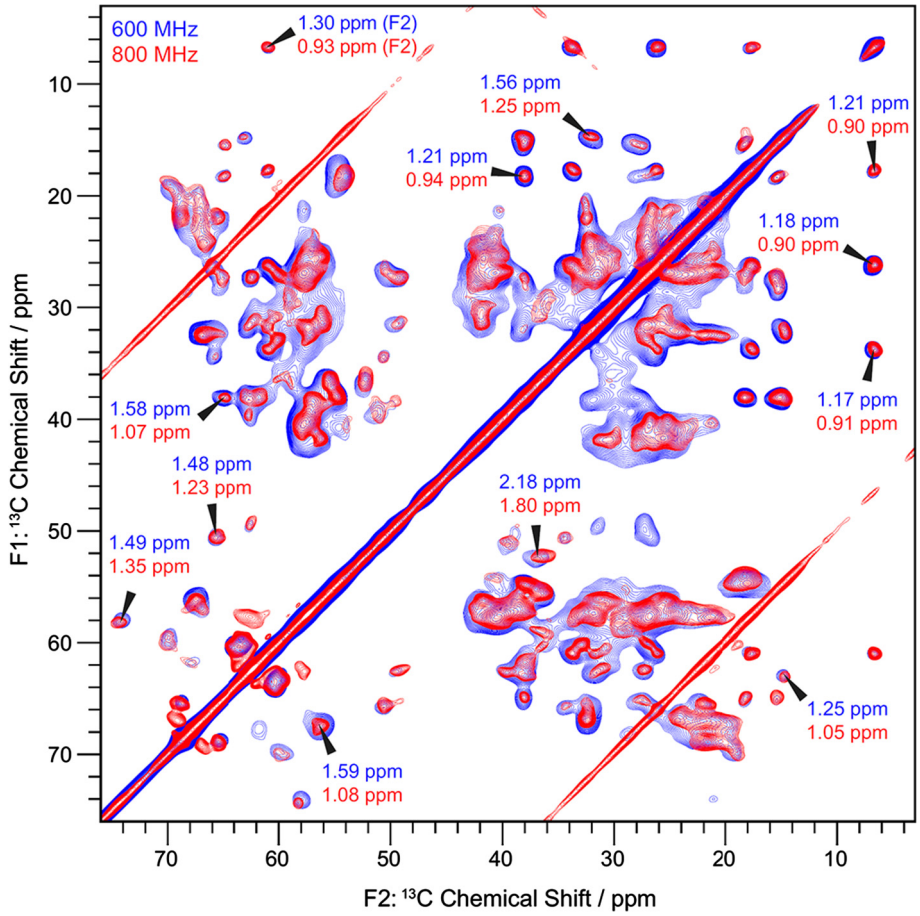

Fig. 47. Overlay of ^{13}C–^{13}C PDSD 2D NMR spectra of MxiH protein needles using DNP at 800 MHz (red, 8 kHz MAS, 95 K, 30 ms mixing time) and at 600 MHz (blue, 11 kHz MAS, 104 K, 20 ms mixing time). The full widths at half height (FWHH) in the direct dimension are annotated for some resolved peaks illustrating the increase in resolution at 800 MHz. Figure taken from [311] with permission.

However, from a practical viewpoint several aspects have not been considered here. For example, the groups of Lafon and Pruski have systematically analyzed the effective sensitivity enhancement (per unit time) in DNP-enhanced ^{13}C and ^{29}Si CPMAS on functionalized mesoporous silica nanoparticles and separated the contributions due to DNP, paramagnetic quenching/bleaching, the presence of frozen solvent, sample temperature (*i.e.,* the increased Boltzmann factor at lower temperatures) as well as the changes in relaxation and cross-polarization behavior [307]. In addition, Takahashi et al. have provided an even more comprehensive discussion of various factors, including experimental temperature, line broadening due to altered experimental conditions (different sample composition and/or temperature), reduced effective analyte concentration, signal loss by bleaching or reduction in transfer efficiencies in sophisticated NMR pulse sequences, as well as differences in equipment, which also come into play when comparing the full scope available for conventional MAS NMR with specialized instruments required for DNP [308]. Thus, for optimal performance, multiple and partially interconnected experimental parameters have to be considered.

6.2. Experimental parameters

6.2.1. External (static) magnetic field

From a basic NMR-spectroscopic point of view, higher external magnetic fields are beneficial in terms of sensitivity and resolution. Thus, most of the DNP-supported MAS experiments aiming at structural investigations are performed at fields $\geqslant$ 9 T. In contrast, SE and CE decrease in efficiency due to a complex interplay between various factors [179]. Mainly, the increasing width of the EPR line associated with incomplete excitation and the lower transition probabilities of the driven e–n transitions at higher fields and Zeeman frequencies are the reason for this dependence. Furthermore, the significant field dependence of electron and nuclear spin relaxation as well as spin diffusion has to be considered. The theoretical description of the underlying interactions is rather complex, nevertheless the general dependence on the external magnetic field is confirmed experimentally [90,309].

As shown in Fig. 46, particular radicals allowing for CE DNP can yield significant signal enhancements at the highest currently available fields. Compared to SE, much larger absolute values of the CE transition probability explain this performance (see Section 2.1.2.3). Still, the loss in enhancement factors as compared to lower fields is tremendous. Differences in instrumental design, for example, the μw-power output of the gyrotron, different conversion factors due to shorter wavelength, and changes in effective sample temperature are likely contributing to this behavior as well. It should be noted that especially at high magnetic fields, the reduction in enhancement could be compensated for, provided larger μw power was available. This is predicted by theory due to the direct scaling of the SE transition moment with B_1 field amplitude [74]; additionally, it was shown in experiment that the observed enhancement due to CE is far from saturation at the largest available power [184].

In view of routine DNP applications at high external fields, the development of novel radicals with narrow EPR lines and long

electronic relaxation times becomes highly desirable. Special interest lies in the further investigation and development of heterodimeric PAs for CE that have shown promising early results (see Section 5.2.3). Furthermore, PAs capable of performing OE DNP in solids might be a promising alternative, as the enhancement becomes more effective at high external magnetic fields [90]. Recent experiments have shown that under certain conditions, the enhancement obtained by OE (using BDPA as PA) can even exceed those generated by CE using highly efficient bis-nitroxide PAs [97]. As another alternative, pulsed transfer schemes are expected to be independent of the external field and could lead to improved enhancements provided that the necessary hardware requirements can be fulfilled [166,310].

Despite the ideally expected linear increase of spectral resolution with the external magnetic field, the exact dependence thereof in DNP-enhanced MAS NMR is still discussed in lively controversy. On the one hand, the introduction of paramagnetic species into the sample is a potential source of line broadening (Section 6.1.3). On the other hand, especially in biomolecular NMR, resolution losses due to the "protein glass transition" [312] have complex reasons that are still not fully understood, see also Section 6.2.4 for further discussion. As described in more detail in this sections, non-equivocal observations have been reported in the literature suggesting a potential conclusion that the line broadening processes may not only be strongly sample-dependent but also be determined by both homogeneous and heterogeneous broadening mechanisms. Due to the significant inhomogeneous contribution, the use of higher external magnetic field is not expected to increase the resolution in a linear fashion, even though substantial improvements have been demonstrated [261,311,313–315] as is shown exemplary in Fig. 47. It should also be noted that especially higher-dimensional correlation experiments suffer less from inhomogeneous broadening experienced at high fields and can be utilized in order to resolve overlapping signals without losing signal intensity [149].

6.2.2. MAS frequency

Resolution and sensitivity of NMR experiments also benefit from high MAS frequencies. From a mechanistic point of view, the MAS frequency can influence the DNP process during several stages. On the one hand, the adiabaticity of LAC during the CE polarization transfer, discussed in Section 2.1.2.5, depends on the MAS frequency, see Eq. (45). However, for a CE event the adiabaticity parameter Γ is small and the Landau-Zener equation predicts an almost linear dependence of the adiabaticity with the MAS frequency in that range. Thus, a reduction of the transfer probability due to faster MAS is compensated for by the increased number of CE events per unit time [83]. Another potential influence of MAS on the observed global DNP enhancement is caused by the dependence of nuclear spin-diffusion processes on the MAS frequency [316–319]. Due to the scaling of the spin-diffusion rate constants with roughly the inverse of the spinning frequency, detrimental effects, such as a less uniform distribution of polarization over the sample, might be expected. However, if spin diffusion is the rate-limiting step for nuclear spin relaxation at the same time, the overall enhancement factor should remain unaffected [101].

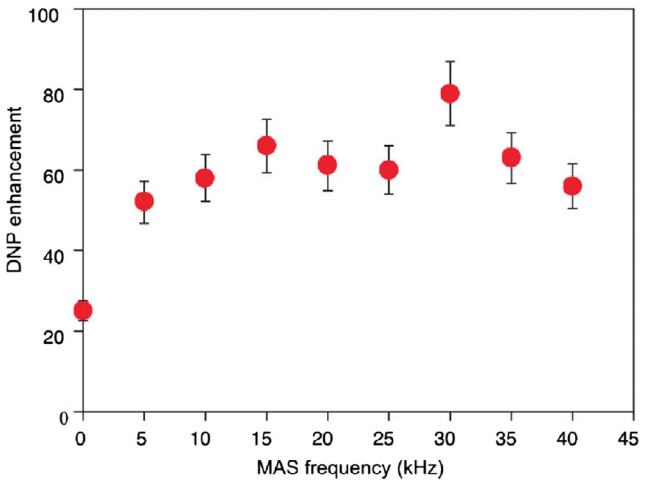

Fig. 48. MAS frequency dependence of the ^{1}H DNP enhancement of 0.25 M proline in a typical glycerol/water mixture (DNP-juice) with 10 mM AMUPol at 115 K and 18.8 T. Reproduced with permission from [86].

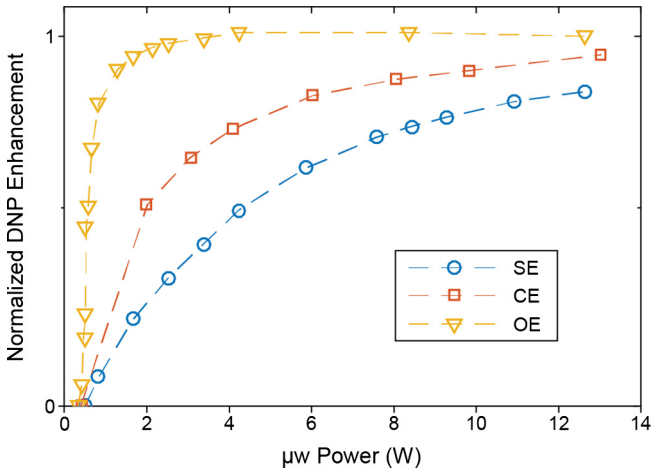

Fig. 49. Microwave power dependence of the normalized DNP enhancement for SE, CE and OE DNP. Data collected from [90,266].

Experimentally, Chaudhari et al. [86] reported only small variations of the ^{1}H CE DNP enhancement factor between 5 and 40 kHz MAS at 18.8 T (Fig. 48), suggesting that ^{1}H spin diffusion still seems to be fast enough to provide for a homogenous distribution of polarization over the whole sample. Rosay et al. performed an investigation for slow to intermediate MAS frequencies at an external field of 9.4 T. In contrast, they observed a significant influence of the MAS frequency on the ^{1}H DNP enhancement, leading to a maximum of $\varepsilon = 80$ at 3 kHz MAS. The decreasing enhancements at MAS frequencies up to 14 kHz were, however, attributed to sample heating effects due to insufficient temperature control (see Section 6.2.4 for further information) [177].

The seemingly simple conclusion of DNP being unaffected by the MAS frequency might no longer be valid for direct DNP on dilute nuclei with small gyromagnetic ratios [318,319]. Here, spin diffusion is generally slower and large overall enhancements might be prohibited by the bottleneck of polarization distribution [138,139]. However, no systematic studies either supporting or refuting this prediction are known to the authors.

It is worth mentioning that in all aforementioned studies, increased enhancement factors were obtained under MAS conditions as compared to static experiments. This indicates significant mechanistic changes of the quantum-mechanic processes in rotating samples compared to static CE-based DNP experiments. Such changes are in line with the theory of CE under MAS by Thurber and Tycko as well as Mentink-Vigier et al. as discussed above and in great detail in Section 2.1.2.

6.2.3. Microwave power

An additional observation in the study of Chaudhari et al. is that the enhancement factors obtained for samples in smaller rotors (*i.e.*, 1.3 mm instead of 3.2 mm outer diameter) are significantly

larger [86]. Similar findings have also been reported by Song et al. who compared the DNP efficiency in 4 mm and 2.5 mm rotors [221]. This was claimed to be caused by an improved μw penetration of the sample due to the reduced wall and sample thickness compared to the larger diameter rotors, finally leading to an increase in average μw field strength and thus larger enhancement factors [87]. In addition to wall thickness, the rotor material can have an influence on the obtained results, as we have explained in more detail in Section 4.4.3.1. Other experimental findings, where the μw field is enhanced inside the sample by the addition of diamagnetic particles [320], support such an explanation.

Fig. 49 shows the general trend of the dependence of the enhancement factor on the incident μw power for several DNP mechanisms. Significant differences can serve as indications to distinguish between the three DNP mechanisms [165]. For SE-type polarization transfer, DNP enhancement factors (as well as the build-up rate constants, see Section 6.1.1) increase almost linearly with increasing μw power. In contrast, maximum CE enhancements can be reached even with lower μw power. This is due to the fact that allowed electronic SQ instead of "forbidden" e–n DQ or ZQ transitions must be excited by μw in this case (see Sections 2.1.1 and 2.1.2). For (solid-state) OE DNP a very steep increase and an early saturation of the transferred polarization as a function of the μw field is observed, explained by efficient electronic SQ saturation due to long T_{1S} of the utilized BDPA in combination with efficient excitation of its narrow EPR line. This effect is especially interesting for cases where the μw power is limited by low-power sources.

In all cases, saturation or even a certain reduction of the enhancement is observed or predicted for very large μw power [74,152,162,163,177]. Sample heating, which leads to increased relaxation, is expected to play a significant role for a limitation of the maximum applied power [321].

6.2.4. Sample temperature: enhancement factors and spectral resolution

A graphical summary of the DNP enhancement as a function of sample temperature is shown in Fig. 50 for various PAs, obtained from several reports [97,214,217,219,250,271,322]. The maximum enhancement factor measured under MAS up to date has been obtained on a sample doped with AMUPol, which yielded $\varepsilon = 680$ for ^{1}H at 55 K [217].[5] A significant contribution towards this increase in DNP enhancement can be traced to the increase in nuclear longitudinal relaxation time constants with decreasing temperature which is important for more efficient accumulation of polarization (see Section 6.1 for further discussion). However, the details of the interplay between electron spin relaxation, nuclear spin-lattice relaxation and motional averaging of dipolar interactions that are responsible for the DNP transfer as well as for the propagation of enhanced nuclear polarization are still unclear, in particular with respect to vanishing enhancement near the glass transition temperature of the solvent [97].

Even though the tremendous increase in sensitivity at low temperature opens up several new fields of applications, the sample constitution under these cryogenic conditions can become an issue. Especially in the case of DNP on biomolecular systems, there has to be a compromise between signal enhancement and a loss of resolution induced by frozen-out dynamics at temperatures below the "protein glass transition" [312,323]. Such a signal broadening for protein samples can already be observed at temperatures that are easily accessible by nitrogen cooling (approximately at 200 K and below) and necessitates a tradeoff between enhancement and desired resolution [324]. If higher temperatures are used to avoid these effects, the losses in DNP enhancement can partially be compensated for by faster signal accumulation due to the accelerated build-up of polarization; additionally, deuteration of the sample has shown to increase DNP enhancement factors especially at elevated temperatures (Fig. 51) [214,325]. However, the conditions are not yet sufficient to perform DNP experiments on biomolecules with significant enhancements at or near room temperature.

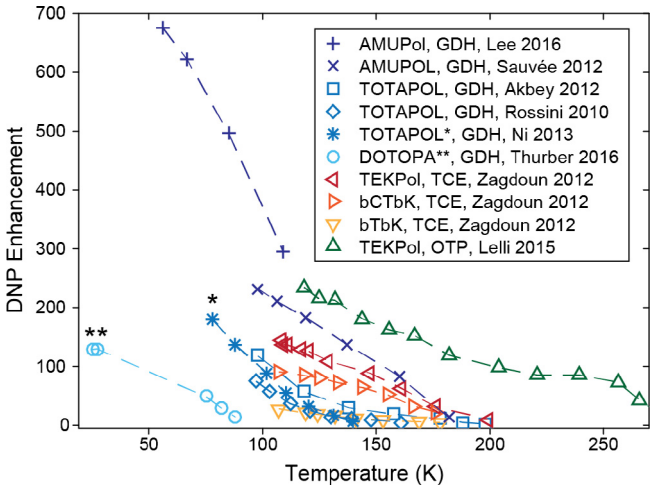

Fig. 50. Temperature dependence of ^{1}H DNP enhancement for various PAs and under different experimental conditions. Data was collected from several studies at a ^{1}H resonance frequency of 400 MHz [97,170,177,214,216,217,271,274]. The data marked with an asterisk (*) were recorded at 380 MHz [216]; the data marked with double asterisk (**) were recorded with a low-power μw. Source [170].

It is noteworthy that in OTP, significant enhancement factors of up to 20 have indeed been obtained close to room temperature, even at a field of 18.8 T [97]. This holds promise for molecules that are soluble in such a matrix as well as for surface-wetting of insoluble materials. Despite this intriguing observation, it is still unclear in how far the larger overall rigidity of the OTP matrix will alleviate resolution problems at these elevated temperatures.

Despite optimized sample preparation procedures to reduce the above-mentioned broadening [263], extraction of structural information under DNP may still be complicated, in particular for large, uniformly isotope-labeled systems prone to spectral crowding. Very recently, multi-dimensional correlation spectroscopy enabled by the large DNP sensitivity enhancement has been shown to overcome this issue and may be applicable in a general manner [149]. Also, selective isotope labeling has been successfully used to simplify the spectra so that sufficient resolution is retained. For example, several studies on retinal proteins such as bacteriorhodopsin [146,226,227], proteorhodopsin [326,327] and channelrhodopsin [228] have been reported. In order to study structural changes during their photo-cycle, the trapping of intermediate states at temperatures of approximately 100 K is an essential requirement of these experiments. This makes MAS DNP a method of choice even though a certain broadening of the resonances is observed. The interested reader is also referred to Section 7.2.2 for more details on these applications.

In the same vein, reduction of the temperature to cryogenic conditions may result in additional information that is otherwise not accessible. In some cases, the local environment can preserve the line widths of specific resonances so that sufficient resolution is obtained at low temperatures and high magnetic fields. Thus, the occurrence of well-resolved signals is also an indicator for structural or dynamical properties [311,313,328]. Furthermore, highly flexible parts of a macromolecule can be invisible in NMR

[5] The reader should note that this enhancement factor is larger than the theoretically predicted maximum from Eq. (2). This is explained by CE-induced depolarization of the off-signal (w/o μw) and explained in more detail in Section 6.1.3.

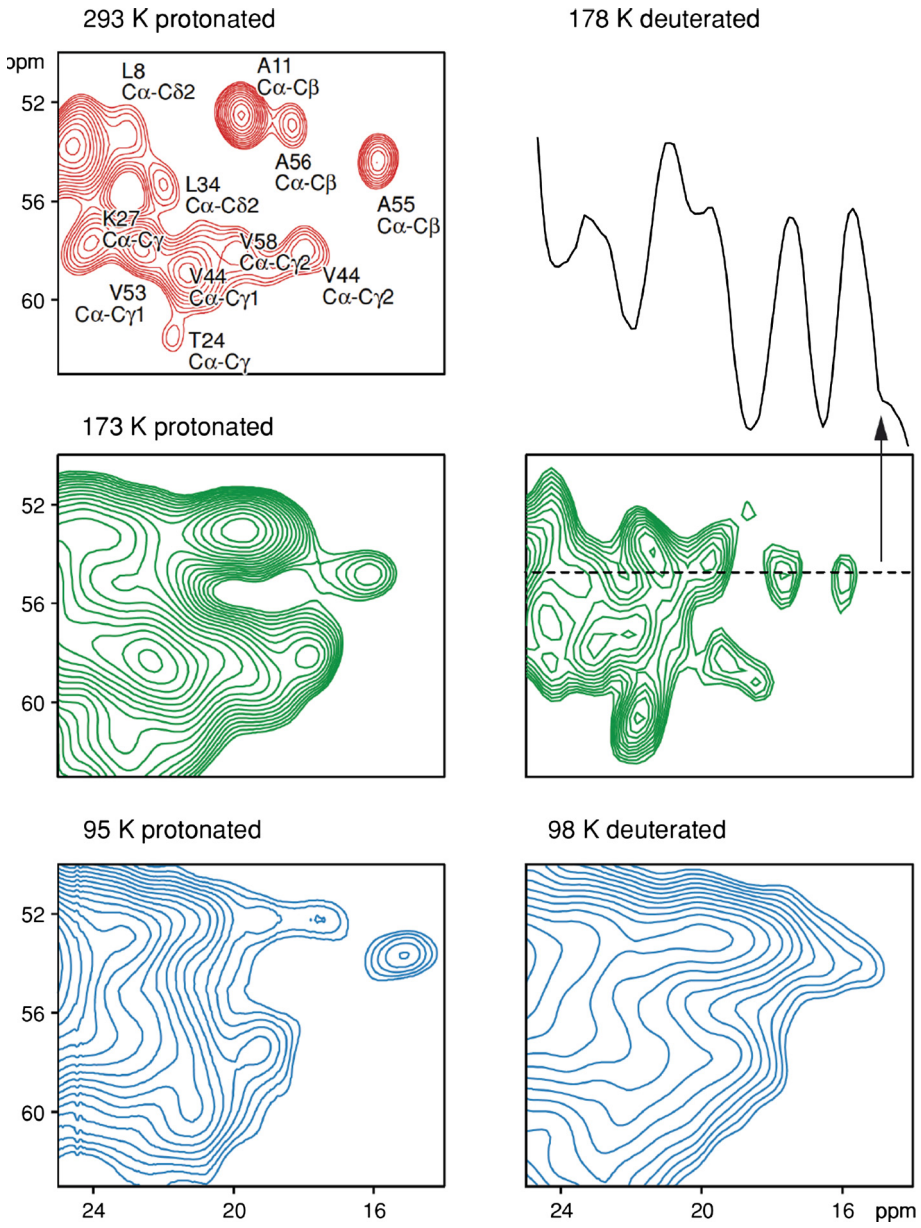

Fig. 51. Comparison of the resolution in 2D ^{13}C–^{13}C spectra of protonated and deuterated SH3 samples at different temperatures. The figure is reproduced from [214] with permission.

spectra recorded at room temperature and only observed under DNP conditions [261].

Similarly, side-chain dynamics can show distinct differences between room temperature and cryogenic conditions. Many aromatic functional groups show twofold symmetric flips that often interfere with NMR detection. At room temperature, this typically leads to rather broad or even undetectable resonances of aromatic side chain signals. Upon slowing down of the responsible interconversion at typical DNP-relevant temperatures of ~100 K the resonances can be recovered [329], allowing for the extraction of a larger number of structural constraints, in particular if coupled with the sensitivity gains from DNP [330,331]. In contrast, threefold symmetric methyl groups reorient rapidly at room temperature, which results in intrinsically narrow ^{13}C resonances [332]. Under typical sample temperatures employed in DNP, these hopping dynamics approach an intermediate-exchange regime and often lead to broad resonances and fast relaxation [324,333]. This situation, however, can give rise to interesting phenomena such as heteronuclear cross-relaxation during DNP (see Section 2.3.5) [141,145].

6.3. DNP sample preparation techniques

6.3.1. DNP in a glass-forming matrix

For most DNP experiments, the PA is dissolved in a solvent at ambient temperatures to ensure a uniform distribution. The analyte can be co-dissolved in a homogeneous mixture or it can be heterogeneously dispersed within the solution. In the first case, solubility of all components in the solvent is obviously essential. In the latter case, the enhanced polarization has to diffuse into the phase containing the analyte, such as a lipid bilayer bearing the membrane protein of interest, or microcrystals. For small

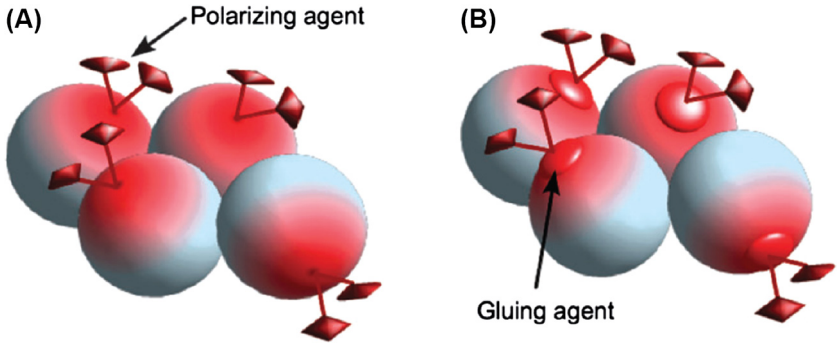

Fig. 52. Sketch of the basic principle behind matrix-free sample preparation. In order to avoid phase separation and aggregation upon freezing, the PA is either (A) covalently bonded to the analyte molecules or (B) a "gluing agent" is used to establish close spatial proximity. Figure reproduced from [342] with permission.

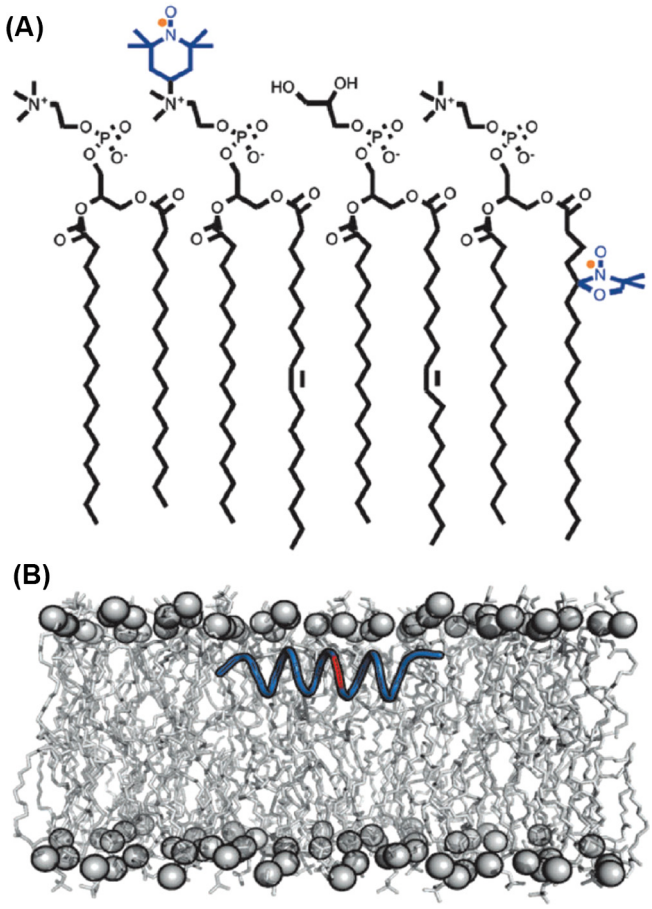

Fig. 53. Spatial proximity between PAs and analyte molecules can be guaranteed by covalently decorating the structure preserving matrix (*e.g.*, lipids) with PA units. Figure adapted from [262] with permission.

nanoscopic systems, polarization can be uniformly spread throughout the analyte by ^{1}H homonuclear spin diffusion, while for larger microscopic systems a polarization gradient is observed as a function of the distance from the surface [138,258].

Crystallization of the solvent upon freezing can cause phase separation between the PA and the analyte molecules, leading to strongly reduced enhancements [281]. For this reason, the solvent should be a good glass-forming agent and additionally offer cryoprotection of the analyte upon freezing. Especially biomolecules might undergo cold-denaturation processes or phase transitions due to solvent crystallite formation. This may lead to heterogeneity of the sample and result in reduced spectral resolution or even to an irreversible adaption of non-functional structures that must be circumvented or minimized by the appropriate solvent. Often, the so-called "DNP-juice" (d_8-glycerol/D_2O/H_2O, 60:30:10%) or d_6-DMSO/water mixtures are used as glass-forming matrix for aqueous solutions [334,335]. While DMSO often provides better solubility for PAs, glycerol is favored for biomolecular systems due to their larger stability in this solvent. In the case of hydrophobic compounds, TCE or OTP can serve as good glass-forming agents [97,274,280,281,336].

6.3.2. Alternative sample preparation techniques

The addition of a large amount of cryoprotectant causes a reduction in sample filling factor and thus a significant reduction in signal intensity that has to be accounted for when assessing the absolute sensitivity ratio (see Section 6.1.3). Additionally, the matrix might disturb the properties of the analyte. In order to tackle these issues, alternative ways of preparing samples in order to achieve a homogenous radical distribution while avoiding any (excess) solvent matrix are being developed.

One such sample preparation technique is "incipient wetness impregnation" that is specifically suitable for porous samples that are insoluble in the PA-bearing solvent [255]. Here, the solution is added to the sample in such a small volume that the pores and the surface are saturated with solvent while excess volume is avoided to optimize the sample filling factor. Also, due to the altered physical properties of the solvent molecules upon direct contact with the surface, crystallization upon sample freezing is prevented.

Other techniques are co-sedimentation of large biomolecules [337,338], co-condensation for functionalization of mesoporous silica with nitroxide radicals [142], film casting of polymers, [339] or co-milling of solid samples with a matrix-forming agent [340]. In the special case of amorphous polymers, a solvent-free sample preparation is feasible. In order to avoid phase separation, the PA is covalently bonded to (a fraction of) the analyte molecules [341].

6.3.3. Matrix-free approaches

Recent approaches explore the possibility to study systems without the use of the typical glass-forming solvents. Aggregation and phase separation of the individual components of the sample upon removing the solvent can be avoided if the PA exhibits a certain binding affinity to the analyte (Fig. 52A). Otherwise, "gluing agents" establish contacts between PA and analyte (Fig. 52B) [342]. Such an approach is especially appealing in systems that are prepared in a structure-preserving matrix. For example, membrane proteins are usually reconstituted in a lipid matrix that mimics their native environment. For matrix-free DNP experiments,

such liposomes have been stabilized in combination with small amounts of alternative cryoprotectants like trehalose [343]. Furthermore, the PA can be bonded covalently to molecules in the environment (Fig. 53B) rather than distributed randomly over the whole sample [262,340,342,343]. A maximized filling factor of the NMR rotor and the close spatial proximity between PA and analyte lead to promising sensitivity gains compared to samples where the PAs are distributed statistically over the sample. Furthermore, under certain conditions, signal broadening was reported to be less severe than in the classic approach using bulk glass-forming agents [342].

In the context of applications to materials science, solvent-free DNP-enhanced NMR of an organic–inorganic hybrid material has been demonstrated on mesoporous silica functionalized with TEMPO moieties. Lilly Thankamony et al. incorporated TEMPO into porous inorganic silica materials by co-condensation, enhancing ^{29}Si NMR signals by direct DNP. Due to the close vicinity between PA and nuclear spins, the ^{29}Si signals rapidly build up in direct DNP experiments—which further improves the NMR sensitivity [142]. Later, Gajan et al. also demonstrated matrix-free DNP applications to insoluble hybrid organic–inorganic silica materials containing homogeneously distributed mono- or dinitroxide radicals [344]. Meanwhile, the fast acquisition of 2D ^{13}C–^{13}C NMR correlation spectra of natural abundance microcrystalline cellulose—in which the PA is again uniformly distributed without any solvent—was also reported by the group of Gaël de Paëpe [345]. Later, they also introduced a novel matrix-free sample preparation approach for the study of nanoassemblies such as diphenylalanine (FF) dipeptide [260].

6.3.4. Localized and targeted DNP

More recently, several studies on localized or targeted DNP using site-directed spin labeling (SDSL) schemes or non-covalent labeling with PA-bearing tags or ligands have been reported. In the localized DNP approach, a close and well defined spatial proximity between PA and target molecules is achieved by specifically attaching the PA to native or point-mutated cysteine sites in proteins by SDSL [139,262,346–348], a technique often utilized in EPR spectroscopy or for PRE/PCS studies by NMR spectroscopy. In a very elegant demonstration, it has been shown that the contact interfaces of two proteins within a heterodimer can be probed, using CE DNP in combination with SDSL. By attaching one (mono-)nitroxide PA tag to each of the two subunits, CE DNP is only enabled if the complex adopts a closed conformation thus that the two nitroxides are in dipolar contact [348].

For targeted DNP, a modified ligand or paramagnetic metal ion is specifically bound to the biomolecule of interest [140,349,350]. Endogenous radicals such as the flavin mononucleotide semiquinone in the flavodoxin protein have also been shown to act as PA [92]. These approaches allow for selective DNP transfer to the analyte while loss of hyperpolarization due to spreading to the bulk can be prevented by deuteration of the latter [349,350], or by employing direct DNP of a biomolecule that is enriched with low-γ nuclear isotopes [140]. Further information about the application of these techniques is provided in Section 7.2.

6.4. Sample constitution

6.4.1. Isotopic enrichment and depletion

As mentioned above, the initial polarization transfer step from the electron spins to nearby "core" nuclear spins is followed by spin-diffusion processes that are responsible for a spatial distribution of the magnetization to bulk nuclei and thus play an important role for efficient DNP. The proton concentration of the matrix was found to have a strong impact on the DNP enhancement, hence the typically used ratios of deuterated and protonated components

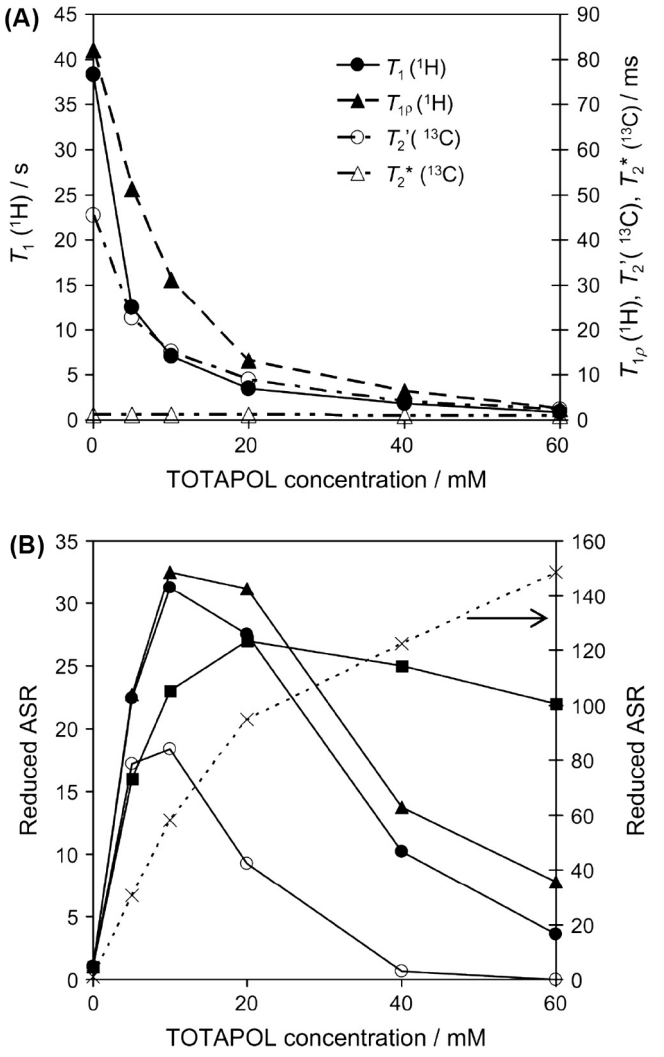

Fig. 54. (A) Influence of the concentration of TOTAPOL on ^{1}H and ^{13}C relaxation times on 2 M ^{13}C-urea in d_6-DMSO/D_2O/H_2O (60/30/10 vol%). (B) Resulting absolute sensitivity ratio (ASR) in a refocused INADEQUATE experiment, combining DNP and relaxation effects. Data show DNP enhancement factor only (squares), as well as cumulatively adding the following parameters: acceleration of experiment due to reduction of build-up time constants (crosses), loss of signal due to bleaching (triangles), reduced CP efficiencies due to increased relaxation in the rotating frame (full circles) and loss of signal during mixing due to increased transverse relaxation (open circles). The right ordinate axis is used for data represented by crosses. Reprinted from [308] with permission.

(see also Section 6.3.1) [335]. While a sufficiently high level of protonation has to be provided in order to guarantee efficient pathways for nuclear spin diffusion, the deuteration increases the electronic as well as nuclear relaxation times and in turn the DNP enhancements [74,351]. This depends strongly on the PA and DNP mechanism involved [74]. Also, recent reports have shown indications that no loss in DNP enhancement is observed even for fully protonated matrices when highly-efficient PAs such as AMUPol are used [141]. However, systematic studies are required to identify the optimal ^{1}H bulk concentration over a large range of experimental parameters.

Additionally, deuteration of the PAs [250,352] and target molecules [325] has been shown to improve the DNP enhancement due to optimized relaxation properties. As proton detection may become feasible with the latest generation of commercially available fast-spinning DNP probes, a dilution of the strongly dipolar-coupled proton network has the obvious advantage of

improved resolution of ^{1}H spectra [353]. Because in most DNP experiments to date the ^{1}H magnetization is read out after CP to the respective nucleus, a certain degree of protonation is required for improved sensitivity [354]. Thus, optimal ratios under DNP-enhancement are expected to be dependent on the PA and the sample under study.

Similar arguments also hold for direct DNP of low-γ nuclei. In that case, proton-driven spin diffusion leads to a significant distribution of the polarization, however, it requires sufficiently high concentration of the low-γ nuclear species (*e.g.*, upon isotopic enrichment). In contrast, certain parts of the sample (*e.g.*, solvent matrix, linker) in natural abundance or even depleted in the magnetically active isotope can selectively block transfer pathways [139–141,349]. Trivially, isotope depletion of the solvent also eliminates background signals that otherwise might overlap with the spectrum of the analyte [337].

6.4.2. Polarizing agent concentration

As should be clear from the discussion in the previous sections, the concentration of the PA has to be adjusted carefully such that optimal enhancement, sensitivity and resolution are obtained [252,308,340]. The underlying effects are complex, and in most cases difficult to predict.

On the one hand, a certain number of unpaired electrons need to be available, serving as source of polarization. Furthermore, the relative contributions of various DNP mechanisms depend on the radical concentration (see Section 3 for further information). In particular, e–e contacts required for the CE become more probable if monoradicals are used in high concentrations. For biradicals, this proximity is always given and a rather low concentration is generally sufficient to obtain sufficient enhancements by CE.

On the other hand, a high (global or local) concentration of radicals causes unfavorable quenching effects (Sections 6.1.2 and 6.1.3) resulting in reduced sensitivity and potentially in a loss of spectral resolution and information [85,225,253]. The increased relaxation rates may also cause losses in efficiency during recoupling and polarization transfer experiments [252,253]. However, the reduction of polarization build-up times (Fig. 54A) is beneficial as it allows for increased repetition rates.

Experimental findings (Fig. 54B) indicate optimum PA concentrations between 10 and 20 mM for homogeneous solutions. In particular cases, for example if long coherence decay times are necessary for efficient transfer of polarization between nuclei over intermediate/long distances, a reduced PA concentration can be beneficial [259]. In addition, it should be noted that in more complex samples, interactions between the analyte and the PA can result in larger effective, local concentration of paramagnetic centers around the nuclear spin systems of interest (see below). In this case, the global concentration has to be adjusted accordingly, such that excessive line broadening or quenching is avoided [355].

6.4.3. Interactions between polarizing agents and analytes

In addition to an influence on electronic relaxation properties, the molecular size and geometry of the radicals may also have application-specific consequences. For example, larger radicals may not enter porous materials, which on the one hand may lead to lower signal enhancements but on the other hand cause less quenching. Thus, the dimensions of the radicals themselves can be a useful parameter to investigate [356], see more details in Section 7.3.2.

In any case, a possible interaction between the radical and the substrate has to be considered because a very large local concentration of PA can cause line broadening of the NMR resonances (see above section). For example, Ravera et al. exploited non-specific interactions for co-sedimentation of proteins and PAs [338]; furthermore, specific interactions with TOTAPOL have been observed in BSA [337]. PAs have also been found to bind to amyloid surfaces [355] and active surface sites in porous materials [357]. Highly specific interactions between a PA-carrying ligand and a protein have been utilized deliberately to obtain selective hyperpolarization in the case of targeted DNP [349,350]; this approach is covered in more detail in Sections 6.3.4 and 7.2.5. Finally, possible reactions of the PA with other components of the sample—leading to a destruction of radical functionality and consequently to a loss of DNP (but possibly a gain in resolution)—have to be considered as well [358].

7. Structure determination enabled by DNP enhancement

MAS DNP has come a long way since the earliest pioneering applications on polymers and materials in the laboratories of Wind and Schaefer and the groundbreaking later works dominated by Griffin. Applications in the first ~2½ decades (*i.e.*, 1983–2009) were largely guided by the development of custom-built hardware. Furthermore, DNP applications towards biomolecular systems required a significant amount of proof-of-concept development in order to become interesting for the young, quickly developing field of biological MAS NMR.

Nevertheless, the commercialization of MAS DNP instrumentation around 2009—in combination with a quickly growing and highly creative community—paved the way for the popularity of MAS DNP today. This has led to a tremendous increase in reported state-of-the-art DNP applications towards structural problems from various research groups, first in the field of materials science, and more recently also in the field of structural biology. In the following, we will give an overview of these developments and of the diverse field of applications.

7.1. Pioneering works on MAS DNP

7.1.1. Early applications on polymers and diamonds

Wind and coworkers introduced the instrumentation suitable for MAS DNP and presented the first DNP-enhanced MAS NMR of coal as well as BDPA-doped polystyrene as early as 1983 [359]. During the following years they applied the method to study the structural properties of various materials such as undoped trans-polyacetylene [360], doped polymers [361], coal [362], amorphous silicon [363], organic conducting polymers [364], ceramic fibers [365], and diamond films [366]. All of these experiments were performed at room temperature using an external magnetic field of 1.4 T (40 GHz e^{-}, 60 MHz ^{1}H).

The structural defects of undoped trans-polyacetylene were studied in detail by indirect ^{13}C DNP NMR, using intrinsic defects (*i.e.*, unpaired electrons in the material) as PA. Spectra recorded before and after air oxidation showed the formation of oxygen bridges, as well as epoxide, hydroxyl and carbonyl groups in ^{13}C spectra [360]. It was also shown that direct and indirect DNP can probe the surface structure of ^{13}C-enriched chemical-vapor-deposited diamond films [366]. Using indirect DNP (^{1}H–^{13}C CPMAS), all carbon atoms in the sample were enhanced uniformly because of fast spin diffusion among ^{1}H. This signal enhancement enabled the acquisition of spectra, which would require impossibly long measurement times under conventional MAS NMR conditions. Besides that, by employing ^{13}C (direct) DNP in samples with natural isotopic abundance, only the rare ^{13}C spins near to the radicals were enhanced [367]. An excellent overview of these pioneering works is given in a review by Wind et al. [63].

Later, the group of Schaefer studied heterogeneous blends of undoped polycarbonate (PC) and of polystyrene that was homogeneously doped with BDPA, by using indirect [231,368] and direct DNP of ^{13}C [369]. Filtering to retain only enhanced NMR signals

of PC by comparing μw on- and off-signals allowed for selective detection of the polymer interface. As a result, it was possible to show that molecular dynamics of interface chains were retarded as compared to those within the PC bulk [370].

Another early effort towards MAS DNP was undertaken by the Zhou lab, using a custom-built 53 GHz (1.8 T) instrument. They were able to investigate the structures of different natural [78] and synthetic [79] diamonds using direct ^{13}C DNP NMR. Such studies are usually prohibited by extremely long spin-lattice relaxation time constants; however, a DNP enhancement factor of ~1000 allowed for acquisition of sufficient signal intensity after reasonable polarization times. Further studies involved hyperpolarization of pitch using the intrinsic unpaired electrons as PA [371].

7.1.2. Pioneering developments enabling biomolecular DNP

In the early days, the development required for DNP-enhanced MAS NMR spectroscopy on biological samples was almost exclusively driven by the pioneering work of Griffin and co-workers. In principle, NMR-sensitivity for most biomolecular systems is smaller than that of (bulk) materials or powdered systems because biomolecules form crystals with a high water content, or are embedded in conformation-stabilizing matrices such as lipids. Therefore, the first seminal demonstration of possible sensitivity enhancement by DNP transfer from a co-dissolved PA to a small biomolecule (1-^{13}C-glycine) in frozen solution showed a way to overcome this problem. Shortly thereafter, Hall et al. hyperpolarized the amino acid L-arginine as well as ^{15}N-Ala-labeled T4 lysozyme using TEMPO as PA and achieved DNP enhancements up to 50-fold, proving that protein structural biology by MAS NMR can benefit from a large sensitivity gain [218].

Subsequently, Rosay et al. extended the investigation to soluble and membrane proteins as well as to an intact bacteriophage, consisting of virus capsid and the contained genome. By analyzing the DNP enhancement factors of the coat protein and the single-stranded DNA core of fd bacteriophages, it was shown that ^{1}H polarization can efficiently diffuse through the 20 Å thick coat layer, allowing for hyperpolarization of the encapsulated genome that is not in direct contact with the solvent [372]. Furthermore, it was demonstrated, that structurally relevant amino acid signals of (membrane) proteins can be resolved in the DNP-enhanced spectra even for uniformly isotope-labeled samples [373].

Another proof-of-principle has been provided by van der Wel et al. by hyperpolarization of GNNQQNY nanocrystals. This oligopeptide forms the core of the yeast prion protein Sup35p and can undergo fibrillization; consequently, it served as a test-bed for the investigations of amyloid fibrils that play a key role in many neurodegenerative diseases. DNP caused a polarization gradient within the relatively large nanocrystals that not only allowed for direct analysis of the spin-diffusion kinetics governing the spreading of enhanced ^{1}H polarization, but also served as proof that heterogeneous, nanoscopic structures such as amyloid fibrils can be effectively investigated by DNP-enhanced NMR [258].

7.2. Modern applications on biological systems

Especially for large biomolecular systems like protein–protein complexes or membrane proteins, the intrinsically low sensitivity imposes challenges for structure elucidation by solid-state NMR. Thus, biomolecular NMR spectroscopy can benefit in several ways from the signal enhancements provided by DNP. Obviously, the increased signal-to-noise ratio allows for gathering the required information in less experimental time and the measurement of higher-dimensional spectra in fully labeled compounds becomes feasible which can provide additional structural information or simplify spectral assignment [149].

Furthermore, the required isotope labeling is often cost-expensive or the enriched samples can hardly be produced and purified in copious amounts. Provided the DNP enhancement is sufficiently large, multidimensional experiments of samples at natural abundance even in rather small amounts may be envisioned, as has been demonstrated for small organic molecules [138,151,342,374] and for a peptide embedded in bioinspired silica [375]. For samples at natural abundance, the structurally relevant long-distance restraints can be measured reliably, as no dipolar-truncation effects by strong dipolar couplings (*e.g.*, between neighboring carbons) suppress the polarization transfer between weakly-coupled nuclei [376].

7.2.1. Amyloid fibrils

The principle of DNP on amyloid fibrils was demonstrated by Debelouchina et al. on GNNQQNY fibrils [330]; this system has already been described in above Section 7.1.2. Due to their structural rigidity amyloid fibrils are an ideal sample system for investigation by DNP-enhanced NMR. There is experimental evidence that for amyloid-β (Aβ40), this can result in comparable line widths at room temperature and at cryogenic temperatures relevant for DNP [315].

The large sensitivity gains from DNP can greatly facilitate the measurement of medium- to long-range distances that typically require the acquisition of a large number of different mixing times. This advantage has been utilized by Bayro et al. for the generation of intermolecular constraints in order to elucidate the arrangement of β-strands within fibrils formed by the 86-residue SH3 domain of PI3 kinase (PI3-SH3). Under MAS DNP conditions, a significantly larger number of intermolecular constraints could be obtained that was attributed not only to the larger signal intensity due to DNP, but also due to the occurrence of resonances at cryogenic temperatures that are dynamically quenched at or near room temperature. Based on a total of 111 intermolecular ^{13}C–^{13}C and ^{15}N–^{13}C constraints, it was established that the PI3-SH3 protein strands are aligned in a parallel arrangement within the amyloid fibril [331].

Similarly, investigation of the higher-order structure of fibrils is a pivotal step towards understanding the extraordinary stability of the amyloid architecture. Debelouchina et al. succeeded in deriving the protofilament arrangement within fibrils formed by an eleven-residue segment of the amyloidogenic protein transthyretin. Due to large savings in acquisition time, it was possible to obtain a large number of quantitative distance and torsion-angle restraints in order to derive an accurate structure (Fig. 55) [377].

The formation of Aβ40 fibrils has been studied by Tycko and co-workers by DNP-enhanced MAS NMR at very low temperatures near 30 K. Potapov et al. were able to monitor intermediate steps of the self-assembly process of Aβ40 from monomers *via* oligomers and protofibrils to form fibrils by freeze-quenching the fibrillization process at different points of time [378]. They found that the supramolecular β-sheet structure only forms during the fibril stage, but that the molecular conformation is qualitatively similar at all stages [378].

Weirich et al. have elucidated the structure of amyloid fibrils formed from islet amyloid polypeptides that are a hallmark of type-2 diabetes mellitus and are known to be cytotoxic to pancreatic β-cells. Here, DNP-enhanced MAS NMR at cryogenic conditions supported the study of the conformational flexibility of the N-terminal residues [379].

An intriguing observation was made by Nagaraj et al. when investigating functional amyloids formed by CsgA protein. They found that TOTAPOL has the propensity to bind to the fibril surface, similar to the fluorescent dye thioflavin-T (ThT). DNP from only 0.25 mM TOTAPOL allowed for the extraction of long-range distance constraints, which were difficult to obtain without

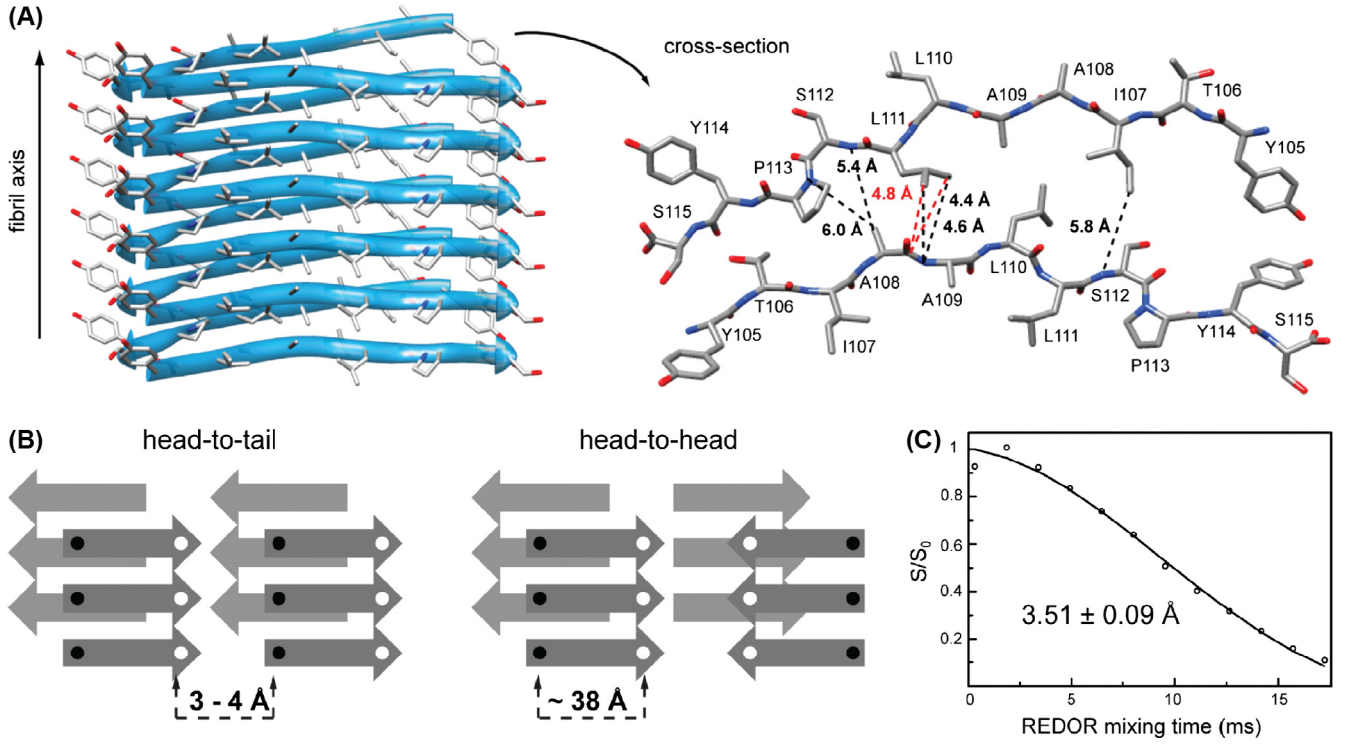

Fig. 55. (A) Structure of the amyloidogenic protein transthyretin TTR(105–115) protofilament (PDB ID: 2m5n). View along the fibril axis with an emphasis on the parallel, in-register β-strands within each β-sheet (left), and summary of the observed quantitative contacts that constrain the odd–even-odd–even antiparallel β-sheet interface (right). (B) Two possible arrangements of the protofilaments are head-to-tail and head-to-head arrangements. (C) DNP-enhanced ^{15}N–^{13}C experiment with REDOR mixing was used to measure the distance between the two labels. The fitted distance is 3.51 ± 0.09 Å, consistent with a head-to-tail protofilament organization. Figure adapted with permission from [377].

sensitivity enhancement. The small PA concentration reduced the line broadening occurring under conventional PA concentrations. Such affinity towards fibril surfaces is proposed to be a general feature of amyloids [355].

7.2.2. Membrane proteins

The function of membrane proteins is crucial in understanding many transport processes in biology that are often linked to diseases and their treatment. Therefore, they offer an intriguing target for solid-state NMR while being constituted within an immobilizing lipid bilayer. This, however, leads to a small effective protein concentration and thus typically low NMR sensitivity that can be overcome by DNP.

Interestingly, the requirement for cryogenic temperatures in order to conduct DNP experiments and the resulting freezing of biomolecular dynamics—which often imposes a substantial challenge due to signal broadening—also offers the possibility to access states that may otherwise be hidden in conventional NMR at or near room temperature. Such trapping of states has been impressively demonstrated with the first major biological application of MAS DNP. Griffin and co-workers have trapped several intermediate states of the photocycle of bacteriorhodopsin (bR) by photoactivation due to *in-situ* optical irradiation (see Section 4.4.3.3) and controlled thermal relaxation. The conformational ensemble is then conserved and spectroscopically accessible during the acquisition of DNP-enhanced MAS NMR spectra at cryogenic temperature. Such a technique has enabled the first observation of the early K state of bR by NMR. Mak-Jurkauskas et al. identified significant changes in retinal Schiff-base/counterion interactions between the light-adapted resting state (bR_{568}), the K state, and the L state that is reached by thermal relaxation [226]. Furthermore, in a subsequent study by Bajaj et al., the interaction with the counterion was found to play a crucial role in the adoption of several possible L-state conformations: out of a discrete set of four observed L substates, only one functional state with a very strong counterion interaction allows the further photocycle evolution towards the M state, while three shunt substates of L directly revert the system back to bR_{568} [227].

Similar investigations have been conducted by Glaubitz and co-workers on the related retinal proteins proteorhodopsin (PR) and channelrhodopsin-2 (ChR2). By employing an *in-situ* light-irradiation technique similar to that used in the above-described studies, Becker-Baldus et al. have been able to investigate the conformation of retinal and its interactions within the active site in ChR2 (Fig. 56). They found three distinct intermediates of the photocycle; whereby two of those could be trapped by repeated illumination, freezing, and thermal relaxation, the third could only be detected during continuous illumination [228]. The same group has also applied ex-situ illumination in combination with freeze-quenching of photointermediates of PR, which allowed for the detailed analysis of photoactive-site interactions during the photocycle with DNP-enhanced MAS NMR [380]. Furthermore, Mao et al. were able to accurately determine the structural changes in the retinal that give rise to green/blue color switching caused by a single point mutation [326] and Maciejko et al. studied the contacts across protomers in PR oligomers. In the latter case, it was shown that one specific salt-bridge is responsible for the formation of pentamers or hexamers [327].

DNP is also a powerful tool for the investigation of ligand binding to (membrane) proteins where orthogonal labeling strategies (*e.g.*, ^{13}C-ligand/^{15}N-protein or vice versa) allow for selective spectroscopy of ligand–protein contacts even in the presence of substantial line broadening. Such an approach was pursued by Andreas et al. for studying the binding of the small drug molecule rimantadine to the $M2_{18-60}$ proton transporter from influenza A virus. By employing a rather small TOTAPOL concentration of only

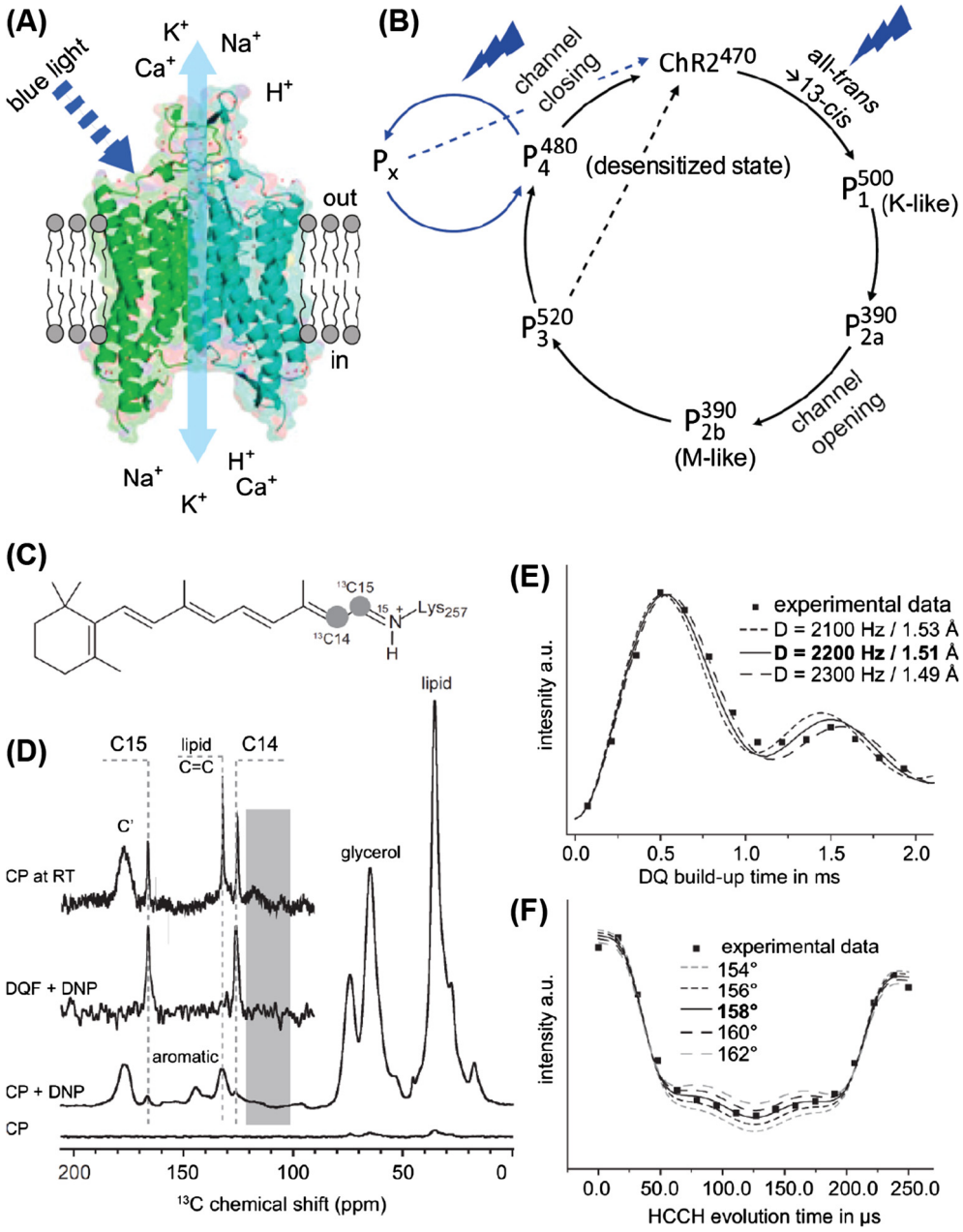

Fig. 56. (A) Visualization of dimeric ChR2 reconstituted into a lipid bilayer. Blue light illumination activates ChR2. (B) Single turnover (black arrows) and continuous illumination photocycle (blue arrows). (C) Chemical structure of 14,15-^{13}C all-trans retinal. (D) DNP-enhanced MAS NMR of U-^{15}N-ChR2 containing 14,15-^{13}C retinal. A 62-fold signal enhancement is achieved for ^{13}C CP; the natural abundance background can be efficiently suppressed by a double-quantum filter (DQF). (E) ^{13}C14-^{13}C15 double-quantum (DQ) build-up curve. (F) HCCH dephasing curves for the C14–C15 spin system in ChR2 reporting on the HCCH dihedral angle. Figure adapted from [228] with permission.

~5 mM, the measurement of intermediate/long-range distances of 4 Å and larger allowed for the localization of the binding site within the pore with an accuracy of 0.2 Å, and furthermore allowed for the observation of weak (dynamical) external binding sites [259]. In the same vein, Ong et al. investigated the binding of two different substrates to the secondary multidrug efflux pump EmrE by DNP-enhancement of homonuclear, intermolecular contacts between ^{13}C-labeled substrate and 2-^{13}C-glycerol-labeled protein. It was possible to identify a common binding pocket occupied by both substrates while at the same time the bound ligand population showed some degree of heterogeneity [381].

Further DNP-supported studies of membrane proteins and membrane-embedded peptides include the assembly of a correctly-folded and functional heptahelical membrane protein by protein trans-splicing [382], the observation of multiple conformations of lipid-anchored peptide vaccines [383], as well as the refinement of the membrane-embedded channel structure of a potassium channel (KcsA) [313]. The latter study by Koers et al. revealed conformational sub-states in two different stages of the channel's gating cycle.

Amongst very recent efforts, DNP has been explored by Glaubitz and co-workers as a method for the investigation of *E. coli* MsbA as a model ATP-binding cassette (ABC) transporter and signal enhancement factors of ~20 have been obtained [384]. Shortly thereafter, the same group has applied DNP-enhanced MAS NMR for studying the human transporter associated with antigen

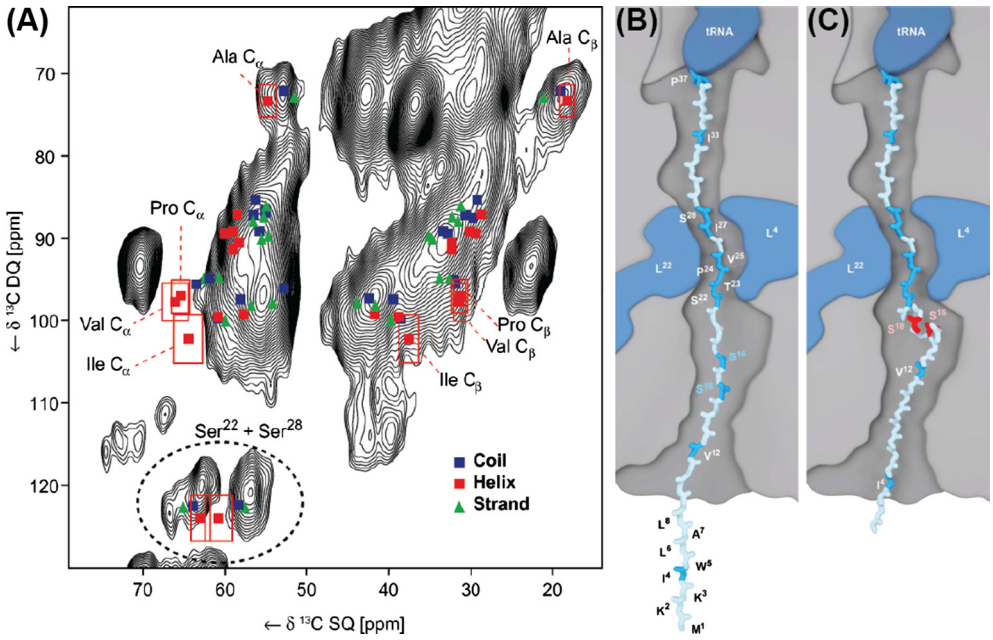

Fig. 57. (A) Comparison of DNP-enhanced POST-C7 DQ–SQ spectra of the ribosome embedded nascent chain S16A/S18A-DsbA-SecM overlaid with predicted chemical shifts for three different tertiary structures. (B + C) Structure models of nascent chains assuming a stretched (B) and a partial helical conformation (C). Reproduced from [387] with permission.

processing (TAP), a 150 kDa heterodimeric ABC transport complex. The successful identification of the binding cavity of an antigenic peptide as well as its backbone conformation and interactions with the protein is the first step to determine the structural basis for the function of TAP in human health [385].

7.2.3. Structure of biomolecules in large complexes

DNP has been intensively employed in the investigation of large biomolecular complexes that often suffer from potential spectral crowding and the small volume concentration of the sought-after species. For example, Oschkinat and co-workers have recently studied the structure of a chromophore in phytochrome photoreceptors. DNP-enhanced MAS NMR supported the localization of the positive charge of the phycocyanobilin (PCB) chromophore. Furthermore, the proximity of PCB ring nitrogen atoms and functionally relevant water molecules was also determined, both of which play a role in proton exchange pathways [386].

The same group has also investigated the structure of a signal sequence of disulfide oxidoreductase A (DsbA), stalled within the nascent chain exit tunnel of the ribosome. Such a situation not only imposes a selectivity problem due to the large background of the ribosome (>5000 a.a. *vs.* 37 a.a. of the peptide) but also a sensitivity problem due to the small effective concentration of the nascent peptide [387]. While the former problem can be compensated for by isotope labeling strategies, the latter problem can be overcome by DNP as has been first demonstrated by Bodenhausen and co-workers on a protein subunit within a ribosomal complex [388]. In the above-mentioned study, enhancement factors between 15 and 20 have allowed Lange et al. to investigate the conformational states of the peptide resembling the nascent chain. In conclusion, the chain adopts an extended structure in the ribosome with only minor populations of helical structure (Fig. 57) [387].

The epidermal growth factor receptor (EGFR) has been recently investigated in a collaborative effort headed by Baldus and van Bergen en Henegouwen. As one of the most common protein targets in anti-cancer therapy, its activation by epidermal growth factor (EGF) is of utmost interest. Therefore, Kaplan et al. studied the changes in EGFR dynamics upon binding of EGF (Fig. 58). By employing DNP-supported MAS NMR they found that in the ligand-unbound state, the extracellular domain (ECD) is highly flexible, while the intracellular kinase domain (KD) is rigid. Upon binding of EGF, the ECD becomes restricted in its motions, which favors cooperative binding. The latter is required for receptor dimerization, which in turn causes allosteric activation of the intracellular tyrosine kinase [389].

Furthermore, the 36 MDa filamentous circular single-stranded DNA bacteriophage Pf1 has been studied by McDermott and co-workers. The virion consists of the genome (7.3 kb) distributed over two non-complementary DNA strands embedded within a capsid of ~2 μm in length. Due to the ~5-fold smaller signal intensity of NMR signals from DNA as compared to coat protein, the investigation of interactions between the genome strands as well as between DNA and the protein imposes a significant challenge. Nevertheless, Sergeyev et al. have succeeded in shedding light on the unusual structure of the DNA in uniformly ^{13}C, ^{15}N-labeled Pf1 by analysis of chemical shifts made accessible by a ~22-fold DNP enhancement [390].

Very recently, the study of viral structure and function by DNP-enhanced MAS NMR has been extended towards human immunodeficiency virus (HIV-1) tubular assemblies of CA capsid protein in a collaborative effort. By achieving a DNP-enhancement factor of 64 at 14.1 T and a remarkable resolution of NMR spectra at 109 K, Gupta et al. were able to observe functionally relevant "invisible" species, such as dynamically disordered states, which are not detectable using other methods. Furthermore, it was concluded that within a CA-SP1 assembly, the SP1 spacer peptide is unstructured and in a random-coil conformation [391].

7.2.4. Biomolecules embedded in complex environments

The study of biomolecules that are embedded in their native environment (ideally within the complete cell/organism) is one of the major aims of structural biology. However, such studies are often impeded by similar problems as discussed in the above sections (*i.e.*, selectivity and sensitivity). First strides towards this aim in combination with DNP have been taken by Griffin and co-workers by reconstitution of bR in purple membrane

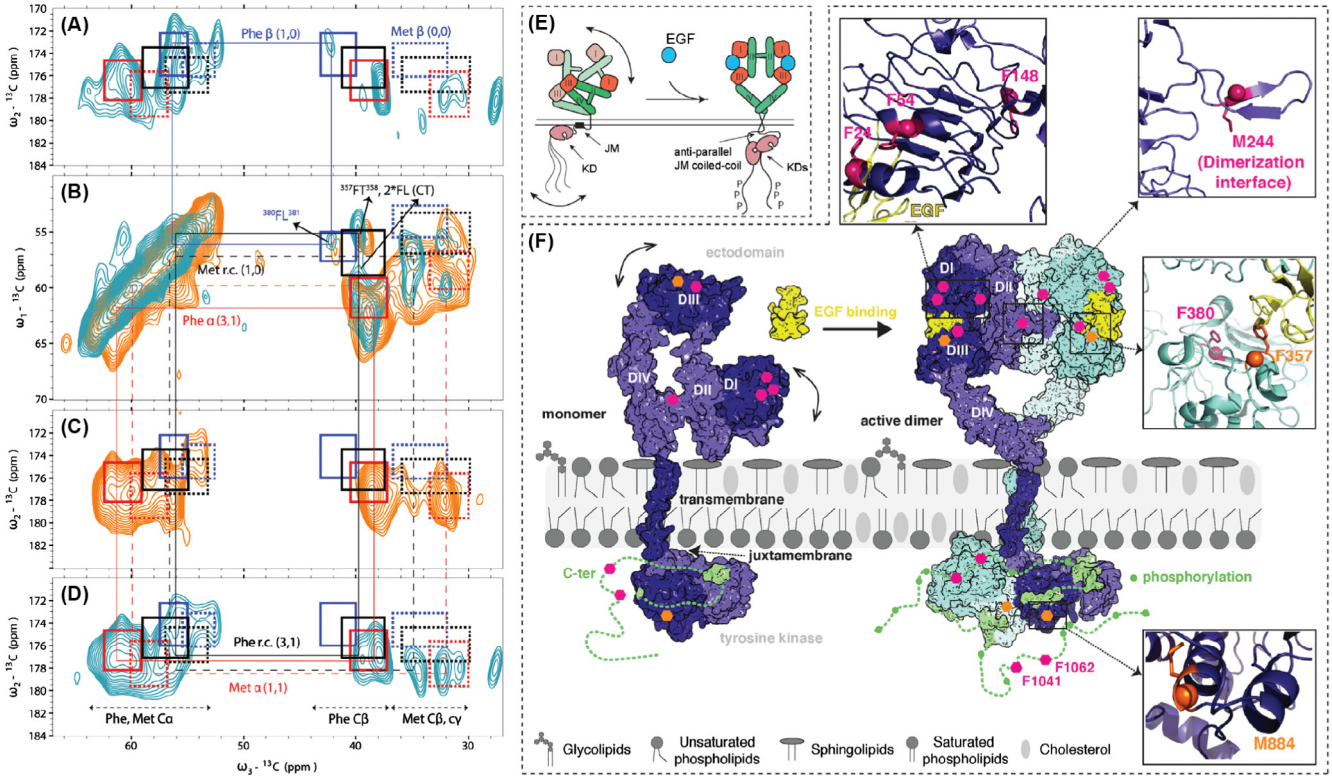

Fig. 58. (A, C, and D) 2D planes of 3D NCOCX spectra on EGFR before (C, orange) and after (A and D, cyan) addition of EGF shown at 124 ppm (A), and 120.5 ppm (C and D) ^{15}N chemical shifts. (B) 2D N-edited ^{13}C–^{13}C experiment of cell membrane obtained with (cyan) and without (orange) EGF. (E) Model of EGFR activation *via* conformational selection in the ECD. (F) Various ^{13}C-labeled residues act as NMR probes, revealing changes in the local dynamics of different domains of EGFR. Figure reproduced from [389] with permission.

[148,226,227]. Further explorative developments have been driven by Reif and co-workers by characterization of membrane proteins in isolated native cellular membranes: Jacso et al. have demonstrated that membranes can be directly isolated from *E. coli* cultures in which the membrane protein is over-expressed, without need for purification and reconstitution [392]. In a similar vein, Renault et al. have investigated the prospect of DNP-enhanced MAS NMR spectroscopy of whole cells as well as cellular envelope preparations [393]. This technique has been subsequently applied in order to investigate the structure of the type IV secretion system core complex (T4SScc) that is a 1-MDa part of a larger machine (T4SS) being embedded in both the inner and outer membranes of Gram-negative bacteria. DNP allowed for the study of T4SScc embedded in the cellular envelope of *E. coli* by 2D and 3D correlation spectroscopy (NCACX/NCOCX) at fields of 9.4 and 18.8 T. Kaplan et al. were able to confirm earlier structural models based on *in vitro* and *in silico* data, but also observed the folds of parts of the complex at the periplasmic surface that have evaded detection in purified complexes [394].

Hong and co-workers have studied the binding of expansin to plant cell walls. This protein plays a crucial role in loosening the cell wall, yet its course of action has been mostly unknown due to its presence in typically minute quantities during cell growth. By DNP-enhanced spin-diffusion and 2D ^{13}C correlation spectroscopy, the authors have observed highly specific binding of expansin to cellulose domains enriched in xyloglucan. These bound domains in turn appear to have altered conformations, leading to the cell wall loosening [395].

A very recent field of interest made accessible by DNP is the study of biomacromolecules embedded within silica networks. In these hybrid organic/inorganic materials, the sought-after biomolecule is sparsely dispersed within the embedding matrix—similar to the examples given above—which makes NMR-spectroscopic investigation for structural biology difficult. Signal enhancement by DNP has allowed several groups to examine such systems, stimulated by a proof-of-concept demonstration by Ravera et al. on biosilica-entrapped enzymes [396]. Subsequent studies were able to determine the structure of the incorporated proteins and peptides in intact diatom biosilica [397] as well as of a silaffin-derived pentalysine peptide embedded in bioinspired silica [375].

7.2.5. Towards in-cell DNP

In-cell NMR holds the ultimate promise of observing biomolecules and investigating their structure and function within their native environment. It has been shown that processes such as ligand binding [398], protein–protein interactions [399], and even protein folding [400] strongly depend on the environment and can differ when observed within cells or in a "sterile" *in vitro* buffer. However, in-cell NMR significantly suffers from similar problems encountered for large complexes but to a much larger degree, leading to extremely weak sensitivity and poor selectivity in order to differentiate between sought-after molecules present in minute concentrations and large amounts of diverse cellular background components.

Strategies for the selective introduction of isotope-labeled proteins have been introduced to overcome the latter issue to some degree [401]. By application of multidimensional correlation spectroscopy or multiple-quantum filters, the selectivity can be improved by the appropriate power of the ratio of the isotopic enrichment (*e.g.*, ~10,000-fold by double-quantum filtering in the case of pairs of ^{13}C nuclei). A similar approach was pursued by Frederick et al. who have been able to demonstrate that macro-

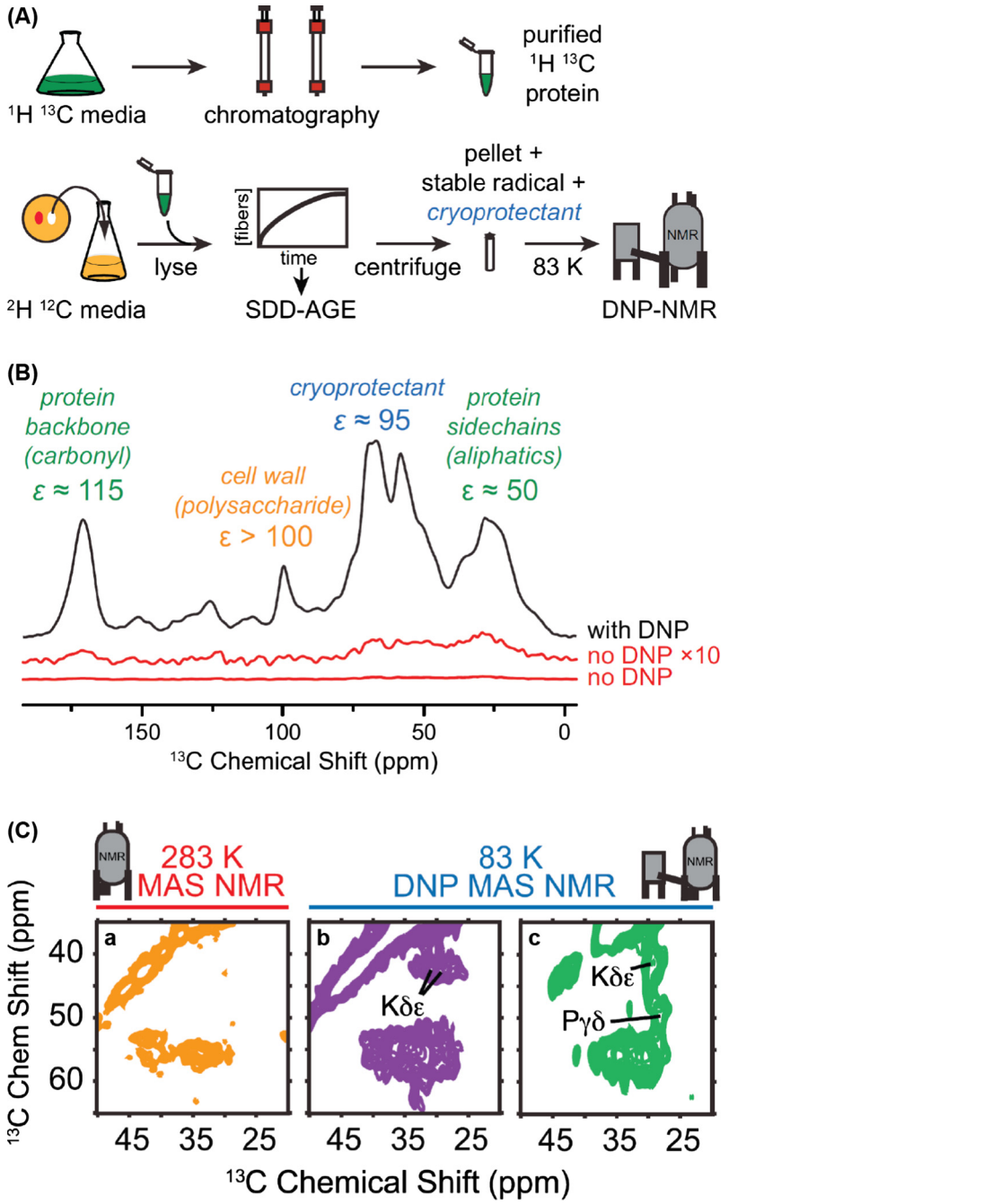

Fig. 59. (A) Preparation of samples for DNP MAS NMR of proteins at endogenous levels in biological environments. (B) 1D ^{13}C CPMAS spectra both with (black) and without DNP. (C) Side chains of NM fibers in cellular lysates have a different chemical environment than *in vitro* templated NM. Aliphatic region of (a) purified NM fibers at 283 K in protonated assembly buffer (b) purified NM fibers at 83 K in 60% d_8-glycerol and (c) NM fibers at 83 K in 60% d_8-glycerol, templated into the amyloid form in the presence of cellular lysates. Figure adapted from [402] with permission.

molecular folding of proteins in fibrillar structures significantly differs when fibrillization occurs in cellular milieus (*i.e.*, from proteins in native concentration within eukaryotic cell lysates) as compared to induction in purified media (Fig. 59). In this case, selective detection of NMR signals from the analyte protein (NM domain of eukaryotic translation release factor Sup35) was achieved by introduction of isotope-enriched protein to the cell lysate upon which the amyloid formation was induced in the complex cellular milieu. By choosing appropriate NMR techniques using DNP-enhancement after adding TOTAPOL to the lysate, it was possible to provide evidence for significant structuring of the middle (M) domain that otherwise adopted a disordered random-coil conformation *in vitro* [402].

As mentioned in Sections 6.3.3 and 6.3.4, an alternative approach providing high selectivity is the introduction of the PA in a "targeted" or "site-specific" manner. This promising technique has recently emerged in several independent and parallel demonstrations and has already been successfully applied within a cell lysate [349]. In general, a covalent bonding of the PA to the sample [139,346,347] or the surrounding structure-preserving matrix [262,343] ensures a close spatial proximity of the sources of polarization to the target molecules. Also a non-covalent binding affinity

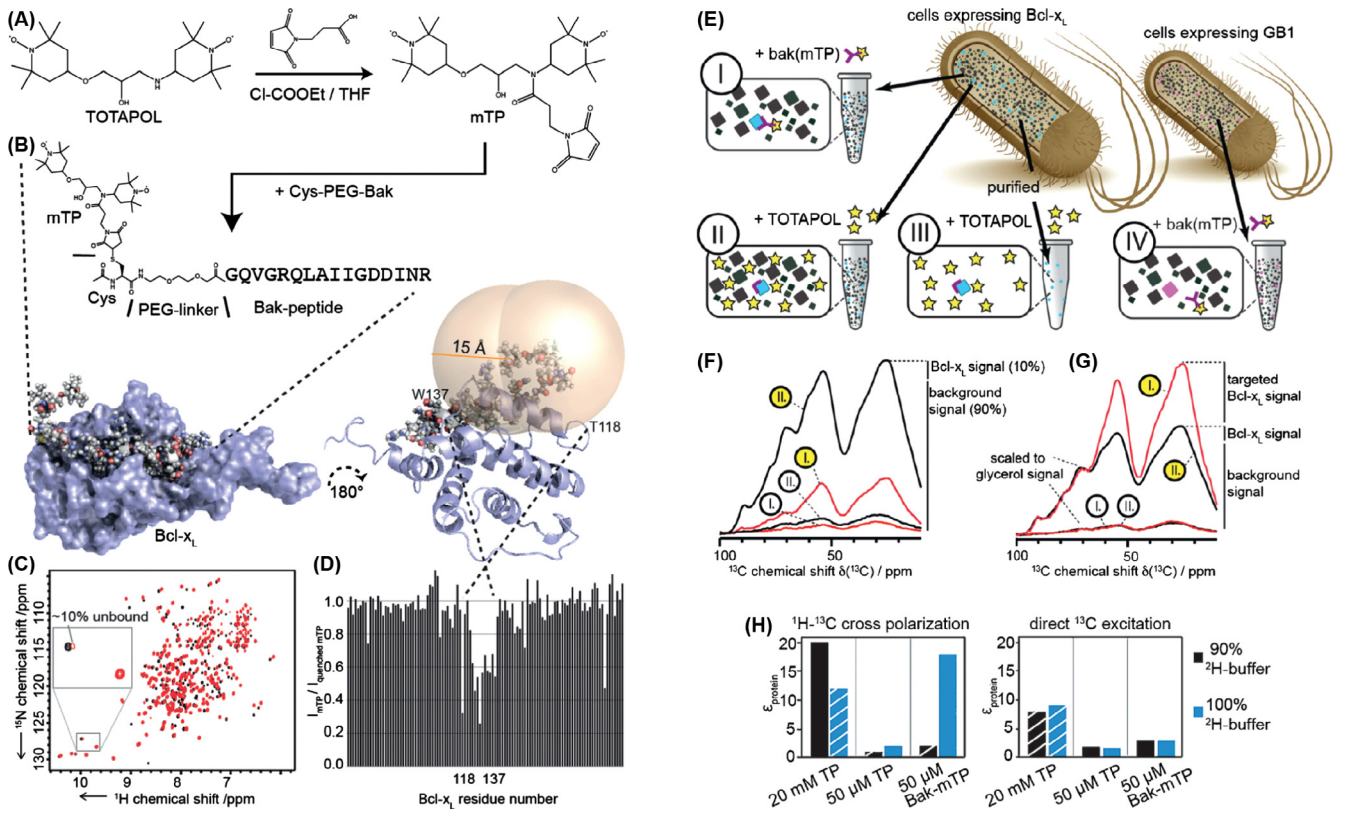

Fig. 60. Targeted DNP for structural investigation of Bak-peptide binding to the protein Bcl-x_L. (A) TOTAPOL is linked to the peptide and (B) due to selective binding well defined spatial proximity is established. (C) ^{15}N–^{1}H HSQC spectra of pure protein and protein-ligand complex confirm high binding affinity. (D) The binding position can be identified by PRE effects on close-by residues. (E) Schematic of used samples. (F) 1D spectra in the presence (yellow label) and absence (white label) of µw for the conventional (black) and targeted (red) setup. Expected signal contributions are indicated. (G) Same spectra as in (F), but scaled to the glycerol background. (H) Polarization by targeted DNP can be selectively confined to the protein in perdeuterated matrix. Reproduced from [349] with permission.

of the PA to the analyte can be exploited [140,349,350,355] In addition to the above, such an affinity has been introduced by a "gluing agent" such as trehalose [342].

A simplification of the spectra and an optimized ε is found experimentally as the enhancement of (parts of) the target molecules is favored over the enhancement of the matrix. Due to such a selective enhancement using protein-specific ligands, this approach would also facilitate in-cell NMR experiments [394] or experiments in systems, which are difficult to purify [392]. In a similar vein, Viennet et al. [349] and Rogawski et al. [350] independently obtained a localized position of the PA by docking a radical-carrying ligand to the target protein (Fig. 60). In both studies, enhancement factors on the order of ~20 were observed at a field of 14.1 T (600 MHz/395 GHz) using the protein-bound PA in stoichiometric concentration with respect to the protein. Interestingly, virtually no global quenching or bleaching of protein resonances was observed, despite the close vicinity of the paramagnet. A related approach was applied in the case of metal-binding biomolecules, such as RNA, where a native binding ion can be exchanged by a paramagnetic transition metal (*e.g.*, Mg^{2+} by Mn^{2+}), introducing localized PA centers for DNP [140]. Also, molecules that contain endogenous radicals have been studied using DNP [92].

All these approaches have in common that the position of the radical is known *ab initio* or can be identified from paramagnetic relaxation effects (Fig. 60D) [403]. Thus, additional site-specific information can be deduced [313,347]. Future prospect could also be the analysis of site-specific DNP enhancement in order to obtain more quantitative distance information.

7.3. Applications to materials research

After the early MAS DNP studies had been reported as described in Section 7.1.1, it took more than a decade to develop the dedicated hardware technology that is now commercially available. This, however, led to an extraordinary interest in using DNP-enhanced NMR particularly to characterize inorganic and hybrid materials where isotope labeling is usually impossible or difficult. Also, due to the oftentimes already intrinsically inhomogeneously broadened signals encountered in solid materials, the incorporation of the analyte within a glass-forming matrix at cryogenic temperatures (see Section 6.3.1) was not accompanied by a further detrimental loss in resolution as had been observed for biological samples.

7.3.1. Enabling surface probing: DNP-SENS

First applications of high-field DNP to materials were initiated by the groups of Emsley, Bodenhausen and Lafon. In 2010, Lesage et al. described the first surface-enhancement of hybrid organic silica materials with a 50-fold increase in the NMR sensitivity. They used TOTAPOL to enhance the ^{13}C CPMAS spectra of organic groups (phenol or imidazolium units) in natural isotopic abundance,[6] covalently attached to the surface of porous silica (Fig. 61) [255]. This general approach for enhancing the surface signals by DNP was dubbed "DNP surface-enhanced NMR spectroscopy"

[6] In the following, natural isotopic abundance is to be assumed if not stated otherwise.

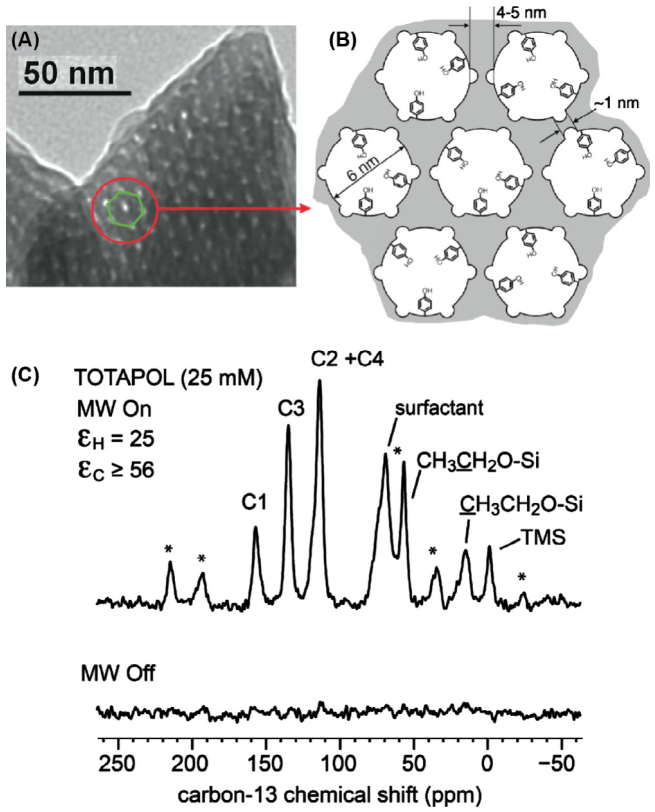

Fig. 61. (A) Transmission electronic microscopy image and (B) schematic representation of nanoporous silica functionalized with phenol moieties. (C) ^{13}C CPMAS spectra with (top) and without (bottom) μw irradiation of the material impregnated with TOTAPOL solution, showing selective DNP enhancement of the surface phenol functional groups. Figure adapted from [255] with permission.

(DNP-SENS) and is applicable to porous materials impregnated by radical solutions. The PA occupies the pores of the material and hyperpolarizes the protons in the solvent. Efficient ^{1}H spin diffusion aides in spreading the polarization towards the pore surface. The enhanced polarization is then transferred to the nuclei of interest within the material by CP. This method that allowed for selective enhancement of surfaces and surface-bound species in contrast to the larger amount of nuclear spins in bulk, was quickly recognized as a seminal step towards a broad field of applications [404].

For example, surface-enhanced ^{29}Si DNP spectra served as evidence for the incorporation of functional groups on silica surfaces by identifying the surface Q- and T-sites in a functionalized silica material (Fig. 62); in addition, the large enhancement factors allowed the acquisition of 2D ^{1}H–^{29}Si correlation spectra in a short time [256]. Shortly thereafter, Lafon et al. presented the complementarities of direct and indirect DNP. Indirect DNP was found to be selective for surface sites, whereas direct DNP allows for the observation of both surface and subsurface sites. In particular, the ^{29}Si NMR spectra of subsurface sites were enhanced by direct DNP with a 30-fold enhancement using TOTAPOL (Fig. 63) [143]. They also showed that dispersed nanoparticles of laponites can also be enhanced by indirect or direct ^{29}Si DNP [144].

A further important demonstration of the applicability of DNP to mesoporous systems has been provided by Lafon et al. A one-dimensional ^{1}H spin-diffusion model was employed to analyze the enhancement factors of an organic/inorganic hybrid material with surfactant (S-MSN) and without surfactant (Ex-MSN). It has been proven that DNP can be used to indirectly enhance the NMR signals of ^{13}C and ^{29}Si in S-MSN where the nuclei (within the pores) and the PA (trapped in the surrounding disordered

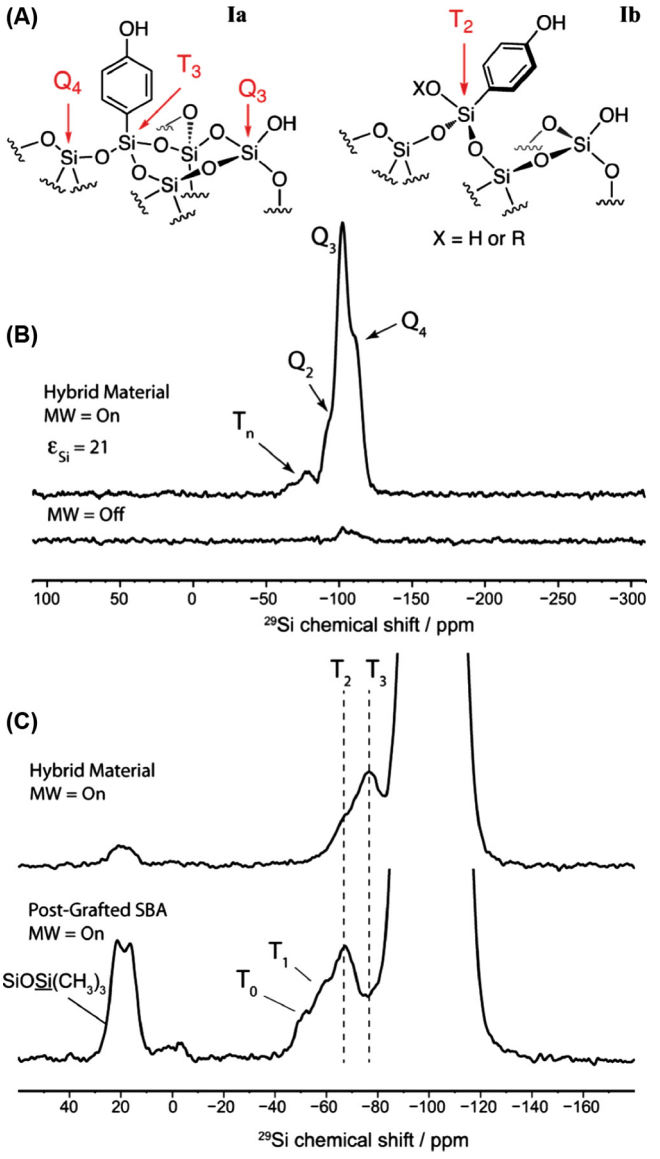

Fig. 62. (A) Structures of the T_3 and T_2 species that are present on phenol-functionalized silica surfaces. (B) ^{29}Si CPMAS spectra of **I** with (top) and without (below) DNP enhancement. (C) DNP-enhanced ^{29}Si CPMAS spectra of two different phenol functionalized mesoporous materials showing different ratios of surface species. Figure taken from [256] with permission.

water matrix) are spatially separated by several hundreds of nanometers (see Fig. 64). This is due to the diffusion of ^{1}H spin hyperpolarization into the mesopores before it is being transferred to the rare spins by CP [356].

In 2014, Guo et al. exploited the signal enhancement of DNP by TOTAPOL to identify different amine sites and to quantify the binding of Pt^{2+} to a zirconium-containing metal-organic framework (MOF), UiO-66-NH_2 [405]. By ^{1}H–^{15}N CPMAS NMR in combination with X-ray absorption spectroscopy and density functional theory (DFT) calculations, they determined the stereoisomerism of Pt^{2+} binding and rationalized the lack of affinity of Cu^{2+} for the host material. It is worth mentioning that TOTAPOL is too large to enter the pores of the framework, so that the observed enhancement must be based on an efficient distribution of polarization by spin diffusion.

DNP has also been used to elucidate the binding sites in a catalyst constructed from dirhodium acetate dimer ($Rh_2(OAc)_4$) units covalently linked to amine- and carboxyl-bifunctionalized

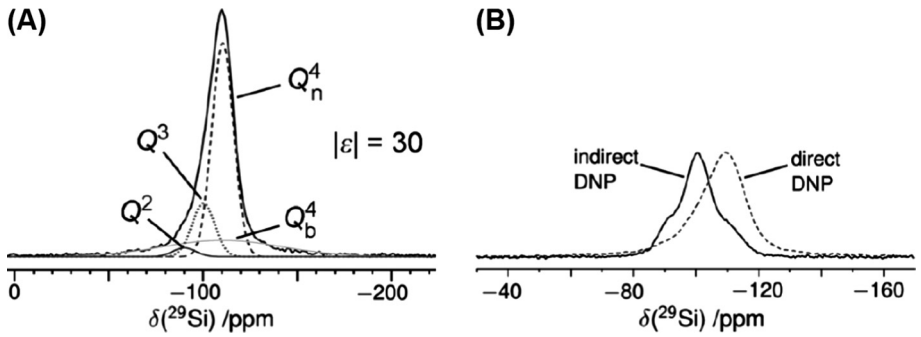

Fig. 63. (A) Direct DNP-enhanced ^{29}Si NMR spectra of porous silica. The deconvolution of the direct DNP spectrum is also displayed. (B) Comparison between the ^{29}Si NMR spectra obtained with direct DNP (dashed line) and indirect DNP *via* ^{1}H (continuous line). Figure adapted from [143] with permission.

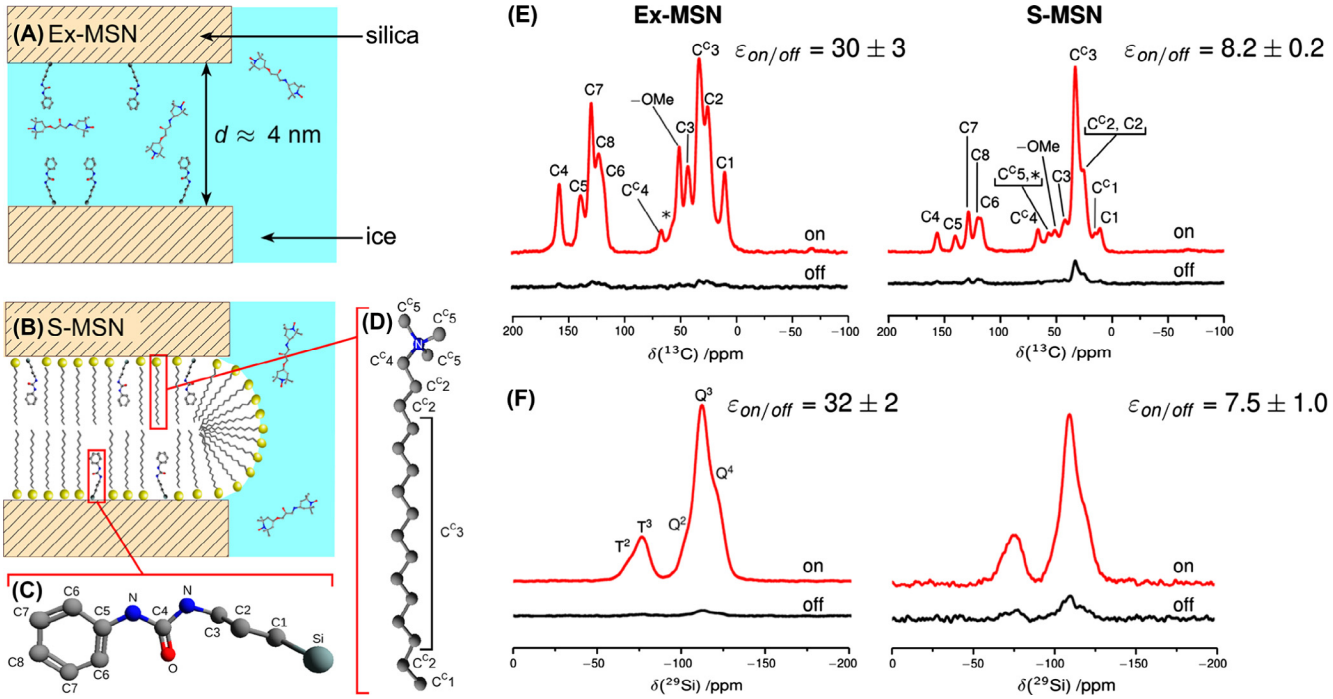

Fig. 64. (A and B) Sketches of (A) Ex-MSN (where the aqueous solution of TOTAPOL can penetrate into the mesopores) and of (B) S-MSN functionalized by covalently bound 3-(N-phenylureido)propyl (PUP) and impregnated with the surfactant cetyl trimethyl ammonium bromide (CTAB). (C and D) Numbering of carbon atoms in (C) PUP and (D) CTAB. (E and F) CPMAS spectra of (E) ^{13}C and (F) ^{29}Si in Ex-MSN (left) and S-MSN (right) impregnated with a 12.5 mM TOTAPOL in H_2O. Figure adapted from [356] with permission.

mesoporous silica (SBA-15-NH_2-COOH) by Gutmann et al. The binding sites of carbonyl and amine groups were detected using DNP enhanced ^{13}C and ^{15}N CPMAS spectra within a short experimental time [406]. Furthermore, ^{15}N CPMAS enhanced by DNP allowed the discrimination between covalently bound and adsorbed peptides on collagen-like peptides immobilized on carboxylate functionalized mesoporous silica (COOH/SiO_x) [407].

DNP SENS using 1D and/or 2D NMR has also been applied for structural determination of various other materials, including silica (SiO_2) nanoparticles [408,409], silica-supported zirconium catalyst [410], hybrid mesoporous silica [411], silicates [412], phenylpyridine-based periodic mesoporous organosilicate [413], nanostructured soft matter [414], alumina-supported metal nanoparticles [415,416], heterogeneous alkene metathesis catalysts [417], cellulose nanocrystals [418], alumino silicates [419,420], lignocellulosic biomass [421], functional paper materials [422], organometallic complex supported on an amorphous silica [423], nitrogen-containing active pharmaceutical ingredients (APIs) [424], polymorphs of theophylline [425], colloidal quantum dots [426], functionalized nanodiamonds [427], etc. In addition, thermolysis of ammonia borane was also explored by using ^{15}N DNP NMR in combination with other spectroscopic techniques [428].

7.3.2. Materials embedded in organic glass-forming agents

In a search for DNP-supporting glass-forming agents other than the commonly employed glycerol/water mixtures, Zagdoun et al. tested the DNP enhancements on hybrid mesoporous materials for a series of non-aqueous solvents capable of dissolving the hydrophobic PA bTbK. They concluded that TCE is a promising organic solvent that can provide signal enhancements similar to aqueous solvents and can be used with hydrophobic materials for solid-state DNP [336]. Subsequently, the first application of DNP-enhanced ^{15}N and ^{13}C CPMAS NMR to an N-functionalized MOF was tested with bTbK in TCE solution (Fig. 65). A reduction of the experimental time by two orders of magnitude due to DNP

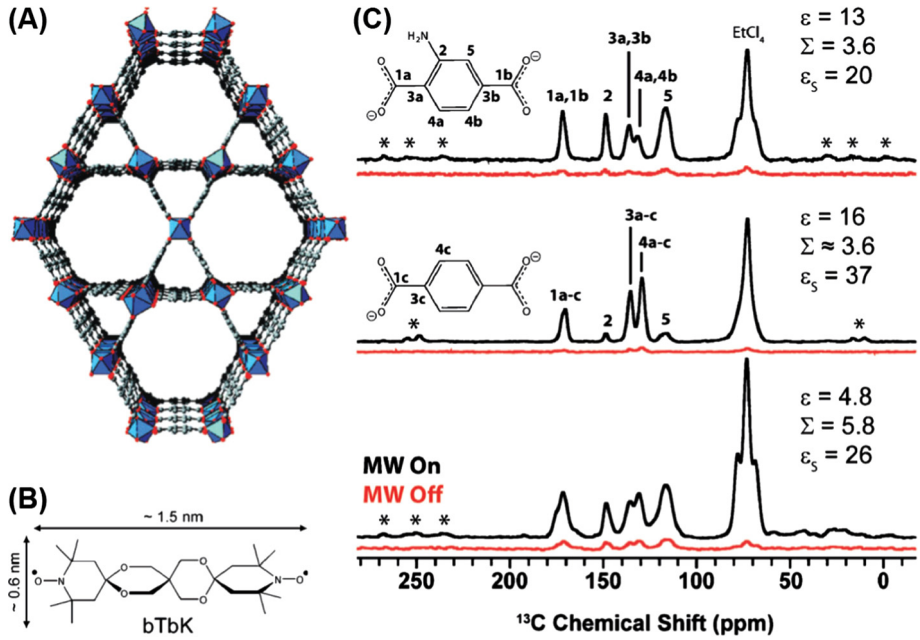

Fig. 65. (A) Crystal structure of the MOF used by Rossini et al. (B) Chemical structure and dimensions of the PA bTbK, indicating possible penetration of the pores. (C) 1D ^{13}C CPMAS spectra of MOF samples impregnated with a 16 mM bTbK solution in TCE, recorded with (black) or without μw irradiation (red). Figure adapted from [429] with permission.

was found irregardless of the ability of bTbK to penetrate the small (1.6 nm) pores of the material [429].

A chemical application of DNP MAS NMR at 14.1 T was reported by Blanc et al. for the molecular structure determination of microporous organic polymers (MOP) using bCTbK as PA dissolved in TCE. A good signal-to-noise ratio of the ^{13}C and ^{15}N CP MAS NMR spectra due to $\varepsilon \geqslant 10$ allowed for the detailed determination of molecular structure of the complex polymer networks of the MOP [430].

Rossini et al. demonstrated the atomic-level characterization of active pharmaceutical ingredients (API) in commercial pharmaceutical formulations (with API contents between 4.8 and 8.7 wt%). They determined the domain sizes of the API using DNP-enhanced ^{13}C and ^{15}N CPMAS spectra. The use of TCE as the solvent for the biradical PA TEKPol minimized potential perturbations of the API [431].

Apart from the DNP studies of nonporous or mesoporous nanoparticles, Lilly Thankamony et al. studied the trend of catalytic activity in a series of fibrous nanosilica oxynitrides with various nitrogen contents (KCC-1) using DNP-enhanced ^{15}N NMR while the samples were impregnated with bTbK in TCE. The reduction of catalytic activity of KCC-1 upon preparation at higher nitridation temperatures was shown to correlate with the disappearance of primary amine sites and the formation of secondary amines [432].

7.3.3. Impregnated microcrystals

Van der Wel et al. demonstrated that microscopic dispersions of insoluble biomolecular assemblies can be hyperpolarized in a glycerol/water mixture doped with PA [258]. This concept had been extended by Rossini et al. towards microcrystalline solids that are soluble in aqueous glass-forming agents but can be dispersed as a solid in hydrophobic organic solvents. This was first demonstrated on powdered microcrystalline solids of small molecules such as glucose, sulfathiazole, and paracetamol that have been impregnated with bCTbK in tetrabromoethane [138]. Signal enhancements on the order of 100 were obtained, which allowed for the rapid acquisition of ^{13}C–^{13}C correlation spectra in natural abundance. Furthermore, it was shown that the analysis of DNP enhancement factors and polarization dynamics can be directly used in order to obtain information about the crystal grain size due to rate-limiting spin diffusion through the crystal bulk [138], a concept that has also been applied to spherical silicon nanoparticles [257].

This impregnation technique has proven extremely valuable for the investigation of pharmaceutical formulations in order to assess the quality of the distribution of the API [431]. Furthermore, the sensitivity gain by DNP has allowed the extraction of quantitative structural constraints for organic powders at natural isotopic abundance by means of NMR crystallography which has been first demonstrated by Viel and co-workers [433]. Märker et al. have extended this approach for the crystal structure determination of molecular assemblies [151]. In particular, by avoiding dipolar truncation [376] in compounds in natural abundance, quantification of distances of up to 7 Å between pairs of ^{13}C allowed for the identification of π-stacking in (nano-)self-assembled cyclic dipeptides [374]. In another demonstration, the structure elucidation of a complex organic framework has been supported by DNP-enhanced NMR crystallography [434].

7.4. Extending the NMR toolkit by DNP methods

Quadrupolar nuclei (see Table 1) often pose as a problem for solid-state NMR when the quadrupole interactions are large. In many cases, even the central transition of nuclei with half-integer spin quantum number experiences a second-order effect that can lead to inhomogeneous broadening with effective line widths that can be much larger than the MAS frequency. In the same vein, nuclei with I = 1/2, but featuring a rather large chemical shift anisotropy, can share similar problems with quadrupolar nuclei such as low sensitivity due to a large resonance dispersion and insufficient excitation/detection bandwidth. Combined with small gyromagnetic ratios and/or a low natural abundance of the nuclear species, the strongly reduced NMR sensitivity significantly limits the application of conventional NMR techniques. For this reason, DNP is a powerful method for the investigation of quadrupolar nuclei.

Table 1
List of selected NMR-active nuclei.

Isotope	Spin S	Gyromagnetic ratio $\gamma/2\pi$ [MHz T^{-1}]	Quadrupole moment Q [fm^2]	Abundance [%]
^{1}H	1/2	42.576	–	~100
^{2}H	1	6.536	0.286	0.01
^{13}C	1/2	10.708	–	1.07
^{14}N	1	3.078	2.044	99.6
^{15}N	1/2	4.317	–	0.37
^{17}O	5/2	5.774	−2.56	0.038
^{27}Al	5/2	11.103	14.66	100
^{29}Si	1/2	8.466	–	4.68
^{35}Cl	3/2	4.177	−8.17	75.8
^{43}Ca	7/2	2.869	−4.08	0.14
^{51}V	7/2	11.213	−4.3	99.8
^{59}Co	7/2	10.077	+42	100
^{119}Sn	1/2	15.966	–	8.59
^{195}Pt	1/2	9.292	–	33.8
^{207}Pb	1/2	9.034	–	22.1

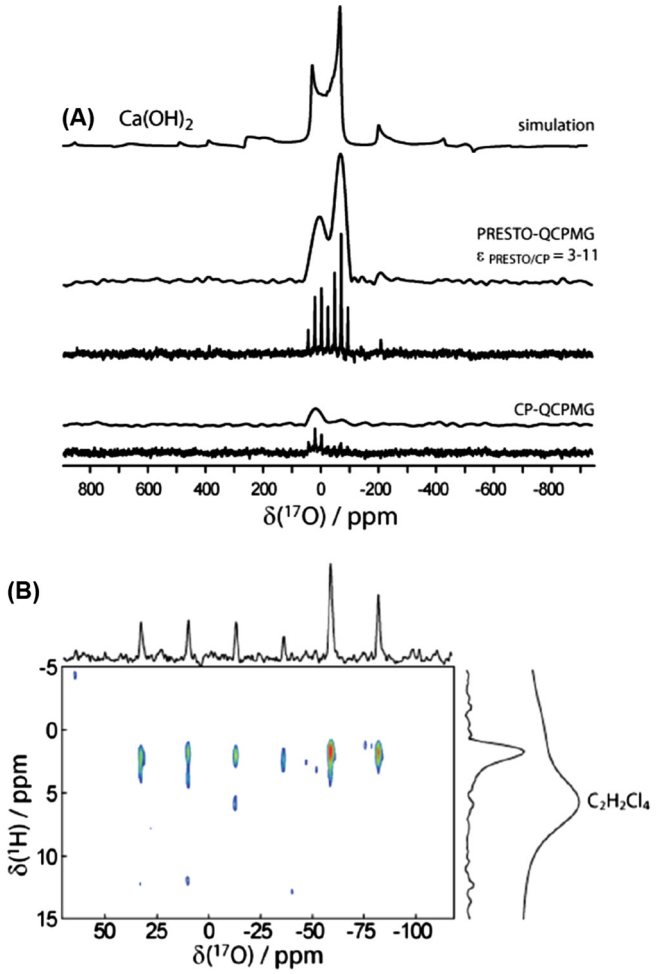

Fig. 66. (A) DNP-enhanced ^{17}O MAS NMR spectra of $Ca(OH)_2$ in natural abundance, acquired using CP-QCPMG (bottom) and PRESTO-QCPMG schemes (middle), as well as simulations of the PRESTO MAS spectra (top). (B) DNP-enhanced ^{1}H–^{17}O MAS PRESTO QCPMG-HETCOR NMR spectra acquired in 4.5 h. Projections along the ^{1}H dimension show that polarization is transferred mainly from the hydroxyl proton and not the solvent. Figure adapted from [437] with permission.

7.4.1. DNP of half-integer spin quadrupolar nuclei

7.4.1.1. ^{17}O (I = 5/2) NMR. ^{17}O is a rather challenging nucleus due to its relatively large quadrupolar moment, small gyromagnetic ratio, and particularly low natural abundance (see Table 1). Nevertheless, the large chemical shift range and quadrupole coupling tensor can yield important information about the local environment of oxygen. Indirect and direct DNP of ^{17}O has first been demonstrated by Michaelis et al. on $H_2{}^{17}O$ in the glycerol/water matrix or on small molecules, while in all cases ^{17}O was partially enriched [236,435]. Shortly afterwards, Blanc et al. extended the method for detection of ^{17}O in natural isotopic abundance within the surface and subsurface sites of inorganic oxides and hydroxides [436].

Later, Perras et al. demonstrated the applicability of the PRESTO technique which can improve the sensitivity of ^{17}O DNP-SENS even further (Fig. 66). This technique is an alternative approach for the direct transfer of polarization from a spin-1/2 to a quadrupolar nucleus for DNP applications. PRESTO was used to distinguish between hydrogen-bonded and lone ^{17}O sites on the surface of the silica gels. Its use enabled undistorted line shape measurements, 2D ^{1}H–^{17}O HETCOR NMR spectra, and accurate internuclear distance measurements [437]. They also demonstrated that PRESTO provides several advantages over conventional CP for a number of different quadrupolar nuclei, including ^{11}B, ^{23}Na, and ^{27}Al [438].

7.4.1.2. ^{27}Al (I = 5/2) NMR. The observation of homo- and heteronuclear proximities involving ^{27}Al is particularly challenging if diluted species such as surface sites or defects are studied. However, DNP enhancement compensates for the low sensitivity as well as for the small efficiency of cross polarization and dipolar recoupling due to the presence of the quadrupole interaction. This is a prerequisite for more sophisticated ^{27}Al–^{27}Al correlation experiments that allow for probing spatial proximities and local environment. Thus, the local coordination sphere of ^{27}Al sites at the surface of the γ-alumina nanoparticles or mesoporous γ-alumina has been successfully probed using standard techniques for high-resolution NMR of bulk quadrupolar nuclei like MQ-MAS [439–441]. As shown in Fig. 67, 2D homonuclear dipolar correlation experiments were utilized to identify penta-coordinated Al sites that act as bridging units between interfacial tetra- and hexa-coordinated Al at the surface of mesoporous γ-alumina [440]. In these studies, spatial information is obtained by exploiting the fact that ^{1}H are located exclusively in hydroxyl groups at the surface. In addition to that, Lee et al. confirmed that penta coordinated Al^{3+} ions are only present in this first surface layer by utilization of indirect DNP *via* ^{1}H–^{27}Al CP [441].

Furthermore, Pourpoint et al. reported the first observation of ^{27}Al–^{13}C proximities in Al-based MOFs impregnated with TOTAPOL using advanced NMR methods, such as dipolar-mediated HMQC (D-HMQC) and symmetry-based RESPDOR (S-RESPDOR), combined

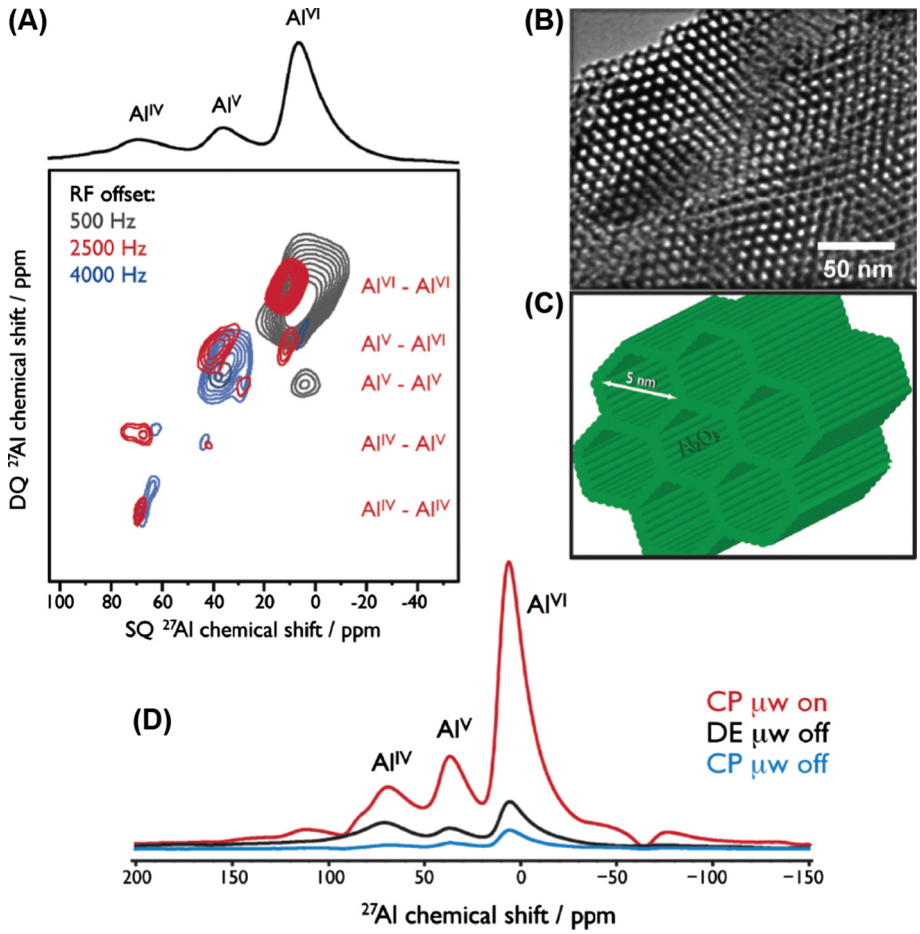

Fig. 67. (A) DNP-enhanced, interface-selective DQ–SQ ^{27}Al homonuclear dipolar correlation spectra of mesoporous alumina. (B) Transmission electron micrograph and (C) schematic representation of ordered hexagonal mesoporous alumina. (D) ^{27}Al NMR spectra of this sample. Figure adapted from [440] with permission.

with a frequency splitter so that the very similar Larmor frequencies of ^{27}Al and ^{13}C can be tuned simultaneously. EPR and DNP-enhanced NMR spectroscopy could prove that TOTAPOL enters the cavities of MOFs within a short timescale of ~minutes even though these cavities are smaller than 0.88 nm [442]. They also investigated the complexity of a geological material using ^{27}Al and ^{13}C DNP NMR. The proximity between the aluminum ions and dissolved organic matter (DOM) from the Kochechum River (Central Siberia) was studied. The DNP sample was prepared by impregnating lyophilized DOM powder with a solution of 10 mM AMUPol in d_6-DMSO/D_2O/H_2O. The DNP-enhanced NMR spectra enabled the detection of proximities between the ^{27}Al and ^{13}C nuclei present in the DOM. They showed that ~8% of the carboxylate groups observed by NMR are connected to the Al^{3+} ions in the DOM sample and that aluminum ions exhibit a tetrahedral environment [443].

The practicality of targeted DNP characterization by varying the functional side groups of mono-radicals was demonstrated by Lund et al. in a systematic study of ^{27}Al direct-DNP-enhanced solid-state NMR on surface-exposed acid sites of mesoporous alumina–silica (Al-SBA-15). By employing 4-amino TEMPO that is attracted to the negatively charged surface sites of Al-SBA-15 in its protonated form, a ^{27}Al signal enhancement factor of 13 was obtained. This was compared to $\varepsilon = 3 - 4$ from other—neutral or negatively charged—mono-radicals that do not adsorb as strongly to Al-SBA-15. The differences in enhancement factors have been attributed to the local concentrations of the spin probes and their proximity to ^{27}Al on the surface [357].

7.4.1.3. ^{35}Cl (I = 3/2) NMR. Hirsh et al. demonstrated DNP-enhanced ^{1}H–^{35}Cl broadband adiabatic inversion cross polarization (BRAIN-CP) experiments for the detection of APIs. In order to benefit from the significantly larger DNP enhancements under MAS while avoiding the acquisition of spinning side bands within the wideline ^{35}Cl NMR powder pattern, they have applied a technique called spinning-on spinning-off (SOSO) acquisition. During the polarization delay, MAS was applied for efficient DNP and rotation is stopped shortly before acquisition. This provided for an extra 2-fold intensity gain compared with purely static experimental DNP conditions. By impregnation of APIs with 15 mM TEKPol in TCE or 1,3-dibromobutane an overall DNP enhancement of 110 was obtained. This allowed for the molecular-level characterization of APIs in their bulk forms as well as in dosage forms with low Cl contents (0.45 wt%) [444].

7.4.1.4. ^{43}Ca (I = 7/2) NMR. Even though calcium is a very interesting and highly relevant element, its only NMR-active stable isotope, ^{43}Ca, is extremely insensitive due to a combination of effects (see Table 1). Very recently, Lee et al. reported the first DNP application to ^{43}Ca NMR. They demonstrated the differentiation of calcium environments in surface and core species of carbonated hydroxyapatite nanoparticles using ^{43}Ca MAS DNP NMR in a short experimental time. They succeeded to record ^{1}H–^{43}Ca and ^{1}H–^{13}C 2D correlation experiments at the very small natural isotopic abundance of only 0.14%. The analysis revealed that surface species (Ca^{2+} and carbonates) could be distinguished from the core entities [445].

7.4.1.5. ^{51}V (I = 7/2) NMR. Applications of DNP by directly and indirectly enhancing ^{51}V signals on vanadyl sulfate samples under MAS conditions were reported by Perez Linde et al. DNP-enhanced ^{51}V NMR spectra of vanadium species dissolved together with TOTAPOL in a glycerol/water mixture were recorded as a function of pH. The pH-dependent presence of vanadyl radicals was investigated and it was observed that at pH higher than 11, ^{1}H can be most efficiently hyperpolarized by TOTAPOL and the enhanced polarization can be transferred to ^{51}V nuclei through CP. Most interestingly, the presence of vanadyl sulfate resulted in a larger ^{1}H enhancement factor as compared to solutions containing only TOTAPOL. This effect was attributed to the interactions between paramagnetic vanadyl species and the PA [446].

7.4.1.6. ^{59}Co (I = 7/2) NMR. ^{59}Co has been directly hyperpolarized by employing Cr^{3+} as PA by Corzilius et al. The paramagnetic Cr^{3+} has been used to isostructurally substitute the diamagnetic Co^{3+} in crystalline $[Co(en)_3Cl_3]_2{\cdot}NaCl{\cdot}6\ H_2O$ (see Section 5.3.3 and Fig. 45 for details on the sample system). A ^{59}Co DNP enhancement factor of up to 16 was reported. This approach demonstrated the general feasibility of MAS DNP using PAs which have been doped into the host crystalline lattice without inducing structural changes [302].

7.4.2. DNP of integer spin quadrupolar nuclei

7.4.2.1. ^{2}H (I = 1) NMR. Despite carrying an integer spin, the quadrupole moment of ^{2}H is particularly small which results in a relatively narrow NMR spectrum. The concept of direct ^{2}H MAS DNP on isotope-labeled compounds was first demonstrated by Maly et al. [147].

Recently, DNP-enhanced ^{1}H–^{2}H CPMAS of organic solids in natural abundance, such as histidine hydrochloride monohydrate, glycylglycine and theophylline, have been performed by Rossini et al. at 9.4 T and 100 K [353 1803]. Samples were impregnated with TEKPol in TCE; indirect DNP allowed for the acquisition of ^{2}H CPMAS spectra within 1 h. The resolution of the acquired ^{2}H spectra was comparable to that of ^{1}H spectra obtained with state-of-the-art homonuclear decoupling techniques and provided direct access to hydrogen chemical shifts and ^{2}H EFG (electric field gradient) tensor parameters.

7.4.2.2. ^{14}N (I = 1) NMR. ^{14}N poses as an intriguing but challenging target for NMR studies due to its large natural abundance and relevance especially in biological context while at the same time suffering from an integer nuclear spin quantum number that does not give rise to a narrow CT. Although it shares the latter property with ^{2}H, the quadrupole moment of ^{14}N is about one order of magnitude larger which makes direct detection extremely difficult.

Indirect detection of ^{14}N *via* single-quantum correlation (SQC) or double-quantum correlation (DQC) with an $I = 1/2$ nucleus (*e.g.*, ^{13}C) in an HMQC-type experiment can yield correlation spectra under MAS with rather narrow lines [447,448]. Alternatively, excitation of the "forbidden" $\Delta m_I = \pm 2$ transition at twice the nuclear Larmor frequency results in a narrow overtone (OT) NMR spectrum not influenced by the nuclear quadrupole interaction to first order [449,450]. This method has also been demonstrated in combination with MAS [451,452]. However, both techniques typically suffer from low efficiency and therefore DNP is an excellent method to counter that problem.

Indirect ^{14}N detection by HMQC with DNP-enhancement has been demonstrated by Vitzthum et al. [150], based on experiments introduced by the same group earlier without DNP [453]. Indirect ^{13}C DNP enhancement with factors of ~40 were achieved on U-^{13}C-proline dissolved in glycerol/water together with 20 mM TOTAPOL. This allowed for the acquisition of ^{13}C–^{14}N correlation spectra within a few hours while experimental time on the order of at least one week were required without DNP. The detection of DNP-enhanced $^{14}N^{OT}$ MAS NMR spectra has been presented by Rossini et al. Indirect ^{14}N DNP enhancements of around two orders of magnitude were achieved on model amino acids which were impregnated with 15 mM TEKPol in TCE. CP transfer from hyperpolarized ^{1}H nuclei directly to the ^{14}N overtone transition was demonstrated using a standard pulse sequence. It was also shown that DNP enhancement enables ^{1}H–$^{14}N^{OT}$ HETCOR and ^{13}C–$^{14}N^{OT}$ HMQC spectra to be obtained from samples in natural ^{13}C abundance in a short time, proving that such correlation experiments can be used for observing H—N and C—N correlations in completely unlabeled samples [454].

7.4.3. Wideline NMR (I = ½)

7.4.3.1. ^{119}Sn NMR. Gunther et al. demonstrated the first DNP application to ^{119}Sn NMR for characterizing microporous zeolites containing ~2 wt% of natural abundance Sn in the catalytically-active Sn-β. They used TOTAPOL, bTbK, bCTbK, and SPIROPOL (*i.e.*, bTbtK-py) biradicals as PAs and obtained enhancement factors as large as 75 with bCTbK for indirect DNP of ^{119}Sn which allowed the characterization of Sn-β by more than ~2 orders of magnitude reduced acquisition times [455]. ^{119}Sn DNP-SENS has also been applied to allyltributylstannane [$Bu_3Sn(allyl)$] to detect the minor surface species [$(RSiO)_2SnBu_2$], present in low density (<0.1 nm^{-2}). Signal enhancements of 56 for ^{119}Sn in combination with CPMG enabled the acquisition of a ^{1}H–^{119}Sn HETCOR spectrum in less than 6 h and showed the correlations between the two tin resonances and the protons of the butyl group [456].

Protesescu et al. showed that DNP-SENS selectively enhanced the weak ^{119}Sn NMR signal of the natural oxide coating as well as of capping ligands on colloidal Sn/SnO_x nanoparticles (NPs). By combining DNP-SENS with Mössbauer and X-ray absorption spectroscopies, they have determined a $Sn/SnO/SnO_2$ core/shell/shell-structure of the Sn-NPs. They have also shown that DNP-SENS experiments can be carried out for hydrophilic (ion-capped) surfaces and hydrophobic functionalities of surfaces capped by ligands with long hydrocarbon chains in various solvents [457]. At the same time, Wolf et al. presented framework Sn(IV)-active sites in an octahedral environment which are bound to three or four siloxy groups of a Sn-β zeolite framework using DNP-SENS. It was concluded that there are two active sites of Sn(IV) present which have distinct NMR signatures: one site where two water molecules are coordinated to Sn (closed site), and another site where one of the water molecules has opened one of the Sn—O—Si bridges (open site) [458]. Later, they also studied the morphology and atomic-level structure of Sn-β zeolites using DNP-enhanced NMR [459].

7.4.3.2. ^{195}Pt NMR. Recently, Kobayashi et al. have demonstrated that DNP enhancement can be used in combination with BRAIN-CP from ^{1}H and WURST-CPMG detection of wideline ^{195}Pt solid-state NMR. The breadth of the ^{195}Pt spectra reaches ~10,000 ppm, therefore a combination of several sensitivity-enhancing methods was necessary to characterize the atomic-scale geometry of the Pt^{2+} ions coordinated by the linkers in MOFs. It was possible to separate the signals from cis- and trans-coordinated atomic Pt^{2+} species supported on the UiO-66-NH_2 MOF in the DNP-enhanced wideline NMR spectra (Fig. 68). Furthermore, the kinetic effects in the formation of Pt^{2+} complexes and the thermodynamic effects in their reduction to nanoparticles were also studied [460].

7.4.3.3. ^{207}Pb NMR. DNP has been used by Kobayashi et al. to enhance the wideline ^{207}Pb solid-state NMR spectra of lead white [lead carbonate, 2 $PbCO_3{\cdot}Pb(OH)_2$], a model lead soap, and an aged lead-based paint film. The samples were impregnated with 16 mM TEKPol in a TCE/d_4-methanol (96:4) mixture. They performed DNP-enhanced static wideline ^{1}H–^{207}Pb BRAIN-CP and ^{1}H–^{207}Pb CPMAS

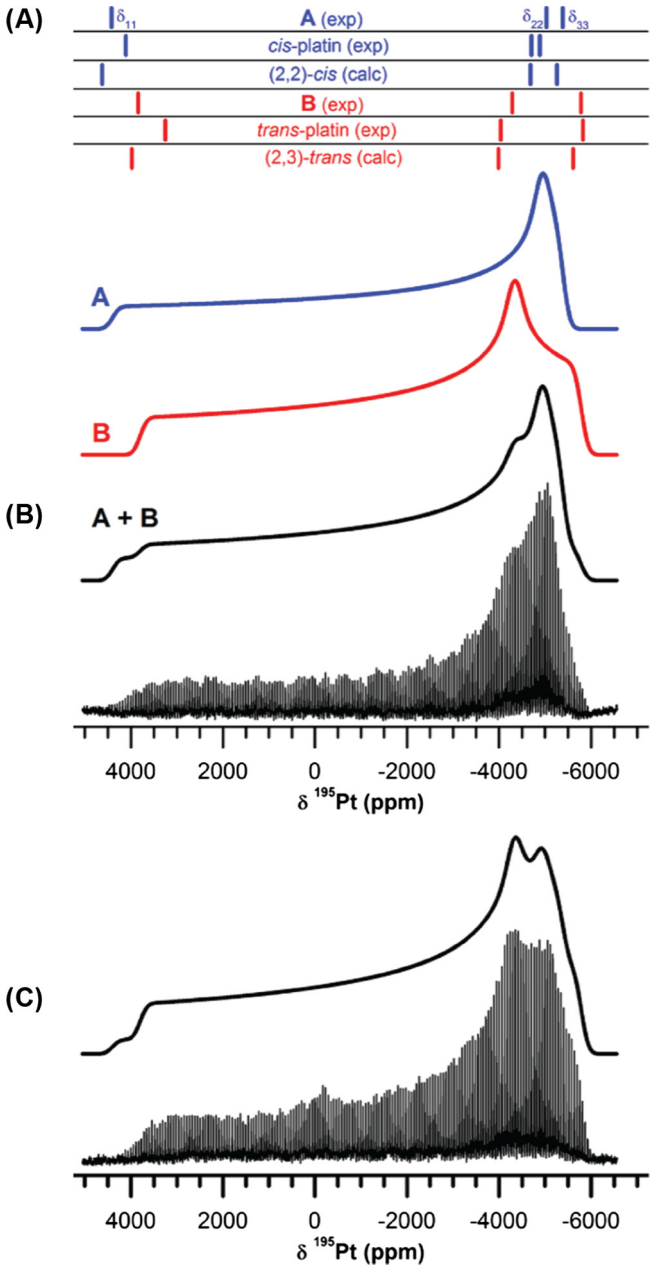

Fig. 68. (A) Simulated powder patterns for the cis and trans sites of Pt^{2+}/UiO-66-NH_2. (B-C) DNP-enhanced wideline ^{195}Pt BRAIN-CP spectra (B) prior and (C) post reductive treatment for 30 min at 150 °C in 10% H_2/Ar. The spectra consist of 14 subspectra acquired in 7.5 h. Figure adapted from [460] with permission.

experiments at a temperature of ~110 K, and ^{207}Pb WURST-CPMG experiments at temperatures ranging from 110 K to 308 K. By applying the above-mentioned set of methods and utilizing selective DNP enhancements of certain chemical components it was possible to disentangle the spectral contributions within the complex mixture. Thus, the formation of a lead soap upon aging could be detected within the paint film and the degradation mechanism of lead pigments in such films could be elucidated [461].

8. Conclusions

We have presented a comprehensive review about the theoretical concepts as well as instrumental and methodological progress in solid-state DNP NMR. Based on the continuously improving theoretical understanding of the underlying microscopic processes and driven by interdisciplinary efforts—such as the development of advanced instrumentation, tailored polarizing agents and optimized sample preparation techniques—not only a tremendous boost in the available maximum enhancement factors but also a much broader general applicability has been reported over the past years. This progress allows for applications of hyperpolarization techniques to various problems in material science and biomolecular solid-state NMR. In this vein, DNP has enabled several investigations of structural properties of materials that would not have been possible without the outstanding gain in sensitivity due to signal enhancement by DNP.

Still, further improvements are to be expected in the next few years. DNP has become the driving force for the development of high-power high-frequency μw sources. Thus, promising developments on frequency-tunability of such sources are expected to simplify the experimental setup. The ongoing quest for sources operating at even higher frequencies is likely to extend the current limitations on the external magnetic fields faced by DNP. Furthermore, several revolutionary techniques that are still in the development/concept phase and have not been covered in this review might prove highly useful in the near future. Such developments include time-domain/pulsed DNP [166,310,462–464] potentially in combination with gyro amplifiers [465,466], frequency-swept techniques [467–469], electron decoupling [74,195,470], DNP of oriented membranes [471,472], or micro-MAS compatible with μw resonating structures [473]. Furthermore, temperature-jump [474–476] or rapid-melt techniques [477,478] which are both based on solid-state DNP could become applicable to signal enhancement in solution NMR.

Initially aimed to improve sensitivity on biomolecules, high-field MAS DNP demonstrated its versatility, in particular in applications to problems in material science. NMR investigations of low-density species, as well as of "challenging" nuclei with low gyromagnetic ratios, low natural isotopic abundance and/or large anisotropic interactions (chemical-shift anisotropy or quadrupolar interaction) were performed in a reasonable experimental time. Also, several methodological developments such as correlation experiments of heteronuclei at low natural isotopic abundance significantly extended the toolkit of conventional solid-sate NMR.

Even though the full potential of DNP in biomolecular NMR spectroscopy has not yet been reached and mostly specialized questions are addressed at the moment, recent advances on tackling the resolution issue show promising results. Among these are improvements in sample preparation which allow for higher sample filling factors and reduce line-broadening effects due to the protein glass transition. Recent progress in localized/targeted DNP studies offers perspectives for further investigations of structural properties of selected species. Not only additional PRE restraints can be determined in such an approach; potentially, site-specific DNP enhancement might also provide quantitative structural information in the near future. Furthermore, the resolution issue can be tackled by multidimensional NMR experiments that become possible with large enhancement factors as well as DNP-accessible magnetic fields greater than 18 T.

Acknowledgments

This work has been funded by the Deutsche Forschungsgemeinschaft through Emmy Noether grant CO802/2-1. BC is greatly indebted to R. G. Griffin for continuous inspiration, outstanding support, and transfer of knowledge; furthermore, ideas exchanged during inspiring discussions with many colleagues, regarding scientific or technical matters, have influenced this article in a direct or indirect way. In that regard, BC thanks in particular D. Akhmetzyanov, L. B. Andreas, A. B. Barnes, M. J. Bayro,

J. Becker-Baldus, J. A. Bryant, T. V. Can, M. A. Caporini, E. Daviso, G. T. Debelouchina, R. DeRocher, M. T. Eddy, A. Feintuch, C. Glaubitz, D. Goldfarb, Y. Hovav, S. Jannin, I. Kuprov, D. Lee, M. Lelli, A. Lesage, M. L. Mak-Jurkauskas, T. Maly, J. Mao, J. Mathies, Y. Matsuki, F. Mentink-Vigier, V. K. Michaelis, E. A. Nanni, Q. Z. Ni, G. Pintacuda, T. Prisner, E. Ravera, D. Ruben, H. Schwalbe, J. R. Sirigiri, D. Shimon, A. A. Smith, A. Thakkar, K. Thurber, A. C. Torrezan, S. Vega, J. J. Walish, and P. P. Woskov. ASLT acknowledges O. Lafon for the inspiration, support and guidance, G. Buntkowsky for constant high support, and D. Carnevale, A. J. Perez Linde for useful discussions and technical assistance. MK expresses sincere gratitude towards G. De Paëpe and D. Lee for guidance, encouragement and continued support.

References

[1] I.J. Lowe, Free induction decays of rotating solids, Phys. Rev. Lett. 2 (1959) 285–287.
[2] E.R. Andrew, A. Bradbury, R.G. Eades, Removal of dipolar broadening of nuclear magnetic resonance spectra of solids by specimen rotation, Nature 183 (1959) 1802–1803.
[3] Y. Ishii, C-13-C-13 dipolar recoupling under very fast magic angle spinning in solid-state nuclear magnetic resonance: applications to distance measurements, spectral assignments, and high-throughput secondary-structure determination, J. Chem. Phys. 114 (2001) 8473–8483.
[4] M.H. Levitt, Symmetry in the design of NMR multiple-pulse sequences, J. Chem. Phys. 128 (2008) 052205.
[5] I. Scholz, J.D. van Beek, M. Ernst, Operator-based Floquet theory in solid-state NMR, Solid State Nucl. Magn. Reson. 37 (2010) 39–59.
[6] A. Schuetz, C. Wasmer, B. Habenstein, R. Verel, J. Greenwald, R. Riek, A. Bockmann, B.H. Meier, Protocols for the sequential solid-state NMR spectroscopic assignment of a uniformly labeled 25 kDa protein: HET-s(1–227), ChemBioChem 11 (2010) 1543–1551.
[7] G. De Paepe, Dipolar recoupling in magic angle spinning solid-state nuclear magnetic resonance, Annu. Rev. Phys. Chem. 63 (63) (2012) 661–684.
[8] T. Gullion, J. Schaefer, Rotational-echo double-resonance NMR, J. Magn. Reson. 81 (1989) 196–200.
[9] P. Robyr, B.H. Meier, R.R. Ernst, Radio-frequency-driven nuclear-spin diffusion in solids, Chem. Phys. Lett. 162 (1989) 417–423.
[10] C. Wasmer, A. Lange, H. Van Melckebeke, A.B. Siemer, R. Riek, B.H. Meier, Amyloid fibrils of the HET-s(218–289) prion form a beta solenoid with a triangular hydrophobic core, Science 319 (2008) 1523–1526.
[11] A.K. Schutz, T. Vagt, M. Huber, O.Y. Ovchinnikova, R. Cadalbert, J. Wall, P. Guntert, A. Bockmann, R. Glockshuber, B.H. Meier, Atomic-resolution three-dimensional structure of amyloid beta fibrils bearing the Osaka mutation, Angew. Chem. Int. Ed. 54 (2015) 331–335.
[12] J.X. Lu, W. Qiang, W.M. Yau, C.D. Schwieters, S.C. Meredith, R. Tycko, Molecular structure of beta-amyloid fibrils in Alzheimer's disease brain tissue, Cell 154 (2013) 1257–1268.
[13] M.T. Colvin, R. Silvers, Q.Z. Ni, T.V. Can, I. Sergeyev, M. Rosay, K.J. Donovan, B. Michael, J. Wall, S. Linse, R.G. Griffin, Atomic resolution structure of monomorphic Aβ42 amyloid fibrils, J. Am. Chem. Soc. 138 (2016) 9663–9674.
[14] M.A. Walti, F. Ravotti, H. Arai, C.G. Glabe, J.S. Wall, A. Bockmann, P. Guntert, B. H. Meier, R. Riek, Atomic-resolution structure of a disease-relevant A beta(1–42) amyloid fibril, Proc. Natl. Acad. Sci. U.S.A. 113 (2016) E4976–E4984.
[15] C.M. Quinn, T. Polenova, Structural biology of supramolecular assemblies by magic-angle spinning NMR spectroscopy, Q. Rev. Biophys. 50 (2017) e1.
[16] S.A. Shahid, B. Bardiaux, W.T. Franks, L. Krabben, M. Habeck, B.J. van Rossum, D. Linke, Membrane-protein structure determination by solid-state NMR spectroscopy of microcrystals, Nat. Methods 9 (2012), 1212-U1119.
[17] S.L. Wang, R.A. Munro, L.C. Shi, I. Kawamura, T. Okitsu, A. Wada, S.Y. Kim, K.H. Jung, L.S. Brown, V. Ladizhansky, Solid-state NMR spectroscopy structure determination of a lipid-embedded heptahelical membrane protein, Nat. Methods 10 (2013) 1007–1012.
[18] E. Daviso, M. Belenky, R.G. Griffin, J. Herzfeld, Gas vesicles across kingdoms: a comparative solid-state nuclear magnetic resonance study, J. Mol. Microbiol. Biotechnol. 23 (2013) 281–289.
[19] Z. Serber, L. Corsini, F. Durst, V. Dotsch, In-cell NMR spectroscopy, Methods Enzymol. 394 (2005) 17–41.
[20] P. Selenko, G. Wagner, Looking into live cells with in-cell NMR spectroscopy, J. Struct. Biol. 158 (2007) 244–253.
[21] L. Barbieri, E. Luchinat, L. Banci, Characterization of proteins by in-cell NMR spectroscopy in cultured mammalian cells, Nat. Protoc. 11 (2016) 1101–1111.
[22] F. Deng, J. Yang, C. Ye, Solid state NMR characterization of solid surface of heterogeneous catalysts, in: G.A. Webb (Ed.), Modern Magnetic Resonance, Springer, Netherlands, Dordrecht, 2006, pp. 205–211.
[23] A.S. Lilly Thankamony, A. Krishnan, M. Sankar, N.K. Kala Raj, P. Manikandan, P. R. Rajamohanan, T.G. Ajithkumar, Immobilization of phosphotungstic acid (PTA) on imidazole functionalized silica: evidence for the nature of PTA binding by solid state NMR and reaction studies, J. Phys. Chem. C 113 (2009) 21114–21122.
[24] T. Narasimhaswamy, M. Monette, D.K. Lee, A. Ramamoorthy, Solid-state NMR characterization and determination of the orientational order of a nematogen, J. Phys. Chem. B 109 (2005) 19696–19703.
[25] N.M. Washton, S.L. Brantley, K.T. Mueller, Probing the molecular-level control of aluminosilicate dissolution: a sensitive solid-state NMR proxy for reactive surface area, Geochim. Cosmochim. Acta 72 (2008) 5949–5961.
[26] T.-J. Park, S.H. Kim, G.H. Li, C.G. Cho, Y. Kim, ^{31}P solid-state NMR Characterization of poly(vinylphosphate-black-styrene) for DMFC membrane, Macromol. Symp. 249–250 (2007) 466–471.
[27] G.J. Rees, S.T. Orr, L.O. Barrett, J.M. Fisher, J. Houghton, G.H. Spikes, B.R.C. Theobald, D. Thompsett, M.E. Smith, J.V. Hanna, Characterisation of platinum-based fuel cell catalyst materials using ^{195}Pt wideline solid state NMR, Phys. Chem. Chem. Phys. 15 (2013) 17195–17207.
[28] T. Komatsu, J. Kikuchi, Selective signal detection in solid-state NMR using rotor-synchronized dipolar dephasing for the analysis of hemicellulose in lignocellulosic biomass, J. Phys. Chem. Lett. 4 (2013) 2279–2283.
[29] Y. Pu, B. Hallac, A.J. Ragauskas, Plant biomass characterization: application of solution- and solid-state NMR spectroscopy, in: C.E. Wyman (Ed.), Aqueous Pretreatment of Plant Biomass for Biological and Chemical Conversion to Fuels and Chemicals, John Wiley & Sons, Ltd, 2013, pp. 369–390.
[30] R.L. Johnson, K. Schmidt-Rohr, Quantitative solid-state ^{13}C NMR with signal enhancement by multiple cross polarization, J. Magn. Reson. 239 (2014) 44–49.
[31] O.D. Bernardinelli, M.A. Lima, C.A. Rezende, I. Polikarpov, E.R. deAzevedo, Quantitative ^{13}C MultiCP solid-state NMR as a tool for evaluation of cellulose crystallinity index measured directly inside sugarcane biomass, Biotechnol. Biofuels 8 (2015) 110.
[32] C. Keeler, G.E. Maciel, Quantitation in the solid-state ^{13}C NMR analysis of soil and organic soil fractions, Anal. Chem. 75 (2003) 2421–2432.
[33] N.J. Mathers, Z. Xu, Solid-state ^{13}C NMR spectroscopy: characterization of soil organic matter under two contrasting residue management regimes in a 2-year-old pine plantation of subtropical Australia, Geoderma 114 (2003) 19–31.
[34] J. Mao, X. Kong, K. Schmidt-Rohr, J.J. Pignatello, E.M. Perdue, Advanced solid-state NMR characterization of marine dissolved organic matter isolated using the coupled reverse osmosis/electrodialysis method, Environ. Sci. Technol. 46 (2012) 5806–5814.
[35] A.P. Deshmukh, B. Chefetz, P.G. Hatcher, Characterization of organic matter in pristine and contaminated coastal marine sediments using solid-state ^{13}C NMR, pyrolytic and thermochemolytic methods: a case study in the San Diego harbor area, Chemosphere 45 (2001) 1007–1022.
[36] P.A. Mirau, Solid-state NMR characterization of polymer interfaces, in: G.A. Webb (Ed.), Modern Magnetic Resonance, Springer, Netherlands, Dordrecht, 2006, pp. 575–581.
[37] K.M. Eldho, P.R. Rajamohanan, R. Anto, N. Bulakh, A.K. Lele, T.G. Ajithkumar, Insights into the molecular dynamics in polysulfone polymers from ^{13}C solid-state NMR experiments, J. Phys. Chem. B 119 (2015) 11287–11294.
[38] Y.-L. Hong, T. Miyoshi, Solid-state NMR characterization of polymer chain structure and dynamics in polymer crystals, in: S. Palsule (Ed.), Encyclopedia of Polymers and Composites, Springer, Berlin, Heidelberg, 2013, pp. 1–17.
[39] J.B. Murdoch, J.F. Stebbins, I.S.E. Carmichael, High-resolution ^{29}Si NMR study of silicate and aluminosilicate glasses: the effect of network-modifying cations, Am. Miner. 70 (1985) 332–343.
[40] H. Eckert, J.P. Yesinowski, L.A. Silver, E.M. Stolper, Water in silicate glasses: quantification and structural studies by ^{1}H solid echo and MAS-NMR methods, J. Phys. Chem. 92 (1988) 2055–2064.
[41] C. Le Losq, B.O. Mysen, G.D. Cody, Water and magmas: insights about the water solution mechanisms in alkali silicate melts from infrared, Raman, and ^{29}Si solid-state NMR spectroscopies, Prog. Earth Planet. Sci. 2 (2015) 22.
[42] N. Baccile, G. Laurent, C. Bonhomme, P. Innocenzi, F. Babonneau, Solid-state NMR characterization of the surfactant–silica interface in templated silicas: acidic versus basic conditions, Chem. Mater. 19 (2007) 1343–1354.
[43] S. Abdulhussain, H. Breitzke, T. Ratajczyk, A. Grünberg, M. Srour, D. Arnaut, H. Weidler, U. Kunz, H.J. Kleebe, U. Bommerich, J. Bernarding, T. Gutmann, G. Buntkowsky, Synthesis, solid-state NMR characterization, and application for hydrogenation reactions of a novel Wilkinson's-type immobilized catalyst, Chem. – Eur. J. 20 (2014) 1159–1166.
[44] A.S. Cattaneo, C. Ferrara, A.M. Marculescu, F. Giannici, A. Martorana, P. Mustarelli, C. Tealdi, Solid-state NMR characterization of the structure and thermal stability of hybrid organic-inorganic compounds based on a $HLaNb_2O_7$ Dion-Jacobson layered perovskite, Phys. Chem. Chem. Phys. 18 (2016) 21903–21912.
[45] C. Bonhomme, C. Coelho, N. Baccile, C. Gervais, T. Azaïs, F. Babonneau, Advanced solid state NMR techniques for the characterization of sol–gel-derived materials, Acc. Chem. Res. 40 (2007) 738–746.
[46] F. Babonneau, C. Bonhomme, Solid-state NMR characterization of sol–gel materials: recent advances, in: D. Levy, M. Zayat (Eds.), The Sol-Gel Handbook, Wiley-VCH Verlag GmbH & Co. KGaA, 2015, pp. 651–672.
[47] S.E. Ashbrook, S. Sneddon, New methods and applications in solid-state NMR spectroscopy of quadrupolar nuclei, J. Am. Chem. Soc. 136 (2014) 15440–15456.
[48] A. Sutrisno, Y. Huang, Solid-state NMR: a powerful tool for characterization of metal–organic frameworks, Solid State Nucl. Magn. Reson. 49–50 (2013) 1–11.
[49] G. Mali, Looking into metal-organic frameworks with solid-state NMR Spectroscopy, in: F. Zafar, E. Sharmin (Eds.), Metal Organic Frameworks, 2016, http://dx.doi.org/10.5772/64134, ISBN 978-953-51-2663-8, Print ISBN 978-953-51-2662-1.

[50] S.R. Hartmann, E.L. Hahn, Nuclear double resonance in the rotating frame, Phys. Rev. 128 (1962) 2042–2053.
[51] V. Agarwal, S. Penzel, K. Szekely, R. Cadalbert, E. Testori, A. Oss, J. Past, A. Samoson, M. Ernst, A. Bockmann, B.H. Meier, De novo 3D structure determination from sub-milligram protein samples by solid-state 100 kHz MAS NMR spectroscopy, Angew. Chem. Int. Ed. Engl. 53 (2014) 12253–12256.
[52] L.B. Andreas, K. Jaudzems, J. Stanek, D. Lalli, A. Bertarello, T. Le Marchand, D.C. D. Paepe, S. Kotelovica, I. Akopjana, B. Knott, S. Wegner, F. Engelke, A. Lesage, L. Emsley, K. Tars, T. Herrmann, G. Pintacuda, Structure of fully protonated proteins by proton-detected magic-angle spinning NMR, Proc. Natl. Acad. Sci. U.S.A. 113 (2016) 9187–9192.
[53] S.B. Duckett, R.E. Mewis, Application of parahydrogen induced polarization techniques in NMR spectroscopy and imaging, Acc. Chem. Res. 45 (2012) 1247–1257.
[54] R.G. Lawler, Chemically induced dynamic nuclear polarization (CIDNP). II. Radical-pair model, Acc. Chem. Res. 5 (1972) 25–33.
[55] G.W. Thad, Fundamentals of spin-exchange optical pumping, J. Phys.: Conf. Ser. 294 (2011) 012001.
[56] A.W. Overhauser, Polarization of nuclei in metals, Phys. Rev. 92 (1953) 411–415.
[57] T.R. Carver, C.P. Slichter, Polarization of nuclear spins in metals, Phys. Rev. 92 (1953) 212–213.
[58] C.F. Hwang, B.A. Hasher, D.A. Hill, F. Markley, The use of chemically doped polystyrene as a polarized proton target material, Nucl. Instrum. Methods 51 (1967) 254–256.
[59] C.F. Hwang, D.A. Hill, New effect in dynamic polarization, Phys. Rev. Lett. 18 (1967) 110–112.
[60] C.F. Hwang, D.A. Hill, Phenomenological model for new effect in dynamic polarization, Phys. Rev. Lett. 19 (1967) 1011–1014.
[61] D.S. Wollan, Dynamic nuclear-polarization with an inhomogeneously broadened ESR line. 1. Theory, Phys. Rev. B 13 (1976) 3671–3685.
[62] D.S. Wollan, Dynamic nuclear-polarization with an inhomogeneously broadened ESR line. 2. Experiment, Phys. Rev. B 13 (1976) 3686–3696.
[63] R.A. Wind, M.J. Duijvestijn, C. van der Lugt, A. Manenschijn, J. Vriend, Applications of dynamic nuclear polarization in ^{13}C NMR in solids, Prog. Nucl. Magn. Reson. Spectrosc. 17 (1985) 33–67.
[64] M. Afeworki, J. Schaefer, Mechanism of DNP-enhanced polarization transfer across the interface of polycarbonate/polystyrene heterogeneous blends, Macromolecules 25 (1992) 4092–4096.
[65] J.H. Ardenkjaer-Larsen, On the present and future of dissolution-DNP, J. Magn. Reson. 264 (2016) 3–12.
[66] A. Bornet, S. Jannin, Optimizing dissolution dynamic nuclear polarization, J. Magn. Reson. 264 (2016) 13–21.
[67] F. Jähnig, G. Kwiatkowski, M. Ernst, Conceptual and instrumental progress in dissolution DNP, J. Magn. Reson. 264 (2016) 22–29.
[68] A. Comment, Dissolution DNP for in vivo preclinical studies, J. Magn. Reson. 264 (2016) 39–48.
[69] J. van Bentum, B. van Meerten, M. Sharma, A. Kentgens, Perspectives on DNP-enhanced NMR spectroscopy in solutions, J. Magn. Reson. 264 (2016) 59–67.
[70] M.D. Lingwood, S. Han, Solution-state dynamic nuclear polarization, in: A.W. Graham (Ed.), Annu Rep. NMR Spectrosc., Academic Press, 2011, pp. 83–126 (Chapter 3).
[71] E. Ravera, C. Luchinat, G. Parigi, Basic facts and perspectives of Overhauser DNP NMR, J. Magn. Reson. 264 (2016) 78–87.
[72] T. Prisner, V. Denysenkov, D. Sezer, Liquid state DNP at high magnetic fields: instrumentation, experimental results and atomistic modelling by molecular dynamics simulations, J. Magn. Reson. 264 (2016) 68–77.
[73] J.-H. Ardenkjaer-Larsen, G.S. Boebinger, A. Comment, S. Duckett, A.S. Edison, F. Engelke, C. Griesinger, R.G. Griffin, C. Hilty, H. Maeda, G. Parigi, T. Prisner, E. Ravera, J. van Bentum, S. Vega, A. Webb, C. Luchinat, H. Schwalbe, L. Frydman, Facing and overcoming sensitivity challenges in biomolecular NMR spectroscopy, Angew. Chem. Int. Ed. 54 (2015) 9162–9185.
[74] B. Corzilius, A.A. Smith, R.G. Griffin, Solid effect in magic angle spinning dynamic nuclear polarization, J. Chem. Phys. 137 (2012) 054201.
[75] F. Mentink-Vigier, Ü. Akbey, Y. Hovav, S. Vega, H. Oschkinat, A. Feintuch, Fast passage dynamic nuclear polarization on rotating solids, J. Magn. Reson. 224 (2012) 13–21.
[76] M. Abraham, M.A.H. McCausland, F.N.H. Robinson, Dynamic nuclear polarization, Phys. Rev. Lett. 2 (1959) 449–451.
[77] A.A. Smith, B. Corzilius, A.B. Barnes, T. Maly, R.G. Griffin, Solid effect dynamic nuclear polarization and polarization pathways, J. Chem. Phys. 136 (2012) 015101.
[78] J. Zhou, L. Li, H. Hu, B. Yang, Z. Dan, J. Qiu, J. Guo, F. Chen, C. Ye, Study of natural diamonds by dynamic nuclear polarization-enhanced ^{13}C nuclear magnetic resonance spectroscopy, Solid State Nucl. Magn. Reson. 3 (1994) 339–351.
[79] B. Yang, J. Zhou, H. Hu, L. Li, J. Qiu, J. Guo, P. He, J. Lu, C. Ye, Study of synthetic diamonds by dynamic nuclear polarization-enhanced ^{13}C nuclear magnetic resonance spectroscopy, Appl. Magn. Reson. 9 (1995) 379–388.
[80] K.N. Hu, G.T. Debelouchina, A.A. Smith, R.G. Griffin, Quantum mechanical theory of dynamic nuclear polarization in solid dielectrics, J. Chem. Phys. 134 (2011) 125105.
[81] Y. Hovav, A. Feintuch, S. Vega, Theoretical aspects of dynamic nuclear polarization in the solid state – the cross effect, J. Magn. Reson. 214 (2012) 29–41.
[82] V.K. Michaelis, A.A. Smith, B. Corzilius, O. Haze, T.M. Swager, R.G. Griffin, High-field ^{13}C dynamic nuclear polarization with a radical mixture, J. Am. Chem. Soc. 135 (2013) 2935–2938.
[83] K.R. Thurber, R. Tycko, Theory for cross effect dynamic nuclear polarization under magic-angle spinning in solid state nuclear magnetic resonance: the importance of level crossings, J. Chem. Phys. 137 (2012) 084508.
[84] K.R. Thurber, R. Tycko, Perturbation of nuclear spin polarizations in solid state NMR of nitroxide-doped samples by magic-angle spinning without microwaves, J. Chem. Phys. 140 (2014) 184201.
[85] F. Mentink-Vigier, S. Paul, D. Lee, A. Feintuch, S. Hediger, S. Vega, G. De Paepe, Nuclear depolarization and absolute sensitivity in magic-angle spinning cross effect dynamic nuclear polarization, Phys. Chem. Chem. Phys. 17 (2015) 21824–21836.
[86] S.R. Chaudhari, P. Berruyer, D. Gajan, C. Reiter, F. Engelke, D.L. Silverio, C. Coperet, M. Lelli, A. Lesage, L. Emsley, Dynamic nuclear polarization at 40 kHz magic angle spinning, Phys. Chem. Chem. Phys. 18 (2016) 10616–10622.
[87] E.A. Nanni, A.B. Barnes, Y. Matsuki, P.P. Woskov, B. Corzilius, R.G. Griffin, R.J. Temkin, Microwave field distribution in a magic angle spinning dynamic nuclear polarization NMR probe, J. Magn. Reson. 210 (2011) 16–23.
[88] Y. Hovav, D. Shimon, I. Kaminker, A. Feintuch, D. Goldfarb, S. Vega, Effects of the electron polarization on dynamic nuclear polarization in solids, Phys. Chem. Chem. Phys. 17 (2015) 6053–6065.
[89] O. Haze, B. Corzilius, A.A. Smith, R.G. Griffin, T.M. Swager, Water-soluble organic radicals as polarizing agents for high field dynamic nuclear polarization, J. Am. Chem. Soc. 134 (2012) 14287–14290.
[90] T.V. Can, M.A. Caporini, F. Mentink-Vigier, B. Corzilius, J.J. Walish, M. Rosay, W.E. Maas, M. Baldus, S. Vega, T.M. Swager, R.G. Griffin, Overhauser effects in insulating solids, J. Chem. Phys. 141 (2014) 064202.
[91] L.R. Becerra, G.J. Gerfen, B.F. Bellew, J.A. Bryant, D.A. Hall, S.J. Inati, R.T. Weber, S. Un, T.F. Prisner, A.E. McDermott, K.W. Fishbein, K.E. Kreischer, R.J. Temkin, D.J. Singel, R.G. Griffin, A spectrometer for dynamic nuclear polarization and electron paramagnetic resonance at high frequencies, J. Magn. Reson. Ser. A 117 (1995) 28–40.
[92] T. Maly, D. Cui, R.G. Griffin, A.-F. Miller, ^{1}H dynamic nuclear polarization based on an endogenous radical, J. Phys. Chem. B 116 (2012) 7055–7065.
[93] I. Solomon, Relaxation processes in a system of two spins, Phys. Rev. 99 (1955) 559–565.
[94] K.H. Hausser, D. Stehlik, Dynamic nuclear polarisation in liquids, Adv. Magn. Reson. 3 (1968) 79.
[95] F. Bloch, Nuclear induction, Phys. Rev. 70 (1946) 460–474.
[96] N. Enkin, G. Liu, I. Tkach, M. Bennati, High DNP efficiency of TEMPONE radicals in liquid toluene at low concentrations, Phys. Chem. Chem. Phys. 16 (2014) 8795–8800.
[97] M. Lelli, S.R. Chaudhari, D. Gajan, G. Casano, A.J. Rossini, O. Ouari, P. Tordo, A. Lesage, L. Emsley, Solid-state dynamic nuclear polarization at 9.4 and 18.8 T from 100 K to room temperature, J. Am. Chem. Soc. 137 (2015) 14558–14561.
[98] G. Liu, M. Levien, N. Karschin, G. Parigi, C. Luchinat, M. Bennati, One-thousand-fold enhancement of high field liquid nuclear magnetic resonance signals at room temperature, Nat. Chem. 9 (2017) 676–680.
[99] S. Pylaeva, K.L. Ivanov, M. Baldus, D. Sebastiani, H. Elgabarty, Molecular mechanism of Overhauser dynamic nuclear polarization in insulating solids, J. Phys. Chem. Lett. 8 (2017) 2137–2142.
[100] F. Mentink-Vigier, Ü. Akbey, H. Oschkinat, S. Vega, A. Feintuch, Theoretical aspects of magic angle spinning – dynamic nuclear polarization, J. Magn. Reson. 258 (2015) 102–120.
[101] G.R. Khutsishvili, Spin diffusion, Sov. Phys. Uspekhi 8 (1966) 743–769.
[102] D.S. Wollan, J.W. Poulton, Dynamic proton polarization with an inhomogeneously-broadened ESR line, Phys. Lett. A 33 (1970) 33–34.
[103] K.H. Langley, C.D. Jeffries, Theory and operation of a proton-spin refrigerator, Phys. Rev. 152 (1966) 358–376.
[104] C.D. Jeffries, On nuclear relaxation in dilute paramagnetic crystals, Proc. Phys. Soc. 88 (1966) 257–258.
[105] N. Bloembergen, On the interaction of nuclear spins in a crystalline lattice, Physica 15 (1949) 386–426.
[106] A. Abragam, M. Goldman, Principles of dynamic nuclear polarisation, Rep. Prog. Phys. 41 (1978) 395–467.
[107] P.G. de Gennes, Sur la relaxation nucleaire dans les cristaux ioniques, J. Phys. Chem. Solids 7 (1958) 345–350.
[108] W.E. Blumberg, Nuclear spin-lattice relaxation caused by paramagnetic impurities, Phys. Rev. 119 (1960) 79–84.
[109] H.E. Rorschach, Nuclear relaxation in solids by diffusion to paramagnetic impurities, Physica 30 (1964) 38–48.
[110] M. Goldman, Impurity-controlled nuclear relaxation, Phys. Rev. 138 (1965) A1675–A1681.
[111] J.I. Kaplan, Numerical solution of the equation governing nuclear magnetic spin-lattice relaxation in a paramagnetic-spin-doped insulator, Phys. Rev. B 3 (1971) 604–608.
[112] P. Zegers, R. Van Steenwinkel, Strong solid state effect in an inhomogeneous electron spin system, Physica 33 (1967) 332–342.
[113] A. Abragam, M. Borghini, P. Catillon, J. Coustham, P. Roubeau, J. Thirion, Diffusion de protons polarises de 20 MeV par une cible de protons polarises et mesure preliminaire du parametre Cnn, Phys. Lett. 2 (1962) 310–311.
[114] G.R. Khutsishvili, Spin diffusion and magnetic relaxation of nuclei, Sov. Phys. JETP 15 (1962) 909–913.
[115] J.P. Wolfe, Direct observation of a nuclear spin diffusion barrier, Phys. Rev. Lett. 31 (1973) 907–910.

[116] N. Bloembergen, E.M. Purcell, R.V. Pound, Relaxation effects in nuclear magnetic resonance absorption, Phys. Rev. 73 (1948) 679–712.
[117] M. Abraham, R.W. Kedzie, C.D. Jeffries, γ-Ray anisotropy of Co^{60} nuclei polarized by paramagnetic resonance saturation, Phys. Rev. 106 (1957) 165–166.
[118] C.D. Jeffries, Polarization of nuclei by resonance saturation in paramagnetic crystals, Phys. Rev. 106 (1957) 164–165.
[119] E. Erb, J.L. Motchane, J. Uebersfeld, Effet de polarisation nucléaire dans les liquides et les gaz adsorbés sur les charbons, C.R. Hebd. Acad. Sci. 246 (1958) 2121–2123.
[120] A. Abragam, W.G. Proctor, Une nouvelle méthode de polarisation dynamique des noyaux atomiques dans les solides, C.R. Hebd. Acad. Sci. 246 (1958) 2253–2256.
[121] O.S. Leifson, C.D. Jeffries, Dynamic polarization of nuclei by electron-nuclear dipolar coupling in crystals, Phys. Rev. 122 (1961) 1781–1795.
[122] J.L. Motchane, Ann. Phys. (Paris) 7 (1962) 139.
[123] Y. Hovav, A. Feintuch, S. Vega, Dynamic nuclear polarization assisted spin diffusion for the solid effect case, J. Chem. Phys. 134 (2011) 074509.
[124] R. Brüschweiler, R.R. Ernst, Non-ergodic quasi-equilibria in short linear spin 12 chains, Chem. Phys. Lett. 264 (1997) 393–397.
[125] I. Kuprov, Fokker-Planck formalism in magnetic resonance simulations, J. Magn. Reson. 270 (2016) 124–135.
[126] P. Hodgkinson, L. Emsley, Numerical simulation of solid-state NMR experiments, Prog. Nucl. Magn. Reson. Spectrosc. 36 (2000) 201–239.
[127] H.J. Hogben, M. Krzystyniak, G.T.P. Charnock, P.J. Hore, I. Kuprov, Spinach – a software library for simulation of spin dynamics in large spin systems, J. Magn. Reson. 208 (2011) 179–194.
[128] A. Karabanov, I. Kuprov, G.T.P. Charnock, A.v.d. Drift, L.J. Edwards, W. Köckenberger, On the accuracy of the state space restriction approximation for spin dynamics simulations, J. Chem. Phys. 135 (2011) 084106.
[129] A. Karabanov, A. van der Drift, L.J. Edwards, I. Kuprov, W. Kockenberger, Quantum mechanical simulation of solid effect dynamic nuclear polarisation using Krylov-Bogolyubov time averaging and a restricted state-space, Phys. Chem. Chem. Phys. 14 (2012) 2658–2668.
[130] A. Karabanov, D. Wiśniewski, I. Lesanovsky, W. Köckenberger, Dynamic nuclear polarization as kinetically constrained diffusion, Phys. Rev. Lett. 115 (2015) 020404.
[131] A. Karabanov, G. Kwiatkowski, W. Köckenberger, Quantum mechanical simulation of cross effect DNP using Krylov-Bogolyubov averaging, Appl. Magn. Reson. 43 (2012) 43–58.
[132] D. Wiśniewski, A. Karabanov, I. Lesanovsky, W. Köckenberger, Solid effect DNP polarization dynamics in a system of many spins, J. Magn. Reson. 264 (2016) 30–38.
[133] Y. Hovav, I. Kaminker, D. Shimon, A. Feintuch, D. Goldfarb, S. Vega, The electron depolarization during dynamic nuclear polarization: measurements and simulations, Phys. Chem. Chem. Phys. 17 (2015) 226–244.
[134] A. Leavesley, D. Shimon, T.A. Siaw, A. Feintuch, D. Goldfarb, S. Vega, I. Kaminker, S. Han, Effect of electron spectral diffusion on static dynamic nuclear polarization at 7 Tesla, Phys. Chem. Chem. Phys. 19 (2017) 3596–3605.
[135] P. Schosseler, T. Wacker, A. Schweiger, Pulsed ELDOR detected NMR, Chem. Phys. Lett. 224 (1994) 319–324.
[136] J. Granwehr, W. Köckenberger, Multidimensional low-power pulse EPR under DNP conditions, Appl. Magn. Reson. 34 (2008) 355–378.
[137] V.S. Bajaj, C.T. Farrar, M.K. Hornstein, I. Mastovsky, J. Vieregg, J. Bryant, B. Elena, K.E. Kreischer, R.J. Temkin, R.G. Griffin, Dynamic nuclear polarization at 9 T using a novel 250 GHz gyrotron microwave source, J. Magn. Reson. 160 (2003) 85–90.
[138] A.J. Rossini, A. Zagdoun, F. Hegner, M. Schwarzwälder, D. Gajan, C. Copéret, A. Lesage, L. Emsley, Dynamic nuclear polarization NMR spectroscopy of microcrystalline solids, J. Am. Chem. Soc. 134 (2012) 16899–16908.
[139] M. Kaushik, T. Bahrenberg, T.V. Can, M.A. Caporini, R. Silvers, J. Heiliger, A.A. Smith, H. Schwalbe, R.G. Griffin, B. Corzilius, Gd(III) and Mn(II) complexes for dynamic nuclear polarization: small molecular chelate polarizing agents and applications with site-directed spin labeling of proteins, Phys. Chem. Chem. Phys. 18 (2016) 27205–27218.
[140] P. Wenk, M. Kaushik, D. Richter, M. Vogel, B. Suess, B. Corzilius, Dynamic nuclear polarization of nucleic acid with endogenously bound manganese, J. Biomol. NMR 63 (2015) 97–109.
[141] D. Daube, V. Aladin, J. Heiliger, J.J. Wittmann, D. Barthelmes, C. Bengs, H. Schwalbe, B. Corzilius, Heteronuclear cross-relaxation under solid-state dynamic nuclear polarization, J. Am. Chem. Soc. 138 (2016) 16572–16575.
[142] A.S. Lilly Thankamony, O. Lafon, X. Lu, F. Aussenac, M. Rosay, J. Trébosc, H. Vezin, J.-P. Amoureux, Solvent-free high-field dynamic nuclear polarization of mesoporous silica functionalized with TEMPO, Appl. Magn. Reson. 43 (2012) 237–250.
[143] O. Lafon, M. Rosay, F. Aussenac, X. Lu, J. Trébosc, O. Cristini, C. Kinowski, N. Touati, H. Vezin, J.-P. Amoureux, Beyond the silica surface by direct silicon-29 dynamic nuclear polarization, Angew. Chem. Int. Ed. 50 (2011) 8367–8370.
[144] O. Lafon, A.S.L. Thankamony, M. Rosay, F. Aussenac, X.Y. Lu, J. Trebosc, V. Bout-Roumazeilles, H. Vezine, J.P. Amoureux, Indirect and direct Si-29 dynamic nuclear polarization of dispersed nanoparticles, Chem. Commun. 49 (2013) 2864–2866.
[145] M.M. Hoffmann, S. Bothe, T. Gutmann, F.-F. Hartmann, M. Reggelin, G. Buntkowsky, Directly vs indirectly enhanced ^{13}C in dynamic nuclear polarization magic angle spinning NMR experiments of nonionic surfactant systems, J. Phys. Chem. C 121 (2017) 2418–2427.
[146] V.S. Bajaj, M.K. Hornstein, K.E. Kreischer, J.R. Sirigiri, P.P. Woskov, M.L. Mak-Jurkauskas, J. Herzfeld, R.J. Temkin, R.G. Griffin, 250 GHz CW gyrotron oscillator for dynamic nuclear polarization in biological solid state NMR, J. Magn. Reson. 189 (2007) 251–279.
[147] T. Maly, L.B. Andreas, A.A. Smith, R.G. Griffin, H-2-DNP-enhanced H-2-C-13 solid-state NMR correlation spectroscopy, Phys. Chem. Chem. Phys. 12 (2010) 5872–5878.
[148] V.S. Bajaj, M.L. Mak-Jurkauskas, M. Belenky, J. Herzfeld, R.G. Griffin, DNP enhanced frequency-selective TEDOR experiments in bacteriorhodopsin, J. Magn. Reson. 202 (2010) 9–13.
[149] I.V. Sergeyev, B. Itin, R. Rogawski, L.A. Day, A.E. McDermott, Efficient assignment and NMR analysis of an intact virus using sequential side-chain correlations and DNP sensitization, Proc. Natl. Acad. Sci. U.S.A. (2017).
[150] V. Vitzthum, M.A. Caporini, G. Bodenhausen, Solid-state nitrogen-14 nuclear magnetic resonance enhanced by dynamic nuclear polarization using a gyrotron, J. Magn. Reson. 205 (2010) 177–179.
[151] K. Märker, M. Pingret, J.M. Mouesca, D. Gasparutto, S. Hediger, G. De Paëpe, A new tool for NMR crystallography: complete $^{13}C/^{15}N$ assignment of organic molecules at natural isotopic abundance using DNP-enhanced solid-state NMR, J. Am. Chem. Soc. 137 (2015) 13796–13799.
[152] M. Rosay, M. Blank, F. Engelke, Instrumentation for solid-state dynamic nuclear polarization with magic angle spinning NMR, J. Magn. Reson. 264 (2016) 88–98.
[153] A. Feintuch, D. Shimon, Y. Hovav, D. Banerjee, I. Kaminker, Y. Lipkin, K. Zibzener, B. Epel, S. Vega, D. Goldfarb, A dynamic nuclear polarization spectrometer at 95 GHz/144 MHz with EPR and NMR excitation and detection capabilities, J. Magn. Reson. 209 (2011) 136–141.
[154] K. Ley, E. Müller, K. Scheffler, Zur Unterscheidung möglicher mesomerer Grenzzustände bei "Aroxylen", Angew. Chem. 70 (1958) 74–75.
[155] T.J. Schmugge, C.D. Jeffries, High dynamic polarization of protons, Phys. Rev. 138 (1965) A1785–A1801.
[156] F. Mentink-Vigier, S. Vega, G. De Paepe, Fast and accurate MAS-DNP simulations of large spin ensembles, Phys. Chem. Chem. Phys. 19 (2017) 3506–3522.
[157] Y. Hovav, A. Feintuch, S. Vega, Theoretical aspects of dynamic nuclear polarization in the solid state – the solid effect, J. Magn. Reson. 207 (2010) 176–189.
[158] D. Shimon, Y. Hovav, A. Feintuch, D. Goldfarb, S. Vega, Dynamic nuclear polarization in the solid state: a transition between the cross effect and the solid effect, Phys. Chem. Chem. Phys. 14 (2012) 5729–5743.
[159] B. Corzilius, A.A. Smith, A.B. Barnes, C. Luchinat, I. Bertini, R.G. Griffin, High-field dynamic nuclear polarization with high-spin transition metal ions, J. Am. Chem. Soc. 133 (2011) 5648–5651.
[160] T.A. Siaw, M. Fehr, A. Lund, A. Latimer, S.A. Walker, D.T. Edwards, S.-I. Han, Effect of electron spin dynamics on solid-state dynamic nuclear polarization performance, Phys. Chem. Chem. Phys. 16 (2014) 18694–18706.
[161] Y. Hovav, A. Feintuch, S. Vega, D. Goldfarb, Dynamic nuclear polarization using frequency modulation at 3.34 T, J. Magn. Reson. 238 (2014) 94–105.
[162] T.A. Siaw, A. Leavesley, A. Lund, I. Kaminker, S. Han, A versatile and modular quasi optics-based 200 GHz dual dynamic nuclear polarization and electron paramagnetic resonance instrument, J. Magn. Reson. 264 (2016) 131–153.
[163] K.R. Thurber, W.M. Yau, R. Tycko, Low-temperature dynamic nuclear polarization at 9.4 T with a 30 mW microwave source, J. Magn. Reson. 204 (2010) 303–313.
[164] A. Bornet, J. Milani, B. Vuichoud, A.J. Perez Linde, G. Bodenhausen, S. Jannin, Microwave frequency modulation to enhance dissolution dynamic nuclear polarization, Chem. Phys. Lett. 602 (2014) 63–67.
[165] D. Shimon, A. Feintuch, D. Goldfarb, S. Vega, Static ^{1}H dynamic nuclear polarization with the biradical TOTAPOL: a transition between the solid effect and the cross effect, Phys. Chem. Chem. Phys. 16 (2014) 6687–6699.
[166] T.V. Can, J.J. Walish, T.M. Swager, R.G. Griffin, Time domain DNP with the NOVEL sequence, J. Chem. Phys. 143 (2015) 054201.
[167] B. Corzilius, Theory of solid effect and cross effect dynamic nuclear polarization with half-integer high-spin metal polarizing agents in rotating solids, Phys. Chem. Chem. Phys. 18 (2016) 27190–27204.
[168] M. Kaushik, M. Qi, A. Godt, B. Corzilius, Bis-gadolinium complexes for solid effect and cross effect dynamic nuclear polarization, Angew. Chem. Int. Ed. Engl. 56 (2017) 4295–4299.
[169] D. Banerjee, D. Shimon, A. Feintuch, S. Vega, D. Goldfarb, The interplay between the solid effect and the cross effect mechanisms in solid state ^{13}C DNP at 95 GHz using trityl radicals, J. Magn. Reson. 230 (2013) 212–219.
[170] K. Thurber, R. Tycko, Low-temperature dynamic nuclear polarization with helium-cooled samples and nitrogen-driven magic-angle spinning, J. Magn. Reson. 264 (2016) 99–106.
[171] Y. Matsuki, K. Ueda, T. Idehara, R. Ikeda, I. Ogawa, S. Nakamura, M. Toda, T. Anai, T. Fujiwara, Helium-cooling and -spinning dynamic nuclear polarization for sensitivity-enhanced solid-state NMR at 14 T and 30 K, J. Magn. Reson. 225 (2012) 1–9.
[172] M. Borghini, W. de Boer, K. Morimoto, Nuclear dynamic polarization by resolved solid-state effect and thermal mixing with an electron spin-spin interaction reservoir, Phys. Lett. A 48 (1974) 244–246.
[173] W. de Boer, Dynamic orientation of nuclei at low temperatures, J. Low Temp. Phys. 22 (1976) 185–212.

[174] A.A. Smith, B. Corzilius, O. Haze, T.M. Swager, R.G. Griffin, Observation of strongly forbidden solid effect dynamic nuclear polarization transitions via electron-electron double resonance detected NMR, J. Chem. Phys. 139 (2013) 214201.

[175] D. Shimon, Y. Hovav, I. Kaminker, A. Feintuch, D. Goldfarb, S. Vega, Simultaneous DNP enhancements of ^{1}H and ^{13}C nuclei: theory and experiments, Phys. Chem. Chem. Phys. 17 (2015) 11868–11883.

[176] I. Kaminker, D. Shimon, Y. Hovav, A. Feintuch, S. Vega, Heteronuclear DNP of protons and deuterons with TEMPOL, Phys. Chem. Chem. Phys. 18 (2016) 11017–11041.

[177] M. Rosay, L. Tometich, S. Pawsey, R. Bader, R. Schauwecker, M. Blank, P.M. Borchard, S.R. Cauffman, K.L. Felch, R.T. Weber, R.J. Temkin, R.G. Griffin, W.E. Maas, Solid-state dynamic nuclear polarization at 263 GHz: spectrometer design and experimental results, Phys. Chem. Chem. Phys. 12 (2010) 5850–5860.

[178] Y. Matsuki, T. Idehara, J. Fukazawa, T. Fujiwara, Advanced instrumentation for DNP-enhanced MAS NMR for higher magnetic fields and lower temperatures, J. Magn. Reson. 264 (2016) 107–115.

[179] T. Maly, G.T. Debelouchina, V.S. Bajaj, K.N. Hu, C.G. Joo, M.L. Mak-Jurkauskas, J.R. Sirigiri, P.C.A. van der Wel, J. Herzfeld, R.J. Temkin, R.G. Griffin, Dynamic nuclear polarization at high magnetic fields, J. Chem. Phys. 128 (2008) 052211.

[180] A.B. Barnes, G. De Paëpe, P.C.A. van der Wel, K.N. Hu, C.G. Joo, V.S. Bajaj, M.L. Mak-Jurkauskas, J.R. Sirigiri, J. Herzfeld, R.J. Temkin, R.G. Griffin, High-field dynamic nuclear polarization for solid and solution biological NMR, Appl. Magn. Reson. 34 (2008) 237–263.

[181] G.J. Gerfen, L.R. Becerra, D.A. Hall, R.G. Griffin, R.J. Temkin, D.J. Singel, High frequency (140 GHz) dynamic nuclear polarization: Polarization transfer to a solute in frozen aqueous solution, J. Chem. Phys. 102 (1995) 9494–9497.

[182] L.R. Becerra, G.J. Gerfen, R.J. Temkin, D.J. Singel, R.G. Griffin, Dynamic nuclear polarization with a cyclotron resonance maser at 5 T, Phys. Rev. Lett. 71 (1993) 3561–3564.

[183] Y. Matsuki, H. Takahashi, K. Ueda, T. Idehara, I. Ogawa, M. Toda, H. Akutsu, T. Fujiwara, Dynamic nuclear polarization experiments at 14.1 T for solid-state NMR, Phys. Chem. Chem. Phys. 12 (2010) 5799.

[184] A.B. Barnes, E. Markhasin, E. Daviso, V.K. Michaelis, E.A. Nanni, S.K. Jawla, E.L. Mena, R. DeRocher, A. Thakkar, P.P. Woskov, J. Herzfeld, R.J. Temkin, R.G. Griffin, Dynamic nuclear polarization at 700 MHz/460 GHz, J. Magn. Reson. 224 (2012) 1–7.

[185] V.L. Granatstein, R.K. Parker, C.M. Armstrong, Vacuum electronics at the dawn of the twenty-first century, Proc. IEEE 87 (1999) 702–716.

[186] G.S. Nusinovich, M.K.A. Thumm, M.I. Petelin, The gyrotron at 50: historical overview, J. Infrared Millimeter Terahertz Waves 35 (2014) 325–381.

[187] A.C. Torrezan, S.T. Han, I. Mastovsky, M.A. Shapiro, J.R. Sirigiri, R.J. Temkin, A. B. Barnes, R.G. Griffin, Continuous-wave operation of a frequency-tunable 460-GHz second-harmonic gyrotron for enhanced nuclear magnetic resonance, IEEE Trans. Plasma Sci. 38 (2010) 1150–1159.

[188] A.C. Torrezan, M.A. Shapiro, J.R. Sirigiri, R.J. Temkin, R.G. Griffin, Operation of a continuously frequency-tunable second-harmonic CW 330-GHz gyrotron for dynamic nuclear polarization, IEEE Trans. Electron Dev. 58 (2011) 2777–2783.

[189] A.B. Barnes, E.A. Nanni, J. Herzfeld, R.G. Griffin, R.J. Temkin, A 250 GHz gyrotron with a 3 GHz tuning bandwidth for dynamic nuclear polarization, J. Magn. Reson. 221 (2012) 147–153.

[190] S. Jawla, Q.Z. Ni, A. Barnes, W. Guss, E. Daviso, J. Herzfeld, R. Griffin, R. Temkin, Continuously tunable 250 GHz gyrotron with a double disk window for DNP-NMR spectroscopy, J. Infrared Millimeter Terahertz Waves 34 (2013) 42–52.

[191] Y. Matsuki, K. Ueda, T. Idehara, R. Ikeda, K. Kosuga, I. Ogawa, S. Nakamura, M. Toda, T. Anai, T. Fujiwara, Application of continuously frequency-tunable 0.4 THz gyrotron to dynamic nuclear polarization for 600 MHz solid-state NMR, J. Infrared Millimeter Terahertz Waves 33 (2012) 745–755.

[192] T. Idehara, Y. Tatematsu, Y. Yamaguchi, E.M. Khutoryan, A.N. Kuleshov, K. Ueda, Y. Matsuki, T. Fujiwara, The development of 460 GHz gyrotrons for 700 MHz DNP-NMR spectroscopy, J. Infrared Millimeter Terahertz Waves 36 (2015) 613–627.

[193] T. Idehara, E.M. Khutoryan, Y. Tatematsu, Y. Yamaguchi, A.N. Kuleshov, O. Dumbrajs, Y. Matsuki, T. Fujiwara, High-speed frequency modulation of a 460-GHz gyrotron for enhancement of 700-MHz DNP-NMR spectroscopy, J Infrared Millimeter Terahertz Waves 36 (2015) 819–829.

[194] K.J. Pike, T.F. Kemp, H. Takahashi, R. Day, A.P. Howes, E.V. Kryukov, J.F. MacDonald, A.E.C. Collis, D.R. Bolton, R.J. Wylde, M. Orwick, K. Kosuga, A.J. Clark, T. Idehara, A. Watts, G.M. Smith, M.E. Newton, R. Dupree, M.E. Smith, A spectrometer designed for 6.7 and 14.1 T DNP-enhanced solid-state MAS NMR using quasi-optical microwave transmission, J. Magn. Reson. 215 (2012) 1–9.

[195] D.E.M. Hoff, B.J. Albert, E.P. Saliba, F.J. Scott, E.J. Choi, M. Mardini, A.B. Barnes, Frequency swept microwaves for hyperfine decoupling and time domain dynamic nuclear polarization, Solid State Nucl. Magn. Reson. 72 (2015) 79–89.

[196] S. Alberti, J.P. Ansermet, K.A. Avramides, D. Fasel, J.P. Hogge, S. Kern, C. Lievin, Y. Liu, A. Macor, I. Pagonakis, M. Silva, M.Q. Tran, T.M. Tran, D. Wagner, Design of a frequency-tunable gyrotron for DNP-enhanced NMR spectroscopy, in: 2009 34th International Conference on Infrared, Millimeter, and Terahertz Waves, 2009, pp. 1–2.

[197] S. Alberti, J.-P. Ansermet, K.A. Avramides, F. Braunmueller, P. Cuanillon, J. Dubray, D. Fasel, J.-P. Hogge, A. Macor, E. de Rijk, M. da Silva, M.Q. Tran, T.M. Tran, Q. Vuillemin, Experimental study from linear to chaotic regimes on a terahertz-frequency gyrotron oscillator, Phys. Plasmas 19 (2012) 123102.

[198] S. Alberti, F. Braunmueller, T.M. Tran, J. Genoud, J.P. Hogge, M.Q. Tran, J.P. Ansermet, Nanosecond pulses in a THz gyrotron oscillator operating in a mode-locked self-consistent Q-switch regime, Phys. Rev. Lett. 111 (2013) 205101.

[199] M. Blank, P. Borchard, S. Cauffman, K. Felch, M. Rosay, L. Tometich, High-frequency gyrotrons for DNP-enhanced NMR applications, in: IEEE International Vacuum Electronics Conference, 2014, pp. 7–8.

[200] V. Denysenkov, T. Prisner, Liquid state dynamic nuclear polarization probe with Fabry-Perot resonator at 9.2 T, J. Magn. Reson. 217 (2012) 1–5.

[201] J.R. Sirigiri, T. Maly, L. Tarricone, A compact 395 GHz gyrotron for dynamic nuclear polarization, in: 2011 International Conference on Infrared, Millimeter, and Terahertz Waves, 2011, pp. 1–2.

[202] S.P. Kuo, B.R. Cheo, Analysis of the electron cyclotron maser instability, Phys. Lett. A 103 (1984) 427–432.

[203] A. Stock, A high-order particle-in-cell method for low density plasma flow and the simulation of gyrotron resonator devices, Fakultät Luft- und Raumfahrttechnik und Geodäsie, Universität Stuttgart, 2013.

[204] M.K. Hornstein, V.S. Bajaj, R.G. Griffin, K.E. Kreischer, I. Mastovsky, M.A. Shapiro, J.R. Sirigiri, R.J. Temkin, Second harmonic operation at 460 GHz and broadband continuous frequency tuning of a gyrotron oscillator, IEEE Trans. Electron Dev. 52 (2005) 798–807.

[205] R. Sirigiri, T. Maly, Integrated high-frequency generator system utilizing the magnetic field of the target application, in: Bridge12 Technologies, Inc. Framingham, MA, 2014.

[206] V.L. Bratman, A.E. Fedotov, Y.K. Kalynov, P.B. Makhalov, A. Samoson, THz gyrotron and BWO designed for operation in DNP-NMR spectrometer magnet, J. Infrared Millimeter Terahertz Waves 34 (2013) 837–846.

[207] V.L. Bratman, A.E. Fedotov, Y.K. Kalynov, P.B. Makhalov, V.N. Manuilov, Project of gyrotron for DNP applications based on NMR magnet, in: 2016 41st International Conference on Infrared, Millimeter, and Terahertz waves (IRMMW-THz), 2016, pp. 1–2.

[208] H. Ryan, J. van Bentum, T. Maly, A ferromagnetic shim insert for NMR magnets – towards an integrated gyrotron for DNP-NMR spectroscopy, J. Magn. Reson. 277 (2017) 1–7.

[209] T.F. Kemp, H.R. Dannatt, N.S. Barrow, A. Watts, S.P. Brown, M.E. Newton, R. Dupree, Dynamic nuclear polarization enhanced NMR at 187 GHz/284 MHz using an extended interaction klystron amplifier, J. Magn. Reson. 265 (2016) 77–82.

[210] D. Berry, H. Deng, R. Dobbs, P. Horoyski, M. Hyttinen, A. Kingsmill, R. MacHattie, A. Roitman, E. Sokol, B. Steer, Practical aspects of EIK technology, IEEE Trans. Electron Dev. 61 (2014) 1830–1835.

[211] J. Benford, J.A. Swegle, E. Schamiloglu, High Power Microwaves, third ed., CRC Press, 2015.

[212] D.R. Bolton, P.S. Cruickshank, D.A. Robertson, G.M. Smith, Sub-nanosecond coherent pulse generation at millimetre-wave frequencies, Electron. Lett. 43 (2007) 346–348.

[213] A.A. Smith, B. Corzilius, J.A. Bryant, R. DeRocher, P.P. Woskov, R.J. Temkin, R.G. Griffin, A 140 GHz pulsed EPR/212 MHz NMR spectrometer for DNP studies, J. Magn. Reson. 223 (2012) 170–179.

[214] Ü. Akbey, A.H. Linden, H. Oschkinat, High-temperature dynamic nuclear polarization enhanced magic-angle-spinning NMR, Appl. Magn. Reson. 43 (2012) 81–90.

[215] A.B. Barnes, M.L. Mak-Jurkauskas, Y. Matsuki, V.S. Bajaj, P.C.A. van der Wel, R. DeRocher, J. Bryant, J.R. Sirigiri, R.J. Temkin, J. Lugtenburg, J. Herzfeld, R.G. Griffin, Cryogenic sample exchange NMR probe for magic angle spinning dynamic nuclear polarization, J. Magn. Reson. 198 (2009) 261–270.

[216] Q.Z. Ni, E. Daviso, T.V. Can, E. Markhasin, S.K. Jawla, T.M. Swager, R.J. Temkin, J. Herzfeld, R.G. Griffin, High frequency dynamic nuclear polarization, Acc. Chem. Res. 46 (2013) 1933–1941.

[217] D. Lee, E. Bouleau, P. Saint-Bonnet, S. Hediger, G. De Paëpe, Ultra-low temperature MAS-DNP, J. Magn. Reson. 264 (2016) 116–124.

[218] D.A. Hall, D.C. Maus, G.J. Gerfen, S.J. Inati, L.R. Becerra, F.W. Dahlquist, R.G. Griffin, Polarization-enhanced NMR spectroscopy of biomolecules in frozen solution, Science 276 (1997) 930–932.

[219] E. Bouleau, P. Saint-Bonnet, F. Mentink-Vigier, H. Takahashi, J.F. Jacquot, M. Bardet, F. Aussenac, A. Purea, F. Engelke, S. Hediger, D. Lee, G. De Paëpe, Pushing NMR sensitivity limits using dynamic nuclear polarization with closed-loop cryogenic helium sample spinning, Chem. Sci. 6 (2015) 6806–6812.

[220] K.R. Thurber, R. Tycko, Biomolecular solid state NMR with magic-angle spinning at 25 K, J. Magn. Reson. 195 (2008) 179–186.

[221] C. Song, K.-N. Hu, C.-G. Joo, T.M. Swager, R.G. Griffin, TOTAPOL: a biradical polarizing agent for dynamic nuclear polarization experiments in aqueous media, J. Am. Chem. Soc. 128 (2006) 11385–11390.

[222] R.A. McKay, Probes for special purposes, eMagRes, John Wiley & Sons, Ltd, 2007.

[223] E.A. Nanni, S.K. Jawla, M.A. Shapiro, P.P. Woskov, R.J. Temkin, Low-loss transmission lines for high-power terahertz radiation, J Infrared Millimeter Terahertz Waves 33 (2012) 695–714.

[224] B.D. Armstrong, D.T. Edwards, R.J. Wylde, S.A. Walker, S. Han, A 200 GHz dynamic nuclear polarization spectrometer, Phys. Chem. Chem. Phys. 12 (2010) 5920–5926.

[225] B. Corzilius, L.B. Andreas, A.A. Smith, Q.Z. Ni, R.G. Griffin, Paramagnet-induced signal quenching in MAS-DNP experiments on frozen homogeneous solutions, J. Magn. Reson. 240 (2014) 113–123.

[226] M.L. Mak-Jurkauskas, V.S. Bajaj, M.K. Hornstein, M. Belenky, R.G. Griffin, J. Herzfeld, Energy transformations early in the bacteriorhodopsin photocycle revealed by DNP-enhanced solid-state NMR, Proc. Natl. Acad. Sci. U.S.A. 105 (2008) 883–888.
[227] V.S. Bajaj, M.L. Mak-Jurkauskas, M. Belenky, J. Herzfeld, R.G. Griffin, Functional and shunt states of bacteriorhodopsin resolved by 250 GHz dynamic nuclear polarization-enhanced solid-state NMR, Proc. Natl. Acad. Sci. U.S.A. 106 (2009) 9244–9249.
[228] J. Becker-Baldus, C. Bamann, K. Saxena, H. Gustmann, L.J. Brown, R.C.D. Brown, C. Reiter, E. Bamberg, J. Wachtveitl, H. Schwalbe, C. Glaubitz, Enlightening the photoactive site of channelrhodopsin-2 by DNP-enhanced solid-state NMR spectroscopy, Proc. Natl. Acad. Sci. U.S.A. 112 (2015) 9896–9901.
[229] K.N. Hu, Polarizing agents and mechanisms for high-field dynamic nuclear polarization of frozen dielectric solids, Solid State Nucl. Magn. Reson. 40 (2011) 31–41.
[230] C.F. Koelsch, Syntheses with triarylvinylmagnesium bromides. α,γ-Bisdiphenylene-β-phenylallyl, a stable free radical, J. Am. Chem. Soc. 79 (1957) 4439–4441.
[231] M. Afeworki, R.A. McKay, J. Schaefer, Selective observation of the interface of heterogeneous polycarbonate/polystyrene blends by dynamic nuclear polarization carbon-13 NMR spectroscopy, Macromolecules 25 (1992) 4084–4091.
[232] C.T. Farrar, D.A. Hall, G.J. Gerfen, S.J. Inati, R.G. Griffin, Mechanism of dynamic nuclear polarization in high magnetic fields, J. Chem. Phys. 114 (2001) 4922–4933.
[233] J.H. Ardenkjær-Larsen, I. Laursen, I. Leunbach, G. Ehnholm, L.G. Wistrand, J.S. Petersson, K. Golman, EPR and DNP properties of certain novel single electron contrast agents intended for oximetric imaging, J. Magn. Reson. 133 (1998) 1–12.
[234] T.J. Reddy, T. Iwama, H.J. Halpern, V.H. Rawal, General synthesis of persistent trityl radicals for EPR imaging of biological systems, J. Org. Chem. 67 (2002) 4635–4639.
[235] I. Dhimitruka, O. Grigorieva, J.L. Zweier, V.V. Khramtsov, Synthesis, structure, and EPR characterization of deuterated derivatives of Finland trityl radical, Bioorg. Med. Chem. Lett. 20 (2010) 3946–3949.
[236] V.K. Michaelis, B. Corzilius, A.A. Smith, R.G. Griffin, Dynamic nuclear polarization of ^{17}O: direct polarization, J. Phys. Chem. B 117 (2013) 14894–14906.
[237] J.H. Ardenkjær-Larsen, B. Fridlund, A. Gram, G. Hansson, L. Hansson, M.H. Lerche, R. Servin, M. Thaning, K. Golman, Increase in signal-to-noise ratio of >10,000 times in liquid-state NMR, Proc. Natl. Acad. Sci. U.S.A. 100 (2003) 10158–10163.
[238] J.H. Ardenkjaer-Larsen, S. Macholl, H. Jóhannesson, Dynamic nuclear polarization with trityls at 1.2 K, Appl. Magn. Reson. 34 (2008) 509–522.
[239] S. Anderson, K. Golman, F. Rise, H. Wikström, L.-G. Wistrand, Free radicals, in: U.S. patent, 5,530,140, 1996.
[240] C. Gabellieri, V. Mugnaini, J.C. Paniagua, N. Roques, M. Oliveros, M. Feliz, J. Veciana, M. Pons, Dynamic nuclear polarization with polychlorotriphenylmethyl radicals: supramolecular polarization-transfer effects, Angew. Chem. Int. Ed. 49 (2010) 3360–3362.
[241] F. Mentink Vigier, D. Shimon, V. Mugnaini, J. Veciana, A. Feintuch, M. Pons, S. Vega, D. Goldfarb, The ^{13}C solid DNP mechanisms with perchlorotriphenylmethyl radicals – the role of ^{35,37}Cl, Phys. Chem. Chem. Phys. 16 (2014) 19218–19228.
[242] E.J. Hustedt, A.I. Smirnov, C.F. Laub, C.E. Cobb, A.H. Beth, Molecular distances from dipolar coupled spin-labels: the global analysis of multifrequency continuous wave electron paramagnetic resonance data, Biophys. J. 72 (1997) 1861–1877.
[243] E.J. Hustedt, A.H. Beth, Nitroxide spin-spin interactions: applications to protein structure and dynamics, Annu. Rev. Biophys. Biomol. Struct. 28 (1999) 129–153.
[244] K.N. Hu, C. Song, H.H. Yu, T.M. Swager, R.G. Griffin, High-frequency dynamic nuclear polarization using biradicals: a multifrequency EPR lineshape analysis, J. Chem. Phys. 128 (2008) 052302.
[245] V.N. Parmon, A.I. Kokorin, G.M. Zhidomirov, The interpretation of the polycrystalline ESR spectra of nitroxide biradicals, J. Magn. Reson. 28 (1977) 339–349.
[246] N.E. Shepherd, R. Gamsjaeger, M. Vandevenne, L. Cubeddu, J.P. Mackay, Site directed nitroxide spin labeling of oligonucleotides for NMR and EPR studies, Tetrahedron 71 (2015) 813–819.
[247] S.A. Shelke, G.B. Sandholt, S.T. Sigurdsson, Nitroxide-labeled pyrimidines for non-covalent spin-labeling of abasic sites in DNA and RNA duplexes, Org. Biomol. Chem. 12 (2014) 7366–7374.
[248] S.A. Shelke, S.T. Sigurdsson, Site-directed nitroxide spin labeling of biopolymers, in: C.R. Timmel, J.R. Harmer (Eds.), Structural Information from Spin-Labels and Intrinsic Paramagnetic Centres in the Biosciences, Springer, Berlin, Heidelberg, 2013, pp. 121–162.
[249] G. Audran, E.G. Bagryanskaya, P. Bremond, M.V. Edeleva, S.R.A. Marque, D.A. Parkhomenko, O.Y. Rogozhnikova, V.M. Tormyshev, E.V. Tretyakov, D.V. Trukhin, S.I. Zhivetyeva, Trityl-based alkoxyamines as NMP controllers and spin-labels, Polym. Chem. 7 (2016) 6490–6499.
[250] M.-A. Geiger, M. Orwick-Rydmark, K. Marker, W.T. Franks, D. Akhmetzyanov, D. Stoppler, M. Zinke, E. Specker, M. Nazare, A. Diehl, B.-J. van Rossum, F. Aussenac, T. Prisner, U. Akbey, H. Oschkinat, Temperature dependence of cross-effect dynamic nuclear polarization in rotating solids: advantages of elevated temperatures, Phys. Chem. Chem. Phys. 18 (2016) 30696–30704.
[251] H. Sato, V. Kathirvelu, A. Fielding, J.P. Blinco, A.S. Micallef, S.E. Bottle, S.S. Eaton, G.R. Eaton, Impact of molecular size on electron spin relaxation rates of nitroxyl radicals in glassy solvents between 100 and 300 K, Mol. Phys. 105 (2007) 2137–2151.
[252] S. Lange, A.H. Linden, Ü. Akbey, W.T. Franks, N.M. Loening, B.-J. van Rossum, H. Oschkinat, The effect of biradical concentration on the performance of DNP-MAS-NMR, J. Magn. Reson. 216 (2012) 209–212.
[253] A.J. Rossini, A. Zagdoun, M. Lelli, D. Gajan, F. Rascon, M. Rosay, W.E. Maas, C. Coperet, A. Lesage, L. Emsley, One hundred fold overall sensitivity enhancements for silicon-29 NMR spectroscopy of surfaces by dynamic nuclear polarization with CPMG acquisition, Chem. Sci. 3 (2012) 108–115.
[254] K.N. Hu, H.H. Yu, T.M. Swager, R.G. Griffin, Dynamic nuclear polarization with biradicals, J. Am. Chem. Soc. 126 (2004) 10844–10845.
[255] A. Lesage, M. Lelli, D. Gajan, M.A. Caporini, V. Vitzthum, P. Miéville, J. Alauzun, A. Roussey, C. Thieuleux, A. Mehdi, G. Bodenhausen, C. Copéret, L. Emsley, Surface enhanced NMR spectroscopy by dynamic nuclear polarization, J. Am. Chem. Soc. 132 (2010) 15459–15461.
[256] M. Lelli, D. Gajan, A. Lesage, M.A. Caporini, V. Vitzthum, P. Miéville, F. Héroguel, F. Rascón, A. Roussey, C. Thieuleux, M. Boualleg, L. Veyre, G. Bodenhausen, C. Coperet, L. Emsley, Fast characterization of functionalized silica materials by silicon-29 surface-enhanced NMR spectroscopy using dynamic nuclear polarization, J. Am. Chem. Soc. 133 (2011) 2104–2107.
[257] U. Akbey, B. Altin, A. Linden, S. Ozcelik, M. Gradzielski, H. Oschkinat, Dynamic nuclear polarization of spherical nanoparticles, Phys. Chem. Chem. Phys. 15 (2013) 20706–20716.
[258] P.C.A. van der Wel, K.N. Hu, J. Lewandowski, R.G. Griffin, Dynamic nuclear polarization of amyloidogenic peptide nanocrystals: GNNQQNY, a core segment of the yeast prion protein Sup35p, J. Am. Chem. Soc. 128 (2006) 10840–10846.
[259] L.B. Andreas, A.B. Barnes, B. Corzilius, J.J. Chou, E.A. Miller, M. Caporini, M. Rosay, R.G. Griffin, Dynamic nuclear polarization study of inhibitor binding to the M218–60 proton transporter from influenza A, Biochemistry 52 (2013) 2774–2782.
[260] H. Takahashi, B. Viverge, D. Lee, P. Rannou, G. De Paëpe, Towards structure determination of self-assembled peptides using dynamic nuclear polarization enhanced solid-state NMR spectroscopy, Angew. Chem. Int. Ed. 52 (2013) 6979–6982.
[261] P. Fricke, J.P. Demers, S. Becker, A. Lange, Studies on the MxiH protein in T3SS needles using DNP-enhanced ssNMR spectroscopy, ChemPhysChem 15 (2014) 57–60.
[262] A.N. Smith, M.A. Caporini, G.E. Fanucci, J.R. Long, A method for dynamic nuclear polarization enhancement of membrane proteins, Angew. Chem. Int. Ed. 54 (2015) 1542–1546.
[263] S.Y. Liao, M. Lee, T. Wang, I.V. Sergeyev, M. Hong, Efficient DNP NMR of membrane proteins: sample preparation protocols, sensitivity, and radical location, J. Biomol. NMR 64 (2016) 223–237.
[264] W.-M. Yau, K.R. Thurber, R. Tycko, Synthesis and evaluation of nitroxide-based oligoradicals for low-temperature dynamic nuclear polarization in solid state NMR, J. Magn. Reson. 244 (2014) 98–106.
[265] Y. Matsuki, T. Maly, O. Ouari, H. Karoui, F. Le Moigne, E. Rizzato, S. Lyubenova, J. Herzfeld, T. Prisner, P. Tordo, R.G. Griffin, Dynamic nuclear polarization with a rigid biradical, Angew. Chem. Int. Ed. 48 (2009) 4996–5000.
[266] E.L. Dane, B. Corzilius, E. Rizzato, P. Stocker, T. Maly, A.A. Smith, R.G. Griffin, O. Ouari, P. Tordo, T.M. Swager, Rigid orthogonal bis-TEMPO biradicals with improved solubility for dynamic nuclear polarization, J. Org. Chem. 77 (2012) 1789–1797.
[267] M.K. Kiesewetter, B. Corzilius, A.A. Smith, R.G. Griffin, T.M. Swager, Dynamic nuclear polarization with a water-soluble rigid biradical, J. Am. Chem. Soc. 134 (2012) 4537–4540.
[268] C. Ysacco, E. Rizzato, M.-A. Virolleaud, H. Karoui, A. Rockenbauer, F. Le Moigne, D. Siri, O. Ouari, R.G. Griffin, P. Tordo, Properties of dinitroxides for use in dynamic nuclear polarization (DNP), Phys. Chem. Chem. Phys. 12 (2010) 5841–5845.
[269] C. Ysacco, H. Karoui, G. Casano, F. Le Moigne, S. Combes, A. Rockenbauer, M. Rosay, W. Maas, O. Ouari, P. Tordo, Dinitroxides for solid state dynamic nuclear polarization, Appl. Magn. Reson. 43 (2012) 251–261.
[270] A. Zagdoun, G. Casano, O. Ouari, G. Lapadula, A.J. Rossini, M. Lelli, M. Baffert, D. Gajan, L. Veyre, W.E. Maas, M. Rosay, R.T. Weber, C. Thieuleux, C. Coperet, A. Lesage, P. Tordo, L. Emsley, A Slowly relaxing rigid biradical for efficient dynamic nuclear polarization surface-enhanced NMR spectroscopy: expeditious characterization of functional group manipulation in hybrid materials, J. Am. Chem. Soc. 134 (2012) 2284–2291.
[271] C. Sauvée, M. Rosay, G. Casano, F. Aussenac, R.T. Weber, O. Ouari, P. Tordo, Highly efficient, water-soluble polarizing agents for dynamic nuclear polarization at high frequency, Angew. Chem. Int. Ed. 52 (2013) 10858–10861.
[272] V.K. Michaelis, T.-C. Ong, M.K. Kiesewetter, D.K. Frantz, J.J. Walish, E. Ravera, C. Luchinat, T.M. Swager, R.G. Griffin, Topical developments in high-field dynamic nuclear polarization, Isr. J. Chem. 54 (2014) 207–221.
[273] P. Gast, D. Mance, E. Zurlo, K.L. Ivanov, M. Baldus, M. Huber, A tailored multi-frequency EPR approach to accurately determine the magnetic resonance parameters of dynamic nuclear polarization agents: application to AMUPol, Phys. Chem. Chem. Phys. 19 (2017) 3777–3781.

[274] A. Zagdoun, G. Casano, O. Ouari, M. Schwarzwalder, A.J. Rossini, F. Aussenac, M. Yulikov, G. Jeschke, C. Coperet, A. Lesage, P. Tordo, L. Emsley, Large molecular weight nitroxide biradicals providing efficient dynamic nuclear polarization at temperatures up to 200 K, J. Am. Chem. Soc. 135 (2013) 12790–12797.

[275] C. Sauvee, G. Casano, S. Abel, A. Rockenbauer, D. Akhmetzyanov, H. Karoui, D. Siri, F. Aussenac, W. Maas, R.T. Weber, T. Prisner, M. Rosay, P. Tordo, O. Ouari, Tailoring of polarizing agents in the bTurea series for cross-effect dynamic nuclear polarization in aqueous media, Chem. – Eur. J. 22 (2016) 5598–5606.

[276] D.J. Kubicki, G. Casano, M. Schwarzwalder, S. Abel, C. Sauvee, K. Ganesan, M. Yulikov, A.J. Rossini, G. Jeschke, C. Coperet, A. Lesage, P. Tordo, O. Ouari, L. Emsley, Rational design of dinitroxide biradicals for efficient cross-effect dynamic nuclear polarization, Chem. Sci. 7 (2016) 550–558.

[277] A.P. Jagtap, M.-A. Geiger, D. Stoppler, M. Orwick-Rydmark, H. Oschkinat, S.T. Sigurdsson, bcTol: a highly water-soluble biradical for efficient dynamic nuclear polarization of biomolecules, Chem. Commun. 52 (2016) 7020–7023.

[278] J. Mao, D. Akhmetzyanov, O. Ouari, V. Denysenkov, B. Corzilius, J. Plackmeyer, P. Tordo, T.F. Prisner, C. Glaubitz, Host-guest complexes as water-soluble high-performance DNP polarizing agents, J. Am. Chem. Soc. 135 (2013) 19275–19281.

[279] M.K. Kiesewetter, V.K. Michaelis, J.J. Walish, R.G. Griffin, T.M. Swager, High field dynamic nuclear polarization NMR with surfactant sheltered biradicals, J. Phys. Chem. B 118 (2014) 1825–1830.

[280] M. Lelli, A.J. Rossini, G. Casano, O. Ouari, P. Tordo, A. Lesage, L. Emsley, Hydrophobic radicals embedded in neutral surfactants for dynamic nuclear polarization of aqueous environments at 9.4 Tesla, Chem. Commun. 50 (2014) 10198–10201.

[281] T.-C. Ong, M.L. Mak-Jurkauskas, J.J. Walish, V.K. Michaelis, B. Corzilius, A.A. Smith, A.M. Clausen, J.C. Cheetham, T.M. Swager, R.G. Griffin, Solvent-free dynamic nuclear polarization of amorphous and crystalline ortho-terphenyl, J. Phys. Chem. B 117 (2013) 3040–3046.

[282] K.N. Hu, V.S. Bajaj, M. Rosay, R.G. Griffin, High-frequency dynamic nuclear polarization using mixtures of TEMPO and trityl radicals, J. Chem. Phys. 126 (2007) 044512.

[283] G. Mathies, M.A. Caporini, V.K. Michaelis, Y. Liu, K.-N. Hu, D. Mance, J.L. Zweier, M. Rosay, M. Baldus, R.G. Griffin, Efficient dynamic nuclear polarization at 800 MHz/527 GHz with trityl-nitroxide biradicals, Angew. Chem. Int. Ed. 54 (2015) 11770–11774.

[284] E.L. Dane, T. Maly, G.T. Debelouchina, R.G. Griffin, T.M. Swager, Synthesis of a BDPA-TEMPO Biradical, Org. Lett. 11 (2009) 1871–1874.

[285] N.S. Garif'yanov, B.M. Kozyrev, V.N. Fedotov, Width of the EPR line of liquid solutions of ethylene glycol complexes for even and odd chromium isotopes, Dokl. Phys. 13 (1968) 107.

[286] H. Glättli, M. Odehnal, J. Ezratty, A. Malinovski, A. Abragam, Polarisation dynamique des protons dans le glycol ethylique, Phys. Lett. A 29 (1969) 250–251.

[287] A.P. Stepanov, V.N. Fedotov, V.I. Baldin, N.B. Yunosov, Dynamic polarization of protons in Cr(V) and Mo(V) complex compound solutions in weak magnetic fields, Dokl. Akad. Nauk SSSR 194 (1970) 871.

[288] M. Borghini, T.O. Niinikoski, F. Udo, P. Weymuth, Dynamic polarization and relaxation of protons in 1,6-hexanediol and 1,8-octanediol: a feasibility study for a frozen spin polarized target, Nucl. Instrum. Methods 105 (1972) 215–220.

[289] W. De Boer, High proton polarization in 1,2-propanediol at ^{3}He temperatures, Nucl. Instrum. Methods 107 (1973) 99–104.

[290] J. Svoboda, Dynamic polarization and relaxation of protons in the glycerol:Cr (V) complex, J. Phys. C: Solid State Phys. 7 (1974) L144.

[291] A. Abragam, B. Bleaney, Electron Paramagnetic Resonance of Transition Metal Ions, Oxford University Press, Oxford, 1970.

[292] K.D. Bowers, J. Owen, Paramagnetic resonance II, Rep. Prog. Phys. 18 (1955) 304–375.

[293] R.H. Ruby, H. Benoit, C.D. Jeffries, Paramagnetic resonance below 1°K: spin-lattice relaxation of Ce^{3+} and Nd^{3+} in lanthanum magnesium nitrate, Phys. Rev. 127 (1962) 51–56.

[294] A.M. Raitsimring, A.V. Astashkin, O.G. Poluektov, P. Caravan, High-field pulsed EPR and ENDOR of Gd^{3+} complexes in glassy solutions, Appl. Magn. Reson. 28 (2005) 281–295.

[295] M. Benmelouka, J. Van Tol, A. Borel, M. Port, L. Helm, L.C. Brunel, A.E. Merbach, A high-frequency EPR study of frozen solutions of Gd-III complexes: straightforward determination of the zero-field splitting parameters and simulation of the NMRD profiles, J. Am. Chem. Soc. 128 (2006) 7807–7816.

[296] M. Qi, A. Groß, G. Jeschke, A. Godt, M. Drescher, Gd(III)-PyMTA label is suitable for in-cell EPR, J. Am. Chem. Soc. 136 (2014) 15366–15378.

[297] A. Martorana, G. Bellapadrona, A. Feintuch, E. Di Gregorio, S. Aime, D. Goldfarb, Probing protein conformation in cells by EPR distance measurements using Gd^{3+} spin labeling, J. Am. Chem. Soc. 136 (2014) 13458–13465.

[298] H. Kamimura, Anisotropic spin-orbit coupling of d^3 and d^8 solutes in corundum, Phys. Rev. 128 (1962) 1077–1084.

[299] S. Sugano, Y. Tanabe, Absorption spectra of Cr^{3+} in Al_2O_3 part A. Theoretical studies of the absorption bands and lines, J. Phys. Soc. Jpn. 13 (1958) 880–899.

[300] S. Sugano, I. Tsujikawa, Absorption spectra of Cr^{3+} in Al_2O_3 part B. Experimental studies of the zeeman effect and other properties of the line spectra, J. Phys. Soc. Jpn. 13 (1958) 899–910.

[301] H. Klein, U. Scherz, M. Schulz, H. Setyono, K. Wisznewski, Temperature dependence of the EPR spectrum of ruby, Z. Phys. B 28 (1977) 149–157.

[302] B. Corzilius, V.K. Michaelis, S.A. Penzel, E. Ravera, A.A. Smith, C. Luchinat, R.G. Griffin, Dynamic nuclear polarization of ^{1}H, ^{13}C, and ^{59}Co in a tris (ethylenediamine)cobalt(III) crystalline lattice doped with Cr(III), J. Am. Chem. Soc. 136 (2014) 11716–11727.

[303] B.R. McGarvey, Spin Hamiltonian for Cr III complexes. Calculation from crystal field and molecular orbital models and ESR determination for some ethylenediammine complexes, J. Chem. Phys. 41 (1964) 3743–3758.

[304] R.D. Shannon, Revised effective ionic radii and systematic studies of interatomic distances in halides and chalcogenides, Acta Crystallogr. Sect. A 32 (1976) 751–767.

[305] R.R. Ernst, G. Bodenhausen, A. Wokaun, Principles of Nuclear Magnetic Resonance in One and Two Dimensions, Oxford University Press, Oxford, 1987.

[306] A.J. Perez Linde, S. Chinthalapalli, D. Carnevale, G. Bodenhausen, Rotation-induced recovery and bleaching in magnetic resonance, Phys. Chem. Chem. Phys. 17 (2015) 6415–6422.

[307] T. Kobayashi, O. Lafon, A.S. Lilly Thankamony, I.I. Slowing, K. Kandel, D. Carnevale, V. Vitzthum, H. Vezin, J.-P. Amoureux, G. Bodenhausen, M. Pruski, Analysis of sensitivity enhancement by dynamic nuclear polarization in solid-state NMR: a case study of functionalized mesoporous materials, Phys. Chem. Chem. Phys. 15 (2013) 5553–5562.

[308] H. Takahashi, C. Fernández-de-Alba, D. Lee, V. Maurel, S. Gambarelli, M. Bardet, S. Hediger, A.-L. Barra, G. De Paëpe, Optimization of an absolute sensitivity in a glassy matrix during DNP-enhanced multidimensional solid-state NMR experiments, J. Magn. Reson. 239 (2014) 91–99.

[309] D. Mance, P. Gast, M. Huber, M. Baldus, K.L. Ivanov, The magnetic field dependence of cross-effect dynamic nuclear polarization under magic angle spinning, J. Chem. Phys. 142 (2015) 234201.

[310] G. Mathies, S. Jain, M. Reese, R.G. Griffin, Pulsed dynamic nuclear polarization with trityl radicals, J. Phys. Chem. Lett. 7 (2016) 111–116.

[311] P. Fricke, D. Mance, V. Chevelkov, K. Giller, S. Becker, M. Baldus, A. Lange, High resolution observed in 800 MHz DNP spectra of extremely rigid type III secretion needles, J. Biomol. NMR 65 (2016) 121–126.

[312] K.L. Ngai, S. Capaccioli, N. Shinyashiki, The protein "glass" transition and the role of the solvent, J. Phys. Chem. B 112 (2008) 3826–3832.

[313] E.J. Koers, E.A.W. van der Cruijsen, M. Rosay, M. Weingarth, A. Prokofyev, C. Sauvée, O. Ouari, J. van der Zwan, O. Pongs, P. Tordo, W.E. Maas, M. Baldus, NMR-based structural biology enhanced by dynamic nuclear polarization at high magnetic field, J. Biomol. NMR 60 (2014) 157–168.

[314] M.M. Maricq, J.S. Waugh, NMR in rotating solids, J. Chem. Phys. 70 (1979) 3300–3316.

[315] J.-M. Lopez del Amo, D. Schneider, A. Loquet, A. Lange, B. Reif, Cryogenic solid state NMR studies of fibrils of the Alzheimer's disease amyloid-β peptide: perspectives for DNP, J. Biomol. NMR 56 (2013) 359–363.

[316] A. Kubo, C.A. McDowell, Spectral spin diffusion in polycrystalline solids under magic-angle spinning, J. Chem. Soc., Faraday Trans. 1 84 (1988) 3713–3730.

[317] Z. Jia, L. Zhang, Q. Chen, E.W. Hansen, Proton spin diffusion in polyethylene as a function of magic-angle spinning rate. A phenomenological approach, J. Phys. Chem. A 112 (2008) 1228–1233.

[318] J.-N. Dumez, L. Emsley, A master-equation approach to the description of proton-driven spin diffusion from crystal geometry using simulated zero-quantum lineshapes, Phys. Chem. Chem. Phys. 13 (2011) 7363–7370.

[319] J.J. Wittmann, L. Hendriks, B.H. Meier, M. Ernst, Controlling spin diffusion by tailored rf-irradiation schemes, Chem. Phys. Lett. 608 (2014) 60–67.

[320] D.J. Kubicki, A.J. Rossini, A. Purea, A. Zagdoun, O. Ouari, P. Tordo, F. Engelke, A. Lesage, L. Emsley, Amplifying dynamic nuclear polarization of frozen solutions by incorporating dielectric particles, J. Am. Chem. Soc. 136 (2014) 15711–15718.

[321] P. Miéville, V. Vitzthum, M.A. Caporini, S. Jannin, S. Gerber-Lemaire, G. Bodenhausen, A spinning thermometer to monitor microwave heating and glass transitions in dynamic nuclear polarization, Magn. Reson. Chem. 49 (2011) 689–692.

[322] K.R. Thurber, A. Potapov, W.-M. Yau, R. Tycko, Solid state nuclear magnetic resonance with magic-angle spinning and dynamic nuclear polarization below 25 K, J. Magn. Reson. 226 (2013) 100–106.

[323] A.B. Siemer, K.-Y. Huang, A. McDermott, Protein linewidth and solvent dynamics in frozen solution NMR, PLoS One 7 (2012) e47242.

[324] A.H. Linden, W.T. Franks, U. Akbey, S. Lange, B.J. van Rossum, H. Oschkinat, Cryogenic temperature effects and resolution upon slow cooling of protein preparations in solid state NMR, J. Biomol. NMR 51 (2011) 283–292.

[325] Ü. Akbey, W.T. Franks, A. Linden, S. Lange, R.G. Griffin, B.J. van Rossum, H. Oschkinat, Dynamic nuclear polarization of deuterated proteins, Angew. Chem. Int. Ed. 49 (2010) 7803–7806.

[326] J. Mao, N.N. Do, F. Scholz, L. Reggie, M. Mehler, A. Lakatos, Y.S. Ong, S.J. Ullrich, L.J. Brown, R.C. Brown, J. Becker-Baldus, J. Wachtveitl, C. Glaubitz, Structural basis of the green-blue color switching in proteorhodopsin as determined by NMR spectroscopy, J. Am. Chem. Soc. 136 (2014) 17578–17590.

[327] J. Maciejko, M. Mehler, J. Kaur, T. Lieblein, N. Morgner, O. Ouari, P. Tordo, J. Becker-Baldus, C. Glaubitz, Visualizing specific cross-protomer interactions in the homo-oligomeric membrane protein proteorhodopsin by dynamic-nuclear-polarization-enhanced solid-state NMR, J. Am. Chem. Soc. 137 (2015) 9032–9043.

[328] T. Bauer, C. Dotta, L. Balacescu, J. Gath, A. Hunkeler, A. Bockmann, B.H. Meier, Line-broadening in low-temperature solid-state NMR spectra of fibrils, J. Biomol. NMR 67 (2017) 51–61.
[329] A.B. Barnes, B. Corzilius, M.L. Mak-Jurkauskas, L.B. Andreas, V.S. Bajaj, Y. Matsuki, M.L. Belenky, J. Lugtenburg, J.R. Sirigiri, R.J. Temkin, J. Herzfeld, R.G. Griffin, Resolution and polarization distribution in cryogenic DNP/MAS experiments, Phys. Chem. Chem. Phys. 12 (2010) 5861–5867.
[330] G.T. Debelouchina, M.J. Bayro, P.C.A. van der Wel, M.A. Caporini, A.B. Barnes, M. Rosay, W.E. Maas, R.G. Griffin, Dynamic nuclear polarization-enhanced solid-state NMR spectroscopy of GNNQQNY nanocrystals and amyloid fibrils, Phys. Chem. Chem. Phys. 12 (2010) 5911–5919.
[331] M.J. Bayro, G.T. Debelouchina, M.T. Eddy, N.R. Birkett, C.E. MacPhee, M. Rosay, W.E. Maas, C.M. Dobson, R.G. Griffin, Intermolecular structure determination of amyloid fibrils with magic-angle spinning and dynamic nuclear polarization NMR, J. Am. Chem. Soc. 133 (2011) 13967–13974.
[332] O.B. Peersen, S.O. Smith, Rotational resonance NMR of biological membranes, Concepts Magn. Reson. 5 (1993) 303–317.
[333] Q.Z. Ni, E. Markhasin, T.V. Can, B. Corzilius, K.O. Tan, A.B. Barnes, E. Daviso, Y. Su, J. Herzfeld, R.G. Griffin, Peptide and protein dynamics and low-temperature/DNP magic angle spinning NMR, J. Phys. Chem. B 121 (2017) 4997–5006.
[334] A. Baudot, L. Alger, P. Boutron, Glass-forming tendency in the system water-dimethyl sulfoxide, Cryobiology 40 (2000) 151–158.
[335] M.M. Rosay, Sensitivity Enhanced Nuclear Magnetic Resonance of Biological Solids, Chemistry, Massachusetts Institute of Technology, Cambridge, MA, 2001.
[336] A. Zagdoun, A.J. Rossini, D. Gajan, A. Bourdolle, O. Ouari, M. Rosay, W.E. Maas, P. Tordo, M. Lelli, L. Emsley, A. Lesage, C. Coperet, Non-aqueous solvents for DNP surface enhanced NMR spectroscopy, Chem. Commun. 48 (2012) 654–656.
[337] E. Ravera, B. Corzilius, V.K. Michaelis, C. Luchinat, R.G. Griffin, I. Bertini, DNP-Enhanced MAS NMR of bovine serum albumin sediments and solutions, J. Phys. Chem. B 118 (2014) 2957–2965.
[338] E. Ravera, B. Corzilius, V.K. Michaelis, C. Rosa, R.G. Griffin, C. Luchinat, I. Bertini, Dynamic nuclear polarization of sedimented solutes, J. Am. Chem. Soc. 135 (2013) 1641–1644.
[339] D. Le, G. Casano, T.N.T. Phan, F. Ziarelli, O. Ouari, F. Aussenac, P. Thureau, G. Mollica, D. Gigmes, P. Tordo, S. Viel, Optimizing sample preparation methods for dynamic nuclear polarization solid-state NMR of synthetic polymers, Macromolecules 47 (2014) 3909–3916.
[340] E. Elisei, M. Filibian, P. Carretta, S.C. Serra, F. Tedoldi, J.F. Willart, M. Descamps, A. Cesaro, Dynamic nuclear polarization of a glassy matrix prepared by solid state mechanochemical amorphization of crystalline substances, Chem. Commun. 51 (2015) 2080–2083.
[341] V. Vitzthum, F. Borcard, S. Jannin, M. Morin, P. Miéville, M.A. Caporini, A. Sienkiewicz, S. Gerber-Lemaire, G. Bodenhausen, Fractional spin-labeling of polymers for enhancing NMR sensitivity by solvent-free dynamic nuclear polarization, ChemPhysChem 12 (2011) 2929–2932.
[342] H. Takahashi, S. Hediger, G. De Paëpe, Matrix-free dynamic nuclear polarization enables solid-state NMR ^{13}C–^{13}C correlation spectroscopy of proteins at natural isotopic abundance, Chem. Commun. 49 (2013) 9479–9481.
[343] C. Fernández-de-Alba, H. Takahashi, A. Richard, Y. Chenavier, L. Dubois, V. Maurel, D. Lee, S. Hediger, G. De Paëpe, Matrix-free DNP-enhanced NMR spectroscopy of liposomes using a lipid-anchored biradical, Chem. – Eur. J. 21 (2015) 4512–4517.
[344] D. Gajan, M. Schwarzwälder, M.P. Conley, W.R. Grüning, A.J. Rossini, A. Zagdoun, M. Lelli, M. Yulikov, G. Jeschke, C. Sauvée, O. Ouari, P. Tordo, L. Veyre, A. Lesage, C. Thieuleux, L. Emsley, C. Copéret, Solid-phase polarization matrixes for dynamic nuclear polarization from homogeneously distributed radicals in mesostructured hybrid silica materials, J. Am. Chem. Soc. 135 (2013) 15459–15466.
[345] H. Takahashi, D. Lee, L. Dubois, M. Bardet, S. Hediger, G. De Paëpe, Rapid natural-abundance 2D ^{13}C–^{13}C correlation spectroscopy using dynamic nuclear polarization enhanced solid-state NMR and matrix-free sample preparation, Angew. Chem. Int. Ed. 51 (2012) 11766–11769.
[346] M.A. Voinov, D.B. Good, M.E. Ward, S. Milikisiyants, A. Marek, M.A. Caporini, M. Rosay, R.A. Munro, M. Ljumovic, L.S. Brown, V. Ladizhansky, A.I. Smirnov, Cysteine-specific labeling of proteins with a nitroxide biradical for dynamic nuclear polarization NMR, J. Phys. Chem. B 119 (2015) 10180–10190.
[347] E.A.W. van der Cruijsen, E.J. Koers, C. Sauvée, R.E. Hulse, M. Weingarth, O. Ouari, E. Perozo, P. Tordo, M. Baldus, Biomolecular DNP-supported NMR spectroscopy using site-directed spin labeling, Chem. – Eur. J. 21 (2015) 12971–12977.
[348] B.J. Wylie, B.G. Dzikovski, S. Pawsey, M. Caporini, M. Rosay, J.H. Freed, A.E. McDermott, Dynamic nuclear polarization of membrane proteins: covalently bound spin-labels at protein–protein interfaces, J. Biomol. NMR 61 (2015) 361–367.
[349] T. Viennet, A. Viegas, A. Kuepper, S. Arens, V. Gelev, O. Petrov, T.N. Grossmann, H. Heise, M. Etzkorn, Selective protein hyperpolarization in cell lysates using targeted dynamic nuclear polarization, Angew. Chem. Int. Ed. 55 (2016) 10746–10750.
[350] R. Rogawski, I.V. Sergeyev, Y. Li, M.F. Ottaviani, V. Cornish, A.E. McDermott, Dynamic nuclear polarization signal enhancement with high-affinity biradical tags, J. Phys. Chem. B 121 (2017) 1169–1175.
[351] A. Zagdoun, A.J. Rossini, M.P. Conley, W.R. Grüning, M. Schwarzwälder, M. Lelli, W.T. Franks, H. Oschkinat, C. Copéret, L. Emsley, A. Lesage, Improved dynamic nuclear polarization surface-enhanced NMR spectroscopy through controlled incorporation of deuterated functional groups, Angew. Chem. Int. Ed. 52 (2013) 1222–1225.
[352] F.A. Perras, R.R. Reinig, I.I. Slowing, A.D. Sadow, M. Pruski, Effects of biradical deuteration on the performance of DNP: towards better performing polarizing agents, Phys. Chem. Chem. Phys. 18 (2016) 65–69.
[353] A.J. Rossini, J. Schlagnitweit, A. Lesage, L. Emsley, High-resolution NMR of hydrogen in organic solids by DNP enhanced natural abundance deuterium spectroscopy, J. Magn. Reson. 259 (2015) 192–198.
[354] Ü. Akbey, S. Lange, W.T. Franks, R. Linser, K. Rehbein, A. Diehl, B.-J. van Rossum, B. Reif, H. Oschkinat, Optimum levels of exchangeable protons in perdeuterated proteins for proton detection in MAS solid-state NMR spectroscopy, J. Biomol. NMR 46 (2010) 67–73.
[355] M. Nagaraj, T.W. Franks, S. Saeidpour, T. Schubeis, H. Oschkinat, C. Ritter, B.-J. van Rossum, Surface binding of TOTAPOL assists structural investigations of amyloid fibrils by dynamic nuclear polarization NMR spectroscopy, ChemBioChem 17 (2016) 1308–1311.
[356] O. Lafon, A.S.L. Thankamony, T. Kobayashi, D. Carnevale, V. Vitzthum, Slowing II, K. Kandel, Vezin H., J.P. Amoureux, G. Bodenhausen, M. Pruski, Mesoporous silica nanoparticles loaded with surfactant: low temperature magic angle spinning C-13 and Si-29 NMR enhanced by dynamic nuclear polarization, J. Phys. Chem. C 117 (2013) 1375–1382.
[357] A. Lund, M.F. Hsieh, T.A. Siaw, S.I. Han, Direct dynamic nuclear polarization targeting catalytically active Al-27 sites, Phys. Chem. Chem. Phys. 17 (2015) 25449–25454.
[358] A.H. Linden, S. Lange, W.T. Franks, Ü. Akbey, E. Specker, B.-J. van Rossum, H. Oschkinat, Neurotoxin II bound to acetylcholine receptors in native membranes studied by dynamic nuclear polarization NMR, J. Am. Chem. Soc. 133 (2011) 19266–19269.
[359] R.A. Wind, F.E. Anthonio, M.J. Duijvestijn, J. Smidt, J. Trommel, G.M.C. de Vette, Experimental setup for enhanced ^{13}C NMR spectroscopy in solids using dynamic nuclear polarization, J. Magn. Reson. 52 (1983) 424–434.
[360] R.A. Wind, M.J. Duijvestijn, J. Vriend, Structural defects in undoped trans-polyacetylene, before and after air oxidation, studied by DNP-enhanced ^{13}C NMR, Solid State Commun. 56 (1985) 713–716.
[361] R.A. Wind, N. Zumbulyadis, R.H. Young, Y. Hung, L. Li, R.H.D. Nuttall, G. Maciel, EPR and ^{1}H and ^{13}C dynamic nuclear polarization studies of a molecularly doped polymer: bisphenol A polycarbonate doped with trianisylamine and trianisylaminium perchlorate, Solid State Nucl. Magn. Reson. 1 (1992) 55–65.
[362] R.A. Wind, M.J. Duijvestijn, C. van der Lugt, J. Smidt, H. Vriend, An investigation of coal by means of e.s.r., ^{1}H n.m.r., ^{13}C n.m.r. and dynamic nuclear polarization, Fuel 66 (1987) 876–885.
[363] H. Lock, R.A. Wind, G.E. Maciel, N. Zumbulyadis, ^{29}Si dynamic nuclear polarization of dehydrogenated amorphous silicon, Solid State Commun. 64 (1987) 41–44.
[364] R.A. Wind, H. Lock, M. Mehring, ^{13}C knight shift saturation and ^{1}H dynamic nuclear polarization in a polycrystalline sample of the organic conductor (fluoranthenyl)2PF6, Chem. Phys. Lett. 141 (1987) 283–288.
[365] R.H. Lewis, R.A. Wind, G.E. Maciel, Investigation of cured hydridopolysilazane-derived ceramic fibers via dynamic nuclear polarization, J. Mater. Res. 8 (1993) 649–654.
[366] H. Lock, R.A. Wind, G.E. Maciel, C.E. Johnson, A study of ^{13}C-enriched chemical vapor deposited diamond film by means of ^{13}C nuclear magnetic resonance, electron paramagnetic resonance, and dynamic nuclear polarization, J. Chem. Phys. 99 (1993) 3363–3373.
[367] M.J. Duijvestijn, R.A. Wind, J. Smidt, A quantitative investigation of the dynamic nuclear polarization effect by fixed paramagnetic centra of abundant and rare spins in solids at room temperature, Physica B+C 138 (1986) 147–170.
[368] M. Afeworki, R.A. McKay, J. Schaefer, Dynamic nuclear polarization enhanced nuclear magnetic resonance of polymer-blend interfaces, Mater. Sci. Eng., A 162 (1993) 221–228.
[369] M. Afeworki, S. Vega, J. Schaefer, Direct electron-to-carbon polarization transfer in homogeneously doped polycarbonates, Macromolecules 25 (1992) 4100–4105.
[370] M. Afeworki, J. Schaefer, Molecular dynamics of polycarbonate chains at the interface of polycarbonate/polystyrene heterogeneous blends, Macromolecules 25 (1992) 4097–4099.
[371] J. Zhou, B. Yang, J. Hu, H. Hu, L. Li, J. Qiu, F. Zeng, C. Ye, Investigation of a naphthalene pitch by high-resolution solid-state dynamic nuclear polarization, Solid State Nucl. Magn. Reson. 6 (1996) 127–133.
[372] M. Rosay, A.-C. Zeri, N.S. Astrof, S.J. Opella, J. Herzfeld, R.G. Griffin, Sensitivity-enhanced NMR of biological solids: dynamic nuclear polarization of Y21M fd bacteriophage and purple membrane, J. Am. Chem. Soc. 123 (2001) 1010–1011.
[373] M. Rosay, J.C. Lansing, K.C. Haddad, W.W. Bachovchin, J. Herzfeld, R.J. Temkin, R.G. Griffin, High-frequency dynamic nuclear polarization in MAS spectra of membrane and soluble proteins, J. Am. Chem. Soc. 125 (2003) 13626–13627.
[374] K. Märker, S. Paul, C. Fernández-de-Alba, D. Lee, J.-M. Mouesca, S. Hediger, G. De Paëpe, Welcoming natural isotopic abundance in solid-state NMR: probing π-stacking and supramolecular structure of organic nanoassemblies using DNP, Chem. Sci. 8 (2017) 974–987.

[375] Y. Geiger, H.E. Gottlieb, U. Akbey, H. Oschkinat, G. Goobes, Studying the conformation of a silaffin-derived pentalysine peptide embedded in bioinspired silica using solution and dynamic nuclear polarization magic-angle spinning NMR, J. Am. Chem. Soc. 138 (2016) 5561–5567.

[376] M.J. Bayro, M. Huber, R. Ramachandran, T.C. Davenport, B.H. Meier, M. Ernst, R.G. Griffin, Dipolar truncation in magic-angle spinning NMR recoupling experiments, J. Chem. Phys. 130 (2009) 114506.

[377] G.T. Debelouchina, M.J. Bayro, A.W. Fitzpatrick, V. Ladizhansky, M.T. Colvin, M.A. Caporini, C.P. Jaroniec, V.S. Bajaj, M. Rosay, C.E. MacPhee, M. Vendruscolo, W.E. Maas, C.M. Dobson, R.G. Griffin, Higher order amyloid fibril structure by MAS NMR and DNP spectroscopy, J. Am. Chem. Soc. 135 (2013) 19237–19247.

[378] A. Potapov, W.-M. Yau, R. Ghirlando, K.R. Thurber, R. Tycko, Successive stages of amyloid-β self-assembly characterized by solid-state nuclear magnetic resonance with dynamic nuclear polarization, J. Am. Chem. Soc. 137 (2015) 8294–8307.

[379] F. Weirich, L. Gremer, E.A. Mirecka, S. Schiefer, W. Hoyer, H. Heise, Structural characterization of fibrils from recombinant human islet amyloid polypeptide by solid-state NMR: the central FGAILS segment is part of the β-sheet core, PLoS One 11 (2016) e0161243.

[380] M. Mehler, F. Scholz, Sandra J. Ullrich, J. Mao, M. Braun, Lynda J. Brown, Richard C.D. Brown, Sarah A. Fiedler, J. Becker-Baldus, J. Wachtveitl, C. Glaubitz, The EF Loop in green proteorhodopsin affects conformation and photocycle dynamics, Biophys. J. 105 (2013) 385–397.

[381] Y.S. Ong, A. Lakatos, J. Becker-Baldus, K.M. Pos, C. Glaubitz, Detecting substrates bound to the secondary multidrug efflux pump EmrE by DNP-enhanced solid-state NMR, J. Am. Chem. Soc. 135 (2013) 15754–15762.

[382] M. Mehler, C.E. Eckert, A. Busche, J. Kulhei, J. Michaelis, J. Becker-Baldus, J. Wachtveitl, V. Dötsch, C. Glaubitz, Assembling a correctly folded and functional heptahelical membrane protein by protein trans-splicing, J. Biol. Chem. 290 (2015) 27712–27722.

[383] E.J. Koers, M.P. López-Deber, M. Weingarth, D. Nand, D.T. Hickman, D. Mlaki Ndao, P. Reis, A. Granet, A. Pfeifer, A. Muhs, M. Baldus, Dynamic nuclear polarization NMR spectroscopy: revealing multiple conformations in lipid-anchored peptide vaccines, Angew. Chem. Int. Ed. 52 (2013) 10905–10908.

[384] H. Kaur, A. Lakatos, R. Spadaccini, R. Vogel, C. Hoffmann, J. Becker-Baldus, O. Ouari, P. Tordo, H. McHaourab, C. Glaubitz, The ABC exporter MsbA probed by solid state NMR – challenges and opportunities, Biol. Chem. 396 (2015) 1135–1149.

[385] E. Lehnert, J. Mao, A.R. Mehdipour, G. Hummer, R. Abele, C. Glaubitz, R. Tampé, Antigenic peptide recognition on the human ABC transporter TAP resolved by DNP-enhanced solid-state NMR spectroscopy, J. Am. Chem. Soc. 138 (2016) 13967–13974.

[386] D. Stöppler, C. Song, B.-J. van Rossum, M.-A. Geiger, C. Lang, M.-A. Mroginski, A.P. Jagtap, S.T. Sigurdsson, J. Matysik, J. Hughes, H. Oschkinat, Dynamic Nuclear polarization provides new insights into chromophore structure in phytochrome photoreceptors, Angew. Chem. Int. Ed. 55 (2016) 16017–16020.

[387] S. Lange, W.T. Franks, N. Rajagopalan, K. Döring, M.A. Geiger, A. Linden, B.-J. van Rossum, G. Kramer, B. Bukau, H. Oschkinat, Structural analysis of a signal peptide inside the ribosome tunnel by DNP MAS NMR, Sci. Adv. 2 (2016) e1600379.

[388] I. Gelis, V. Vitzthum, N. Dhimole, M.A. Caporini, A. Schedlbauer, D. Carnevale, S.R. Connell, P. Fucini, G. Bodenhausen, Solid-state NMR enhanced by dynamic nuclear polarization as a novel tool for ribosome structural biology, J. Biomol. NMR 56 (2013) 85–93.

[389] M. Kaplan, S. Narasimhan, C. de Heus, D. Mance, S. van Doorn, K. Houben, D. Popov-Celeketic, R. Damman, E.A. Katrukha, P. Jain, W.J.C. Geerts, A.J.R. Heck, G.E. Folkers, L.C. Kapitein, S. Lemeer, P.M.P. van Bergen en Henegouwen, M. Baldus, EGFR dynamics change during activation in native membranes as revealed by NMR, Cell 167 (2016) 1241–1251.

[390] I.V. Sergeyev, L.A. Day, A. Goldbourt, A.E. McDermott, Chemical shifts for the unusual DNA structure in Pf1 bacteriophage from dynamic-nuclear-polarization-enhanced solid-state NMR spectroscopy, J. Am. Chem. Soc. 133 (2012) 20208–20217.

[391] R. Gupta, M. Lu, G. Hou, M.A. Caporini, M. Rosay, W. Maas, J. Struppe, C. Suiter, J. Ahn, I.J. Byeon, W.T. Franks, M. Orwick-Rydmark, A. Bertarello, H. Oschkinat, A. Lesage, G. Pintacuda, A.M. Gronenborn, T. Polenova, Dynamic nuclear polarization enhanced MAS NMR spectroscopy for structural analysis of HIV-1 protein assemblies, J. Phys. Chem. B 120 (2016) 329–339.

[392] T. Jacso, W.T. Franks, H. Rose, U. Fink, J. Broecker, S. Keller, H. Oschkinat, B. Reif, Characterization of membrane proteins in isolated native cellular membranes by dynamic nuclear polarization solid-state NMR spectroscopy without purification and reconstitution, Angew. Chem. Int. Ed. 51 (2012) 432–435.

[393] M. Renault, S. Pawsey, M.P. Bos, E.J. Koers, D. Nand, R. Tommassen-van Boxtel, M. Rosay, J. Tommassen, W.E. Maas, M. Baldus, Solid-state NMR spectroscopy on cellular preparations enhanced by dynamic nuclear polarization, Angew. Chem. Int. Ed. 51 (2012) 2998–3001.

[394] M. Kaplan, A. Cukkemane, G.C.P. van Zundert, S. Narasimhan, M. Daniels, D. Mance, G. Waksman, A.M.J.J. Bonvin, R. Fronzes, G.E. Folkers, M. Baldus, Probing a cell-embedded megadalton protein complex by DNP-supported solid-state NMR, Nat. Methods 12 (2015) 649–652.

[395] T. Wang, Y.B. Park, M.A. Caporini, M. Rosay, L. Zhong, D.J. Cosgrove, M. Hong, Sensitivity-enhanced solid-state NMR detection of expansin's target in plant cell walls, Proc. Natl. Acad. Sci. U.S.A. 110 (2013) 16444–16449.

[396] E. Ravera, V.K. Michaelis, T.-C. Ong, E.G. Keeler, T. Martelli, M. Fragai, R.G. Griffin, C. Luchinat, Biosilica-entrapped enzymes studied by using dynamic nuclear-polarization-enhanced high-field NMR spectroscopy, ChemPhysChem 16 (2015) 2751–2754.

[397] A. Jantschke, E. Koers, D. Mance, M. Weingarth, E. Brunner, M. Baldus, Insight into the supramolecular architecture of intact diatom biosilica from DNP-supported solid-state NMR spectroscopy, Angew. Chem. Int. Ed. 54 (2015) 15069–15073.

[398] J.A. Hubbard, L.K. MacLachlan, G.W. King, J.J. Jones, A.P. Fosberry, Nuclear magnetic resonance spectroscopy reveals the functional state of the signalling protein CheY in vivo in *Escherichia coli*, Mol. Microbiol. 49 (2003) 1191–1200.

[399] D.S. Burz, K. Dutta, D. Cowburn, A. Shekhtman, Mapping structural interactions using in-cell NMR spectroscopy (STINT-NMR), Nat. Meth. 3 (2006) 91–93.

[400] M.M. Dedmon, C.N. Patel, G.B. Young, G.J. Pielak, FlgM gains structure in living cells, Proc. Natl. Acad. Sci. U.S.A. 99 (2002) 12681–12684.

[401] L.A. Baker, M. Daniëls, E.A.W. van der Cruijsen, G.E. Folkers, M. Baldus, Efficient cellular solid-state NMR of membrane proteins by targeted protein labeling, J. Biomol. NMR 62 (2015) 199–208.

[402] K.K. Frederick, V.K. Michaelis, B. Corzilius, T.C. Ong, A.C. Jacavone, R.G. Griffin, S. Lindquist, Sensitivity-enhanced NMR reveals alterations in protein structure by cellular milieus, Cell 163 (2015) 620–628.

[403] C.P. Jaroniec, Structural studies of proteins by paramagnetic solid-state NMR spectroscopy, J. Magn. Reson. 253 (2015) 50–59.

[404] R.G. Griffin, Spectroscopy: clear signals from surfaces, Nature 468 (2010) 381–382.

[405] Z. Guo, T. Kobayashi, L.-L. Wang, T.W. Goh, C. Xiao, M.A. Caporini, M. Rosay, D. D. Johnson, M. Pruski, W. Huang, Selective host-guest interaction between metal ions and metal-organic frameworks using dynamic nuclear polarization enhanced solid-state NMR Spectroscopy, Chem. – Eur. J. 20 (2014) 16308–16313.

[406] T. Gutmann, J. Liu, N. Rothermel, Y. Xu, E. Jaumann, M. Werner, H. Breitzke, S. T. Sigurdsson, G. Buntkowsky, Natural abundance ^{15}N NMR by dynamic nuclear polarization: fast analysis of binding sites of a novel amine-carboxyl-linked immobilized dirhodium catalyst, Chem. – Eur. J. 21 (2015) 3798–3805.

[407] M. Werner, A. Heil, N. Rothermel, H. Breitzke, P.B. Groszewicz, A.S. Thankamony, T. Gutmann, G. Buntkowsky, Synthesis and solid state NMR characterization of novel peptide/silica hybrid materials, Solid State Nucl. Magn. Reson. 72 (2015) 73–78.

[408] D. Lee, G. Monin, N.T. Duong, I.Z. Lopez, M. Bardet, V. Mareau, L. Gonon, G. De Paëpe, Untangling the condensation network of organosiloxanes on nanoparticles using 2D ^{29}Si–^{29}Si solid-state NMR enhanced by dynamic nuclear polarization, J. Am. Chem. Soc. 136 (2014) 13781–13788.

[409] T. Kobayashi, D. Singappuli-Arachchige, Z. Wang, I.I. Slowing, M. Pruski, Spatial distribution of organic functional groups supported on mesoporous silica nanoparticles: a study by conventional and DNP-enhanced ^{29}Si solid-state NMR, Phys. Chem. Chem. Phys. 19 (2017) 1781–1789.

[410] N. Eedugurala, Z.R. Wang, U. Chaudhary, N. Nelson, K. Kandel, T. Kobayashi, Slowing II, M. Pruski, A.D. Sadow, Mesoporous silica-supported amidozirconium-catalyzed carbonyl hydroboration, Acs Catal. 5 (2015) 7399–7414.

[411] M.P. Conley, R.M. Drost, M. Baffert, D. Gajan, C. Elsevier, W.T. Franks, H. Oschkinat, L. Veyre, A. Zagdoun, A. Rossini, M. Lelli, A. Lesage, G. Casano, O. Ouari, P. Tordo, L. Emsley, C. Copéret, C. Thieuleux, A well-defined Pd hybrid material for the Z-selective semihydrogenation of alkynes characterized at the molecular level by DNP SENS, Chem. – Eur. J. 19 (2013) 12234–12238.

[412] R.P. Sangodkar, B.J. Smith, D. Gajan, A.J. Rossini, L.R. Roberts, G.P. Funkhouser, A. Lesage, L. Emsley, B.F. Chmelka, Influences of dilute organic adsorbates on the hydration of low-surface-area silicates, J. Am. Chem. Soc. 137 (2015) 8096–8112.

[413] W.R. Gruning, A.J. Rossini, A. Zagdoun, D. Gajan, A. Lesage, L. Emsley, C. Coperet, Molecular-level characterization of the structure and the surface chemistry of periodic mesoporous organosilicates using DNP-surface enhanced NMR spectroscopy, Phys. Chem. Chem. Phys. 15 (2013) 13270–13274.

[414] R. Graf, M.R. Hansen, D. Hinderberger, K. Muennemann, H.W. Spiess, Advanced magnetic resonance strategies for the elucidation of nanostructured soft matter, Phys. Chem. Chem. Phys. 16 (2014) 9700–9712.

[415] R.L. Johnson, F.A. Perras, T. Kobayashi, T.J. Schwartz, J.A. Dumesic, B.H. Shanks, M. Pruski, Identifying low-coverage surface species on supported noble metal nanoparticle catalysts by DNP-NMR, Chem. Commun. 52 (2016) 1859–1862.

[416] F.A. Perras, H. Luo, X. Zhang, N.S. Mosier, M. Pruski, M.M. Abu-Omar, Atomic-level structure characterization of biomass pre- and post-lignin treatment by dynamic nuclear polarization-enhanced solid-state NMR, J. Phys. Chem. A 121 (2017) 623–630.

[417] T.C. Ong, W.C. Liao, V. Mougel, D. Gajan, A. Lesage, L. Emsley, C. Coperet, Atomistic description of reaction intermediates for supported metathesis catalysts enabled by DNP SENS, Angew. Chem. Int. Ed. 55 (2016) 4743–4747.

[418] L. Zhao, W. Li, A. Plog, Y. Xu, G. Buntkowsky, T. Gutmann, K. Zhang, Multi-responsive cellulose nanocrystal-rhodamine conjugates: an advanced structure study by solid-state dynamic nuclear polarization (DNP) NMR, Phys. Chem. Chem. Phys. 16 (2014) 26322–26329.

[419] A.R. Mouat, C. George, T. Kobayashi, M. Pruski, R.P. van Duyne, T.J. Marks, P.C. Stair, Highly dispersed SiO_x/Al_2O_3 catalysts illuminate the reactivity of isolated silanol sites, Angew. Chem. Int. Ed. 54 (2015) 13346–13351.

[420] M. Valla, A.J. Rossini, M. Caillot, C. Chizallet, P. Raybaud, M. Digne, A. Chaumonnot, A. Lesage, L. Emsley, J.A. van Bokhoven, C. Coperet, Atomic description of the interface between silica and alumina in aluminosilicates through dynamic nuclear polarization surface-enhanced NMR spectroscopy and first-principles calculations, J. Am. Chem. Soc. 137 (2015) 10710–10719.
[421] F.A. Perras, J.D. Padmos, R.L. Johnson, L.-L. Wang, T.J. Schwartz, T. Kobayashi, J. H. Horton, J.A. Dumesic, B.H. Shanks, D.D. Johnson, M. Pruski, Characterizing substrate-surface interactions on alumina-supported metal catalysts by dynamic nuclear polarization-enhanced double-resonance NMR spectroscopy, J. Am. Chem. Soc. 139 (2017) 2702–2709.
[422] T. Gutmann, B. Kumari, L. Zhao, H. Breitzke, S. Schöttner, C. Rüttiger, M. Gallei, Dynamic nuclear polarization signal amplification as a sensitive probe for specific functionalization of complex paper substrates, J. Phys. Chem. C 121 (2017) 3896–3903.
[423] P. Berruyer, M. Lelli, M.P. Conley, D.L. Silverio, C.M. Widdifield, G. Siddiqi, D. Gajan, A. Lesage, C. Copéret, L. Emsley, Three-dimensional structure determination of surface sites, J. Am. Chem. Soc. 139 (2017) 849–855.
[424] S.L. Veinberg, K.E. Johnston, M.J. Jaroszewicz, B.M. Kispal, C.R. Mireault, T. Kobayashi, M. Pruski, R.W. Schurko, Natural abundance ^{14}N and ^{15}N solid-state NMR of pharmaceuticals and their polymorphs, Phys. Chem. Chem. Phys. 18 (2016) 17713–17730.
[425] A.C. Pinon, A.J. Rossini, C.M. Widdifield, D. Gajan, L. Emsley, Polymorphs of theophylline characterized by DNP enhanced solid-state NMR, Mol. Pharm. 12 (2015) 4146–4153.
[426] L. Piveteau, T.-C. Ong, A.J. Rossini, L. Emsley, C. Copéret, M.V. Kovalenko, Structure of colloidal quantum dots from dynamic nuclear polarization surface enhanced NMR spectroscopy, J. Am. Chem. Soc. 137 (2015) 13964–13971.
[427] C. Presti, A.S.L. Thankamony, J.G. Alauzun, P.H. Mutin, D. Carnevale, C. Lion, H. Vezin, D. Laurencin, O. Lafon, NMR and EPR characterization of functionalized nanodiamonds, J. Phys. Chem. C 119 (2015) 12408–12422.
[428] T. Kobayashi, S. Gupta, M.A. Caporini, V.K. Pecharsky, M. Pruski, Mechanism of solid-state thermolysis of ammonia borane: a ^{15}N NMR study using fast magic-angle spinning and dynamic nuclear polarization, J. Phys. Chem. C 118 (2014) 19548–19555.
[429] A.J. Rossini, A. Zagdoun, M. Lelli, J. Canivet, S. Aguado, O. Ouari, P. Tordo, M. Rosay, W.E. Maas, C. Copéret, D. Farrusseng, L. Emsley, A. Lesage, Dynamic nuclear polarization enhanced solid-state NMR spectroscopy of functionalized metal-organic frameworks, Angew. Chem. Int. Ed. 51 (2012) 123–127.
[430] F. Blanc, S.Y. Chong, T.O. McDonald, D.J. Adams, S. Pawsey, M.A. Caporini, A.I. Cooper, Dynamic nuclear polarization NMR spectroscopy allows high-throughput characterization of microporous organic polymers, J. Am. Chem. Soc. 135 (2013) 15290–15293.
[431] A.J. Rossini, C.M. Widdifield, A. Zagdoun, M. Lelli, M. Schwarzwälder, C. Copéret, A. Lesage, L. Emsley, Dynamic nuclear polarization enhanced NMR spectroscopy for pharmaceutical formulations, J. Am. Chem. Soc. 136 (2014) 2324–2334.
[432] A.S. Lilly Thankamony, C. Lion, F. Pourpoint, B. Singh, A.J. Perez Linde, D. Carnevale, G. Bodenhausen, H. Vezin, O. Lafon, V. Polshettiwar, Insights into the catalytic activity of nitridated fibrous silica (KCC-1) nanocatalysts from ^{15}N and ^{29}Si NMR spectroscopy enhanced by dynamic nuclear polarization, Angew. Chem. Int. Ed. 54 (2015) 2190–2193.
[433] G. Mollica, M. Dekhil, F. Ziarelli, P. Thureau, S. Viel, Quantitative structural constraints for organic powders at natural isotopic abundance using dynamic nuclear polarization solid-state NMR spectroscopy, Angew. Chem. Int. Ed. 54 (2015) 6028–6031.
[434] J. Leclaire, G. Poisson, F. Ziarelli, G. Pepe, F. Fotiadu, F.M. Paruzzo, A.J. Rossini, J.-N. Dumez, B. Elena-Herrmann, L. Emsley, Structure elucidation of a complex CO_2-based organic framework material by NMR crystallography, Chem. Sci. 7 (2016) 4379–4390.
[435] V.K. Michaelis, E. Markhasin, E. Daviso, J. Herzfeld, R.G. Griffin, Dynamic nuclear polarization of oxygen-17, J. Phys. Chem. Lett. 3 (2012) 2030–2034.
[436] F. Blanc, L. Sperrin, D.A. Jefferson, S. Pawsey, M. Rosay, C.P. Grey, Dynamic nuclear polarization enhanced natural abundance ^{17}O spectroscopy, J. Am. Chem. Soc. 135 (2013) 2975–2978.
[437] F.A. Perras, T. Kobayashi, M. Pruski, Natural abundance O-17 DNP two-dimensional and surface-enhanced NMR spectroscopy, J. Am. Chem. Soc. 137 (2015) 8336–8339.
[438] F.A. Perras, T. Kobayashi, M. Pruski, PRESTO polarization transfer to quadrupolar nuclei: implications for dynamic nuclear polarization, Phys. Chem. Chem. Phys. 17 (2015) 22616–22622.
[439] V. Vitzthum, P. Mieville, D. Carnevale, M.A. Caporini, D. Gajan, C. Coperet, M. Lelli, A. Zagdoun, A.J. Rossini, A. Lesage, L. Emsley, G. Bodenhausen, Dynamic nuclear polarization of quadrupolar nuclei using cross polarization from protons: surface-enhanced aluminium-27 NMR, Chem. Commun. 48 (2012) 1988–1990.
[440] D. Lee, H. Takahashi, A.S.L. Thankamony, J.-P. Dacquin, M. Bardet, O. Lafon, G. D. Paëpe, Enhanced solid-state NMR correlation spectroscopy of quadrupolar nuclei using dynamic nuclear polarization, J. Am. Chem. Soc. 134 (2012) 18491–18494.
[441] D. Lee, N.T. Duong, O. Lafon, G. De Paëpe, Primostrato solid-state NMR enhanced by dynamic nuclear polarization: pentacoordinated Al^{3+} ions are only located at the surface of hydrated γ-alumina, J. Phys. Chem. C 118 (2014) 25065–25076.
[442] F. Pourpoint, A.S.L. Thankamony, C. Volkringer, T. Loiseau, J. Trebosc, F. Aussenac, D. Carnevale, G. Bodenhausen, H. Vezin, O. Lafon, J.-P. Amoureux, Probing ^{27}Al-^{13}C proximities in metal-organic frameworks using dynamic nuclear polarization enhanced NMR spectroscopy, Chem. Commun. 50 (2014) 933–935.
[443] F. Pourpoint, J. Templier, C. Anquetil, H. Vezin, J. Trébosc, X. Trivelli, F. Chabaux, O.S. Pokrovsky, A.S. Prokushkin, J.-P. Amoureux, O. Lafon, S. Derenne, Probing the aluminum complexation by Siberian riverine organic matter using solid-state DNP-NMR, Chem. Geol. 452 (2017) 1–8.
[444] D.A. Hirsh, A.J. Rossini, L. Emsley, R.W. Schurko, ^{35}Cl dynamic nuclear polarization solid-state NMR of active pharmaceutical ingredients, Phys. Chem. Chem. Phys. 18 (2016) 25893–25904.
[445] D. Lee, C. Leroy, C. Crevant, L. Bonhomme-Coury, F. Babonneau, D. Laurencin, C. Bonhomme, G. De Paëpe, Interfacial Ca^{2+} environments in nanocrystalline apatites revealed by dynamic nuclear polarization enhanced ^{43}Ca NMR spectroscopy, Nat. Commun. 8 (2017) 14104.
[446] A.J. Perez Linde, D. Carnevale, P. Miéville, A. Sienkiewicz, G. Bodenhausen, Dynamic nuclear polarization enhancement of protons and vanadium-51 in the presence of pH-dependent vanadyl radicals, Magn. Reson. Chem. 53 (2015) 88–92.
[447] Z. Gan, Measuring amide nitrogen quadrupolar coupling by high-resolution ^{14}N/^{13}C NMR correlation under magic-angle spinning, J. Am. Chem. Soc. 128 (2006) 6040–6041.
[448] S. Cavadini, A. Lupulescu, S. Antonijevic, G. Bodenhausen, Nitrogen-14 NMR spectroscopy using residual dipolar splittings in solids, J. Am. Chem. Soc. 128 (2006) 7706–7707.
[449] R. Tycko, S.J. Opella, Overtone NMR spectroscopy, J. Chem. Phys. 86 (1987) 1761–1774.
[450] M. Bloom, M.A. LeGros, Direct detection of two-quantum coherence, Can. J. Phys. 64 (1986) 1522–1528.
[451] L.A. O'Dell, C.I. Ratcliffe, ^{14}N magic angle spinning overtone NMR spectra, Chem. Phys. Lett. 514 (2011) 168–173.
[452] L.A. O'Dell, A. Brinkmann, ^{14}N overtone NMR spectra under magic angle spinning: experiments and numerically exact simulations, J. Chem. Phys. 138 (2013) 064201.
[453] S. Cavadini, A. Abraham, G. Bodenhausen, Coherence transfer between spy nuclei and nitrogen-14 in solids, J. Magn. Reson. 190 (2008) 160–164.
[454] A.J. Rossini, L. Emsley, L.A. O'Dell, Dynamic nuclear polarisation enhanced ^{14}N overtone MAS NMR spectroscopy, Phys. Chem. Chem. Phys. 16 (2014) 12890–12899.
[455] W.R. Gunther, V.K. Michaelis, M.A. Caporini, R.G. Griffin, Y. Roman-Leshkov, Dynamic nuclear polarization NMR enables the analysis of Sn-beta zeolite prepared with natural abundance Sn-119 precursors, J. Am. Chem. Soc. 136 (2014) 6219–6222.
[456] M.P. Conley, A.J. Rossini, A. Comas-Vives, M. Valla, G. Casano, O. Ouari, P. Tordo, A. Lesage, L. Emsley, C. Coperet, Silica-surface reorganization during organotin grafting evidenced by Sn-119 DNP SENS: a tandem reaction of gem-silanols and strained siloxane bridges, Phys. Chem. Chem. Phys. 16 (2014) 17822–17827.
[457] L. Protesescu, A.J. Rossini, D. Kriegner, M. Valla, A. de Kergommeaux, M. Walter, K.V. Kravchyk, M. Nachtegaal, J. Stangl, B. Malaman, P. Reiss, A. Lesage, L. Emsley, C. Copéret, M.V. Kovalenko, Unraveling the core-shell structure of ligand-capped Sn/SnO_x nanoparticles by surface-enhanced nuclear magnetic resonance Mössbauer, and X-ray absorption spectroscopies, ACS Nano 8 (2014) 2639–2648.
[458] P. Wolf, M. Valla, A.J. Rossini, A. Comas-Vives, F. Núñez-Zarur, B. Malaman, A. Lesage, L. Emsley, C. Copéret, I. Hermans, NMR signatures of the active sites in Sn-β zeolite, Angew. Chem. Int. Ed. 53 (2014) 10179–10183.
[459] P. Wolf, M. Valla, F. Nunez-Zarur, A. Comas-Vives, A.J. Rossini, C. Firth, H. Kallas, A. Lesage, L. Emsley, C. Coperet, I. Hermans, Correlating synthetic methods, morphology, atomic-level structure, and catalytic activity of Sn-beta catalysts, Acs Catal. 6 (2016) 4047–4063.
[460] T. Kobayashi, F.A. Perras, T.W. Goh, T.L. Metz, W. Huang, M. Pruski, DNP-enhanced ultrawideline solid-state NMR spectroscopy: studies of platinum in metal-organic frameworks, J. Phys. Chem. Lett. 7 (2016) 2322–2327.
[461] T. Kobayashi, F.A. Perras, A. Murphy, Y. Yao, J. Catalano, S.A. Centeno, C. Dybowski, N. Zumbulyadis, M. Pruski, DNP-enhanced ultrawideline ^{207}Pb solid-state NMR spectroscopy: an application to cultural heritage science, Dalton Trans. 46 (2017) 3535–3540.
[462] A. Henstra, P. Dirksen, J. Schmidt, W.T. Wenckebach, Nuclear-spin orientation via electron-spin locking (NOVEL), J. Magn. Reson. 77 (1988) 389–393.
[463] C.T. Farrar, D.A. Hall, G.J. Gerfen, M. Rosay, J.H. Ardenkjær-Larsen, R.G. Griffin, High-frequency dynamic nuclear polarization in the nuclear rotating frame, J. Magn. Reson. 144 (2000) 134–141.
[464] V. Weis, M. Bennati, M. Rosay, R.G. Griffin, Solid effect in the electron spin dressed state: a new approach for dynamic nuclear polarization, J. Chem. Phys. 113 (2000) 6795–6802.
[465] H.J. Kim, E.A. Nanni, M.A. Shapiro, J.R. Sirigiri, P.P. Woskov, R.J. Temkin, Amplification of picosecond pulses in a 140-GHz gyrotron-traveling wave tube, Phys. Rev. Lett. 105 (2010) 135101.
[466] E.A. Nanni, S.M. Lewis, M.A. Shapiro, R.G. Griffin, R.J. Temkin, Photonic-band-gap traveling-wave gyrotron amplifier, Phys. Rev. Lett. 111 (2013) 235101.
[467] A. Henstra, P. Dirksen, W.T. Wenckebach, Enhanced dynamic nuclear-polarization by the integrated solid effect, Phys. Lett. A 134 (1988) 134–136.
[468] I. Kaminker, A. Potapov, A. Feintuch, S. Vega, D. Goldfarb, Population transfer for signal enhancement in pulsed EPR experiments on half integer high spin systems, Phys. Chem. Chem. Phys. 11 (2009) 6799–6806.
[469] A. Doll, S. Pribitzer, R. Tschaggelar, G. Jeschke, Adiabatic and fast passage ultra-wideband inversion in pulsed EPR, J. Magn. Reson. 230 (2013) 27–39.

[470] E.P. Saliba, E.L. Sesti, F.J. Scott, B.J. Albert, E.J. Choi, N. Alaniva, C. Gao, A.B. Barnes, Electron decoupling with dynamic nuclear polarization in rotating solids, J. Am. Chem. Soc. 139 (2017) 6310–6313.
[471] E. Salnikov, M. Rosay, S. Pawsey, O. Ouari, P. Tordo, B. Bechinger, Solid-state NMR spectroscopy of oriented membrane polypeptides at 100 K with signal enhancement by dynamic nuclear polarization, J. Am. Chem. Soc. 132 (2010) 5940–5941.
[472] E.S. Salnikov, O. Ouari, E. Koers, H. Sarrouj, T. Franks, M. Rosay, S. Pawsey, C. Reiter, P. Bandara, H. Oschkinat, P. Tordo, F. Engelke, B. Bechinger, Developing DNP/solid-state NMR spectroscopy of oriented membranes, Appl. Magn. Reson. 43 (2012) 91–106.
[473] A. Brinkmann, S.K. Vasa, H. Janssen, A.P.M. Kentgens, Proton micro-magic-angle-spinning NMR spectroscopy of nanoliter samples, Chem. Phys. Lett. 485 (2010) 275–280.
[474] C.-G. Joo, K.-N. Hu, J.A. Bryant, R.G. Griffin, In situ temperature jump high-frequency dynamic nuclear polarization experiments: enhanced sensitivity in liquid-state NMR spectroscopy, J. Am. Chem. Soc. 128 (2006) 9428–9432.
[475] C.-G. Joo, A. Casey, C.J. Turner, R.G. Griffin, In situ temperature-jump dynamic nuclear polarization: enhanced sensitivity in two dimensional ^{13}C–^{13}C correlation spectroscopy in solution, J. Am. Chem. Soc. 131 (2009) 12–13.
[476] D. Yoon, M. Soundararajan, C. Caspers, F. Braunmueller, J. Genoud, S. Alberti, J.-P. Ansermet, 500-fold enhancement of in situ ^{13}C liquid state NMR using gyrotron-driven temperature-jump DNP, J. Magn. Reson. 270 (2016) 142–146.
[477] M. Sharma, G. Janssen, J. Leggett, A.P.M. Kentgens, P.J.M. van Bentum, Rapid-melt dynamic nuclear polarization, J. Magn. Reson. 258 (2015) 40–48.
[478] P.J.M. van Bentum, M. Sharma, S.G.J. van Meerten, A.P.M. Kentgens, Solid effect DNP in a rapid-melt setup, J. Magn. Reson. 263 (2016) 126–135.

Glossary of abbreviations

AHT: average Hamiltonian theory
AMUPol: Aix-Marseille Université polarizing agent
API: active pharmaceutical ingredient
ASR: absolute sensitivity ratio
AWG: arbitrary waveform generator
bCTbK: bis-cyclohexyl-TEMPO-bisketal
BDPA: 1,3-bisdiphenylene-2-phenyl allyl
BRAIN-CP: broadband adiabatic inversion cross polarization
BT2E: bis-TEMPO-2-ethyleneglycol
bTbK: bis-TEMPO-bisketal
bTbtK: bis-TEMPO-bis-thioketal
bTbtK-py: bis-TEMPO-bis-thioketal-tetra-tetrahydropyran
BTnE: bis-TEMPO-n-ethyleneglycol
BTOXA: bis-TEMPO-oxalyl amide
bTtereph: bis-TEMPO terephthalate
bTurea: bis-TEMPO-urea
BWO: backward wave oscillator
CE: cross effect
ChR: channelrhodopsin
CIDNP: chemically induced dynamic nuclear polarization
CP: cross polarization
CPMG: Carr Purcell Meiboom Gill
CR: cross relaxation
CT: central transition
CTAB: cetyl trimethyl ammonium bromide
cw: continuous wave
dCE: direct cross effect
DCP: double cross polarization
DFT: density functional theory
D-HMQC: dipolar-mediated HMQC
DMSO: dimethyl sulfoxide
DNP: dynamic nuclear polarization
DNP-SENS: dynamic nuclear polarization surface enhanced NMR spectroscopy
DOM: dissolved organic matter
DOTA: 1,4,7,10-tetraazacyclododecane-1,4,7,10-tetraacetic acid
DOTOPA-TEMPO: 4-[N,N-di-(2-hydroxy-3-(TEMPO-4′-oxy)-propyl)]-amino-TEMPO
DPPH: diphenyl-picryl-hydrazyl
DQ: double quantum
DQC: double-quantum correlation
DQF: double-quantum filter
DsbA: disulfide oxidoreductase A
ECD: extracellular domain
EFG: electric field gradient
EGF: epidermal growth factor
EGFR: epidermal growth factor receptor
EIK: extended interaction klystron
EIO: extended interaction oscillator
ELDOR: electron–electron double resonance
EPR: electron paramagnetic resonance
ESEEM: electron spin echo envelope modulation
Ex-MSN: surfactant extracted mesoporous silica nanoparticle
FID: free induction decay
FMN: flavin mononucleotide
FS-TEDOR: frequency-selective transferred-echo double resonance
FWHH: full width at half height
HETCOR: heteronuclear correlation
HFI: hyperfine interaction
HMQC: heteronuclear multiple-quantum correlation
HSQC: heteronuclear single-quantum correlation
iCE: indirect cross effect
INADEQUATE: incredible natural abundance double quantum transfer experiment
KCC-1: fibrous nanosilica oxynitrides synthesized in KAUST Catalysis Center
KD: kinase domain
LAC: level anti crossing
LHe: liquid helium
LMN: lanthanum magnesium double nitrate
LN2: liquid nitrogen
MAS: magic-angle spinning
MD: molecular dynamics
MOF: metal-organic framework
MOP: microporous organic polymers
MQMAS: multiple-quantum MAS
MRI: magnetic resonance imaging
MRS: magnetic resonance spectroscopy
MSN: mesoporous silica nanoparticles
NMR: nuclear magnetic resonance
NQI: nuclear quadrupole interaction
OE: Overhauser effect
OT: overtone
OTP: ortho-terphenyl
PA: polarizing agent
PALI-melittin: Pro14-, Ala15-, Leu16-, and Ile17-isotopically-labeled peptide melittin
PC: polycarbonate
PCB: phycocyanobilin
PCS: pseudo-contact shift
PDSD: proton-driven spin diffusion
PEG: polyethyleneglycol
PHIP: para-hydrogen induced polarization
PI3-SH3: SH3 domain of the PI3 kinase
PMO: periodic mesoporous organosilicate
POST-C7: permutationally offset stabilized C7
PR: proteorhodopsin
PRE: paramagnetic relaxation enhancement
PRESTO: phase-shifted recoupling effects a smooth transfer of order
QCPMG: quadrupolar Carr Purcell Meiboom Gill
REDOR: rotational echo double resonance
RESPDOR: resonance echo saturation pulse double resonance
rf: radio frequency
SA-BDPA: sulfonated BDPA
SD: spin diffusion
SDSL: site-directed spin labeling
SE: solid effect
SEOP: spin-exchange optical pumping
S-MSN: mesoporous silica nanoparticles with surfactant
SN-BDPA: sulfonamide BDPA
SOSO: spinning-on spinning-off
SPC5: supercycled POST C5
SPIROPOL: bTbtK-py (bis-TEMPO-bis-thioketal-tetra-tetrahydropyran)
SQ: single quantum
SQC: single-quantum correlation
S-RESPDOR: symmetry based RESPDOR
ST: satellite transition
TAM: triarylmethyl
TAP: transporter associated with antigen processing
TCE: 1,1,2,2-tetrachloroethane
TEDOR: transferred echo double resonance
TEKPol: tetrakis(phenylcyclohexyl) TEMPO-bisketal
TEMPO: 2,2,6,6-tetramethyl-1-piperidiny-1-oxyl
TEMPOL: 4-hydroxy-TEMPO
TEMTriPol: TEMPO/trityl polarizing agent
THP: tetrahydropyran
ThT: thioflavin-T
TM: thermal mixing
TOTAPOL: 1-(TEMPO-4-oxy)-3-(TEMPO-4-amino)propan-2-ol
VT: variable temperature
WURST: wideband uniform rate and smooth truncation
YES: yttrium ethyl sulfate
ZFS: zero-field splitting
ZQ: zero quantum
μw: microwave